A STUDY ON $GE_5O(PO_4)_6$: AN OXIDE ION CONDUCTOR

Mark Tham

A Thesis Submitted for the Degree of PhD
at the
University of St Andrews

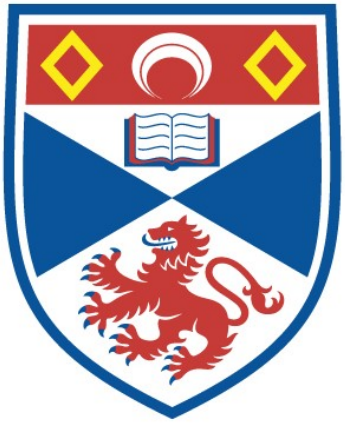

2016

A study on $Ge_5O(PO_4)_6$: an oxide ion conductor

Mark Tham

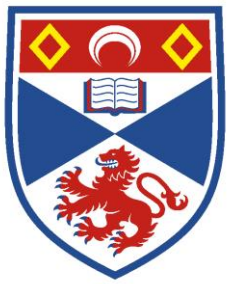

University of
St Andrews

This thesis is submitted in partial fulfilment for the degree of PhD
at the
University of St Andrews

27 April 2016

1. Candidate's declarations:

I, Mark Tham, hereby certify that this thesis, which is approximately 40,000 words in length, has been written by me, and that it is the record of work carried out by me, or principally by myself in collaboration with others as acknowledged, and that it has not been submitted in any previous application for a higher degree.

I was admitted as a research student in September 2011 and as a candidate for the degree of Doctor of Philosophy in August 2012; the higher study for which this is a record was carried out in the University of St Andrews between 2011 and 2016.

Date 25/04/16 signature of candidate ……

2. Supervisor's declaration:

I hereby certify that the candidate has fulfilled the conditions of the Resolution and Regulations appropriate for the degree of Doctor of Philosophy in the University of St Andrews and that the candidate is qualified to submit this thesis in application for that degree.

Date 25/04/16 signature of supervisor ……

3. Permission for publication:

In submitting this thesis to the University of St Andrews I understand that I am giving permission for it to be made available for use in accordance with the regulations of the University Library for the time being in force, subject to any copyright vested in the work not being affected thereby. I also understand that the title and the abstract will be published, and that a copy of the work may be made and supplied to any bona fide library or research worker, that my thesis will be electronically accessible for personal or research use unless exempt by award of an embargo as requested below, and that the library has the right to migrate my thesis into new electronic forms as required to ensure continued access to the thesis. I have obtained any third-party copyright permissions that may be required in order to allow such access and migration, or have requested the appropriate embargo below.

The following is an agreed request by candidate and supervisor regarding the publication of this thesis:

PRINTED COPY

a) Embargo on all or part of print copy for a period of 1 years (maximum five) on the following ground(s):
    - Publication would preclude future publication

Supporting statement for printed embargo request:

ELECTRONIC COPY

a) Embargo on all or part of electronic copy for a period of 1 years (maximum five) on the following ground(s):
    - Publication would preclude future publication

Supporting statement for electronic embargo request: Writing of publications is on going

Date 25/04/16 signature of candidate ……

signature of supervisor ……

Abbreviations

XRD	X-ray diffraction
NPD	Neutron powder diffraction
EDX	Energy-Dispersive X-Ray spectroscopy
SEM	Scanning Electron Microscopy
SOFC	Solid oxide fuel cell
EIS	Electrochemical Impedance spectroscopy
SXRD	Synchrotron X-ray diffraction
TGA	Thermogravimetric analysis
VT-XRD	Variable temperature X-ray diffraction
NTE	Negative thermal expansion
PSI	Paul Scherrer Institute
PSD	Positron-sensitive detector
EMF	Electromotive force
YSZ	Yttria- stabilised zirconia
TOF	Time-of-flight
MEM	Maximum entropy method
GSAS	General structural analysis software

Abstract

The work in this thesis concerns the synthesis, structural, and electrical analysis of the oxide ion conductor $Ge_5O(PO_4)_6$ and related materials. The syntheses of the materials were performed using the traditional solid state method.

Variable temperature NPD was performed on $Ge_5O(PO_4)_6$ and the isostructural material, $Si_5O(PO_4)_6$. For $Ge_5O(PO_4)_6$ this gave an insight into the oxygen conduction mechanism that occurs within the material. NPD provided experimental evidence of the origin of the mobile oxide ion within the 'excess' oxygen structure and the local lattice distortions that mobilise and stabilise migrating oxide ions. Fourier difference calculations were also performed to determine the location of interstitial oxide ions between the temperature range of 300-1073 K. In addition to this, the data was compared and contrasted to the $Si_5O(PO_4)_6$ NPD data to determine structural nuances between the two materials. A comparison of bond lengths and angles also showed there were local differences in the isostructural materials. The structural studies suggest that there was the formation of highly distorted SiO_6 when compared to the more ideal octahedral geometry of the GeO_6 subunit within $Ge_5O(PO_4)_6$.

Related materials are synthesised by the doping of cations such as Si, Sn, Ga, Al and Ti onto the Ge site. A solid solution was established between the Ge and Si end members. This was evaluated by the changes in unit cell parameters with varying Si:Ge ratios. Sn-doped materials were also evaluated. An increase in unit cell size for the Sn-doped materials suggested that tin was successfully entering the structure. Electrical measurements were also performed. It showed that $Ge_5O(PO_4)_6$ has a low activation energy for oxide ion conduction. Whilst the dopants of the Ga, Al and Ti doped compositions did not significantly improve oxide ion conducting properties, they gave an insight into the structural changes that effect oxide ion conductivity.

Acknowledgements

The work presented in this thesis would not be possible without the help and moral support provided by many people. Firstly, I would like to thank Professor. John Irvine for the fantastic opportunity to study within the University of St Andrews and his group. His supervision and guidance over the years has been vital for the completion of this thesis.

I would also like to thank many people within the J.T.S.I group for their help in relation to this work. Ms Julie Nairn has been extremely helpful over the years, providing the necessary equipment to perform experiments. I would also like to acknowledge her amazing ability to keep such a large lab running smoothly over the years I have been at St Andrews. For their useful discussions, I would like to acknowledge Dr Paul Connor for answering my chemistry related questions, Dr Stefan Saxin for his knowledge on the isostructural material, $Si_5O(PO_4)_6$, Dr Lewis Downie for his knowledge in the field of crystallography and for help collecting the neutron data and Dr Yaoqing Zhang for his contributions .Thanks goes to the SinQ neutron facility in Switzerland for providing the neutron beam time and Dr Denis Sheptyakov for help with carrying out the experiment. Ms Iona Ross has been a great source of moral support from within the J.T.S.I group, and for that I greatly acknowledge her.

Finally, I would like to thank my family for their moral support, patience and understanding over the last 4 years. In particular, I would like to thank my sister's Julie and Sally Tham for two reasons. Firstly, the huge number of free cigarettes obtained from them. Secondly, their unbelievable love and support throughout this time.

Contents

List of figures

1 Chapter 1: Introduction

This thesis is concerned with the study of $Ge_5O(PO_4)_6$ and related materials, with an emphasis on their ionic conducting properties and mechanisms. In this discussion it was advantageous to determine fundamental conduction mechanisms for solid electrolytes and how this applied to standard oxide ion conducting materials classed as vacancy, interstitial or interstitialcy oxide ion conductors. This gave an insight into the possible conduction mechanisms that may occur for $Ge_5O(PO_4)_6$, and therefore provided a platform for its future development.

1.1 Solid electrolytes

Solid electrolytes, or fast ion conductors, exhibit high ionic conductivity ($> 10^{-4}$ S cm^{-2})[1]. This involves the migration of ions through an ordered framework. Crystallographic defects typically facilitate the movement of ions through a structure and may be classed as intrinsic or extrinsic defects. A simplified explanation of the formation of intrinsic defects within a crystal may be derived from Gibbs free energy (Equation 1-1)[2].

Equation 1-1 $$\Delta \boldsymbol{G} = \Delta \boldsymbol{H} - \boldsymbol{T}\Delta \boldsymbol{S}$$

Equation 1 shows that at 0 K, Gibbs free energy is described by H. However, when temperatures increase entropy (S) begins to make larger contributions to free energy. This arises in the form of crystallographic defects within the structure to minimise free energy[3]. This may give rise to two types of point defects also known as Schottky and Frenkel. The former arises when oppositely charged atoms or ions leave the crystal lattice forming vacancies within the crystal structure. Frenkel defects are point defects when a single atom does not reside on a crystallographically defined point. Therefore, it resides within the interstitial spaces between atoms[1].

Extrinsic defects are caused by non-stoichiometric crystal compositions or on the addition of dopants to the crystal structure. There are a range of interactions that may occur from this. For example, yttria- stabilised zirconia (YSZ) forms vacancies on the anionic lattice, which is the predominant factor in its high ionic conductivity.

1.2 Conduction mechanisms

Depending on the type of defect the migration of ions may occur via three generalised mechanisms (Figure 1-1). These are also known as the vacancy, interstitial and interstitialcy mechanisms[3].

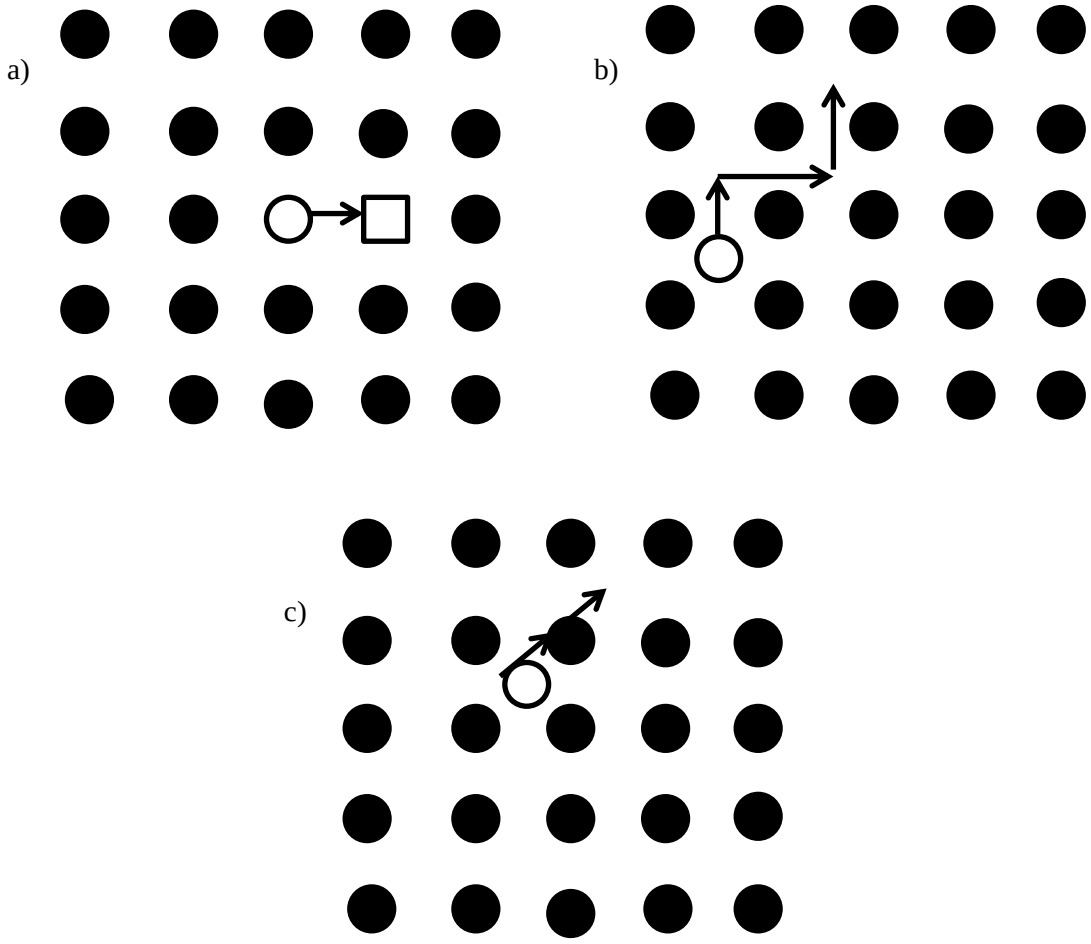

Figure 1-1. Schematic view of three ionic conduction mechanisms where a) shows the vacancy mechanism, (b) shows the interstitial mechanism and c) shows the interstitialcy mechanism.

Firstly, Figure 1-1a shows that the movement of atoms occurs via "hopping" into vacant lattice points. Secondly, as shown in Figure 1-1b, the interstitial mechanism occurs when the migration of atoms occurs through the interstitial spaces within the crystal structure. Finally, the intersticialcy mechanism (Figure 1-1c) occurs when there is an exchange of atoms from the interstitial site with a lattice site which can also be referred to as the "knock on" mechanism[4].

1.3 Oxide ion conductors

One of the first examples of mobile charge carriers are F^- and Ag^+ which were observed within the solids β-PbF_2 and AgI, respectively[3,5]. Subsequently, this has led to the discovery and development of new structures with different charge carriers that have a range of technological applications. One interesting subcategory of these materials is the oxide ion conducting ceramic oxides. Their ability

to permit fast oxide ionic transport has given them a number of functions within electrochemical devices. These include separation membranes, catalysts, membrane for methane conversion to syngas[6–9]. In addition to this, their application as an electrolyte in solid oxide fuel cells (SOFCs) has been of particular interest due to the current demand for alternative renewable energy sources[10]. As a result, there is a constant drive to improve the oxide ion conducting properties within these materials.

In this review traditionally used oxide ion conductors will be discussed which fall under the vacancy oxide ion conductor category. In addition to this, the well-established interstitial oxide ion conductors' lanthanum silicate apatite, calcium aluminate and melilite will be discussed. More specifically, their structural attributes and conduction mechanisms that allow for high oxide ion conductivity. Their structural attributes will then be compared to $Ge_5O(PO_4)_6$, a material that has distinctive structural features that may allow for oxygen transport.

1.4 Vacancy oxide ion conductors

1.4.1 Zirconia based electrolytes

The most commonly used fast oxide ion conductors adopt the fluorite structure with the composition AO_2 (A = tetravalent cation) as shown in Figure 1-2[10,11]. While, the most prominent of these is the acceptor doped Zirconia[1], pure ZrO_2 adopts the cubic fluorite structure at 2400 °C (Figure 1-2). However, on cooling it goes through phase transitions to the tetragonal and monoclinic polymorphs. In consequence, this involves the unit cell expansion of the material which may compromise its integrity[1].

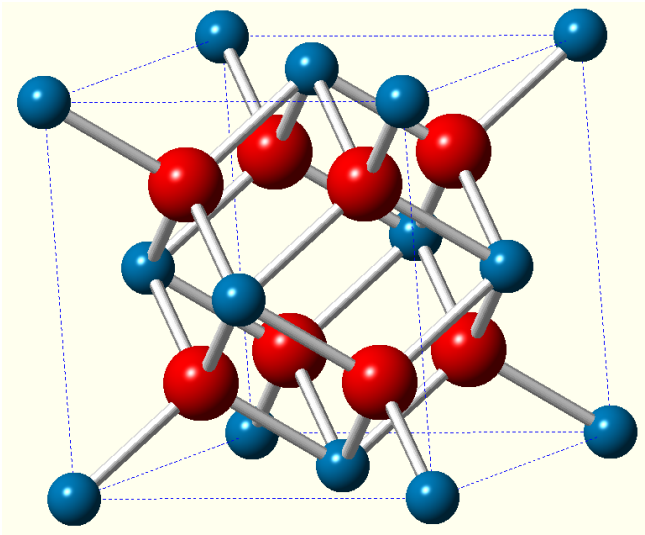

Figure 1-2. Diagram of fluorite structure blue sphere is Zr^{4+} and red spheres are oxygen. Zr^{4+} in tetrahedral coordination. Oxygen occupy the face and corners of the unit cell.

These unfavourable phase transitions are subsequently circumvented by doping of the crystal structure with aliovalent cations. This includes the substitution of Zr^{4+} cations with lower valence cations, of which a few examples are divalent Ca^{2+} and trivalent Sc^{3+} and Y^{3+}.[12] When compared to the pure ZrO_2 significant benefits can be seen for the doped-ZrO_2. Firstly, stabilisation of the cubic fluorite phase is achieved at room temperature; therefore avoiding large unit cell changes from transitions to the lower temperature ZrO_2 polymorphs. Secondly, it induces extrinsic defects to the structure in the form of anionic vacancies to maintain charge neutrality of the material. This allows for the movement of oxide ions through the structure[13]. Optimisation of the parameters that effect oxide ion conductivity has also been studied by a range of sources. These important factors include the concentration and ionic radii of the dopant. The effect on concentration level may be seen in (Figure 1-3) [14].

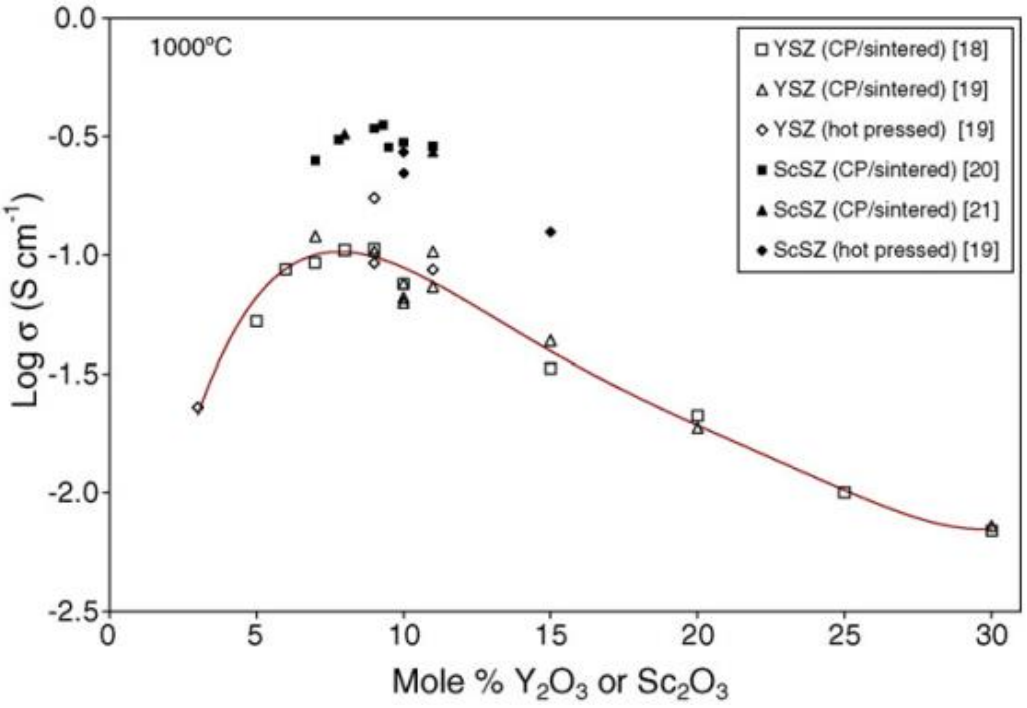

Figure 1-3. The effect of dopant concentration mol % on conductivity with for yttria and Scandia stabilised zirconia[14*].

Figure 1-3 shows with increasing yttria impurities an increase in extrinsic electrical conductivity is seen. This is directly related to the introduction of more vacancies to the anionic sub-lattice. However, this only occurs at low concentration levels. The highest conductivity is seen with 8 % mole YSZ; above this level degradation in performance is seen within the material[15]. This is

[*] Reprinted from *J. Power Sources*, 162, Fergus, J. W., Electrolytes for solid oxide fuel cells, 30–40., Copyright (2006), with permission from Elsevier

resultant from the formation of dopant-vacancy interactions which inhibits the movement of the oxygen vacancies[16]. Furthermore, the matching of cationic size is important for electrical conductivity, as can be seen in the case of scandia-stabilised zirconia (ScSZ) shown in the graph above. ScSZ represents an electrolyte that has higher electrical conducting properties with a lower activation energy when compared to YSZ [12,17]. This is attributed to the smaller difference between the substituting and host cationic radii of Sc^{3+} and Zr^{4+} which are 0.84 Å and 0.87 Å respectively[12,18]. It was confirmed through a range of atomistic and experimental studies that larger differences in ionic radii between the host and substituting cations introduced elastic strain to the crystal structure. This plays a significant role in the dopant-vacancy interaction[19].

1.4.2 Ceria based electrolytes

Unlike pure ZrO_2, CeO_2 exhibits cubic fluorite structure within its pure form. In this state CeO_2 represents a mixed conductor, where it exhibits conductivity in the form of electronic, ionic and hole mechanisms[20], although enhancements in ionic conductivity have been achieved through the doping of aliovalent cations[7]. The monovalent cation Na^+ compositions, $Ce_{0.95}Na_{0.05}O_{1.95}$ and $Ce_{0.93}Na_{0.07}O_{1.895}$ have been reported[21]. Unfortunately, the conductivity was comparable to that of pure CeO_2. The dopant effect of divalent alkaline earth oxides has been comprehensively studied by Arai. H *et al*[22] and Yahiro, H *et al*[23]. Their work showed that there were significant gains in ionic conductivity. However, it is the rare earth metal dopants that represent the highest conductivity within the ceria-based systems. Gd^{3+} doped systems (CGO) showed some of the higher conductivities. This was also related to a good match between the Ce^{4+} and Gd^{3+} ionic radii[24,25]. The high oxide ion conductivity seen in the Gd_2O_3 dopants systems have attracted attention for their potential use in intermediate temperature SOFCs (IT-SOFCs)[26]. This is due to the high oxide ion conductivity, particularly at lower temperatures between 500-700 °C. The largest problem with the use of CGO is that conductivity is no longer purely ionic at low partial pressures and temperatures above 600 °C[11]. There are contributions to conductivity through electronic conduction, resultant from the reduction of Ce^{4+} to Ce^{3+}[15].

1.4.3 Bismuth-based electrolytes

Undoped Bi_2O_3 has been reported to have 4 polymorphic variations which have been often described as α- , β-, γ-, δ-Bi_2O_3. α- , β-, γ-,Bi_2O_3 are the low temperature phases of undoped Bi_2O_3 where β-, γ-, Bi_2O_3 is formed on cooling from the δ-Bi_2O_3[27]. The structure of the high temperature phase δ-Bi_2O_3 was determined to be a simple cubic structure which belongs to the space group *Fm-3m*[28,29]. Moreover, the structure contains intrinsic oxygen vacancies accommodated by the removal of 25 % of the oxygen on the anionic sub-lattice. This is highest conductivity of any material reported with the value of ~ 1 Scm^{-1} at 750 °C[30,31]. However, δ-Bi_2O_3 has a very narrow temperature range in which it is thermodynamically stable; between its phase transition (α → δ) at 730 °C to the

melting point of 824 °C. This is problematic because the lower temperature polymorphic phases show relatively low oxide ion conductivity and the structural changes compromise the integrity of the material as previously seen with pure ZrO_2. The isovalent cations Y^{3+}, Er^{3+} and Gd^{3+} are among a few examples of cations capable of stabilising the δ-Bi_2O_3 cubic fluorite phase. Datta and Meehan[32], who studied the Y_2O_3-Bi_2O_3 system, suggested that the dopant concentration of 25 % mol Y_2O_3 led to a stable cubic δ-Bi_2O_3 at temperatures of ~ 400 °C, preserving its high oxide ion conductivity at lower temperatures. The Bi_2O_3-Er_2O_3 system emphasizes the optimisation of ionic radii for the improvement of oxide ion conductivity for the singly doped – Bi_2O_3[28]. Oxide ion conductivity improves with increasing ionic radii. But with increasing ionic radii, higher concentrations were required to stabilise the cubic fluorite phase which negatively impacted conducting performance.

As a result, Er^{3+} was found to be the most favourable dopant while Gd^{+3} required higher dopant levels which impacted conducting performance as can be seen in Figure 1-4.

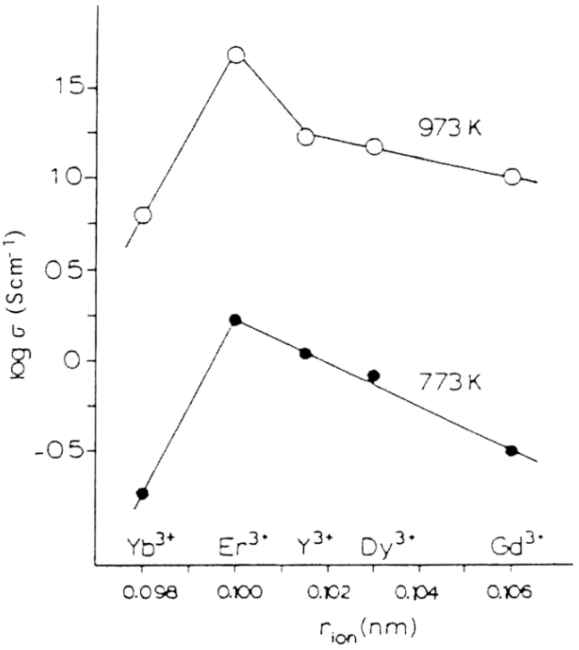

Figure 1-4. The conductivity of $(Bi_2O_3)_{1-x}(Ln_2O_3)_x$ against the ionic radii (in nm) of the Ln^{3+} ions at 737 K (filled circles and 973 K (open circles)[28]. Each point represents the minimum concentration required to stabilise the cubic fluorite phase. †

One of the highest reported conductivities for the Bi_2O_3-Er_2O_3 system was for the composition $(Bi_2O_3)_{0.8}(Er_2O_3)_{0.2}$. For this composition high oxide ion conductivity of 2 x 10^{-2} S cm^{-1} at 500 °C

† Reprinted from *J. Eur. Ceram.* Soc., **19**, Sammes, N. M., Tompsett, G. A., Näfe, H. & Aldinger, F., 1801–1826., Copyright (1999), with permission from Elsevier

and 0.4 S cm^{-1} at 700 $^{\circ}C$ was seen[15]. This shows very promising properties for the use in electrochemical devices. However, the major factor against its use is when operating in reducing conditions these compositions form Bi metal which is non-conductive[28].

1.4.4 Perovskite

ABO_3 denotes the general formula for the perovskite structure as shown in Figure 1-5. The structure is very important within solid state materials due to its rich chemistry afforded by its wide tolerance to a range of dopants.

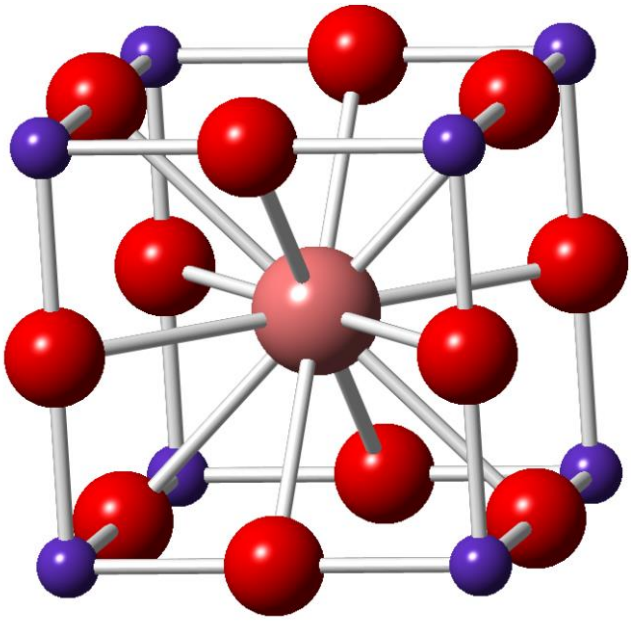

Figure 1-5. Crystal structure of cubic perovskite which consists of BO_6 octahedra with an A cation that is on a 12 coordinate site where red spheres are oxygen, pink spheres are A-cations and purple cations are B cations.[33]

$LaGaO_3$ is a well-studied perovskite material which upon doping is able to form oxygen vacancies that promotes the migration of ions via the vacancy mechanism. The structure is another example of a vacancy oxide ion conductor, but it does not hold the cubic fluorite structure. This conducting behaviour is seen within (Mg, Sr)-$LaGaO_3$ systems (also known as LSGM). Ishihara *et al*[34] reported that the LSGM derivative $La_{0.9}Sr_{0.1}Ga_{0.8}Mg_{0.2}O_{2.85}$ showed promising properties when compared to other high oxide conducting electrolytes. Its conductivity is higher than that of 8 % mol YSZ while being comparable to $Ce_{0.90}Gd_{0.10}O_{1.95}$ as can be seen in Figure 1-6 . In addition to this, LSGM has good chemical stability over a wide range of oxygen partial pressures (P_{O2} = 10^{-20} – 1 atm).

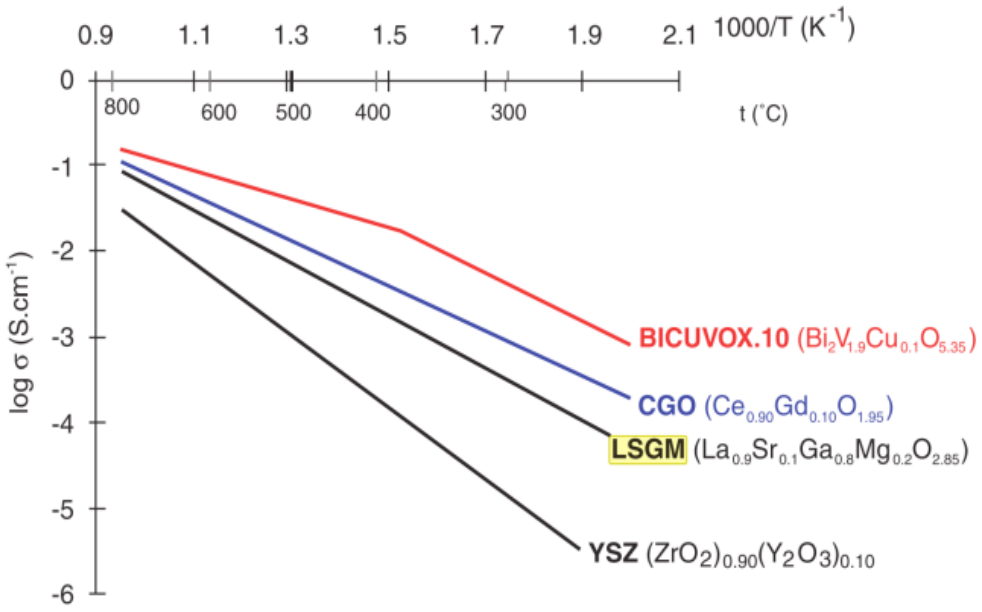

Figure 1-6. Conductivity measurements of LSGM against 8 mol % YSZ, 10 mol % CGO and Bicuvox[19].[‡]

Aging effects have been seen within LSGM[35], particularly after prolonged usage within SOFCs. Inter-diffusion is seen with LSGM and commonly used cathodic materials due to their similar perovskite structures which ultimately causes degradation in performance[36]. Additionally, aging effects in the formation of resistive layers with Ni-YSZ anodes has also been observed[14].

1.5 Interstitial ion conductors

Interstitial oxide ion conductors represent alternative materials to those seen from traditional vacancy oxide ion conductors. They show that distinctive structural features in combination with local lattice distortions can produce high oxide ion conductivity within ceramic oxides. In this section the conduction mechanism for the well-established interstitial oxide ion conductors that have the apatite, mayenite and melilite structures will be discussed. Their underlying structural attributes will then be compared to a novel oxide ion conductor, germanium oxide phosphate, $Ge_5O(PO_4)_6$.

1.5.1 Apatite structure

$A_{10}(BO_4)_6X_2$ denotes the stoichiometric formula for the ideal apatite structure. This structure is very interesting as it is seen in many functional materials however the compositions differ[37]. An important derivative of the structure is the lanthanide silicate family of oxide ion conductors. The structure of these materials adopts the usual apatite structure, with a hexagonal unit cell (space group : *P63/m*) as shown in Figure 1-7. It consists of isolated SiO_4 with La taking on 7 and

[‡] Reprinted from *Mater. Today*, 6, Skinner, S. J. & Kilner, J. A, Oxygen ion conductors., 30–37., Copyright (2003), with permission from Elsevier

9 coordination (Figure 1-7b-c respectively).The material is an ‘excess’ oxygen structure, which deviates from the traditionally used oxide ion conductors. Furthermore, the structure forms interesting structural features such as the channels of lanthanum and oxygen that run along the *c*-axis.

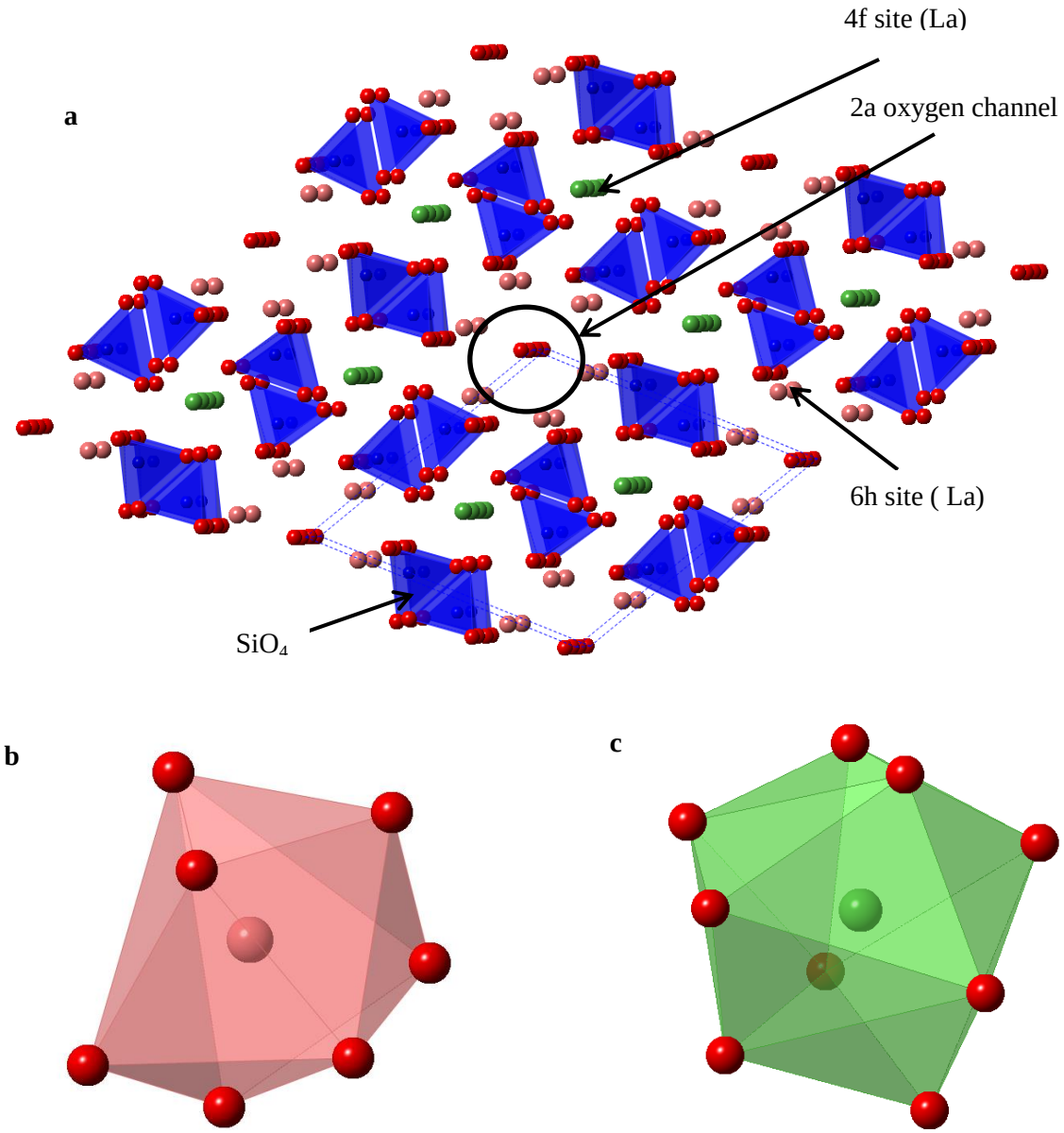

Figure 1-7. a) Schematic diagram of the crystal apatite-type crystal structure in $La_{10}(SiO_4)_6O_3$ showing SiO_4, La on 4f site (green), La on 6h site (pink) and oxygen along 2a channel (red): b) shows the 7-fold coordinate La (6h site) while c) shows the 9-coordinate La (4f La).

A study on the Lanthanide silicate series performed by Nakayama *et al*[38] showed that the structure allowed for high oxide ion conductivity. The stoichiometric lanthanum silicate composition, $La_{10}(SiO_4)_6O_3$, was shown to have the highest conductivity in the series that were tested. Electrical properties at intermediate temperatures were a notable feature within this material. When compared to $(ZrO_2)_{0.92}(Y_2O_3)_{0.08}$ and $(Bi_2O_3)_{0.75}(Y_2O_3)_{0.25}$ the material had higher conductivity at temperatures below 600 °C and 350 °C respectively. The charge carrier was also confirmed to be oxide ions as the EMF was consistent with the theoretical values derived from the Nernst equation between 500-800 °C.[38]

1.5.1.1 Conducting mechanisms

$La_{9.33}(SiO_4)_6O_2$ and $La_8Sr_2(SiO_4)_6O_2$ are derivatives of $La_{10}(SiO_4)_6O_3$. Experimental and atomistic studies on these materials gave an insight into the conduction mechanisms that can occur within the apatite structure. The key difference between the two materials is that $La_{9.33}(SiO_4)_6O_2$ is cation deficient, which leads to the formation of cation vacancies, whereas in $La_8Sr_2(SiO_4)_6O_2$ all the cation sites are filled. When comparing the conductivity of these two materials it can be seen that the cationic deficient material represents a good oxide ion conductor ($\sigma = 1.2 \times 10^{-4}$ S cm^{-1} at 700 °C). This is in contrast to $La_8Sr_2(SiO_4)_6O_2$, which is a poor oxide ion conductor ($\sigma = 2.9 \times 10^{-7}$ S cm^{-1} at 700 °C)[39].This suggested that nuances between the two structures allowed for a change in conductivity. Sansom. H *et al's*[39] neutron study revealed additional details between the two structures. For $La_{9.33}(SiO_4)_6O_2$, cationic vacancies were observed on the 4f site (La) and showed oxygen was missing from the 2a oxygen channel. The location of the missing oxygen was confirmed by the refinement of a possible oxide ion site at 0, 0, 0.38 which was shown to improve the structural model. However, for $La_8Sr_2(SiO_4)_6O_2$ refinement of a similar site led to no improvement to the structural model. This suggested that the disorder within the 2a oxygen channel, which is facilitated by lanthanum vacancies, was responsible for the high oxide ion conductivity within $La_{9.33}(SiO_4)_6O_2$[40].

Islam, S. *et al* [41] and Tolchard, J. *et al* [42] atomistic simulations gave an insight into the mechanisms that lie behind oxygen transport within these materials. They proposed two mechanisms; the vacancy and sinusoidal interstitial mechanisms as shown in Figure 1-8.

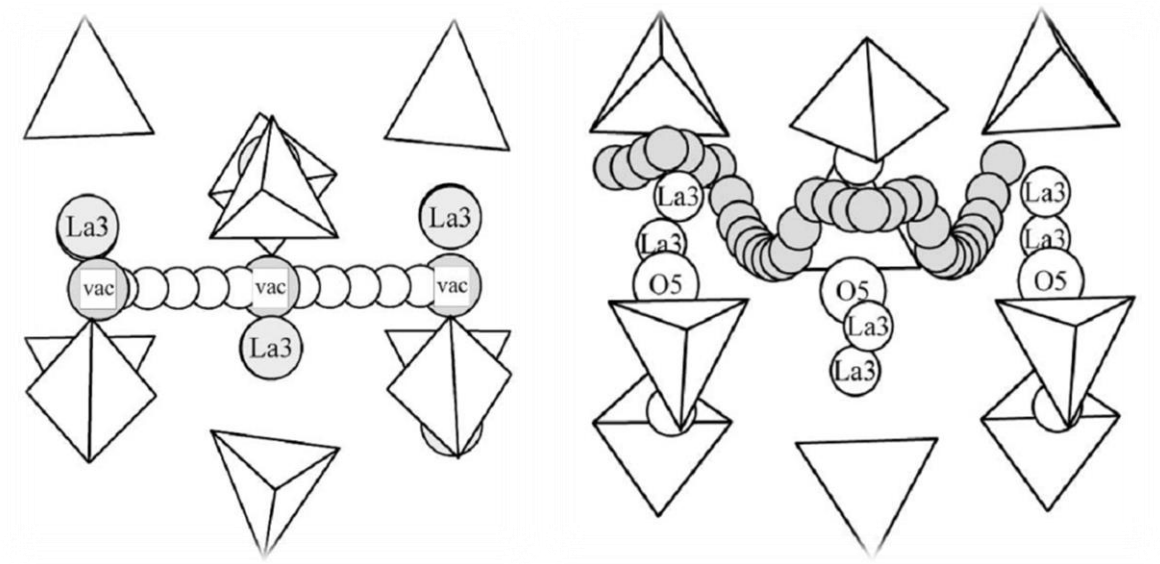

a) b)

Figure 1-8. Ionic conduction for lanthanum silicate[42] where a) shows the vacancy mechanism for the stoichiometric material whilst b) shows the interstitial sinusoidal mechanism that occurs perpendicular to the O5 oxide channel for the non-stoichiometric material.[§]

The data obtained suggested that the oxide ion transport within $La_8Sr_2(SiO_4)_6O_2$ occurred through a vacancy mechanism, whilst $La_{9.33}Si_6O_{26}$ proceeded via a non-linear pathway. Figure 1-8a, shows the vacancy mechanism for $La_8Sr_2(SiO_4)_6O_2$ is comparable to other vacancy oxide ion conductors. The key difference is that vacancies occur within the 2a oxygen channel and therefore conduction occurs anisotropically along the c-axis. For $La_{9.33}Si_6O_{26}$, oxygen transport occurs via a sinusoidal-like pathway of interstitial oxide ions that reside within the periphery of the 2a site oxygen channel. In order for this to occur in the cation deficient systems it must be partly facilitated by the displacement of the isolated SiO_4 tetrahedral units towards (4f site) cation channels. This provides a less restrictive structural environment for the movement of oxide ions.

1.5.1.2 Neutron diffraction

A key aspect of the sinusoidal-like pathway is that there is the presence of interstitial oxide ions within the periphery of the 2a oxygen channels. Further supporting evidence of interstitial oxide ions comes from an independent study of the archetypal material, $La_{9.55}(SiO_4)_6O_{2.32}$, by Leon-Reina, L, *et al*[43]. In their 2004 study they showed a refined interstitial oxide ion site located on -0.001(9) , 0.224(8) , 0.580(6) site. This corroborated with the atomistic simulations as discussed above. This showed the role of neutron diffraction to locate possible missing interstitial oxide ions to support oxide ion conduction mechanisms derived from atomistic simulations.

[§] Reproduced in part from Tolchard, J. R., Islam, M. S. & Slater, P. R. Defect chemistry and oxygen ion migration in the apatite-type materials $La_{9.33}Si_6O_{26}$ and $La_8Sr_2Si_6O_{26}$. *J.Mater.Chem.* **13,** 1956–1961 (2003) with permission of The Royal Society of Chemistry.

Guillot *et al*[43] also performed neutron powder diffraction on the material $La_{9.67}(SiO_4)_6O_{2.5}$. This showed that there was a possible interstitial site on -0.01, 0.04. 0.06, which resided more closely to the oxygen channel rather than the periphery indicative of the previous experiments. This corroborated well with Bechade, E. *et al*[44] from their atomic scale computation modelling in which an alternative mechanism was proposed as shown in Figure 1-9.

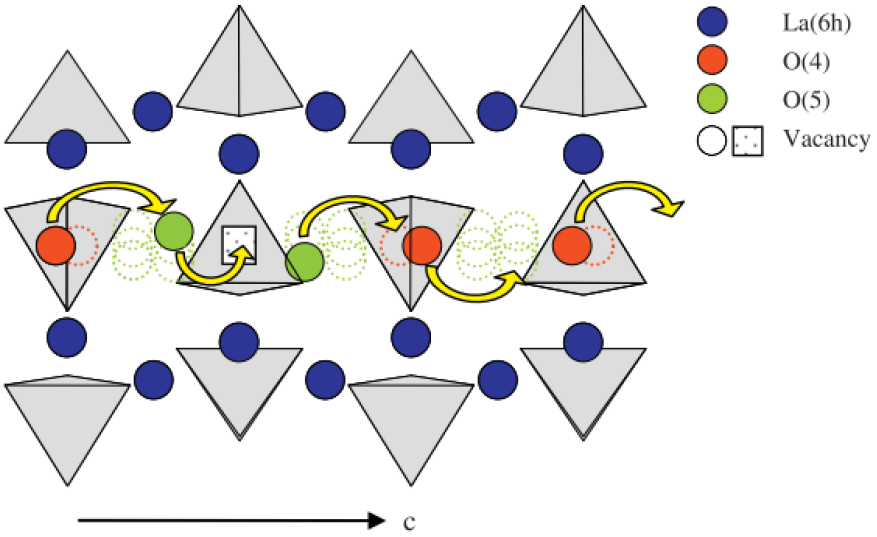

Figure 1-9. Alternative interstitial oxide ion conduction[43**]

This process involves a complex vacancy/interstitial mechanism. This typically involves interstitial oxide ions entering a vacant O4 site. To accommodate this, interstitial oxide ions adjacent to this step must move along the c-axis which causes displacement of an O4 oxide ion, leading to the formation of a new vacant site. At this point, the process begins again further along the c-axis.

1.5.1.3 Optimising oxide ion conductivity

In general high oxide ion conductivity within the apatite system depends on the introduction of "excess" interstitial oxygen. This is seen within the case of $La_8Sr_2(SiO_4)_6O_2$ which has the conductivity of 5.6 x 10^{-7} Scm^{-1} at 800 °C whilst $La_9Sr(SiO_4)_6O_{2.5}$ has ~4 magnitudes higher conductivity at 500 °C.[40]These compositions represent materials with the A sites filled with La and Sr. As Sr content increases from each composition there is a reduction in oxygen content thus this shows that high oxide ion conductivity is due to the difference in oxygen content.

The interplay with A-site cationic vacancies has also been explored. This can be observed for the compositions $La_{8.67}Sr(SiO_4)O_2$ and $La_{8.33}Sr_{1.5}(SiO_4)O_2$ where the oxygen content in the samples are the same however the former is approximately an order of magnitude higher in oxide ion

** Reprinted from *J. Solid State Chem.*, **182**, Guillot, S. *et al*. Evidence of local defects in the oxygen excess apatite $La_{9.67}(SiO_4)_6O_{2.5}$ from high resolution neutron powder diffraction., 3358–3364., Copyright (2009), with permission from Elsevier

conductivity. The difference between these materials is the number of A site cation vacancies. As the Sr content increases there is a decrease in cation vacancies which indicates the importance of optimising this parameter. In addition to this, the size of the cations also have an effect on the conductivity.

1.5.1.4 Doping to optimise oxide ion conductivity

Nakayama et al[38] synthesised a range of materials for the stoichiometric rare earth metal silicate series, $A_{10}(SiO_4)_6O_2$ (where A is Dy, Gd, Sm, Nd, Pr and La). It was shown that as the ionic radius of the A cation increases there was an improvement in ionic conductivity. This is further supported by the partial doping on the La site with divalent cations such as Ca, Sr and Ba [37].This increase in conductivity with larger ionic radii of the cation was attributed to an increased space to allow for a less restrictive structural environment to accommodate interstitial oxide ions[37]

The effect of doping on the Si-site is different to that seen on the La-site. According to modelling studies this site favours the smaller cations, although, Mg^{2+} has been experimentally shown to oppose this trend. This has been attributed to the larger ionic radius providing additional space within the unit cell and a lower electrostatic interaction with oxide ions.[45]

1.5.2 Mayenite

Mayenite, $Ca_{12}Al_{14}O_{33,}$ was most widely known in cement chemistry as a major constituent in clinker aluminites[46]. The structure crystallises in body centered cubic *I-43d* with the lattice constant of 11.99 Å and two formula units per unit cell[47]. This is shown in Figure 1-10.

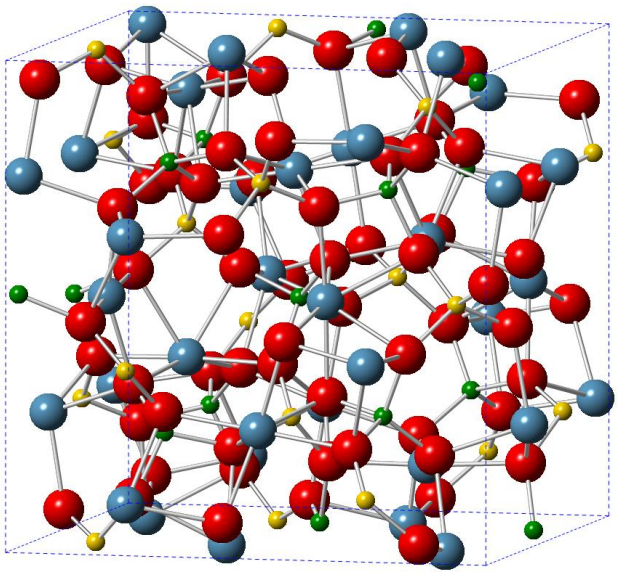

Figure 1-10. Illustration of the structure of $Ca_{12}Al_{14}O_{33}$ body centered cubic *I-43d*. Red spheres are oxygen, blue spheres are calcium, yellow spheres are Al(1) and finally green spheres are Al(2).

It forms 12 crystallographic cages from the Ca-Al-O lattice which contains 64 of the 66 oxygen per unit cell. The two remaining 'excess' oxygen are evenly distributed amongst one sixth of the cages to maintain charge neutrality. These cages are approximately 5-6 Å in diameter with the improper rotation (S_4) as shown in Figure 1-11.

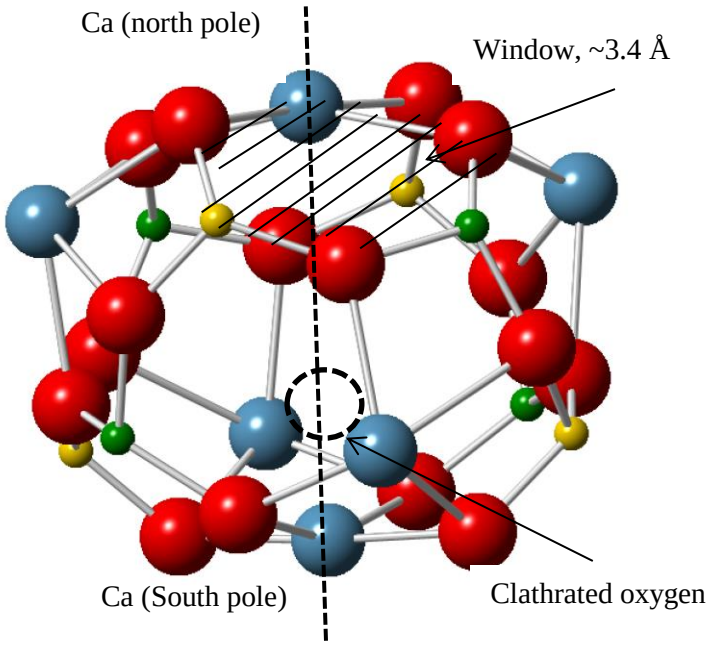

Figure 1-11. Illustration of the local cage structure for $Ca_{12}Al_{14}O_{33}$. The dotted line shows improper rotation of the cage, S_4. Oxygen are red spheres, blue spheres are calcium, yellow spheres are Al(1) and finally green spheres are Al(2). Dotted circle is representative of 'caged' oxide ion. Notice that Ca ions reside in a north and south pole position within the lattice of the cage.

The movement of these oxide ions throughout the material is facilitated by the interconnection of these cages via a six membered ring Ca-O-Al-O-Al-O windows which are ~ 3.7 Å in diameter. There is a significant interest in this material due to its complex defect chemistry which allows the partial exchange of loosely bound oxygen with active ionic species such, as e^-, to form a novel electride material.[48] Various other anionic species such as O^-, H^- have also been seen to replace oxide ions within the structure allowing a wide range of possible applications[49].

Pure oxide ion conductivity of the material was reported by Lacerda, M. *et al*[50]. They showed the material exhibited low activation energy of 0.74 eV with a high oxide ion conductivity, which was comparable to that of 8YSZ as shown in Figure 1-12.

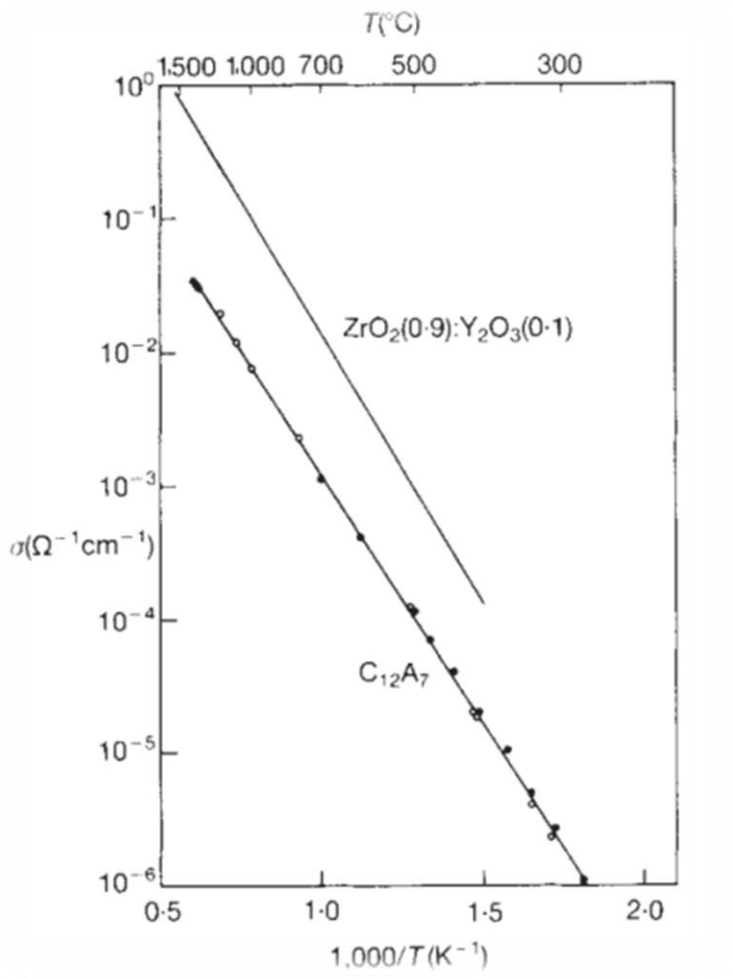

Figure 1-12. Comparison of ionic conductivity between YSZ and C12A7[50].[††]

1.5.2.1 Conduction mechanism

The key aspect of this structure is the presence of clathrated oxide ions, which maintain charge neutrality of the material and the method of which they migrate through the structure. Two competing processes were proposed for the conduction of oxide ions within the structure. The first entails an interstitial mechanism where the propagation of oxide ions occurs through the windows (or intercage opening)[50]. Secondly, an intersticialcy mechanism where there is an exchange of oxide ions from the rigid Ca-Al-O lattice.

Supporting evidence for the latter comes for *ab initio* calculations and MD simulations from Sushko, P. *et al*[51]. The former suggested that the lowest energy for oxygen transport was achieved through an interstitialcy type mechanism. This was related to the energy barrier required for each process. For the interstitial mechanism a much larger activation energy was seen (1.17 eV) when compared to (0.54 eV) for the interstitialcy mechanism. MD simulations gave an insight into the

[††] Reprinted by permission from Macmillan Publishers Ltd: Nature (Lacerda, M., Irvine, J. T. S., Glasser, F. P., & West, A. R. (1988). High oxide ion conductivity in $Ca_{12}Al_{14}O_{33}$. *Nature*, *332*(6164), 525–526.) Copyright (1988).

local lattice structure of the cage. It showed that some of the Ca vibrated ~ 1 Å from its atomic site. This was attributed to the local relaxation of the cage via the Ca north and south pole to accommodate O^{2-} diffusion throughout the structure. This highlights the ability of the structure to provide the spatial requirements of oxygen to move throughout the structure. Furthermore, it showed that the oxygen coordinated within the framework vibrated from its equilibrium site significantly more than the Ca and Al atoms. This suggested that the framework oxygen displacement from its site was more consistent with the clathrated oxide ions as shown in Figure 1-13.

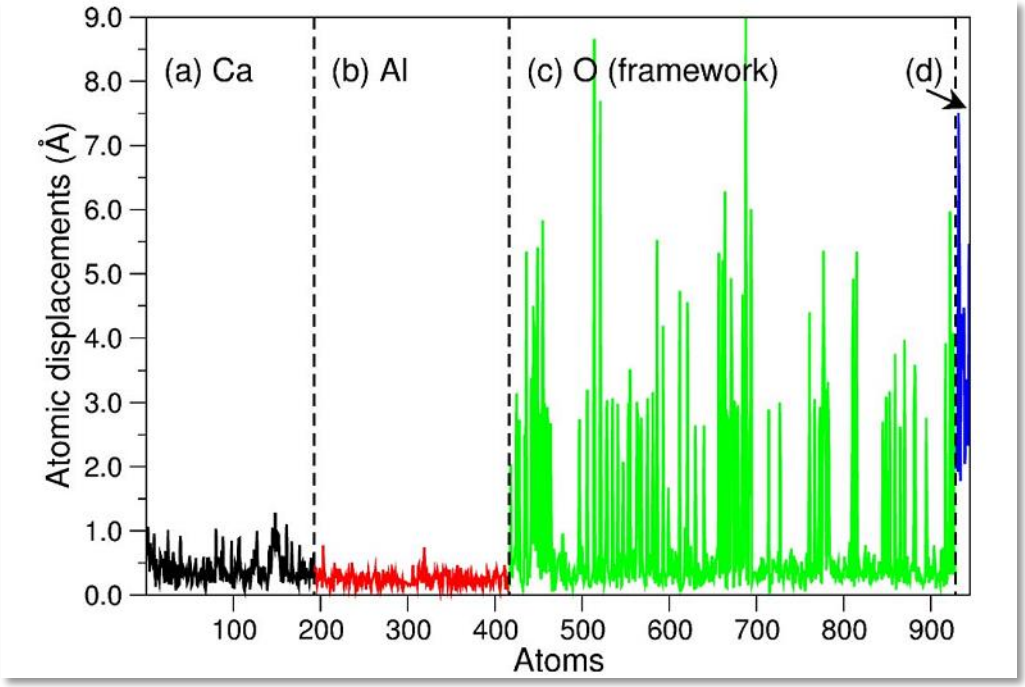

Figure 1-13. Illustration to show that the framework oxygen have similar atomic displace from its equilibrium site when compared to the clathrated oxygen and other atoms within the framework. The Blue line represents the atomic displacement of clathrated oxygen.[51]‡‡

It was suggested that if oxygen transport progressed via an interstitial mechanism the atomic displacement of the framework oxygen would not be as large as the mobile clathrated oxygen. Thus, it was proposed that a cooperative push-pull mechanism was responsible for the movement of oxygen within the structure. This involves the formation of a framework oxide ion vacancy within the lattice structure. The displaced oxide ion then moves into a space provided by the

‡‡ Reprinted figure with permission from as follows: Sushko, P. V, Shluger, A. L., Hayashi, K., Hirano, M., & Hosono, H, Mechanisms of oxygen ion diffusion in a nanoporous complex oxide $12CaO{\cdot}7Al_2O_3$, 73(1), 14101 and 2006. Copyright (2006) by the American Physical Society.
http://dx.doi.org/10.1103/PhysRevB.73.014101

inherently large cage which is further facilitated by the Ca at each pole of the cage. This allows for an interstitial oxide ion from a neighbouring cage to enter the lattice vacancy. The process allows for the oxygen to move freely throughout the structure relatively unhindered which is also shown by its low activation energy. Experimental evidence that corroborates with this has been observed by Boysen, H. *et al*[52] in which variable temperature neutron diffraction on $Ca_{12}Al_{14}O_{33}$ was performed. Furthermore, through their use of Fourier difference plots there appeared to be no appreciable density within the intercage opening at high temperatures. This suggested that there was no indication of the presence of interstitial oxide ions, therefore providing experimental evidence supporting the interstitialcy type mechanism.

1.5.3 Melilite

As previously mentioned, high oxide ion conductivity has been seen with the ceramic oxide LSGM. As a result it has been considered to be a major candidate for its application as an electrolyte in intermediate temperature fuels cells. One major issue in its use was the prominent formation of secondary phases such as $LaSrGaO_4$, $La_4Ga_2O_9$ and $LaSrGa_3O_7$. A range of experiments have been explored to find out the effect of the starting materials, sintering regimes, atmospheres and synthetic routes to form single phase LSGM[53]. However, impurities appeared to remain problematic in the formation of LSGM. Further phase diagrams studies also indicated the great difficulty in this problem as it showed that within the Ga_2O_3-La_2O_3-SrO system the most stable high-temperature ceramic oxide belonged to the impurity $La_{1+x}Sr_{1-x}Ga_3O_{7-\delta}$ system[54].The study of these impurities have shown these materials may have interesting oxide ion conducting properties[55]. Interestingly, $LaSrGa_3O_7$ has been shown to have low oxide ion conducting properties, and therefore its structure type has gained increasing interest as a potential oxide ion conductor. $LaSrGa_3O_7$ crystallizes with the tetragonal melilite-type structure, ABC_3O_7 (where A is a rare earth metal, B is an alkaline earth metal, C is aluminium, gallium or indium). The structure forms layers of GaO_4 which a linked by terminal oxygen. This forms distorted 5-fold tunnels which can be seen along the *c*-axis. When viewed along the *a*-*b* plane it can be seen that the La/Sr cations reside in between the GaO_4 layers and form an 8-coordinate environment Figure 1-14.[11]

1.5.3.1 Conduction mechanism

The highest conductivity is seen in $La_{1.54}Sr_{0.46}Ga_3O_{7.27}$ showing oxide conductivity of 0.02-0.1 Scm^{-1} over a temperature range of 600-900 °C from work performed by *Kuang et al*[55]. In this work, the presence of "excess" interstitial oxide ions within the structure is responsible for its high oxide ion conductivity. The combination of chemical composition and distinctive structural features allow for the stabilisation and mobilisation of oxide ions. The "excess" oxygen structure arises from the charge compensation of non-stoichiometric La/Sr ratios in the cationic layer. As La^{3+} content increases this replaces Sr^{2+} and as a result oxygen content increases to maintain charge neutrality. The location of the interstitial oxide ion was confirmed by performing Fourier

difference calculations on NPD data. This showed there was positive scattering density around a site (~0.33, ~0.17, ~0) which resides in the Gallate layer within the 5-fold tunnels between the La/Sr cations. This was further confirmed by MEM analysis of ambient temperature data, which showed a density in a similar location. The mobilisation and stabilisation of these interstitial oxide ions was attributed to the distinctive structural features of the material. The interatomic spacing between the La/Sr layers is suitably large (≈5.3 Å) to allow the spatial requirements for interstitial oxide ions to reside at its location. Gallate layer also takes part in this process as the "extra" oxygen is coordinated to the GaO_4 to form GaO_5. This showed the flexibility within the gallate cationic lattice to change coordination to allow for a 2D conduction process.

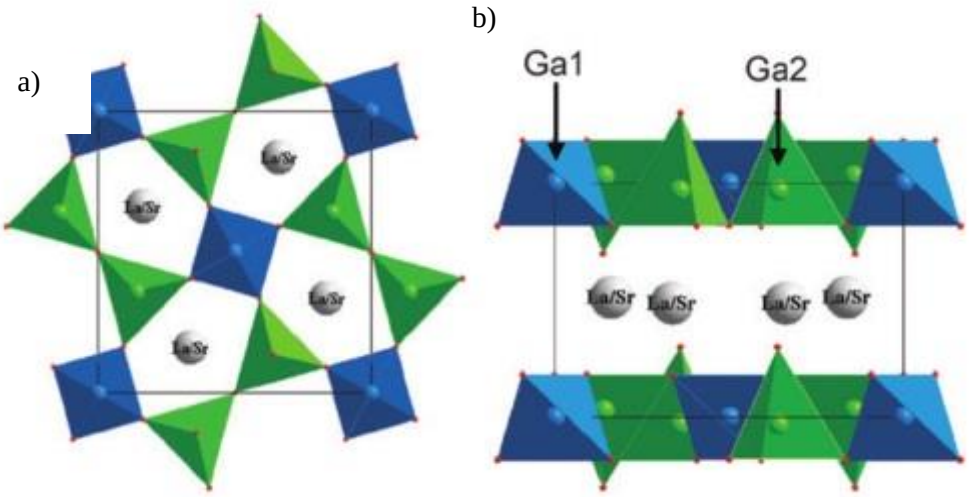

Figure 1-14. Illustration of $LaSrGa_3O_7$ where a) shows the unit cell along the *a*-axis and b) shows the unit cell along the *a*-*b* plane. Ga1 and Ga2 are represented by blue and green spheres respectively whilst grey spheres represent La/Sr cations.[11§§]

Doping studies have been performed on this material to improve oxide ion conductivity. B site doping has been performed using Ca, in the $La_{1+x}Ca_{1-x}Ga_3O_{7+0.5x}$. *Li et al*[56] reported the composition $La_{1.64}Ca_{0.36}Ga_3O_{7.32}$ enabled slightly higher conductivity when at higher temperatures.

Liu et al[57] reported on the effect of Ga deficient and excess systems. They reported altering the concentration of Ga by the following amounts x = -0.1, -0.05, 0 and 0.05 for $La_{1.54}Sr_{0.46}Ga_{3+x}O_{7.27+\delta}$. X = -0.05 and 0 samples were synthesised in pure melilite phase whereas x = -0.1 formed a $LaSrO_3$ impurity. The excess Ga sample formed $LaSrGaO_4$ and Ga_2O_3 impurities. The electrical conductivity examined on the two single phase samples showed the gallium deficient material had slightly higher conductivity at higher temperatures while at lower temperatures there

§§ Reproduced in part from Malavasi, L., Fisher, C. A. J. & Islam, M. S. Oxide-ion and proton conducting electrolyte materials for clean energy applications: structural and mechanistic features. *Chem.Soc.Rev*. 39, 4370–4387 (2010) with permission of The Royal Society of Chemistry

is an overall decrease in conductivity. *Liu et al* also reported the effects of substituting Gallium with Ge, In, Al or Zn. They determined that the doping of Ge or In on the gallium site yielded impurities. On the other hand, the doping of Al or Zn did slightly improve electrical conductivity but inhibited grain growth.

Jung, H. et al[58] synthesised a novel melilite type structure, $Sr_2(Mg_{1-x}Ga_x)Ge_2O_{7+0.5x}$. Their study showed that the optimal oxide ion conducting properties occurred when x = 2 whereas values greater than this showed a decrease in conductivity. The decrease in conductivity was attributed to the formation of impurities or Ga clustering and oxygen ordering. $Sr_2Mg_{O.8}Ga_{0.2}Ge_2O_{7.1}$ exhibited oxide ion conductivity of 10^{-4} Scm^{-1} at 800 °C. Similar to that seen within $La_{1.54}Sr_{0.46}Ga_3O_{7.27}$, it was suggested that the main charge carrier for this system were interstitial oxide ions within the gallate/germanium layer. The GeO_4 tetrahedra exhibited flexibility to transition to GeO_5 to accommodate mobile interstitial oxide ions Figure 1-15.

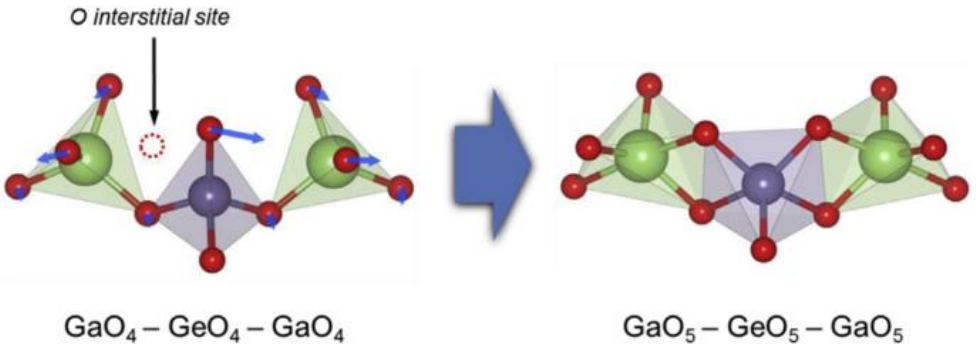

Figure 1-15. Schematic view of the coordination change GeO_4 to GeO_5 to stabilise and mobilise "excess" interstitial oxide ion.[58***]

1.5.4 Pentagermanium orthophosphate $Ge_5(PO_4)_6O$ Structure

An interesting structure which may represent a possible novel oxide ion conductor is $Ge_5O(PO_4)_6$. It was first synthesised by Mayer, H. *et al* in single crystal form[59]. This was later incorporated into the GeO_2-P_2O_5 binary phase diagram which was drawn by Mal'shikov, A.E. *et al*[60] shown in Figure 1-16.

Mayer, H. *et al* reported that the crystal structure of $Ge_5O(PO_4)_6$ belongs to the space group *R-3* with the unit cell parameters *a* = 7.94 Å ± 0.004 , *c* = 24.87 ± 0.01 Å and Z = 3. An illustration of the structure can be seen in Figure 1-17.

*** Reprinted from *J. Power Sources* , **275**, Jung, H. *et al*., $Sr_2(Mg_{1-x}Ga_x)Ge_2O_{7+0.5x}$: Melilite-type oxygen ionic conductor associated with fivefold coordinated germanium and gallium., 884–887., Copyright (2015), with permission from Elsevier

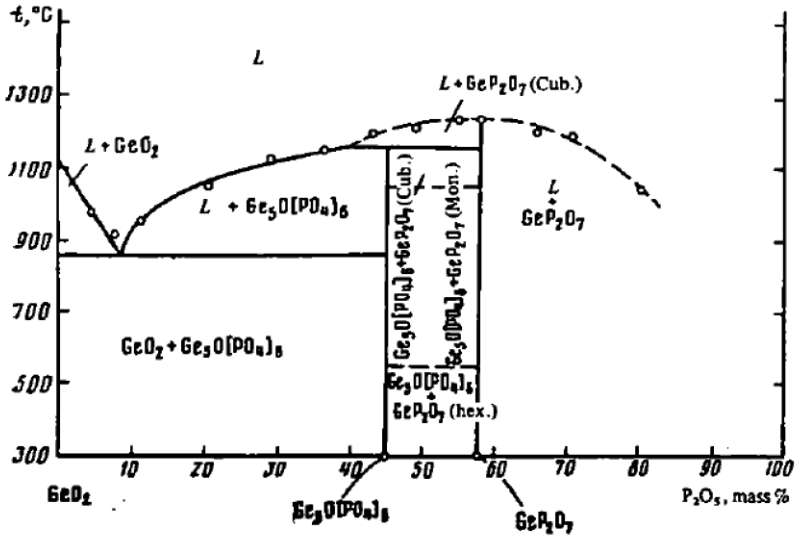

Figure 1-16. The GeO_2-P_2O_5 phase diagram[60].

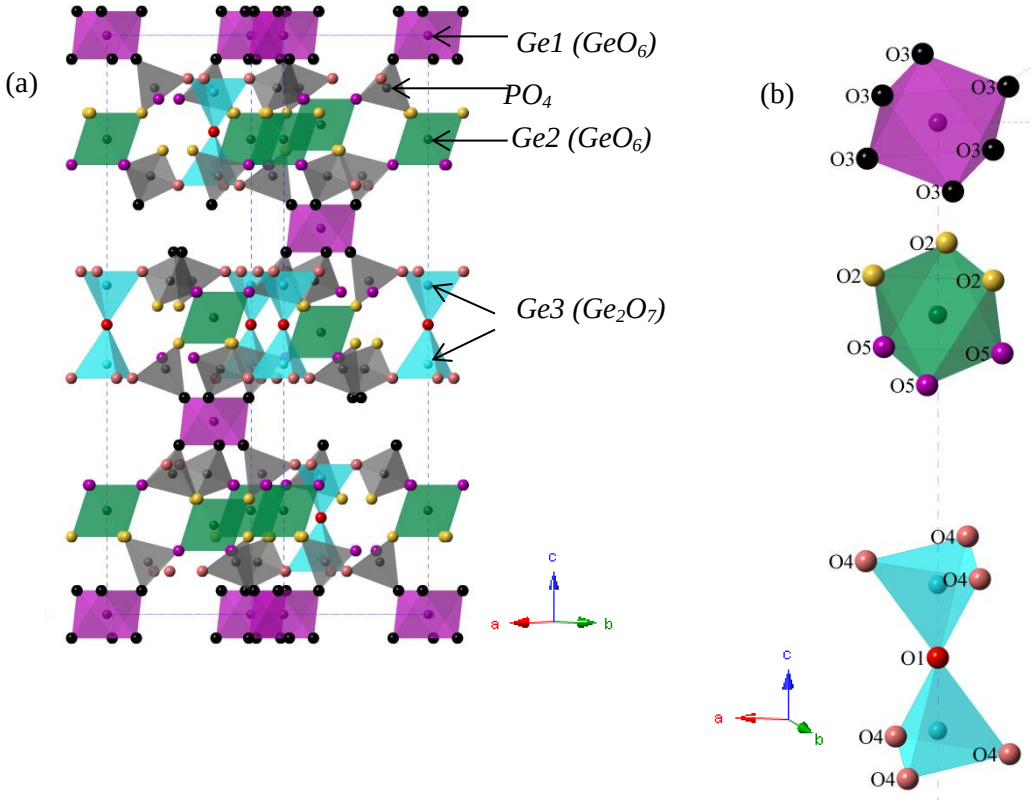

Figure 1-17. Projection of $Ge_5(PO_4)_6O$ where a) is the unit cell showing the atoms crystallography defined as Ge1 (purple), Ge2 (Green), Ge3 (light blue) and phosphorus (grey). b) shows the oxygen atoms crystallographically defined as O1 (red), O2 (yellow), O3 (black), O4 (pink) and O5 (purple)

The crystal structure of $Ge_5O(PO_4)_6$ consists of mixed GeO_6 octahedra and GeO_4 tetrahedra which are linked by PO_4 groups forming a three dimensional network (Figure 1-17). As a result the

chemical composition may be referred to as $Ge_3^{VI}Ge_2^{IV}O(PO_4)_6$ to reflect the two coordination states. There are three Ge environments within the structure which are aligned along the c-axis of the unit cell. Ge(1) and Ge(2) form GeO_6 octahedra. Ge(1) is coordinated with six symmetry related oxygen, O(3), whereas Ge(3) is coordinated with three symmetry related oxygen, O(2) and O(5). Ge(3) forms a GeO_4 tetrahedron with oxygen O(4) and O(1). These tetrahedral structures ultimately form a di-tetrahedral Ge_2O_7 that are linked to PO_4 tetrahedra through six terminal oxygen atoms. As a result, it forms the local structure, $P_6Ge_2O_{25}$, as shown in Figure 1-18. This local structure is a component of the dense layers that run parallel to the [001] plane which are linked through Ge(2)-O_6 octahedra, and so the layers may be referred to as $Ge_2P_6Ge_2O_{25}$[61]. The interlinking of these dense layers is further facilitated by Ge(1)-O_6 octahedra which form the 3D lattice[59,62,63].

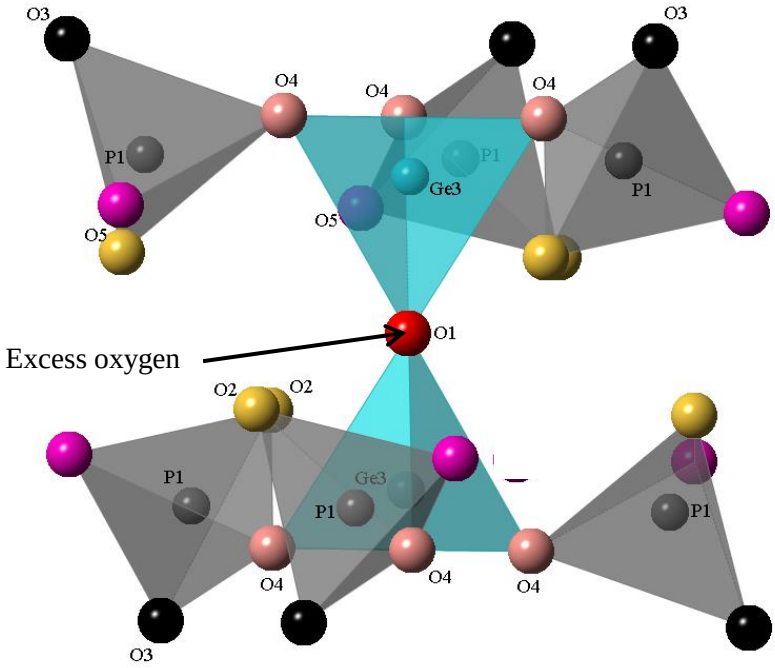

Figure 1-18. Di-tetrahedra local Ge structure, Ge_2O_7.

1.5.4.1 $Ge_5O(PO_4)_6$ an oxide ion conductor – structure

The material shows distinctive structural features which have been observed in other interstitial oxide ion conductors[45]. These features may allow for oxygen transport throughout the material. $La_{10}(SiO_4)_6O_3$, $Ca_{12}Al_{14}O_{33}$ and $La_{1.54}Sr_{0.46}Ga_3O_{7.27}$ represent 'excess' oxygen structures and have spatial requirements to allow mobile oxide ions to move through the structure as previously shown.

$Ge_5O(PO_4)_6$ also has an excess oxygen structure which is derived from an oxygen atom that is not connected to the rigid phosphate backbone as highlighted in Figure 1-18. Subsequently, it may provide a point of origin for the formation of mobile oxide ions. The structure may also provide a less restrictive structural environment for oxide ion mobility. This may be seen by the formation of

large cavities in between the dense layers by the interconnection of tunnels that run along the [100], [010] and [110] plane. In addition to this, the germanium atoms are aligned along the *c*-axis which may provide a platform for the mobilisation and stabilisation of mobile oxide ions anisotropically along the c-axis. This is similar to the melilite structures where the 2D layers of GaO_4 along the *a-b* plane are able to mobilise and stabilise oxide ions through changes in coordination state, and therefore is indicative of a flexible cation lattice. Germanium's ability to take part in this type of mechanism has also been probed by Jung, .H *et al*[58] where germanium was doped into the GaO_4 layers. Through computation methods it was shown that germanium was capable of taking part in the migration of interstitial oxide ions through the 2D layers.

1.5.4.2 Conducting properties

Zhang, Y. *et al*[45] showed that the material was a pure oxide ion conductor by assessing whether there were any protonic or electronic contributions to total conductivity. The possibility of protonic conduction for the material was assessed through the use of AC impedance in dry N_2, humidified N_2 and lab air. It was shown through the Arrhenius plots derived from this data that total conductivity remained similar to one another in each atmosphere. This suggested that protonic contribution to total conductivity was negligible as no significant increase in conductivity was seen in humidified atmospheres. Furthermore, electronic contribution to conductivity was also ruled out through an O_2 gas concentration cell. The EMF results showed that the material had a transport number close to unity at the temperatures of 650 °C and 750 °C, suggesting that electronic contributions to conductivity were negligible.

1.5.4.3 Structures relating to $Ge_5O(PO_4)_6$

The di-tetrahedral local structure seen in $Ge_5O(PO_4)_6$ is a common feature among a range of silicophosphates. The most obvious would be the silicate analogue, $Si_5O(PO_4)_6$, which can be synthesised in a similar manner to $Ge_5O(PO_4)_6$[62,63]. Silicon is more commonly in 4-fold coordination with oxygen in tetrahedral geometry as in a variety of silicas and silicates.[64] Stishovite is an example of Si in octahedral coordination[65]. However, this coordination state for Si is scarce for well characterised inorganic crystalline materials[66,67]. For this reason, it is unusual for $Si_5O(PO_4)_6$ to show the identical flexibility in cationic coordination state as in $Ge_5O(PO_4)_6$. In addition to this, Arrhenius plots of the $Si_5O(PO_4)_6$ showed that oxide ion conductivity within the material is much lower than that seen within the germanate[45,67]. Therefore, structural studies may be of interest to discern differences between the two materials. This is to determine whether any differences arise due to Si adopting the unusual 6-fold coordination state and to find out if differences in oxide ion conductivity are related to the exchange of Ge for Si.

In addition to $Si_5O(PO_4)_6$, other silicates that form a di-tetrahedral subunit exists in structures that are closely related such $AM_3P_6Si_2O_{25}$ (A = K, Rb, Tl, Cs and M = Mo, Ti and Sn) [68–70]. These

materials also have mixed octahedral and tetrahedral cationic structures. In these structures the silicon retains its tetrahedral geometry within the Si_2O_7 structures while the transition metals occupy the octahedral holes within the structure. Furthermore, the germanophosphate, $Ge_3P_6Si_2O_{25}$, contains the di-tetrahedra unit and is of particular interest as it represents a material between the Si and Ge end members. Leclaire, A. *et al* synthesised this material using the traditional solid state method and formed single crystals. Structural analysis suggests that the crystal structure belongs to the *P-31c* space group with the unit cell parameters *a* = 7.99(1) Å *c*, 16.513(2) Å and Z = 2. This structure is shown in Figure 1-19.

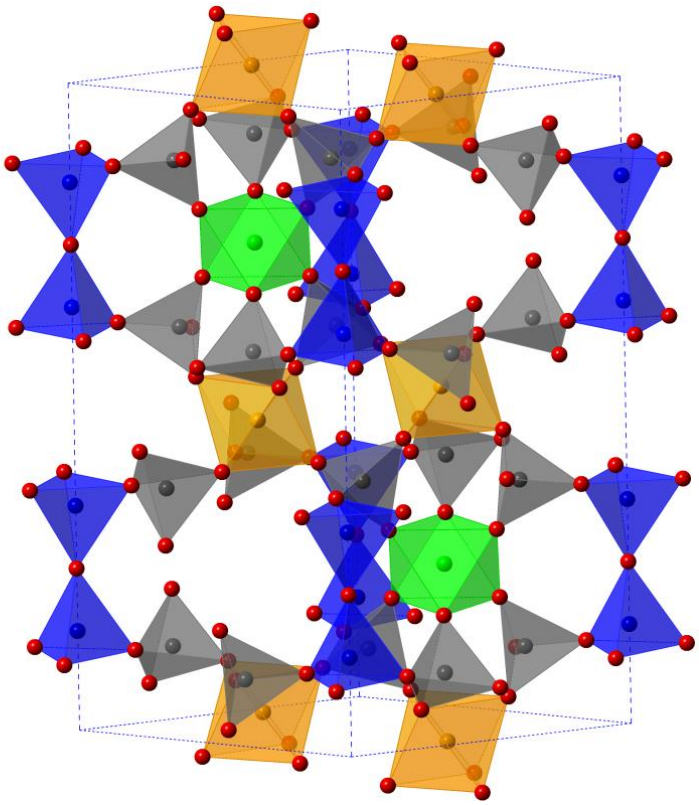

Figure 1-19. The structure of $Ge_3P_6Si_2O_{25}$. The blue spheres represent silicon in 4 fold coordination state, orange spheres represent Ge(1) and green spheres represent Ge(2) and red spheres are oxygen.

1.6 Conclusion and potential research

Traditionally used vacancy oxide ion conductors were briefly discussed. This includes the ZrO_2, CeO_2, Bi_2O_3 and LSGM systems. The interstitial oxide ion conductors relating to the apatite and Mayenite structures were discussed along with their conduction mechanisms. In these materials key structural features were established to be responsible for high oxide ion conductivity. Similar structural features may be seen within the new oxide ion conductor $Ge_5O(PO_5)_6$.

The aims of this project are to establish further understanding of the ceramic oxide $Ge_5O(PO_4)_6$. Understanding the defect chemistry within the material will be key to establishing a conduction mechanism. This will aid in the future development of the material as an oxide ion conductor. This work also concerns investigation of possible dopants for $Ge_5O(PO_4)_6$ with the emphasis on their effect on crystal structure and electrical properties.

1.7 References

1. West, A. R. in *Basic solid state chemistry*. (Wiley New York, 1988).

2. Goodenough, J. B. Review Lecture: Fast Ionic Conduction in Solids. *Proc. R. Soc. London.A.Mathematical Phys. Sci.* **393,** 215–234 (1984).

3. Kumar, P. P. & Yashonath, S. Ionic conduction in the solid state. *J. Chem. Sci.* **118,** 135–154 (2006).

4. Mehrer, H. *Diffusion in Solids: Fundamentals, Methods, Materials, Diffusion-Controlled Processes*. (Springer, 2007).

5. Schulz, H. Crystal structures of fast ion conductors. *Annu. Rev. Mater. Sci.* **12,** 351–376 (1982).

6. Steele, B. C. H. & Heinzel, A. Materials for fuel-cell technologies. **414,** 345–352 (2001).

7. Goodenough, J. B. Oxide-ion electrolytes. *Annu. Rev. Mater. Res.* **33,** 91–128 (2003).

8. Knauth, P. & Tuller, H. L. Solid-state ionics: Roots, status, and future prospects. *J. Am. Ceram. Soc.* **85,** 1654–1680 (2002).

9. Ramamoorthy, R., Dutta, P. K. & Akbar, S. A. Oxygen sensors : Materials , methods , designs. **8,** 4271–4282 (2003).

10. Kilner, J. A. Fast oxygen transport in acceptor doped oxides. *Solid State Ionics* **129,** 13–23 (2000).

11. Malavasi, L., Fisher, C. A. J. & Islam, M. S. Oxide-ion and proton conducting electrolyte materials for clean energy applications: structural and mechanistic features. *Chem. Soc. Rev.* **39,** 4370–4387 (2010).

12. Boivin, J. C. & Mairesse, G. Recent material developments in fast oxide ion conductors. *Chem. Mater.* **10,** 2870–2888 (1998).

13. Etsell, T. H. & Flengas, S. N. Electrical properties of solid oxide electrolytes. *Chem. Rev.* **70,** 339–376 (1970).

14. Fergus, J. W. Electrolytes for solid oxide fuel cells. *J. Power Sources* **162,** 30–40 (2006).

15. Kharton, V. V, Marques, F. M. B. & Atkinson, A. Transport properties of solid oxide electrolyte ceramics: a brief review. *Solid State Ionics Dokiya Meml. Spec. Issue* **174,** 135–149 (2004).

16. Hull, S. Superionics: crystal structures and conduction processes. *Reports Prog. Phys.* **67,** 1233 (2004).

17. Irvine, J. T. S., Dobson, J. W. L., Politova, T., Martín, S. G. & Shenouda, A. Co-doping of scandia–zirconia electrolytes for SOFCs. *Faraday Discuss.* **134,** 41–49 (2006).

18. Shannon, R. D. Revised effective ionic radii and systematic studies of interatomic distances in halides and chalcogenides. *Acta Crystallogr. Sect. A* **32,** 751–767 (1976).

19. Skinner, S. J. & Kilner, J. A. Oxygen ion conductors. *Mater. Today* **6,** 30–37 (2003).

20. Panhans, M. A. & Blumenthal, R. N. A thermodynamic and electrical conductivity study of nonstoichiometric cerium dioxide. *Solid State Ionics* **60,** 279–298 (1993).

21. Pearce, M. C. & Thangadurai, V. Electrical transport properties of aliovalent cation-doped. *Asia-Pac, J. Chem. Eng* **4,** 33–44 (2009).

22. Arai, H., Kunisaki, T., Shimizu, Y. & Seiyama, T. Electrical properties of calcia-doped ceria with oxygen ion conduction. *Solid State Ionics* **20,** 241–248 (1986).

23. Yahiro, H., Eguchi, K. & Arai, H. Electrical properties and microstructure in the system ceria-alkaline earth oxide. *J. Mater. Sci.* **23,** 1036–1041 (1988).

24. Eguchi, K., Setoguchi, T., Inoue, T. & Arai, H. Electrical properties of ceria-based oxides and their application to solid oxide fuel cells. *Solid State Ionics* **52,** 165–172 (1992).

25. Inaba, H. & T. Ceria-based solid based electrolytes. *Solid State Ionics* **2738,** 1–16 (1996).

26. Steele, B. C. H. Appraisal of $Ce_{1-y}Gd_yO1_{-y/2}$ electrolytes for IT-SOFC operation at 500° C. *Solid State Ionics* **129,** 95–110 (2000).

27. Krok, F., Abrahams, I., Wrobel, W., Kozanecka-Szmigiel, a & Dygas, J. R. Oxide-ion conductors for fuel cells. *Mater. Sci.* **24,** 13–22 (2006).

28. Sammes, N. M., Tompsett, G. A., Näfe, H. & Aldinger, F. Bismuth based oxide electrolytes—structure and ionic conductivity. *J. Eur. Ceram. Soc.* **19,** 1801–1826 (1999).

29. Gattow, G. & Schröder, H. Über Wismutoxide. III. Die Kristallstruktur der

Hochtemperaturmodifikation von Wismut (III)-oxid (δ-Bi_2O_3). *Zeitschrift für Anorg. und Allg. Chemie* **318,** 176–189 (1962).

30. Takahashi, T. & Iwahara, H. Oxide ion conductors based on bismuthsesquioxide. *Mater. Res. Bull.* **13,** 1447–1453 (1978).

31. Kuang, X., Payne, J. L., Johnson, M. R. & Radosavljevic Evans, I. Remarkably High Oxide Ion Conductivity at Low Temperature in an Ordered Fluorite-Type Superstructure. *Angew. Chemie* **124,** 714–718 (2012).

32. Datta, R. K. & Meehan, J. P. The system Bi_2O_3–R_2O_3 (R= Y, Gd). *Zeitschrift für Anorg. und Allg. Chemie* **383,** 328–337 (1971).

33. Ishihara, T. Development of new fast oxide ion conductor and application for intermediate temperature solid oxide fuel cells. *Bull. Chem. Soc. Jpn.* **79,** 1155–1166 (2006).

34. Ishihara, T., Matsuda, H. & Takita, Y. Doped LaGaO3 perovskite type oxide as a new oxide ionic conductor. *J. Am. Chem. Soc.* **116,** 3801–3803 (1994).

35. Nikonov, A. V *et al.* Aging of electrolyte $La_{0.88}Sr_{0.12}Ga_{0.82}Mg_{0.18}O_{3-\delta}$ made using magnetic-pulse compaction. *Russ. J. Electrochem.* **47,** 733–736 (2011).

36. Huang, K., Feng, M., Goodenough, J. B. & Schmerling, M. Characterization of Sr-Doped $LaMnO_3$ and $LaCoO_3$ as Cathode Materials for a Doped $LaGaO_3$ Ceramic Fuel Cell. *J. Electrochem. Soc.* **143,** 3630 (1996).

37. Kendrick, E., Islam, M. S. & Slater, P. R. Developing apatites for solid oxide fuel cells: insight into structural, transport and doping properties. *J.Mater.Chem.* **17,** 3104–3111 (2007).

38. Nakayama, S. & Sakamoto, M. Electrical properties of new type high oxide ionic conductor $RE_{10}Si_6O_{27}$(RE= La, Pr, Nd, Sm, Gd, Dy). *J. Eur. Ceram. Soc.* **18,** 1413–1418 (1998).

39. Sansom, J. E. H., Richings, D. & Slater, P. R. A powder neutron diffraction study of the oxide-ion-conducting apatite-type phases, $La_{9.33}Si_6O_{26}$ and $La_8Sr_2Si_6O_{26}$. *Solid State Ionics* **139,** 205–210 (2001).

40. Slater, P. R., Sansom, J. E. H. & Tolchard, J. R. Development of apatite-type oxide ion conductors. *Chem. Rec.* **4,** 373–384 (2004).

41. Islam, M. S., Tolchard, J. R. & Slater, P. R. An apatite for fast oxide ion conduction. *Chem. Commun.* **13,** 1486–1487 (2003).

42. Tolchard, J. R., Islam, M. S. & Slater, P. R. Defect chemistry and oxygen ion migration in the apatite-type materials $La_{9.33}Si_6O_{26}$ and $La_8Sr_2Si_6O_{26}$. *J.Mater.Chem.* **13,** 1956–1961 (2003).

43. Guillot, S. *et al.* Evidence of local defects in the oxygen excess apatite $La_{9.67}(SiO_4)6O_{2.5}$ from high resolution neutron powder diffraction. *J. Solid State Chem.* **182,** 3358–3364 (2009).

44. Béchade, E. *et al.* Diffusion path and conduction mechanism of oxide ions in apatite-type lanthanum silicates. *Chem. Mater.* **21,** 2508–2517 (2009).

45. Zhang, Y. Exploring Novel Functionalities in Oxide Ion Conductors with Excess Oxygen., PhD thesis, (Unversity of St. Andrews, 2011).

46. Lee, D. K. *et al.* Defect chemistry of the cage compound, $Ca_{12}Al_{14}O_{33-\delta}$, understanding the route from a solid electrolyte to a semiconductor and electride. *Phys.Chem.Chem.Phys.* **11,** 3105–3114 (2009).

47. Bartl, H. & Scheller, T. Zur Struktur des $12CaO{\cdot}7Al_2O_3$. *Neues Jahrb. Miner. Monatsh* **35,** 547–552 (1970).

48. Kim, S. W. *et al.* Simple and efficient fabrication of room temperature stable electride: Melt-solidification and glass ceramics. *J. Am. Chem. Soc.* **127,** 1370–1371 (2005).

49. Hayashi, K. *et al.* Nanoporous Crystal $12CaO \cdot 7Al_2O_3$: A Playground for Studies of Ultraviolet Optical Absorption of Negative Ions. *J. Phys. Chem. B* **111,** 1946–1956 (2007).

50. Lacerda, M., Irvine, J. T. S., Glasser, F. P. & West, A. R. High oxide ion conductivity in $Ca_{12}Al_{14}O_{33}$. *Nature* **332,** 525–526 (1988).

51. Sushko, P. V, Shluger, A. L., Hayashi, K., Hirano, M. & Hosono, H. Mechanisms of oxygen ion diffusion in a nanoporous complex oxide $12CaO{\cdot}7Al_2O_3$. *Phys. Rev. B* **73,** 14101 (2006).

52. Boysen, H., Lerch, M., Stys, A. & Senyshyn, A. Structure and oxygen mobility in mayenite ($Ca_{12}Al_{14}O_{33}$): a high-temperature neutron powder diffraction study. *Acta Crystallogr. Sect. B Struct. Sci.* **63,** 675–682 (2007).

53. Djurado, E. & Labeau, M. Second phases in doped lanthanum gallate perovskites. *J. Eur. Ceram. Soc.* **18,** 1397–1404 (1998).

54. Rozumek, M. *et al.* Electrical Conduction Behavior of $La_{1+x}Sr_{1-x}Ga_3O_{7-\delta}$ Melilite-Type

Ceramics. *J. Am. Ceram. Soc.* **87,** 1795–1798 (2004).

55. Kuang, X. *et al.* Interstitial oxide ion conductivity in the layered tetrahedral network melilite structure. *Nat Mater* **7,** 498–504 (2008).

56. Li, M.-R. *et al.* Interstitial oxide ion order and conductivity in $La_{1.64}Ca_{0.36}Ga_3O_{7.32}$ melilite. *Angew. Chem. Int. Ed. Engl.* **49,** 2362–6 (2010).

57. Liu, B., Guo, W., Chen, F. & Xia, C. Ga site doping and concentration variation effects on the conductivities of melilite-type lanthanum strontium gallate electrolytes. *Int. J. Hydrogen Energy* **37,** 961–966 (2012).

58. Park, H. J. *et al.* $Sr_2(Mg_{1-x}Ga_x)Ge_2O_{7+0.5x}$: Melilite-type oxygen ionic conductor associated with fivefold coordinated germanium and gallium. *J. Power Sources* **275,** 884–887 (2015).

59. Mayer, H. & Völlenkle, H. Die Kristallstruktur von $Ge_5O(PO_4)_6$. *Monatshefte für Chemie/Chemical Mon.* **103,** 1560–1571 (1972).

60. Mal'shikov, A. E., Egorova, O. V. & Bondar, I. A. Synthesis and Properties of Germanium Phosphate. *Russ. J . Inorg. Chem.* **33,** 722–726 (1988).

61. Leclaire, A. & Raveau, B. Ge3P6Si2O25: A cage structure closely related to the intersecting tunnel structure $KMo_3P_6Si_2O_{25}$. *J. Solid State Chem.* **75,** 397–402 (1988).

62. Mayer, H. Die Kristallstruktur von $Si_5O(PO_4)_6$. *Monatshefte für Chemie / Chem. Mon.* **105,** 46–54 (1974).

63. Poojary, D. M., Borade, R. B. & Clearfield, A. Structural characterization of silicon orthophosphate. *Inorganica Chim. Acta* **208,** 23–29 (1993).

64. Weeding, T. L., De Jong, B., Veeman, W. S. & Aitken, B. G. Silicon coordination changes from 4-fold to 6-fold on devitrification of silicon phosphate glass. *Nature* **318,** 352–353 (1985).

65. Kirkpatrick, R. J., Smith, K. A., Schramm, S., Turner, G. & Yang, W. H. Solid-State Nuclear Magnetic Resonance Spectroscopy of Minerals. *Annu. Rev. Earth Planet. Sci.* **13,** 29–47 (1985).

66. Liebau, F. *Structural Chemistry of Silicates: Structure, Bonding, and Classification*. (Springer Berlin Heidelberg, 2012).

67. Saxin, S. A possible low-intermediate temperature proton conductor based on Silicon Oxide Phosphate., PhD thesis (University of St Andrews, 2014).

68. Leclaire, A., Monier, J. C. & Raveau, B. A molybdosilicophosphate with an intersecting-tunnel structure which exhibits ion-exchange properties, $AMo_3P_{5.8}Si_2O_{25}$ (A = Rb, Tl). *Acta Crystallogr. Sect. B* **40,** 180–185 (1984).

69. Leclaire, A., Monier, J. C. & Raveau, B. Structure of $CsMo_3P_{5.8}Si_2O_{25}$. *Acta Crystallogr. Sect. C Cryst. Struct. Commun.* **41,** 1719–1720 (1985).

70. Leclaire, A., Borel, M. M., Grandin, A. & Raveau, B. Silicophosphates with an intersecting tunnel structure: $AM_3P_6Si_2O_{25}$ and $AMo_3P_{5.8}Si_2O_{25}$. *Mater. Chem. Phys.* **12,** 537–543 (1985).

2 Experimental

2.1 Synthesis

The traditional solid state method was used in this thesis to produce a range of materials. Precursor reaction mixtures were produced either with ball milling or grinding of the sample using an agate pestle and mortar. The samples were then allowed to dry before firing of the material at low temperatures to drive off NH_3 and H_2O and subsequently refired at higher temperature to form the phase of interest. More details on the firing temperatures and materials used can be seen within the respective chapters.

2.2 Scanning electron microscopy (SEM)

SEM is a form of microscopy that allows high resolution imaging of samples. A tungsten filament is heated to produce an incident electron beam which is redirected to the sample with the use of magnetic lenses Figure 2-1.

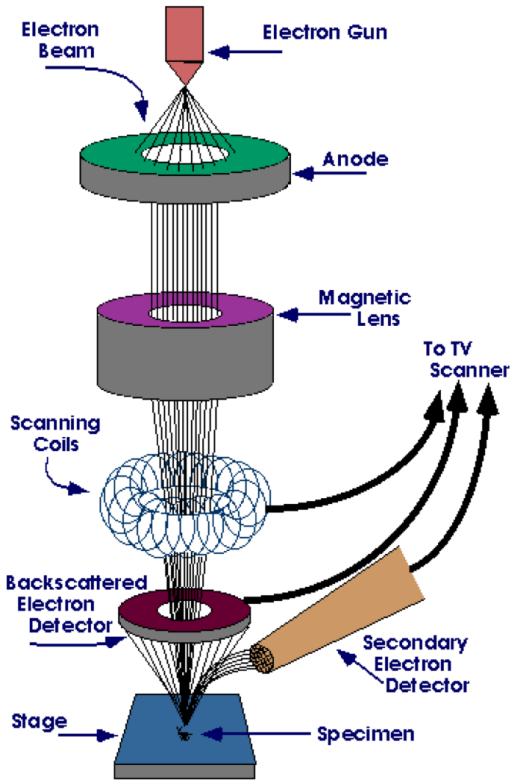

Figure 2-1. Illustration of operating SEM[1].

When the incident electron beam interacts with the sample a process called inelastic scattering may occur. This process involves the excitation of electrons within the sample. Consequently, secondary electrons are produced which are ejected from the sample and are detected as shown in Figure 2-2[2]. The production of secondary electrons typically occurs with low energy electrons (5eV). As a result, only secondary electrons near the surface have enough energy to be ejected (<10 nm). This can provide valuable information on the topography and charging effects on the sample surface. In this thesis, the JEOL 5600 was used to perform this analysis.

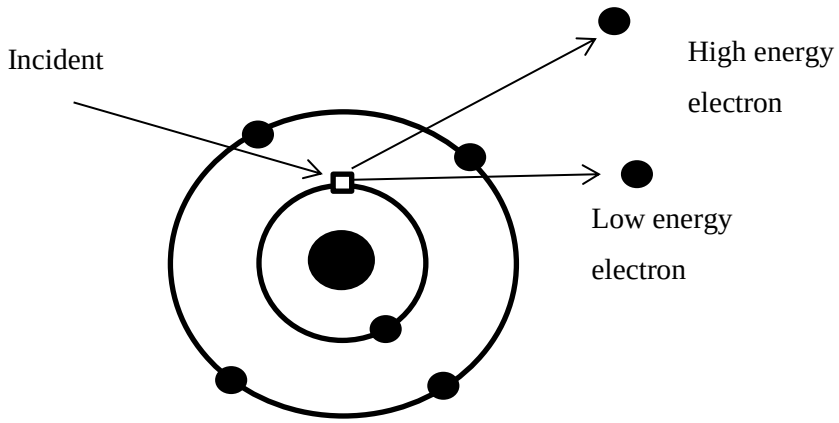

Figure 2-2. Schematic showing the formation of secondary electrons from inelastic scattering from incident beam.

2.3 Energy Dispersive X-ray (EDX)

EDX is often used as a complementary technique to SEM. The production of secondary electrons can lead to the formation of a vacancy on an inner electron shell of an ion. This forms an atom that is in an excited state[3]. The ion can move to a lower energy state by filling this vacancy with an electron from an outer electron shell. This transition typically involves the loss of excess energy in the form of x-ray radiation as shown below.

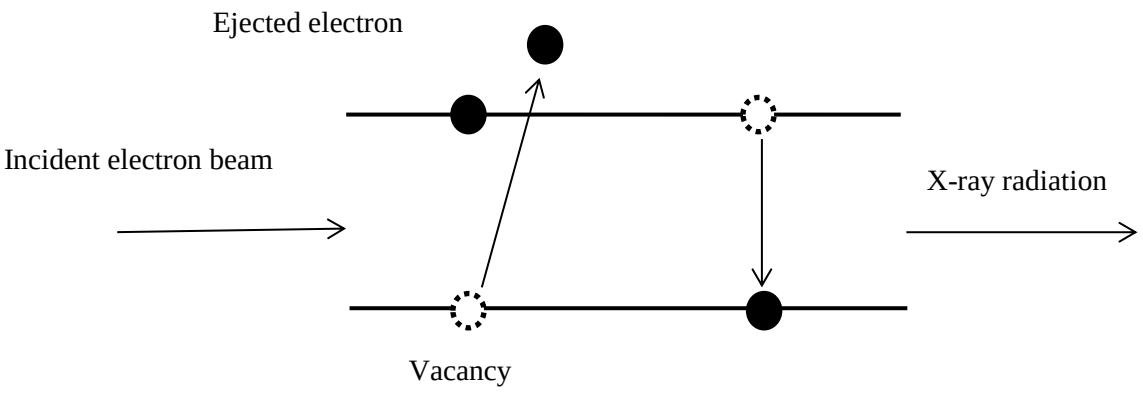

Figure 2-3. EDX is based on electronic transitions between inner atomic shells.

The energy released is equal to the energy difference between the two electronic states. It is therefore particularly useful in the identification of elements as the difference between the electronic states is dependent on the atom.

2.4 Crystal structure

Ionic solids typically present themselves in a crystalline ordered state (or crystal). A crystal is defined by a solid that is formed from an ordered arrangement of regularly repeating internal structures from atoms, molecules or ions. This involves the long range arrangement of identical internal structures (or unit cells) to form a crystal structure. These units cells may be categorised into 7 crystals systems (Table 2-1).

These seven crystal systems may be combined with lattice centering types which describe the identical lattice points of the unit cells. These are known as Bravais lattices. Moreover, additional symmetry elements may be applied to the Bravias lattices. Among a few examples include centre of symmetry, rotation axes, screw axes, etc. In total, this forms 230 potential space groups for the description of a unit cell in a 3D crystal structure. This internal symmetry provides a platform to elucidate atomic positions. The long range ordering of atoms provides the basis for structural elucidation via a phenomenon known as diffraction. This is when the application of an electromagnetic wave to the crystalline structure results in the scattering of the wave by the atoms at a certain angle with respect to the sample. X-ray radiation is typically used in regards to the electromagnetic wave because it has a wavelength of 10^{-10} m (~ 1 Å)[5]. This wavelength is useful for this purpose because it is equal to/or smaller than the spacing between the diffracting atoms within crystalline materials. As x-rays are scattered by the material they may destructively or constructively interfere with each other. In amorphous solids, the diffraction of waves are scattered in all directions due to the short range ordering of the atoms. Consequently, waves leaving the sample are out of phase and, as a result, the net energy that leaves the sample is not enough to produce a diffraction pattern. This is in contrast to, the atoms in crystalline materials which are arranged in a regular pattern, resulting in a few directions in which constructive interference can occur. In this case, the waves leaving the sample are in phase with one another; therefore, their energies may aggregate. The combined energy of the x-rays leads to enough energy leaving the sample to form a diffraction pattern.

Crystal system	Bravais lattice/allowed lattice	Unit cell shape - Axial lengths	Unit cell shape – interaxial angles	Defining symmetry
Cubic	**P, I , F**	a = b = c	α = β = γ = 90 °	Four threefold axes
Tetragonal	**P, I**	a = b ≠ c	α = β = γ = 90 °	One fourfold axis
Orthorhombic	**P, I, C, F**	a ≠ b ≠ c	α = β = γ = 90 °	Three twofold axes or mirror planes
Hexagonal	**P**	a = b ≠ c	α = β = 90 ° γ = 120 °	One sixfold axis
Trigonal	**P, R**	a = b = c	α = β = γ ≠ 90 °	One threefold axis
Monoclinic	**P, C**	a ≠ b ≠ c	α = γ = 90 ° ≠ β	One twofold axis or mirror plane
Triclinic	**P**	a ≠ b ≠ c	α ≠ β ≠ γ ≠ 90 °	None

Table 2-1. The seven crystal systems[4].

Bragg's law describes the conditions that are required for constructive interference within crystalline structures. It details the arrangement of atoms as infinite, semi-transparent planes. The orientation of these planes is described by the miller indices, *h*, *k*, *l*. These planes are separated by an interplanar distance also known as D-spacing (d_{hkl}) which determines the diffraction angle, θ. The interaction with x-rays with these planes is shown in Figure 2-4.

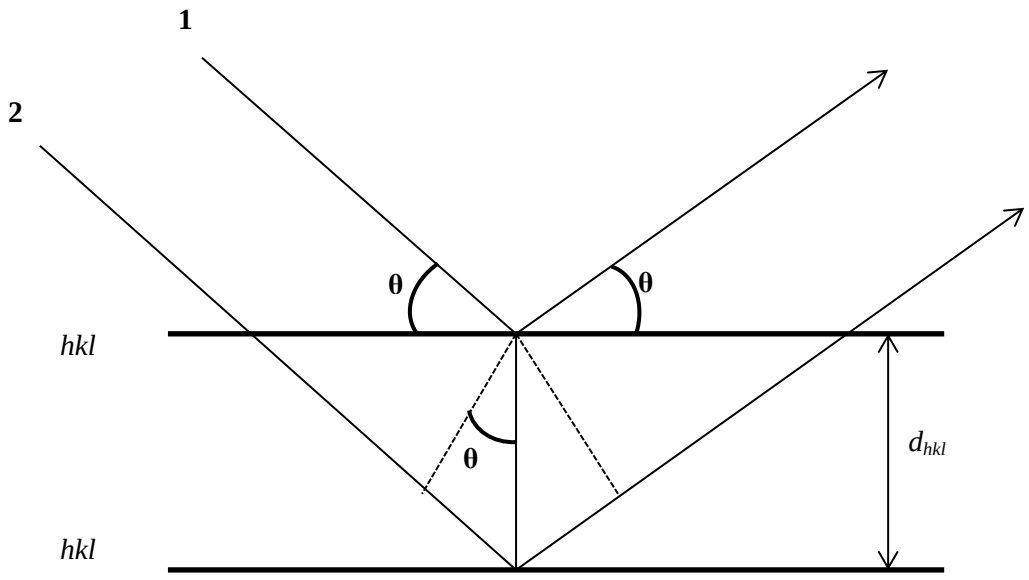

Figure 2-4. Visual representation of Bragg's law.

The illustration shows that there are two waves reflected of the planes within the crystal structure. Wave 2 is required to travel an extra distance to reflect off a neighbouring plane. In order for Bragg's law to be satisfied for constructive interference the extra distance travel must be a whole integer of the wavelengths. This can be simplified in Equation 2-1.

$$\textbf{Equation 2-1 } n\lambda = 2d_{hkl}\sin\theta$$

2.5 Neutron powder diffraction (NPD)

NPD can be used as a complementary technique to XRD. This is related to the nature in which neutrons and x-rays interact with atoms. The diffraction of x-rays is proportional to the electron density of an atom. For this reason, x-rays are particularly good at observing larger atoms due to their larger electron densities. In the case of NPD, neutrons interact with the nuclei of an atom and so the application of NPD is particularly useful in observing the position of smaller atoms within a crystal lattice as neutron diffraction is not proportional to atomic number.

Neutrons are able to interact with materials similar to that seen with X-rays as particles may behave as waves which is described by the de Broglie equation (Equation 2-2)

$$\textbf{Equation 2-2 } \boldsymbol{\lambda = \frac{h}{mv}}$$

(where *h* is planks constant, *m* is mass and *v* is velocity)

It shows that a neutron at a given velocity can have an appropriate wavelength comparable to the distance between lattice planes of crystalline structures and therefore useful for diffraction. The generation of neutrons with a correct wavelength are traditionally produced two ways; a nuclear fission reactor or a "spallation source". Nuclear fission reactors usually produce neutrons by a chain reaction type mechanism from bombarding fissile nuclei (U-235 or Pu-239) with an incident neutron. In this case neutrons are generally of continuous intensity and monochromated to a single wavelength. For spallation sources, the generation of neutrons is caused from bombarding a heavy metal target such as W-183 with protons, which produces a high flux of non-continuous neutrons of various wavelengths. In this case, wavelength is derived from measuring the time it takes for a neutron to travel a fixed distance also known as TOF. This can be substituted into de Broglie's equation as following:

$$\textbf{Equation 2-3 } \boldsymbol{\lambda = \frac{ht}{mL}} = 2d_{hkl}\sin\theta$$

The equation above shows the relation between TOF and bragg's law to allow for coherent scattering of neutrons. In this thesis, NPD was performed at the HRPT beamline at SINQ, PSI, Switzerland. SinQ is a neutron source that is the first of its kind in the world, as it is a spallation

source and a continuous source[6]. The utilisation of these neutrons at the HRPT beamline can be seen in Figure 2-5.

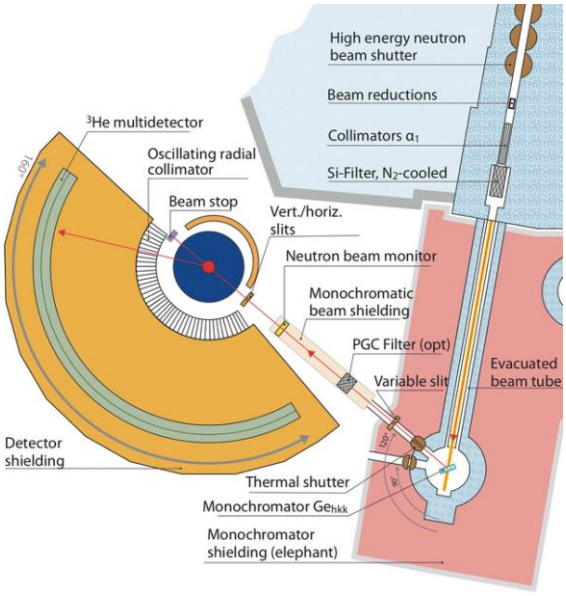

Figure 2-5. Schematic view of the HRPT beamline at SINQ.[7]

The schematic shows that the generated neutrons are passed through a collimator through a vacuum. In the case of HRPT the wavelength of the neutrons are fixed by the use of a monochromator. The neutrons are then diffracted by the sample.

2.6 Rietveld refinement

Rietveld refinement is a method that enables the extraction of structural information of a material from X-ray and neutron diffraction data. The extraction of this information involves comparing diffraction data to known analogue systems. This technique can be viewed as a complex curve fitting problem which is performed by refining parameters of the model to "fit" observed data. Since powder diffraction data essentially consists of peaks/overlapping peaks and a background it is important to understand the parameters that affect the position, intensity and shape of the peaks to account for these parameters within the model. The peak positions are related to the unit cell. Peak intensity is related to the parameters atomic coordinates, thermal displacement and site occupancy which are in some form related to one another. Atomic coordinate parameter accounts for the position of atoms within the crystal structure. However, atoms are rarely fixed at a single point as they move due to the presence of thermal energy also referred to as thermal displacement. Additionally, site occupancy may be modelled and ideally should have a value of 1 or less. The line width of the peak is affected by two main reasons which are the sample (crystallite size and microstrain) and the diffractometer. The latter may be modelled with the use of pre-defined mathematical functions that describe peak shapes such as the Lorenzian and Gaussian line shapes[8].

After these parameters are refined the quality of the model may be assessed by the generation of statistical values what are described as R_p (Equation 2-4) and wR_p (Equation 2-5)[9].

Equation 2-4 $R_p = \frac{\sum |y_i(obs) - y_i(calc)|}{\sum y_i(obs)}$

Equation 2-5 $wR_p = \left\{ \frac{\sum w_i (y_i(obs) - y_i(calc))^2}{\sum w_i (y_i(obs))^2} \right\}^{1/2}$

2.7 Electrochemical impedance spectroscopy (EIS)

EIS allows for the analysis of electrical properties of electroceramic systems[10]. This is performed with the application of a platinum electrode to the electroceramic material and fired at 900 °C to dry the electrodes. During the experiment, a sinusoidal AC potential is applied to the material, which is typically over a wide range of frequencies (10^{-2} – 10^{7} Hz). Subsequently, AC current (I) is measured which can give valuable information of electrochemical processes that occur within the solid state system. The impedance (Z) represents the material's ability to resist the flow of electrons and can be derived when considering Ohm's law. This can be seen in equation 2-6.

$$Z(\omega) = \frac{E}{I} = \frac{E_0 \sin(\omega t)}{I_0 \sin(\omega t)} = Z_0(\cos ø + j \sin ø) = Z'(\omega) + jZ''(\omega)$$

E_0 – magnitude of potential

I_0 – magnitude of current

Ø – Change in phase

Equation 2-6 Expression of AC impedance as a complex number

As the equation shows, Z (ω) is a complex vector which consists of a real (Z') and imaginary (Z'') component. These can be plotted against one another to form the Nyquist plot. An idealised Nyquist plot can be seen in Figure 2-6 here each semicircle represents an electrochemical process.

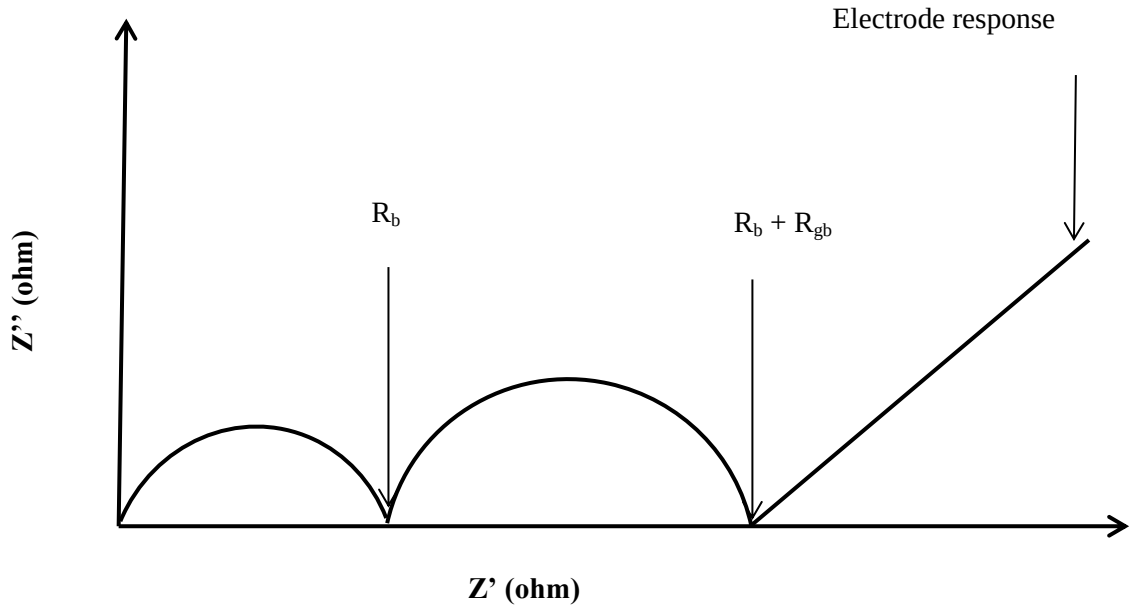

Figure 2-6. This shows idealised Nyquist plot with three electrochemical process which are represented by semicircles, R_b, R_{gb} and electrode response spike.

The figure above shows there are three electrochemical processes. The chord of the first semicircle where it intercepts the x-axis is referred to as the resistance of the bulk, R_b. The semicircle proceeding represents the resistance of the grain, R_{gb}. Therefore, the total resistance is R_b+R_{gb}. Finally, the electrode response represents an interaction of the sample with the electrode and can provide information on the conducting species. The assignment of each process may be observed by the capacitance obtained from each arc. This can be seen in Table 2-2.

Capacitance (F)	Phenomenon Responsible
10^{-12}	Bulk
10^{-11}	Minor, second phase
10^{-11} - 10^{-8}	Grain boundary
10^{-10} - 10^{-9}	Bulk ferroelectric
10^{-9} - 10^{-7}	Surface layer
10^{-7} - 10^{-5}	Sample-electrode interface
10^{-4}	Electrochemical reactions

Table 2-2.The assignment of electrochemical processes derived from capacitance[11].

2.8 References

1. Scanning Electron Microscope. Available at: https://www.purdue.edu/ehps/rem/rs/sem.htm. (Accessed: 5th January 2011)

2. Reimer, L. in *Image Formation in Low-voltage Scanning Electron Microscopy* 43–50 (SPIE Optical Engineering Press, 1993).

3. Bell, D. C. & Garratt-Reed, A. J. in *Energy Dispersive X-ray Analysis in the Electron Microscope* 5–7 (Taylor & Francis, 2003).

4. West, A. R. in *Basic solid state chemistry* 2–3 (Wiley New York, 1988).

5. Glusker, J. P. & Trueblood, K. N. in *Crystal Structure Analysis: A Primer* 35–45 (OUP Oxford, 2010).

6. Fischer, P. *et al.* High-resolution powder diffractometer HRPT for thermal neutrons at SINQ. *Phys. B Condens. Matter* **276-278,** 146–147 (2000).

7. HRPT beamline. Available at: http://sinq.web.psi.ch/sinq/instr/hrpt/index.html. (Accessed: 28th January 2016)

8. McCusker, L. B., Von Dreele, R. B., Cox, D. E., Louër, D. & Scardi, P. Rietveld refinement guidelines. *J. Appl. Crystallogr.* **32,** 36–50 (1999).

9. R. A. Young. *The Rietveld Method*. (Oxford University Press, 1995).

10. Barsoukov, E. & Macdonald, J. R. in *Impedance spectroscopy: theory, experiment, and applications* 2–3 (John Wiley and Sons, 2005).

11. Irvine, J. T. S., Sinclair, D. C. & West, A. R. Electroceramics: characterization by impedance spectroscopy. *Adv. Mater.* **2,** 132–138 (1990).

3 Synthesis of $Ge_5O(PO_4)_6$

3.1 Introduction

$Ge_5O(PO_4)_6$ was first isolated in single crystal form which was prepared from a melt containing H_3PO_4 and GeO_2[1]. It crystallises in the space group *R-3* with the unit cell parameters ***a*** = 7.994(4) and ***c*** = 24.87(1) and Z = 3. In this section, the synthesis of $Ge_5O(PO_4)_6$ in powdered form was re-evaluated using the traditional solid state method. The material was synthesised in single phase and the thermal properties of $Ge_5O(PO_4)_6$ were also assessed using VT-XRD.

3.2 Experimental – PXRD

Powdered $Ge_5O(PO_4)_6$ was prepared by the traditional ceramic method. Stoichiometric amounts of GeO_2 (Alfa Aesar, 99.9999%) and $NH_4H_2PO_4$ (Sigma Aldrich 98+) were ground together. This mixture was then fired at 190 °C for 3 hours to dry the sample and release NH_3. The reaction mixture was then fired at higher temperatures to form $Ge_5O(PO_4)_6$. XRD was used for the purpose of phase identification and/or determining unit cell parameters. Unit cell parameters were derived from using GSAS[2] with EXPgui[3] interface or STOE WinX Pow[4]. The main diffractometer that was used was the Panalytical Empyrean X-ray diffractometer using Cu $K_{\alpha 1}$ radiation for high resolution XRD patterns. This data was collected over a 2θ range of 10-90 ° with a step size 0.017 ° and counting for 93.980s per step. Additionally, VT-XRD was performed using a Panalytical Empyrean x-ray diffractometer with an Anton Paar HTK1200N high temperature chamber using Mo $K_{\alpha 1}/K_{\alpha 2}$ radiation source. Data was collected over a 2θ range of 3-40 ° with a step size of 0.0084 ° and counting 240.665s per step. Alternatively, data were collected over a 2θ range of 4-25 ° with a step size of 0.0084 ° and counting 120.015s per step. This was performed between the temperatures of 25-1025 °C. All diffractometers used were operated in Bragg-Brentano geometry at the University of St Andrews. SEM was performed using the Jeol JSM-5600. The sample was prepared on a brass sample holder using carbon paper.

3.3 Results and discussion

3.3.1 Original heat treatment

The decomposition of $Ge_5O(PO_4)_6$ occurs between 1120-1160 °C[5,6]. Therefore, initial firing temperatures used were between 1000-1100 °C. A sample that was fired for 1000 °C for 20 hours and then 1100 °C showed single phase materials could be synthesised between this temperature range. However, consistently forming single phase materials was an issue. This usually arose in the form of minor GeP_2O_7 impurities. This can be seen in Figure 3-1.

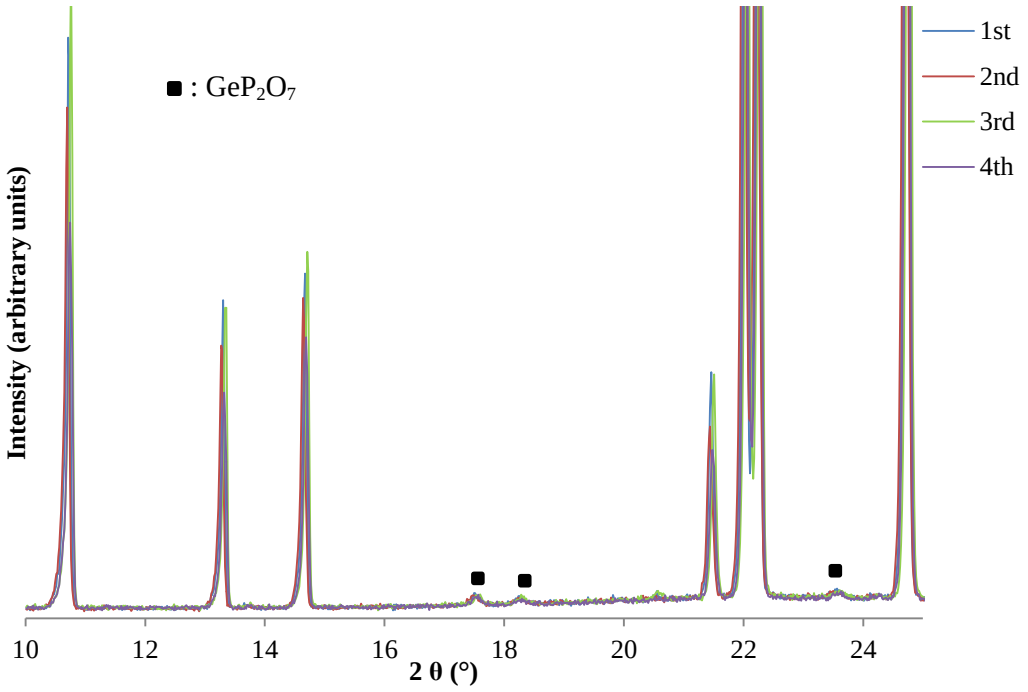

Figure 3-1. Comparison of 1st firing of the sample was 20 hours with an additional 10 hours at 1000 °C (blue XRD pattern), 2nd firing at 1000 °C for 10 hours (red XRD pattern), 3rd Firing at 1000 °C (green XRD pattern) and 4th firing at 1000 °C (Purple XRD pattern).

The impurity peaks are the most intense peaks for GeP_2O_7. It showed that after the consequent firing of the material the impurities remained within the sample. This suggested that the reaction mixture was slightly phosphorus rich. Similarly, Ozeki *et al* reported that $Ge_5O(PO_4)_6$ preferentially formed between the temperatures 1000-1100 °C but minor GeP_2O_7 remained within the sample[5]. This suggested that there may be the loss of germanium from the reaction mixture. It is unlikely that the reaction temperature is high enough for the volatilisation of germanium as this is typically seen with temperatures higher than ~1300 °C[7]. The loss of reactive germanium oxide may be related to the formation of amorphous GeO_2. This is shown in the following VT-XRD section.

3.3.2 Analysis of VT-XRD diffractograms

VT-XRD was performed on the material that contained minor GeP_2O_7 as an impurity phase over the temperature range 25-1025 °C. However, the VT-XRD patterns' do not adequately show these peaks. The XRD patterns for this experiment can be seen in Figure 3-2.

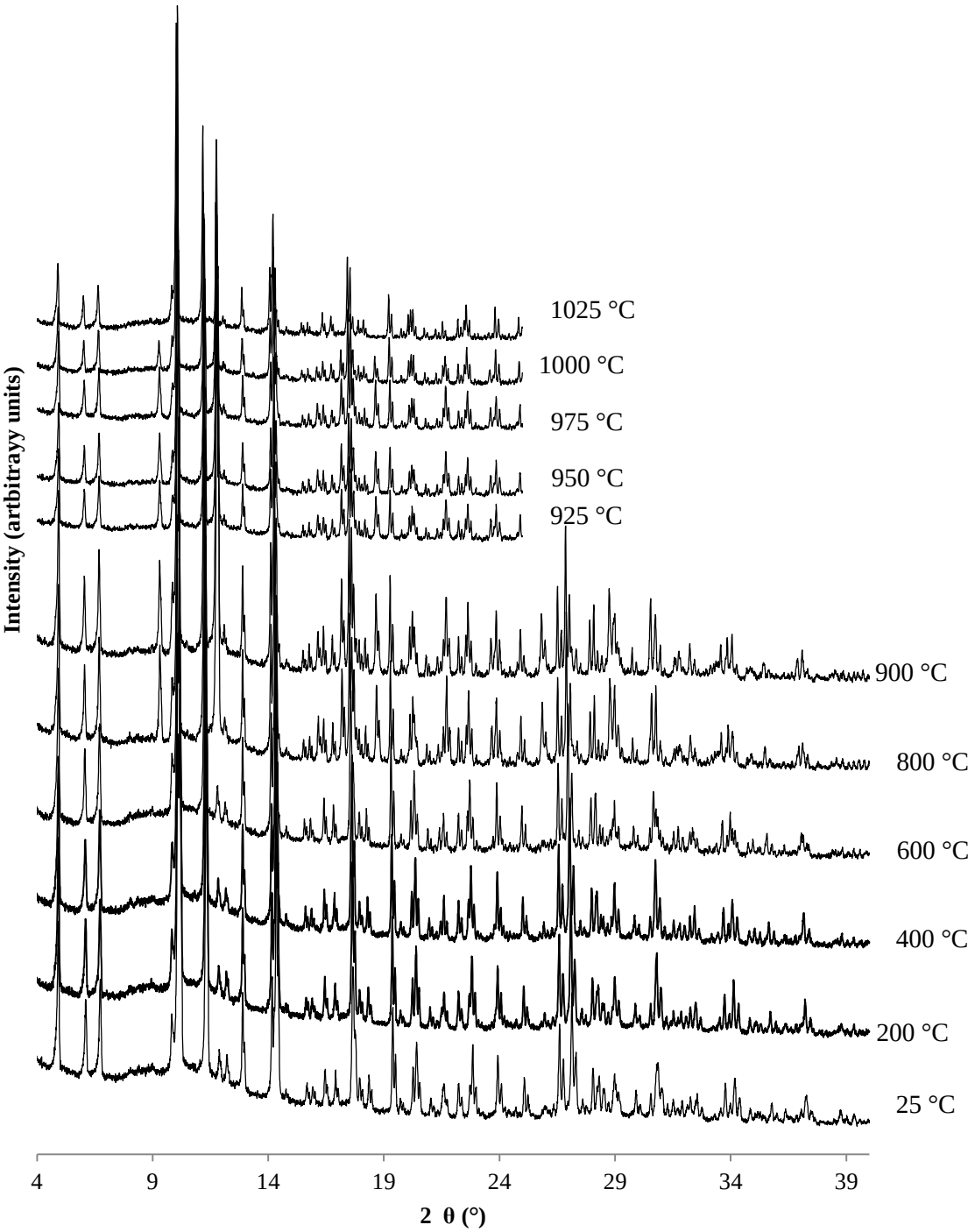

Figure 3-2. VT-XRD of $Ge_5O(PO_4)_6$ between the temperatures 25-1025 °C. Each XRD pattern from bottom to top represents an increase in temperature for the sample.

Under closer examination of the XRD pattern at 800 °C additional peaks arise that are attributed to the formation of α-GeO_2. This is shown in Figure 3-3.

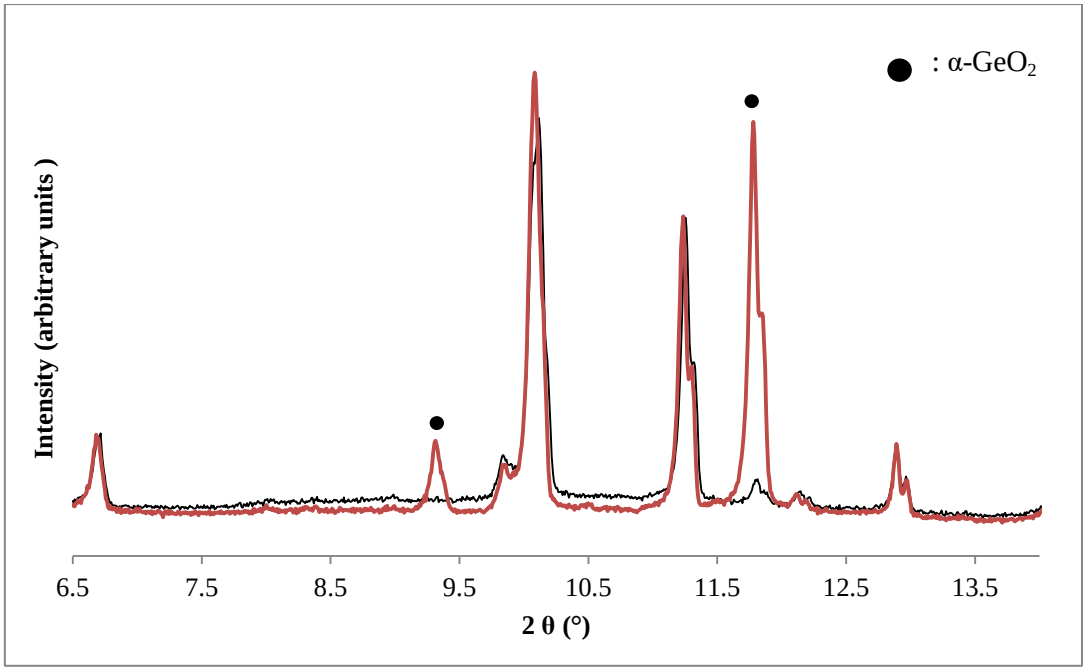

Figure 3-3. XRD patterns' to show that there is the recrystallisation of α-GeO_2 between 600-800 °C. The black XRD pattern represents the sample at 600 °C and the red XRD pattern represents the sample at 800 °C.

The formation of α-GeO_2 at 800 °C was attributed to the recrystallisation of amorphous GeO_2 which is indicative of the reduction in background between the 2θ values of 6-14 °. α-GeO_2 remains stable at1000 °C. As temperature increased to 1025 °C, α-GeO_2 reverts back into a non-crystalline state. Faktor *et al*[8] reported the melting point for α-GeO_2 is 1116±4 °C and for rutile-GeO_2 1086±5 °C. Therefore, the VT-XRD results show that there may be the lowering of the melting point of α-GeO_2 within the composition mixture or a transition into amorphous GeO_2. These results showed that there are two main points to consider when synthesising $Ge_5O(PO_4)_6$ via the traditional solid state synthesis. Firstly, the ideal synthesis temperature for $Ge_5O(PO_4)_6$ lies between a narrow range. However, when the temperature nears 1025 °C there is a propensity to form amorphous GeO_2 which may be stable against a reaction with GeP_2O_7.

3.3.3 Modified synthesis

The starting germanium source was changed to rutile GeO_2 and α-GeO_2. This GeO_2 mixture was obtained by heating α-GeO_2 at 727 °C for 20 hours[9] as shown in Figure 3-4.

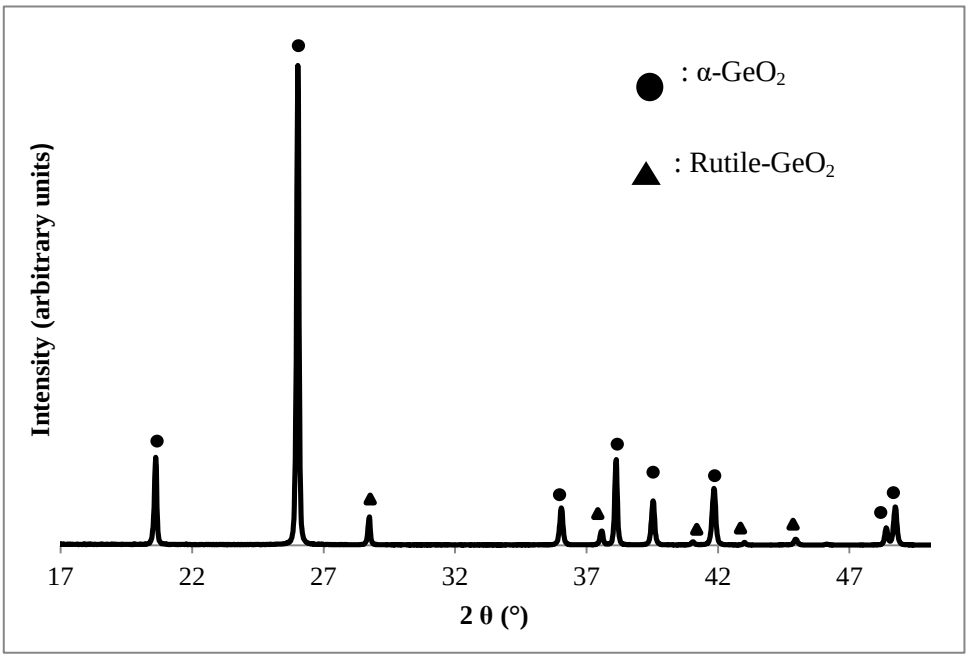

Figure 3-4. XRD pattern of mixed α-, rutile GeO_2 after 20 hours of continuous heating at 767 °C heating to form mixed α-GeO_2 and rutile GeO_2.

The effect of pre-heating α-GeO_2 showed minor formation of rutile like GeO_2. Nevertheless, this was used as a starting source of germanium. Consequently, stoichiometric amounts of GeO_2 and $NH_4H_2PO_4$ were added together. The sample was ball-milled for 1 hour and then fired at 900 °C for 45 minutes then a slow ramp rate of 3 °C/min was used to increase the temperature to 1000 °C and fired for 20 hours. The slow ramp rate was used to limit the overshooting of the furnace temperature. This was then repeated for 12 hours at 1000 °C. The XRD pattern for the resultant material is shown in Figure 3-5.

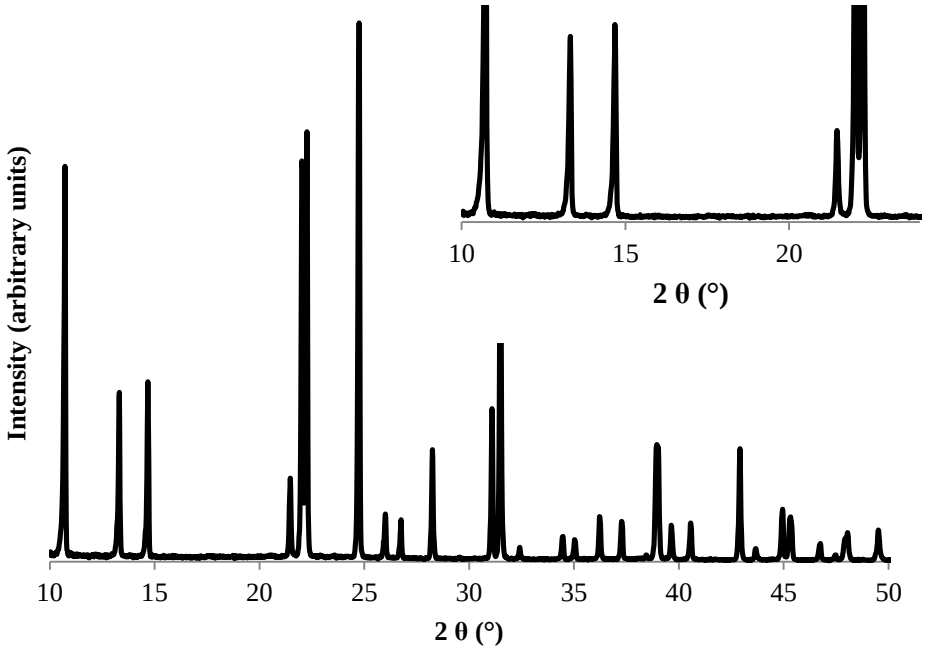

Figure 3-5. The synthesis of single phase $Ge_5O(PO_4)_6$ after firing for 20 hours at 1000 °C and 12 hours at 1000 °C.

Figure 3-5 shows that the material synthesised is single phase. The closer view of the diffractogram between 2θ values of 10-24 ° showed that the largest peaks for GeP_2O_7 do not exist within the diffractogram. SEM was performed on the sample to determine whether there were any amorphous contributions to the overall composition as shown in Figure 3-6.

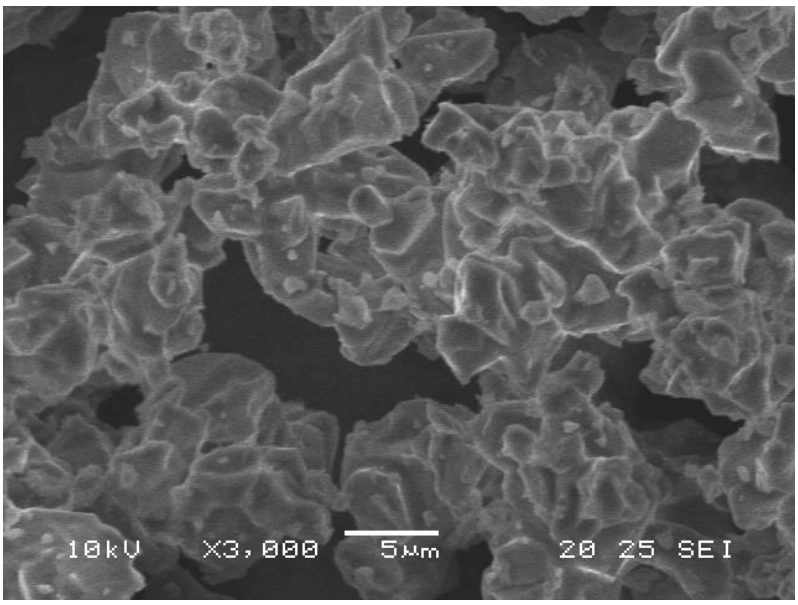

Figure 3-6. SEM image of single phase material, $Ge_5O(PO_4)_6$.

The material does not contain large impurities. The material does appear to have fragmentation of the crystallites due to ball-milling of the sample. EDX showed that there was a slight loss with the molar ratio (P:Ge) of 1.17 compared to the ideal 1.2. This is shown in Table 3-1.

Element	Weight (%)	Atomic (%)
P	18.22	14.89
Ge	36.39	12.77

Table 3-1. EDX results of $Ge_5O(PO_4)_6$.

3.3.4 Anisotropic NTE

VT-XRD also allowed for the assessment of thermal expansion and changes in unit cell parameters of $Ge_5O(PO_4)_6$. The XRD patterns for the VT-XRD experiment is shown in Figure 3-7.

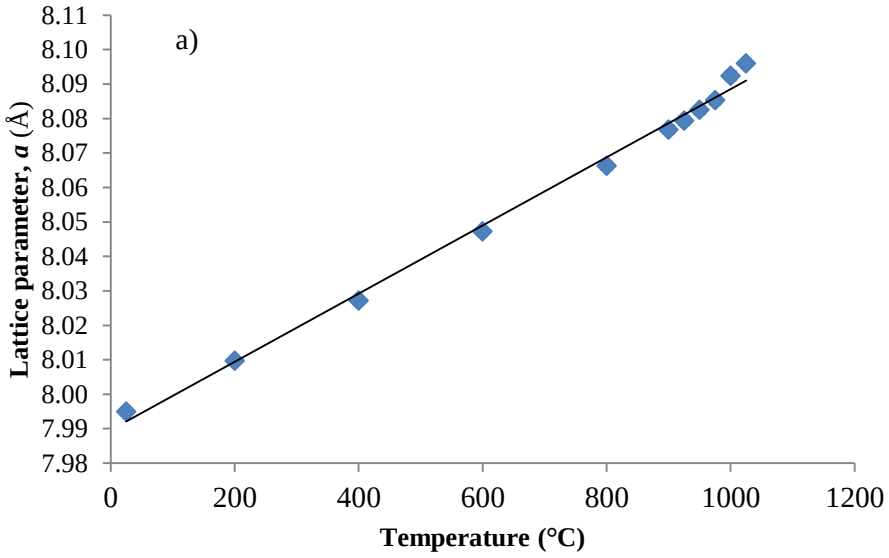

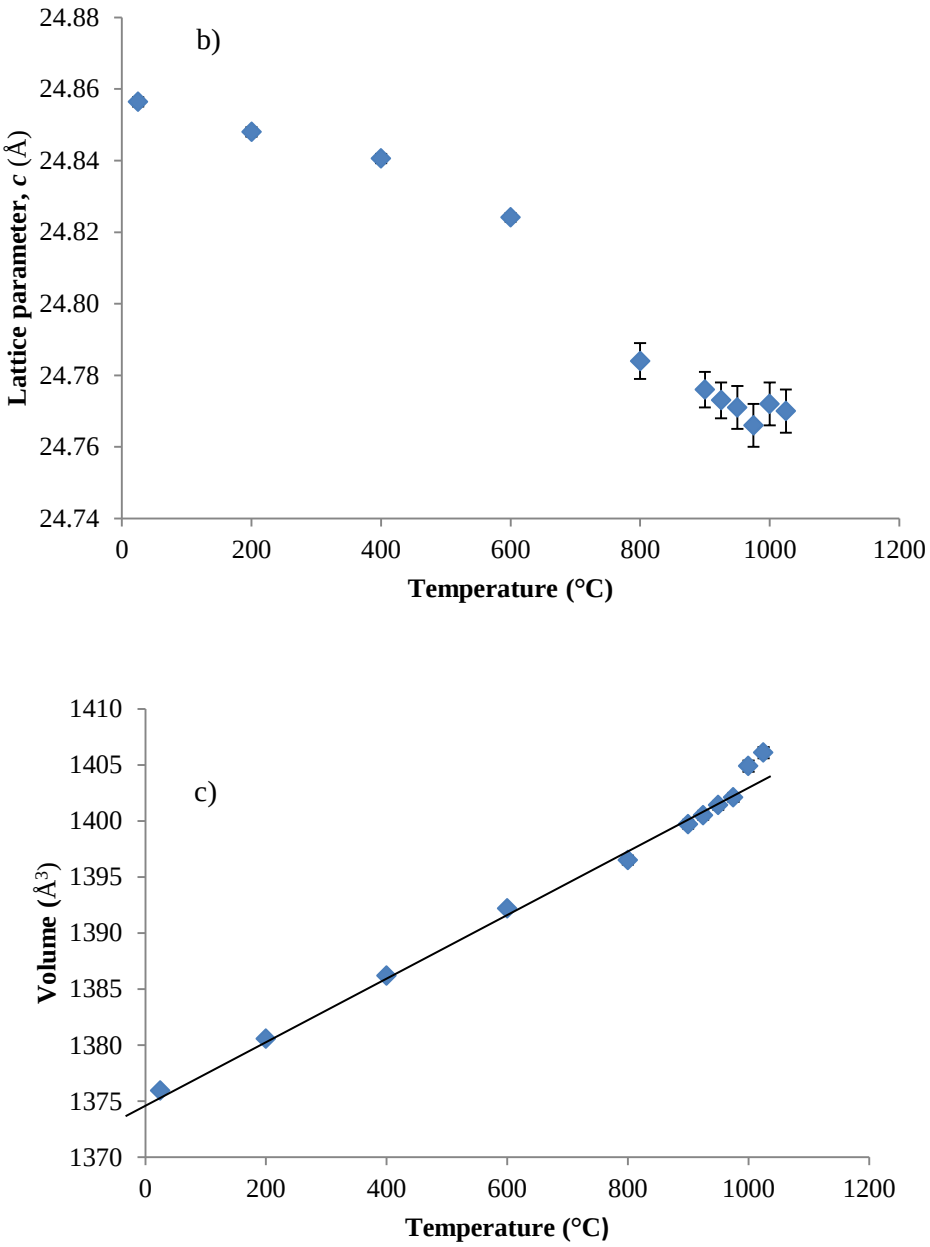

Figure 3-7. Unit cell parameters of $Ge_5O(PO_4)_6$ between the temperatures of 25-1025 °C where a) shows the unit cell parameter *a* (Å), b) shows the unit cell parameter *c* (Å) and c) shows the unit cell volume, *V* (Å^3).

Figure 3-7a, the analysis of unit cell parameters suggested that the unit cell along the *a*-*b* plane expands linearly with temperature until 1000 °C where there is a small jump in unit cell size. The unit cell parameter, ***c***, shows a non-linear NTE behaviour with temperature and again at 1000 °C and above there is a small increase in unit cell size at 1000 °C. NTE is due to the structure of the material where there are cavities aligned along the *c*-axis. As temperature increases there is the rotation and counter rotation of polyhedra that ultimately occupy this space. More details of NTE behaviour will be discussed in section 4.3.1.

3.3.5 Hydrothermal treatment of $Ge_5O(PO_4)_6$

Hydrothermal treatment of single phase $Ge_5O(PO_4)_6$ was also performed to determine whether water could be incorporated into the structure for protonic conductivity.

3.3.6 Experimental

A 0.7g pellet of single phase $Ge_5O(PO_4)_6$ was placed into a vial containing 5 ml of H_2O. This was placed into a teflon liner containing 15 ml of distilled H_2O. The teflon liner was sealed into a steel autoclave and placed into a preheated furnace at 90 °C for 3 hours. XRD was performed on the resultant material after it was ground. The results of this experiment can be seen in Figure 3-8.

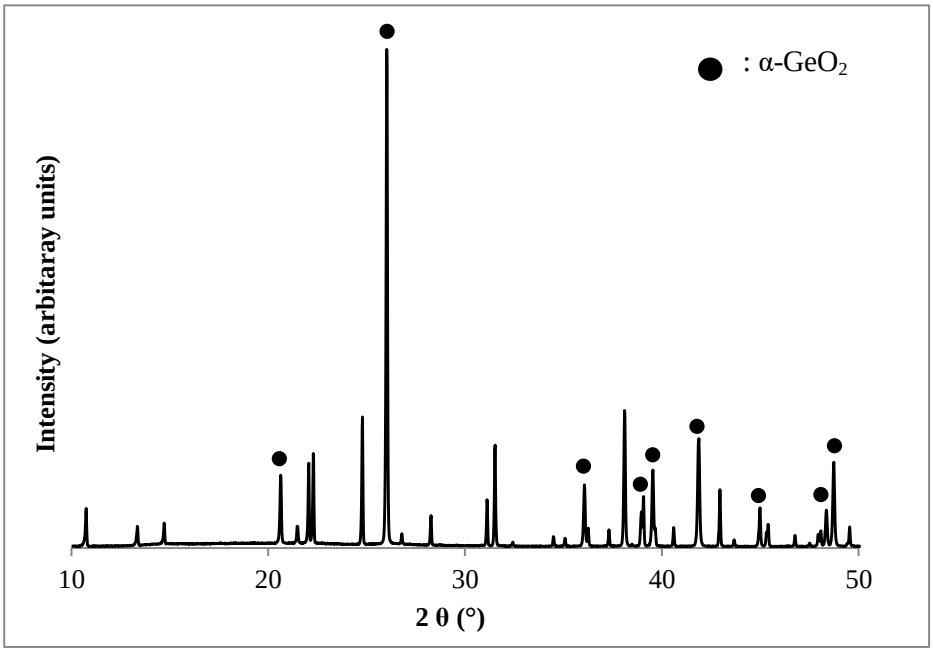

Figure 3-8. XRD pattern of hydrothermal treated sample 90 °C for 3 hours. Unannotated peaks belong to $Ge_5O(PO_4)_6$.

The results showed that after hydrothermal treatment there is the formation of α-GeO_2. This may suggest that there is dissolution of $Ge_5O(PO_4)_6$.The dissolution of $Ge_5O(PO_4)_6$ occurs by the following chemical reaction as suggested by Ozeki, K. *et al*[5].

$$Ge_5O(PO_4)_6 + 9H_2O \rightarrow 5GeO_{2(s)} + 6H_3PO_{4(l)}$$

In their experiment, powdered $Ge_5O(PO_4)_6$ was placed into distilled water and the pH of the solution fell from pH 6.17 to pH = 2.06 due to the proliferation of H_3PO_4 within the solution. This may suggest that the material may have an application at lower temperatures as a proton conductor as phosphoric acid has the highest known intrinsic proton conductivity[10].

3.3.7 Silicon oxide phosphate

The isostructural material, $Si_5O(PO_4)_6$, was synthesised in powdered form. This material consists of 4-and 6-fold silicon polyhedra. In this section, a brief evaluation of the firing conditions required to form $Si_5O(PO_4)_6$ was assessed. Phase analysis was performed using data obtained from the Rigaku miniflex 600.

3.3.8 Experimental

Powdered $Si_5O(PO_4)_6$ was synthesised using the traditional solid state method. Stoichiometric amounts of fumed SiO_2 (Sigma Aldrich, 99.8 %) and $NH_4H_2PO_4$ (Sigma Aldrich 98+ %) was ground together. The resultant material was fired at 190 °C for 3 hours. After this step, the sample was fired at varying temperatures as shown in Table 3-2.

Firing step No.	Ramp rates	Dwell times	Temperature	Phase analysis
1	3 °C/min ↑ and 3 °C/min ↓	24	950 °C	$Si_5O(PO_4)_6$, SiP_2O_7 and SiP_2O_7
2	3 °C/min ↑ and 3 °C/min ↓	24	975 °C	$Si_5O(PO_4)_6$, SiP_2O_7 and SiP_2O_7

Table 3-2. The firing schemes for two samples of $Si_5O(PO_4)_6$.

3.3.9 Results and discussion

The resultant XRD patterns can be seen in Figure 3-9. As can be seen from the XRD patterns the predominant phase synthesised in this sample is $Si_5O(PO_4)_6$. However, there are still minor peaks that can be assigned to cubic and monoclinic SiP_2O_7. With the additional firing of the sample, the peaks assigned to $Si_5O(PO_4)_6$ increase in intensity while the peaks assigned to the silicon pyrophosphate decreased.

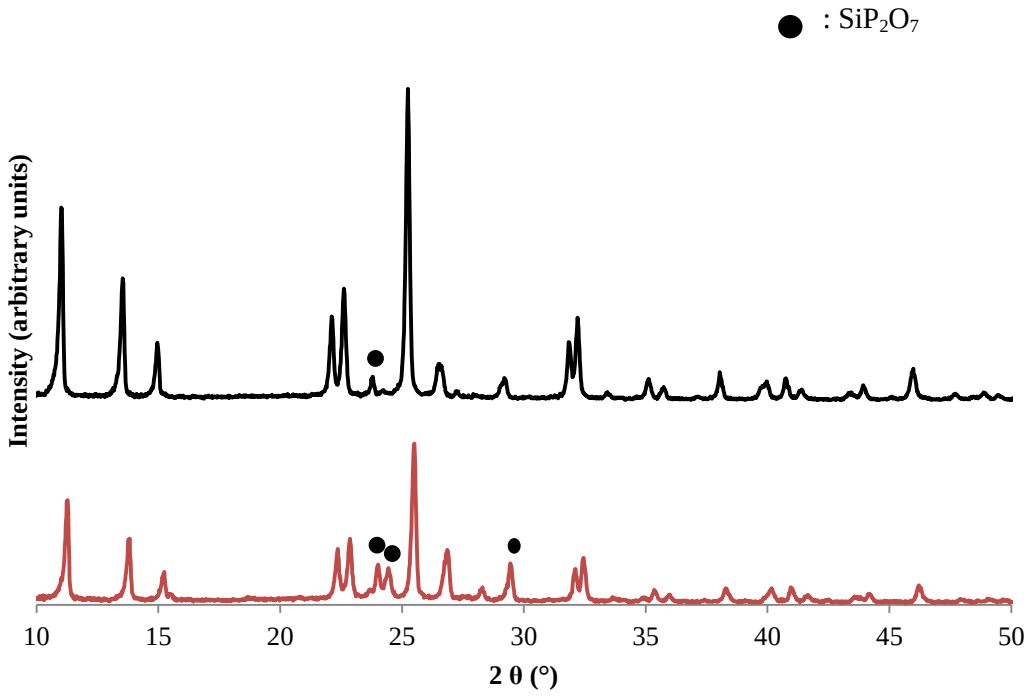

Figure 3-9. Red XRD pattern is for the material fired at 950 °C and the black XRD pattern is fired at 975 °C. Unannotated peaks represent $Si_5O(PO_4)_6$.

3.4 Conclusion

The results showed that $Ge_5O(PO_4)_6$ was successfully synthesised via the solid state method. It was shown that when using the traditional ceramic method consistency in forming single phase $Ge_5O(PO_4)_6$ was problematic. VT-XRD suggested that the material was synthesised at a very narrow temperature range where there is the formation of amorphous GeO_2 which appears to be stable against a reaction to form $Ge_5O(PO_4)_6$. Therefore, the problem was resolved by controlling ramp rates and dwell times to allow for the amorphous GeO_2 to crystallize and become more reactive in the mixture. Also, the starting source of germanium appears to improve reactivity by using alternative polymorphs of GeO_2.

Hydrothermal treatment of $Ge_5O(PO_4)_6$ showed dissolution of the material which may produce phosphoric acid, an intrinsic proton conductor.

VT-XRD showed that the material has anisotropic NTE behaviour along the c-axis. This is related to the structure of the material which has pores along the *c*-axis. As rotation and counter rotation of polyhedra within the structure occurs at higher temperatures, there is the occupation of the cavities and reduction of the unit cell size along the *c*-axis.

3.5 References

1. Mayer, H. & Völlenkle, H. Die Kristallstruktur von $Ge_5O(PO_4)_6$. *Monatshefte für Chemie/Chemical Mon.* **103,** 1560–1571 (1972).

2. Larson, A. C. & Von Dreele, R. B. General Structure Analysis System (GSAS). 86–748 (2004). doi:10.1103/PhysRevLett.101.107006

3. Toby, B. H. General Structure Analysis System - GSAS / EXPGUI, A Graphical user interface for GSAS. *J. Appl. Cryst.*, **34,** 2001 (2001).

4. WinXPOW, S. STOE & Cie GmbH: Darmstadt, Germany, 2004.

5. Ozeki, K., Fukui, Y. & Aoki, H. Preparation of germanium apatite and its cytotoxicity. *Bio-medical materials and engineering* **16,** 33–41 (2006).

6. Mal'shikov, A. E., Egorova, O. V. & Bondar, I. A. Synthesis and Properties of Germanium Phosphate. *Russ. J . Inorg. Chem.* **33,** 722–726 (1988).

7. Abram, E., Kirk, C., Sinclair, D. & West, A. Synthesis and characterisation of lanthanum germanate-based apatite phases. *Solid State Ionics* **176,** 1941–1947 (2005).

8. Faktor, M. M. & Carasso, J. I. Equilibria in the Ge-O-H System. *J .Electrochem. Soc.* **18,** 817–822 (1965).

9. Micoulaut, M., Cormier, L. & Henderson, G. S. The structure of amorphous, crystalline and liquid GeO_2. *J. Phys. Condens. Matter* **18,** R753–R784 (2006).

10. Vilčiauskas, L., Tuckerman, M. E., Bester, G., Paddison, S. J. & Kreuer, K.-D. The mechanism of proton conduction in phosphoric acid. *Nat Chem* **4,** 461–466 (2012).

4 NPD study of $Ge_5O(PO_4)_6$

4.1 Introduction

Fast ion conductors have a range of technological applications in electrochemical devices such as fuel cells, sensors and electrochemical displays[1–3]. Consequently, there is always a drive for the advancement of ion conducting properties by understanding the underlying processes that permit this phenomenon. For example, YSZ is a vacancy oxide ion conductor, which entails 'hopping' of oxide ions through oxygen vacancies. This understanding has led to extensive research into the structural optimisation of YSZ by increasing the concentration of oxygen vacancies to derive a fine-tuned structure for optimal activity[4].

More recently, the structure-property relationships within interstitial oxide ion conductors have been determined. This has revealed elaborate oxide ion conduction pathways as seen in the Apatite-type lanthanum silicates series, $La_{10-x}(SiO_4)_6O_{3-3x2}$[5–7] and the melilite series, $La_{1+x}Sr_{1-x}Ga_3O_7$[8]. For apatite, this involves local lattice distortions such as the movement of SiO_4 which allow for the spatial requirements for travelling oxide ions. The material $La_{1.54}Sr_{0.46}Ga_3O_{7.27}$, shows the intrinsic ability for the Ga coordination state to change from GaO_4 to GaO_5 trigonal bipyramids for the stabilisation of mobile interstitial oxide ions. This is also seen for the melilite-type structure materials, $Sr_2(Mg_{1-x}Ga_x)Ge_2O_{7+0.5x}$ where it was suggested that germanium may also stabilise interstitial oxide ions by adopting trigonal bipyramidal geometry[9].

Germanium oxide phosphate, $Ge_5O(PO_4)_6$, also contains distinctive features that lend themselves to form less restrictive structural constraints for oxygen transport. The crystal structure consists of isolated GeO_6 octahedra and Ge_2O_7 ditetrahedra which are linked by PO_4 groups forming a three dimensional network as shown in Figure 4-1 [10]. The chemical formula may be written as $Ge_3^{VI}Ge_2^{IV}O(PO_4)_6$ to emphasized both 4- and 6-fold oxygen coordinated environments. Interestingly, its silicate analogue also shows the identical flexibility in coordination states, despite silicon strongly favouring the tetrahedral geometry. In relation to oxide ion conductivity, the structure may be described by three distinctive features that promote this process. Firstly, Ge_2O_7 subunit hosts an 'excess' oxide ion which becomes mobile for transport through the structure. Secondly, the structure is zeolitic where the open framework contains tunnels that run along the [100], [010] and [110]. These tunnels interconnect with each other to form large voluminous cages which are able to accommodate large interstitial oxide ions (1.4 Å). Finally, germanium channels run along the c-axis which offers a network for the formation and stabilisation of mobile oxide ions through the flexibility that is afforded from local germanium lattice distortions.

To elaborate further on this, a general mechanism postulated from considering its structure is shown in Figure 4-1.

(a)

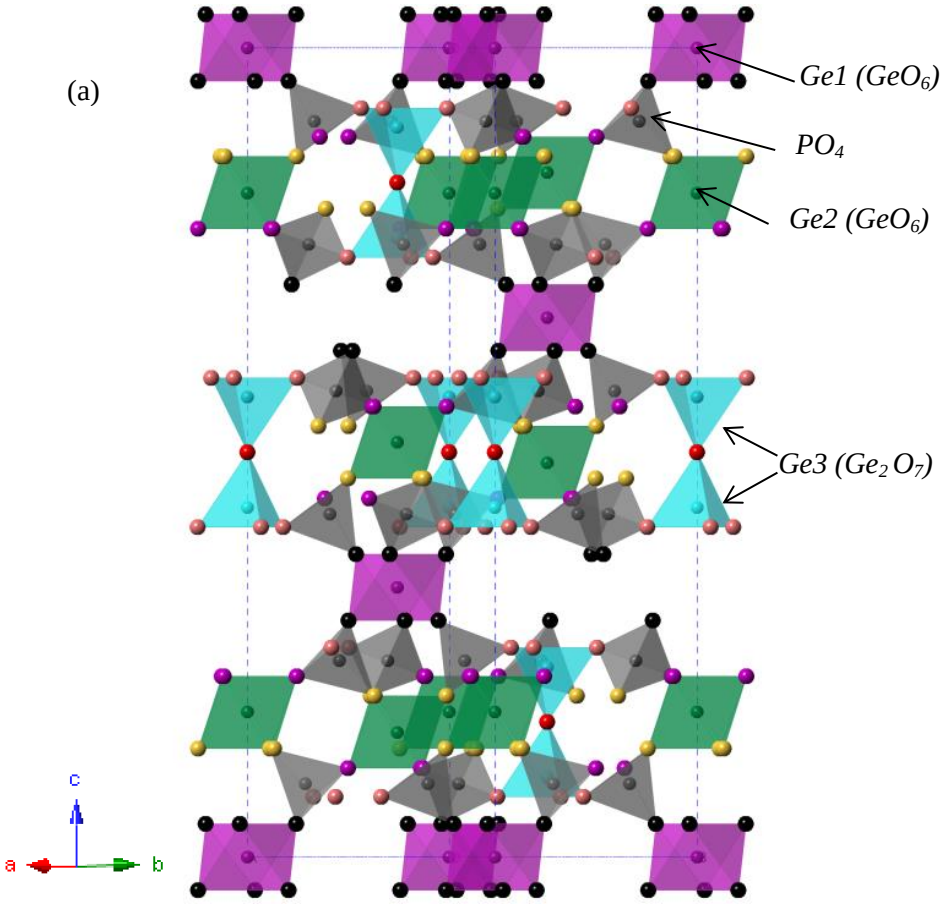
Ge1 (GeO6)
PO4
Ge2 (GeO6)
Ge3 (Ge2 O7)
c
a
b

(b)

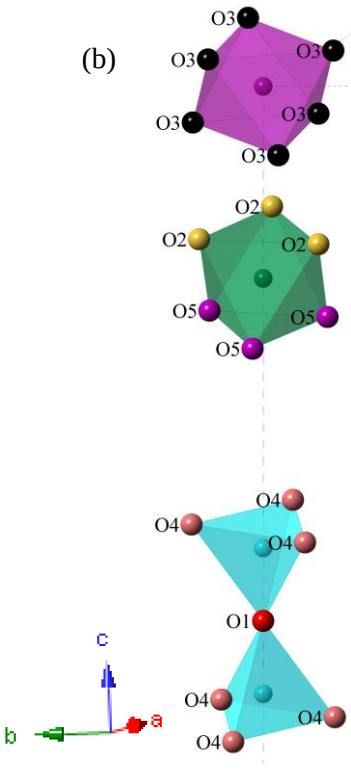
O3
O3
O3
O3
O3
O3
O2
O2
O2
O5
O5
O5
O4
O4
O4
O1
O4
O4
O4
c
b
a

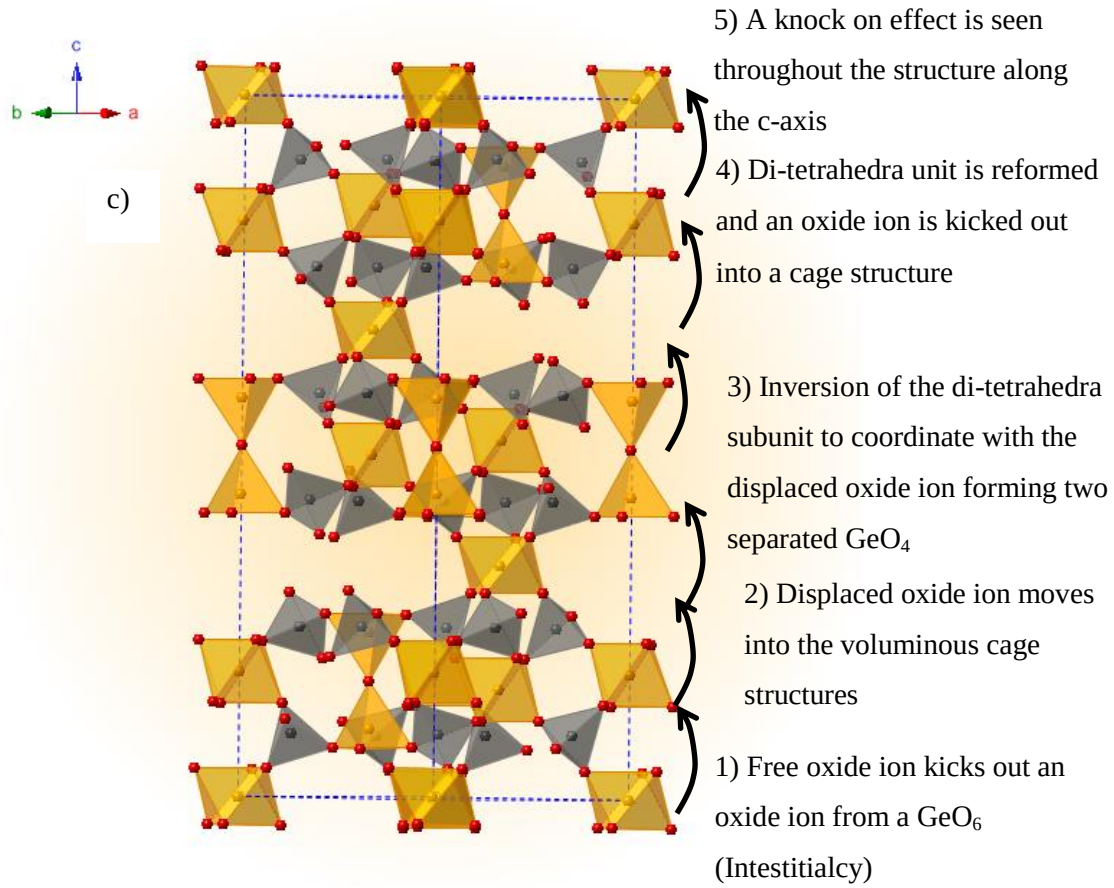

Figure 4-1. Illustration of the crystal structure of $Ge_5O(PO_4)_6$ where a) highlights the different germanium environments and coordination states. In addition to this, the PO_4 subunit can also be seen. b) Shows the various oxygen environments and c) shows the postulated oxide ion conduction pathway mechanism.

In this chapter, NPD data has provided confirmation of the origin of the mobile oxide ion and given an insight into the key local lattice distortions that allow oxygen transport to occur within $Ge_5O(PO_4)_6$. It may also give an insight into the oxide conduction properties of structurally related materials. For example, the cage structure, $Ge_3P_6Si_2O_{25}$[11], shares many of its distinctive structural features with $Ge_5O(PO_4)_6$.

4.2 Experimental

The synthesis of this compound was performed using the ceramic method. Stoichiometric amounts of GeO_2 (Alfa Aesar 99.999 %) and $NH_4H_2(PO_4)_6$ (Sigma Aldrich 98+ %) were ground together and calcined for 3 hours at 180 °C. This was then fired for 20 hours at 1000°C and then for an additional 12 hours at 1000 °C. Each firing step required intermittent ball milling with 10mm ZrO_2 balls for 2 hours in acetone.

$Ge_5O(PO_4)_6$ was synthesised in powdered form and the assessment of its structure was performed using NPD. The NPD data were collected from the PSI, HRPT, Switzerland at the temperatures of 300 K, 523 K, 823 K and 1073 K for 3 hours per scan with a step size of 0.05 ˚. In addition to this, a 1 hour scan was performed at 723 K with a step size of 0.05 ˚, predominantly for the determination of U_{iso} values and unit cell parameters. The neutron beam was monochromated to a constant wavelength of 1.494 Å. Diffracted neutrons were detected by 3He position-sensitive detectors (PSDs) over a 2θ range of 10-164 °. Structural refinement[12] was performed in which the following parameters were refined; atomic coordinates, unit cell parameters and profile parameters, unless specified. This was performed using the GSAS[13] software with EXPgui[14].

An 8 mm steel can was used in the collection of this data and was subsequently included in the structural refinement of each pattern. The steel can belongs to the cubic unit cell with the space group *Fm3m*. The determination of the unit cell parameters of the steel can was also used to measure the consistency and equilibration of the heated system. The isothermal steps on heating included 10 °C/min to the scanning temperatures.

4.2.1 Fourier difference calculations

Fourier difference calculations were performed on the material to determine positive scattering excess densities that were not accounted for by the structural model. This information provided details on missing atoms with increasing temperature. These calculations were performed on NPD data for the material $Ge_5O(PO_4)_6$ at the temperatures 300 K, 523 K, 823 K and 1073 K. Fourier difference calculations were performed by selecting the "DELF" function for difference Fourier maps in GSAS[13]. The Fourier difference calculations were performed with a map step value of 0.1 Å along the *a*-,*b*- and *c*-axis with a value of 0 and 1 for the min and max for all cell edges. These values were default parameters suggested by the GSAS manual. Fourier peaks were searched by using the "Forsh" option in GSAS. The min peak value was set to zero so that only positive neutron density was considered due to the scattering nature of neutrons with oxygen. The located peaks for each temperature were then placed into their respective refinement model to determine whether there was an improvement in structural fit. This was performed by assuming the positive scattering densities were potential interstitial oxygen sites. Therefore, the U_{iso} value for the positive scattering density was set to an average value of all of the other crystallographically defined oxygen within the structure. To evaluate the potential sites R-factors were referred to observe if there were improvements of the structural fit. In addition to this, site occupancy of the sites were evaluated to determine whether the extracted information was correct. For example, if site occupancy was a negative value the site would be discarded as the information suggests that no significant scattering has occurred. It should also be noted that atomic coordinates were not refined for the positive neutron densities as this was pre-determined by the diffraction data.

4.3 Results and discussion

The steel internal standard suggested that heating was consistent throughout the entirety of the experiment as shown in Figure 4-2. The unit cell of the steel expands linearly with temperature suggesting that at each recorded temperature it had reach an equilibrated thermal state.

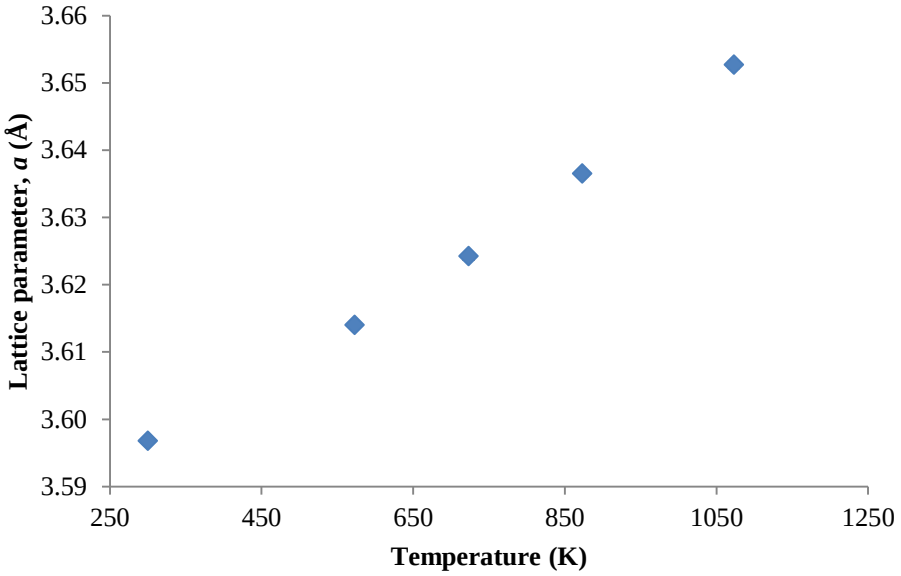

Figure 4-2. Unit cell parameters, *a* (Å) for steel (model : *Fm3m*) between the temperature range of 300-1073 K. This is presented to show the system was thermally equilibrated as can be seen by the linear thermal expansion of the steel can.

The phase, $Ge_5(PO_4)_6O$, gave a good fit against the rhombohedral structure with the best space group being *R-3*. No additional peaks beyond this phase and the internal standard were observed below 573K. This is illustrated for the 300 K data as shown in Figure 4-3. These fits were also performed for each pattern at higher temperatures. More specifically, structural fits included refining peak profiles using the Pseudo-Voight function (profile 2 when using GSAS with EXPGUI), atomic coordinates, atomic displacement factors (U_{iso}) and unit cell parameters. Site occupancy was constrained to one for all atoms. The phase fraction of steel was also constrained to one as a reference point for the refinement of the other phases.

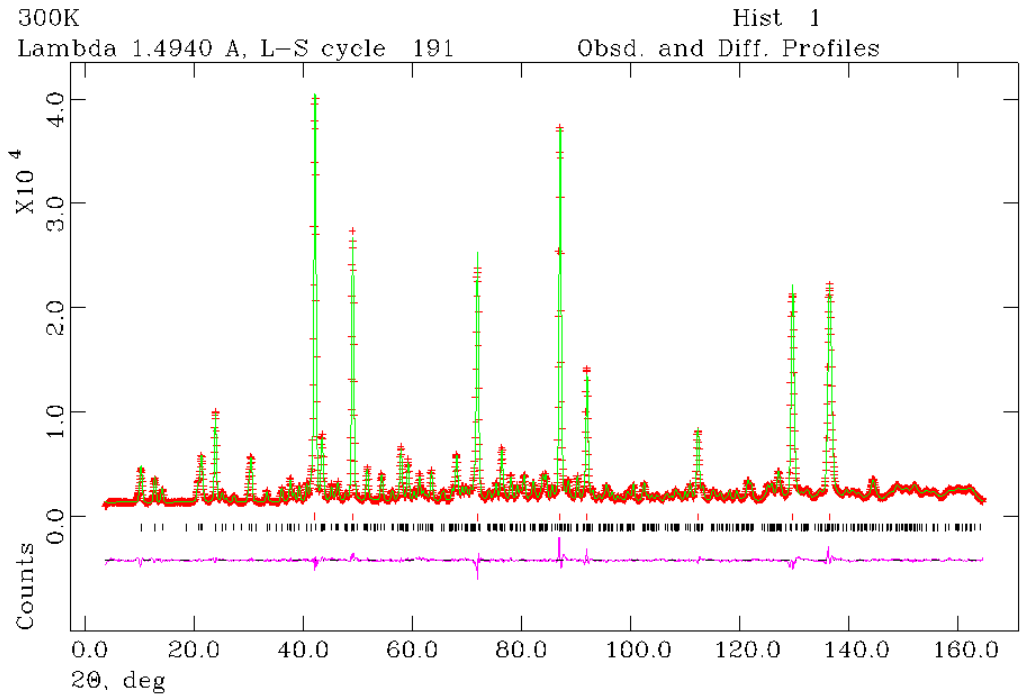

Figure 4-3. Full Rietveld plot of $Ge_5O(PO_4)_6$ (model : *R -3*) at 300 K which includes a difference, calculated and observed plots over the 2θ range of 0-164 Å from NPD data.

The quality of fit is satisfactory and supported by the R-factor values. Subsequent to this, refinement of the higher temperature patterns' yielded R-factors also consistent with a good fit. These values can be seen in Table 4-1.[†††]

		Fitted		- Background	
Temperature (K)	χ^2	wR_p (%)	R_p (%)	wR_p (%)	R_p (%)
300	4.443	3.91	2.96	3.67	2.84
573	5.087	4.18	3.2	3.83	3.09
723	3.375	4.97	3.85	4.22	3.56
873	4.682	4.09	3.09	3.16	2.70
1073	7.892	5.39	4.06	4.57	3.76

.

Table 4-1. A comparison of χ^2 and R-factor at 300 K, 573 K, 723 K, 873 K and 1073 K to show the measure of agreement between the *R-3* model and the NPD data. All values are indicative of a satisfactory structural fit between the *R-3* model and NPD data.

The above fit for NPD data at 300 K is inclusive of the refinement of atomic coordinates[‡‡‡] which corroborates with the reported single crystal data performed by Mayer, H *et al* (Table 4-2[10]).

[†††] All difference plots for the $Ge_5O(PO_4)_6$ shown in appendix 1A

Atom	Wyckoff position	X	Y	Z
Single crystal XRD				
Ge(1)	3a	0	0	0
Ge(2)	6c	0	0	0.1767(1)
Ge(3)	6c	0	0	0.4327(1)
P	18f	0.2892(6)	0.2668(6)	0.0915(2)
O(1)	3b	0	0	0.5
O(2)	18f	0.1347(17)	0.2222(17)	0.1334(5)
O(3)	18f	0.2185(17)	0.1439(16)	0.0412(5)
O(4)	18f	0.3616(17)	0.4832(18)	0.0738(5)
O(5)	18f	0.4513(15)	0.2462(15)	0.1128(5)
NPD				
Ge(1)	3a	0	0	0
Ge(2)	6c	0	0	0.17730(15)
Ge(3)	6c	0	0	0.43224(15)
P	18f	0.2901(5)	0.2687(4)	0.09080(16)
O(1)	3b	0	0	0.5
O(2)	18f	0.1320(6)	0.2209(6)	0.13293(14)
O(3)	18f	0.2204(5)	0.1433(5)	0.04097(15)
O(4)	18f	0.3630(5)	0.4815(4)	0.07321(15)
O(5)	18f	0.4550(4)	0.2484(5)	0.11278(11)

Table 4-2. A comparison of atomic coordinates of single crystal X-ray and NPD data with refined coordinates for $Ge_5O(PO_4)_6$ (*R-3* model) at 300 K. The NPD data is consistent with that seen previously from single crystal data[10].

The NPD patterns' for the temperatures 573-1073 K show the presence of an impurity which is characterised by the increased intensity of the peak at 2θ of 25.054 °. This was attributed to the possible recrystallization of GeO_2 from a minor amorphous phase. As a result, GeO_2 (*$P3_121$* model) was included into the structural refinement to account for this. This is illustrated in Figure 4-4.

‡‡‡ Refined structural parameters for $Ge_5O(PO_4)_6$ between the temperatures 300-1073 K in Appendix 1B

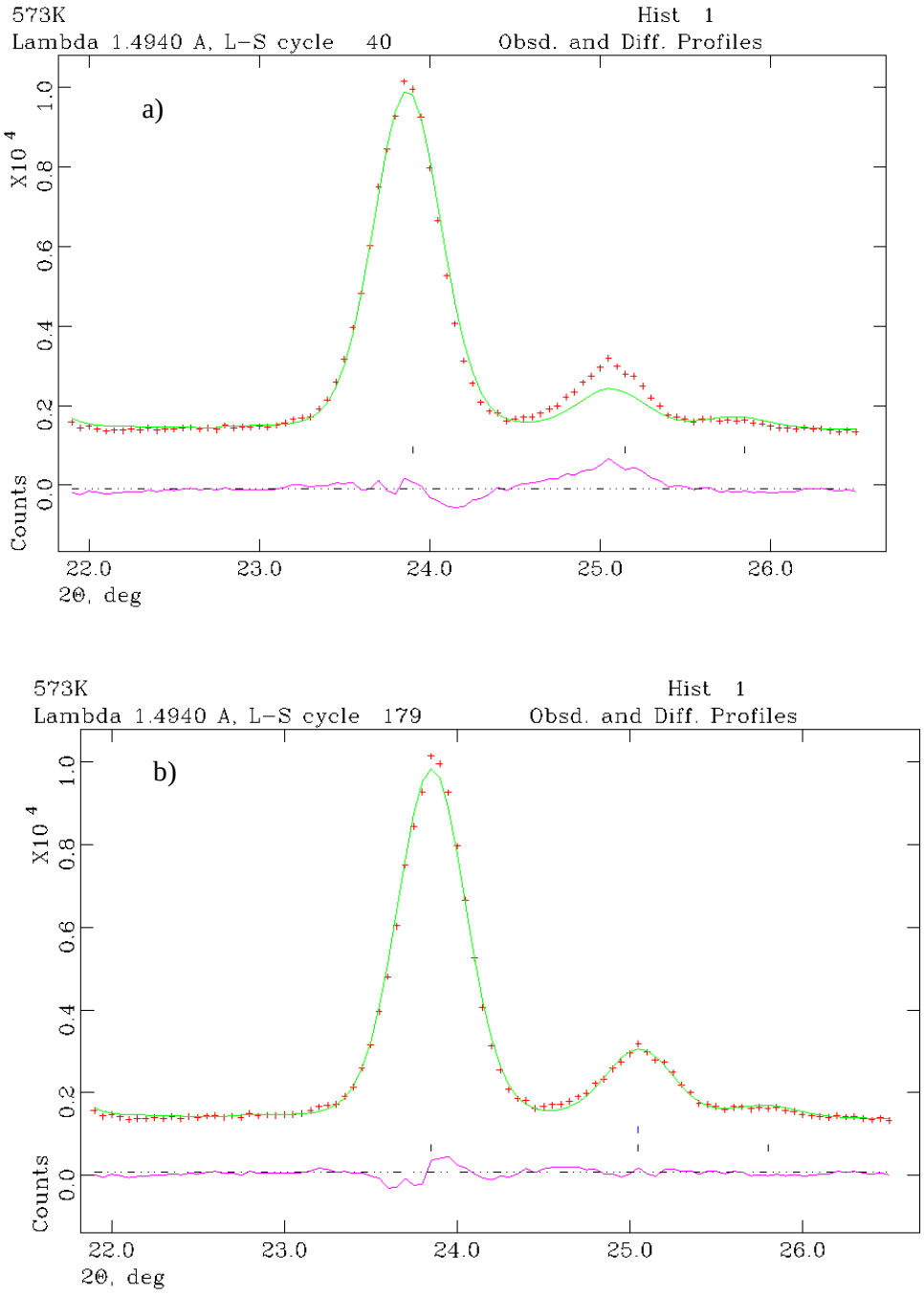

Figure 4-4. The Rietveld plot with the 2θ range 22-26.5. Black tick marks are the reflections for $Ge_5O(PO_4)_6$ (Model : *R-3*). Blue ticks marks are the reflections for GeO_2 (a) shows the Rietveld plot at 573 K without GeO_2 and b) shows the Rietveld plot at 573 K with GeO_2 (*$P3_121$* model) used in structural refinements.

As can be seen in Figure 4-4b the small peak at 25.054 2θ is more appropriately fitted and resulted in improved R-factors. As previously mentioned, this can also be seen in the higher temperature patterns; therefore, this was also applied to their refinement. At 1073 K, there is the minor

transition of α-GeO_2 to rutile GeO_2 so future analysis could be to include the rutile GeO_2 improve the structural fit.

4.3.1 NTE behaviour

A comparison of the unit cell parameters at various temperatures can be seen in Table 4-3.The results show that for the 300 K pattern the unit cell parameters are consistent with the single crystal data reported by Mayer, H. *et al.*[10]

Temperature (K)	*a* (Å)	*c* (Å)	*v* (Å^3)	*c/a*
NPD	7.99859(11)	24.8874(6)	1378.92(4)	3.11135
Single crystal XRD	7.994(4)	24.87(1)	1376.4	3.11108

Table 4-3. Comparison of unit cell parameters of $Ge_5O(PO_4)_6$ of single crystal XRD (Ref. 10) and NPD of $Ge_5O(PO_4)_6$ (*R-3* model). The data collected at 300 K showed that the unit cell parameters are consistent with that previously seen from single crystal XRD.

This sample was consequently used for the high temperature scans and used to determine the unit cell parameters of $Ge_5O(PO_4)_6$. This can be seen in Figure 4-5.

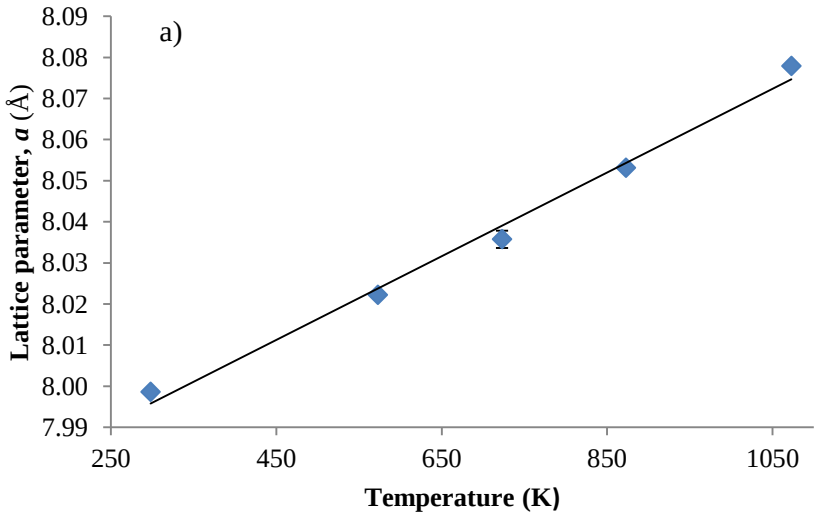

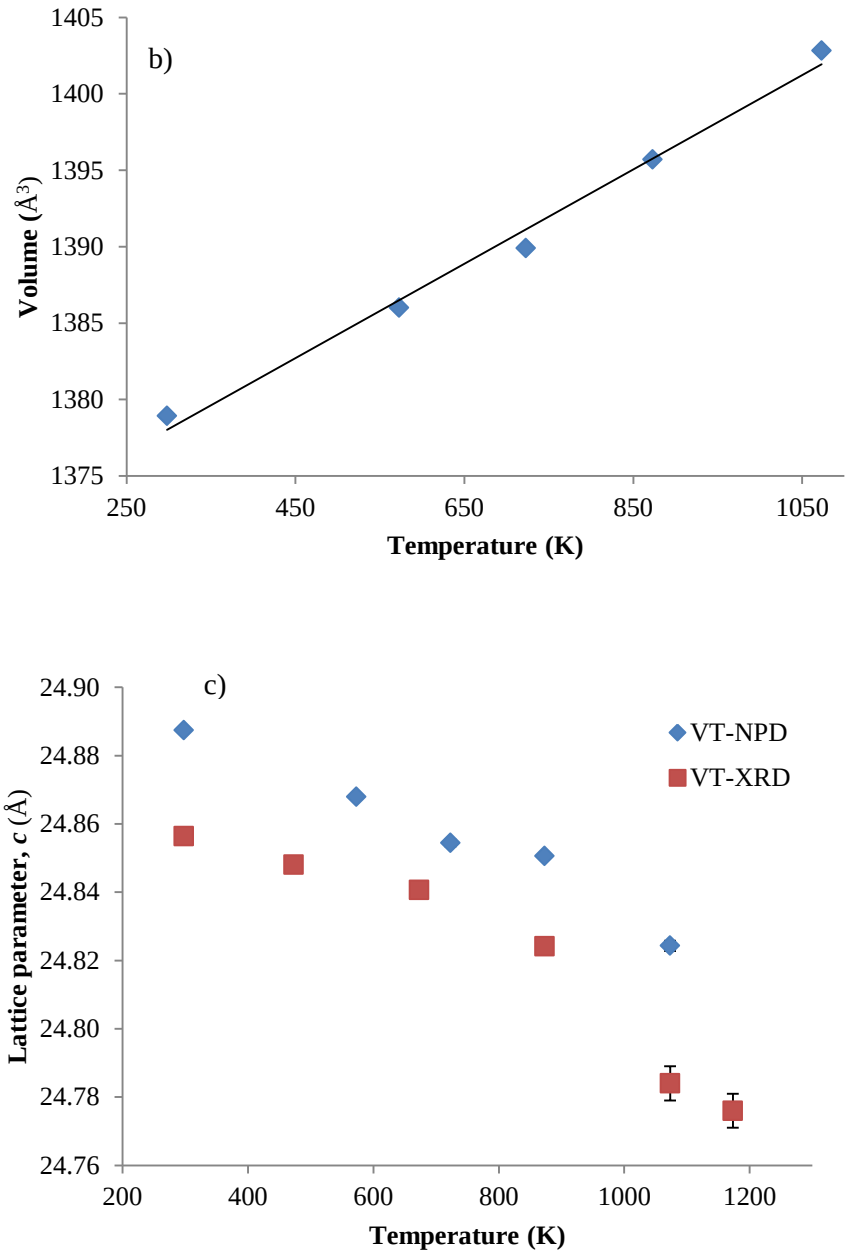

Figure 4-5. Comparison of unit cell parameters for $Ge_5O(PO_4)_6$ over the temperature range of 300-1073 K where a) is the lattice parameter *a*, b) is the lattice parameter *c* and c) is unit cell volume, *V* Å^3. The symbol blue diamond represents VT-NPD whilst the red square represents the VT-XRD data of $Ge_5O(PO_4)_6$.

It shows that unit cell parameter, *a* and volume increase with temperature. On the other hand, NTE is seen along the *c*-axis which is supported by VT-XRD. This is attributed to the rotation and counter-rotation of polyhedra into the cavities which reside along the *c*-axis and arises as anisotropic NTE.

On heating, lattice parameter ***a*** increases linearly with temperature. On the other-hand, the *c*-axis is shown to decrease in size. The increase in unit cell size is larger in the a-b direction and dominates over the changes seen in the *c*-direction. This is reflected in the overall increase in size for the volume. In Figure 4-5c, the unit cell parameters for a sample with a *c*/*a* value of 3.1090 at 300 K (similar to the NPD sample of *c*/*a* = 3.11135) was obtained using VT-XRD. The graph shows that both samples follow similar trends. There is the linear decrease in unit cell size along the *c*-direction until ≈ 873 K. In the NPD data, this change is seen as a small increase in unit cell size along the *c*-axis whereas in the VT-XRD data there is a small decrease. This showed that at this temperature there appears to be a change in the underlying processes that effects the reduction of the c-axis. For example, local lattice distortions that are specific to this temperature. These changes appear to persist at higher temperature due to the further reduction of cell size at 1073 K. This NTE behaviour may benefit anisotropic oxide ion conductivity along the c-axis as this decreases the size of the large cavities. This in turn allows for interstitial oxide ions to 'hop' more easily to neighbouring crystallographic sites.

NTE has been known to occur in a range of materials. One of the most studied materials showing this property is ZrW_2O_8 where recent studies include neutron diffraction to discern additional information on the underlying mechanism of its isotropic NTE[15]. $Ge_5O(PO_4)_6$ NTE behaviour is more like that seen in silicate quartz, cordierite and some zeolites where contraction is along one direction[16]. A generally accepted mechanism for NTE may be described as the occurrence of low energy structural vibrations that do not significantly distort the polyhedra within the material. These polyhedra are often referred to as 'rigid unit modes' (RUMs) where these structural vibrations lead to the rotation of the RUMs and counter rotation of connected polyhedra. As a result, rotation into large cavities may lead to the partial occupation of these spaces with temperature.

The presence of RUMS within this material should give rise to changes in certain bond angles[15] with temperature, however, bond angle analysis of $Ge_5O(PO_4)_6$ does not change significantly with temperature. This is most likely due to the nature of diffraction where only the average structure is represented. Despite this, the presence of RUMS within this material is possible. This is indicated by difference Fourier calculations which suggested a rotation of the tetrahedra in the Ge_2O_7 subunit. This process will be described in more detail later in this chapter.

Further studies are required to determine whether the RUMs model is applicable to the $Ge_5O(PO_4)$. X-ray absorption spectroscopy (XAS) is a possible experiment that would be sensitive to the local environment of the absorbing atom and show local correlated deviations from the average structure.

4.3.2 The origin of mobile oxide ion

To locate the origin of the mobile oxide ion within the structure isotropic ellipsoids were refined to determine the atomic displacement factors, U_{iso}. The U_{iso} value is the result of temperature-dependent atomic vibration or static disorder within the crystal lattice. Therefore, analysis of the U_{iso} values of all oxygen determined the most mobile oxide ion within the structure. A comparison of all the U_{iso} values can be seen in Figure 4-6. The graph showed O1 U_{iso} can be described in three main trends. Firstly, O1 over the temperature range 300 – 1073 K has a relatively high U_{iso} value. Secondly, U_{iso} steadily increases with temperature until ~ 873 K where there is a small but significant increase in U_{iso}. Finally, at 1073 K, U_{iso} is dramatically higher when compared to the other oxygen within the structure. These results showed that the O1 oxygen is the most mobile within the structure and therefore, an integral part of oxygen transport within the material.

This corresponded well with the crystallographic positioning of O1 which is hosted in the Ge_2O_7 subunit and more importantly not a part of the phosphate lattice. The phosphate lattice is considered a rigid component within $Ge_5O(PO_4)_6$ with the explanation being two-fold. Phosphorus has the predisposition to reside in a 4-fold coordination state and forms shorter and stronger P-O bonds (1.472-1.586 Å) when compared to Ge-O(1) (1.693(8) Å) at 1073 K. Consequently, oxygen within this rigid phosphate lattice is held more tightly within the structure. This conclusion is also supported by the comparatively low U_{iso} for O2, O3 and O5.

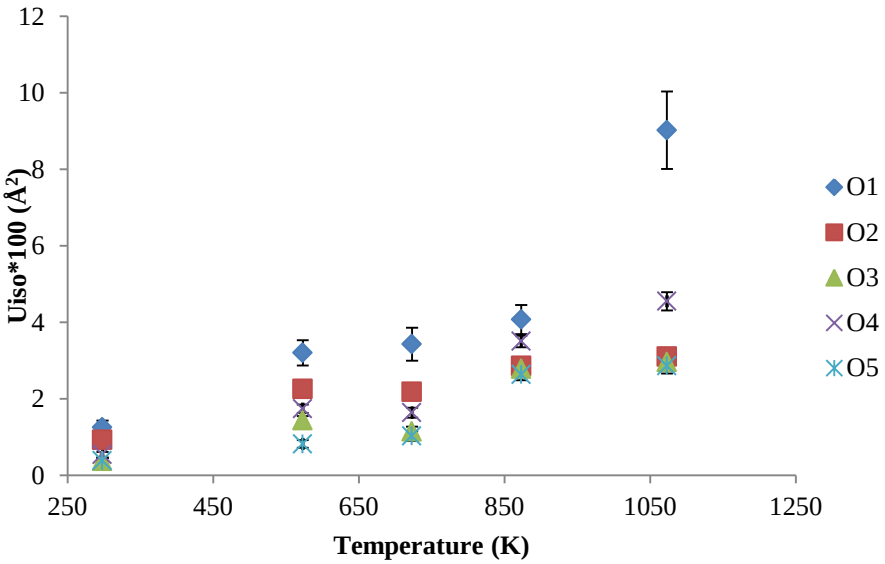

Figure 4-6. A comparison of U_{iso} for the oxygen crystallographically defined as O1, O2, O3, O4 and O5 over the temperature range of 300-1073 K. This graph shows that O1 over the specified temperature range has higher mobility when compared to O2, O3, O4 and O5.

The U_{iso} values for these oxygen environments increased with temperature as expected but do not show a large increase in the case with O1 at the highest temperature. Additionally, the relative

immobility of these oxygen may also be related to the effects of the NTE behaviour of the material. At this temperature for example, it could represent the maximum limit to the rotation of the polyhedra. This may then constrain the movement of the oxygen atoms, as they are held in the phosphate lattice. The decrease in unit cell size along the *c*-axis could also limit the spatial requirements for large movements of the oxygen. Interestingly, O4 oxygen is part of the Ge_2O_7 subunit and represents the second highest values for U_{iso} at the temperatures 873 K and 1073 K. This suggested that a large lattice distortion within the Ge_2O_7 occurs from the formation and stabilisation of mobile interstitial oxide ions.

4.3.3 Location of interstitial oxide ions around Ge_2O_7

Difference Fourier calculations were performed to locate the position of possible interstitial oxide ion sites around the Ge_2O_7 subunit and to generate a migration pathway for the O1 oxide ion. A comparison of the Fourier peaks around the O1 position can be seen in Figure 4-7.

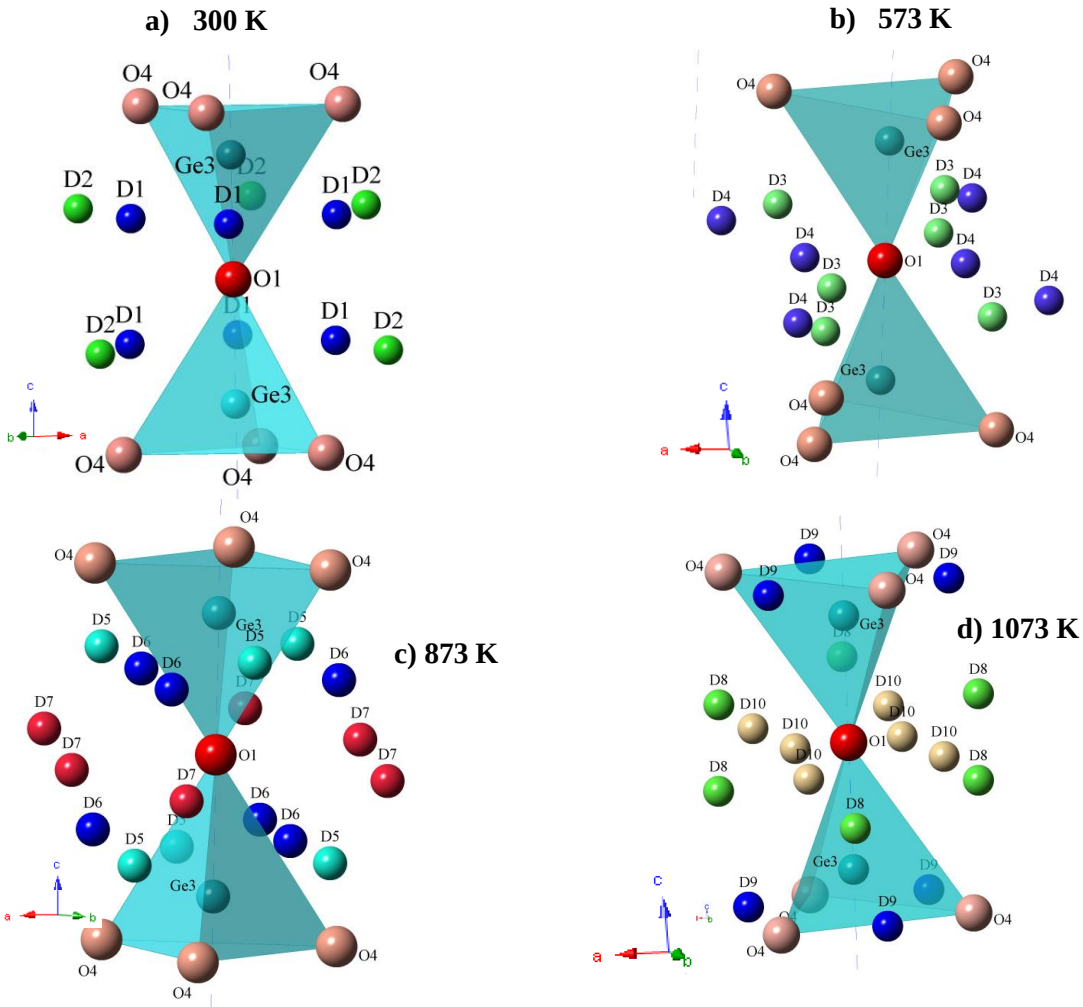

Figure 4-7. Schematic view of the location of the positive neutron densities generated by Fourier peak calculations around the Ge_2O_7 subunit at (a) 300 K, (b) 573 K, (c) 873 K and (d) 1073 K.

Initial analysis of these densities yielded information on their interatomic distances with neighbouring atoms around the Ge_2O_7 subunit which can be seen in Table 4-4. This gave an insight into the relative location of the densities and was consequently used in conjugation with the refinement results to evaluate possible interstitial oxide ion sites.

Density No.	Ge(3)-D (Å)	O(1)-D (Å)	O4-D (Å)
D1	1.82998(2)	1.80678(2)	1.53263(3)
D2	2.35923(3)	2.49187(3)	2.28944(3)
D3	1.7803(24)	1.66670(3)	1.580(6)
D4	2.5725(22)	2.31384(4)	1.948(6)
D5	1.46685(3)	1.85974(3)	1.43355(3)
D6	1.64400(3)	1.85974(3)	1.82533(4)
D7	2.5374(18)	2.19690(4)	2.04016(6)
D8	2.1748(34)	2.11192(6)	1.977(10)
D9	1.5192(27)	2.62609(9)	1.613(9)

Table 4-4. Interatomic distances between the positive neutron densities D1-D9 to neighbouring atoms around the Ge_2O_7 subunit. This is shown to give a further insight into the location of the densities.

As mentioned, the positive scattering densities found in the periphery of the 3b site were used to model interstitial O1 oxide ions (which will be referred to as O1'). Refinement of the interstitial sites were performed with the following parameters; U_{iso} of the interstitial atom was set to an average U_{iso} of the crystallographically defined oxygen, atomic coordinates were not refined as this was pre-determined by the difference Fourier calculations. Site occupancy was refined for these oxide ion sites to determine whether the location of these densities represent a site that is significantly occupied. The results can be seen in Table 4-5.

573 K

	χ^2	wRp (%)	X	Y	Z	Fractional occupancy
Original refinement (573 K) R-factors	5.087	4.18				
D3	5.011	4.15	0.034520	0.832660	0.4708	0.083(14)
D4			0.027360	0.6115	0.147880	0.026(14)

873 K

Original refinement (873 K) R-factors	4.682	4.09				
D5	4.606	4.05	0.234620	0.466440	0.117240	0.079(11)
D6			0.139420	0.506860	0.130800	0.074(19)

1073 K

Original refinement 1073 K R-factors	7.892	5.39				
D8	7.670	5.31	0.061810	0.467260	0.135780	0.0184(11)
D9			0.157610	0.48800	0.077980	0.1011(10)

Table 4-5. A comparison of Rietveld refinement results derived from positive scattering density around the 3b site (O1) with temperature. The table shows the densities that were successfully modelled for the temperatures 573 K, 873 K and 1073 K.

The structural refinement at 300 K yielded divergent results and led to unreasonable site occupancy values for D1 and D2. This suggested the O1 atom has insufficient energy to dissociate from the 3b site to become mobile at 300 K. At the temperatures 573 K, 873 K and 1073 K, improvements to the fit were obtained on the addition of the Fourier peaks to the refinement. In addition to this, the obtained values for site occupancy were between 0.0184-0.1011. These values showed a low site occupancy which is fitting to the nature of mobile oxide ions on interstitial sites.

At 573 K, D3 and D4 are located loosely in the periphery of the 3b site and therefore, represent possible locations for O1'. This suggested that the thermal vibration of O1 has increased with temperature and now scarcely reside in the *a*-*b* plane of the 3b site. As the temperature increases to 873 K, the site occupancy of the interstitial oxide ions along the *a*-*b* plane appears to decrease which is indicated by the refinement of the Fourier peak, D7. This led to an unstable refinement and an unrealistic site occupancy level. This is contrasted by the refinement results of D5 and D6. The location of these Fourier peaks resided more closely in the periphery of Ge3 atom with the

Ge3-D interatomic distance of 1.46685 (3) and 1.64400 (3) Å, respectively. This suggested at higher temperatures there is a larger tendency for the mobile oxide ion to move along the c-axis after the initial displacement of O1 into the *a-b* plane. This is a consequence of the increased thermal vibrational energy of the O1 atom. This is further supported from the refinement of the density D8 and D10 at 1073 K. The refinement of D8 led to minor improvements of the fit with the site occupancy of 0.0184 while the refinement of D10 (resides more closely to the 3b site) led to unrealistic negative occupancy values. This suggested that the close periphery of the 3b site is not as frequently occupied with temperature. However, as the distance from the 3b site increases, as in the case with D8 (2.114 Å from 3b site), it leads to a more reasonable site occupancy. The most significant improvement to the fit was the refinement of the D9 density. This density is in the alternating spaces in plane with the O4 oxygen. The bond distance of Ge3-D9 (1.5192 Å) is not dissimilar to Ge-O4 (1.634 Å) and has a D9-Ge3-O1 angle of 109.57 °. These values are characteristic features of a tetrahedron unit which in turn suggested that the D9 density represents corner-sharing oxygen from a rotated tetrahedron (Figure 4-8).

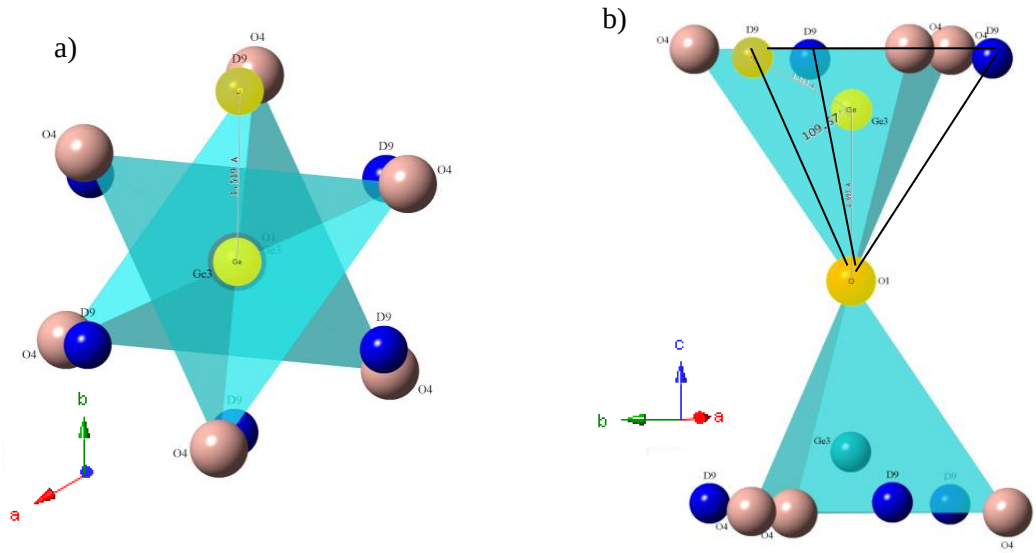

Figure 4-8. Schematic of Ge_2O_7 where a) shows 001 view and the bond distance between D9-Ge3 and b) shows the 100 view which displays the bond angle between D9-Ge3-O1 within the Ge_2O_7 subunit at 1073 K.

Fourier difference calculations have made clear that the formation of mobile O1 ions is concomitant with local lattice distortions around Ge_2O_7. The locations of these densities give a detailed insight into the nature of the local lattice distortion around the Ge_2O_7 during the oxide ion conducting process which can be seen in Figure 4-9.

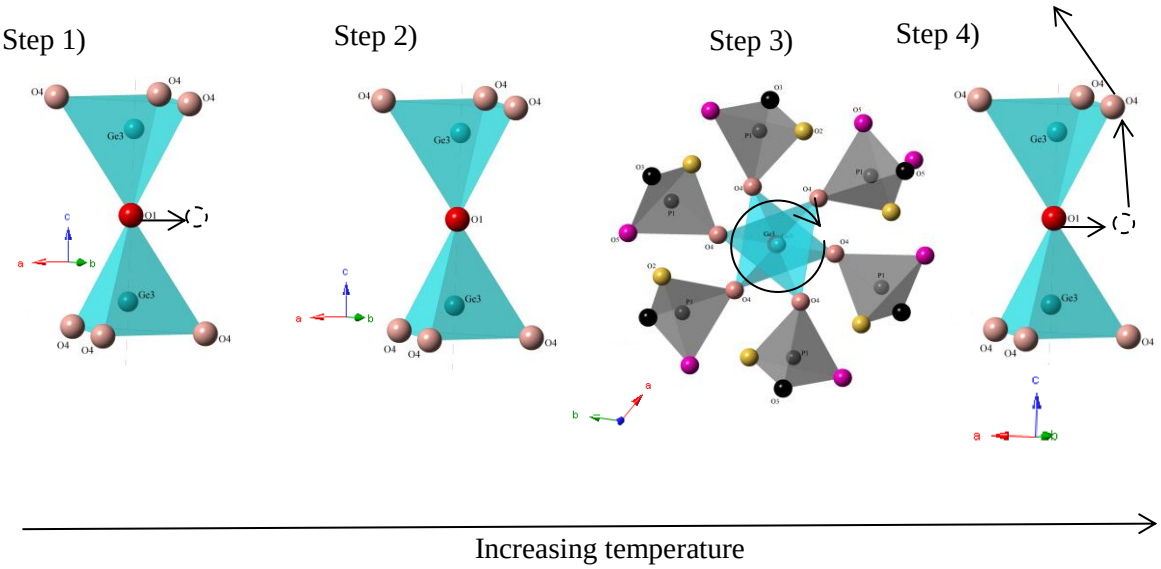

Figure 4-9. Illustration of the formation of mobile oxide ions from the Ge_2O_7 subunit detailed in 4 steps. These local lattice distortions arise as a result of an increase in temperature. Consequently, the O1' moves from its initial 3b site along the *c*-axis. Stabilisation of the O1' is facilitated by low vibration distortion of the Ge_2O_7 in the form of a rotation of the Ge_2O_7 subunit and finally an interstitialcy mechanism occurs with the O4 atom.

This illustration shows that in step 1, the O1 has low level displacement from the 3b site at lower temperatures. It is preferentially displaced into the *a*-*b* plane because a direct displacement along the *c*-axis would cause a significantly larger distortion to the Ge_2O_7 subunit. If O1 were to move directly along the *c*-axis, this would move towards the Ge3 atom causing charge compensation to occur in the form of O4 moving away from the Ge3 atom. However, the O4 are strongly bound to a phosphorus atom so has the tendency to remain rigid. Consequently, the mobility of the O1 atom is restricted to the *a*-*b* plane. In step 2, when the temperature increases, the O1' thermal vibration increases which effects the directionality of the travelling mobile interstitial oxide ion. The gain in additional vibrational energy allows O1' to move further from its 3b site. O1' is stabilised by the Ge3 which promotes the propensity for it to travel along the *c*-axis into its periphery. In step 3, as the O1' moves closer to the O4 oxygen, the O4 atoms compensate for the charge and size of the oncoming O1' by moving away from it. However, as mentioned previously, O4 is restricted in its movement as it is retained within the phosphate lattice. As a result, rotation of the GeO_4 occurs due to the limited degree of freedom imposed by the phosphate lattice to stabilise O1'. In step 4, an interstitialcy mechanism occurs and an O4 oxide ion is displaced into to the structural cavities (O4'').

O4'' was located by using difference Fourier calculations when a more focused look at the densities within the cavities was performed. An illustration of the positive scattering densities of interest can be seen in Figure 4-10.

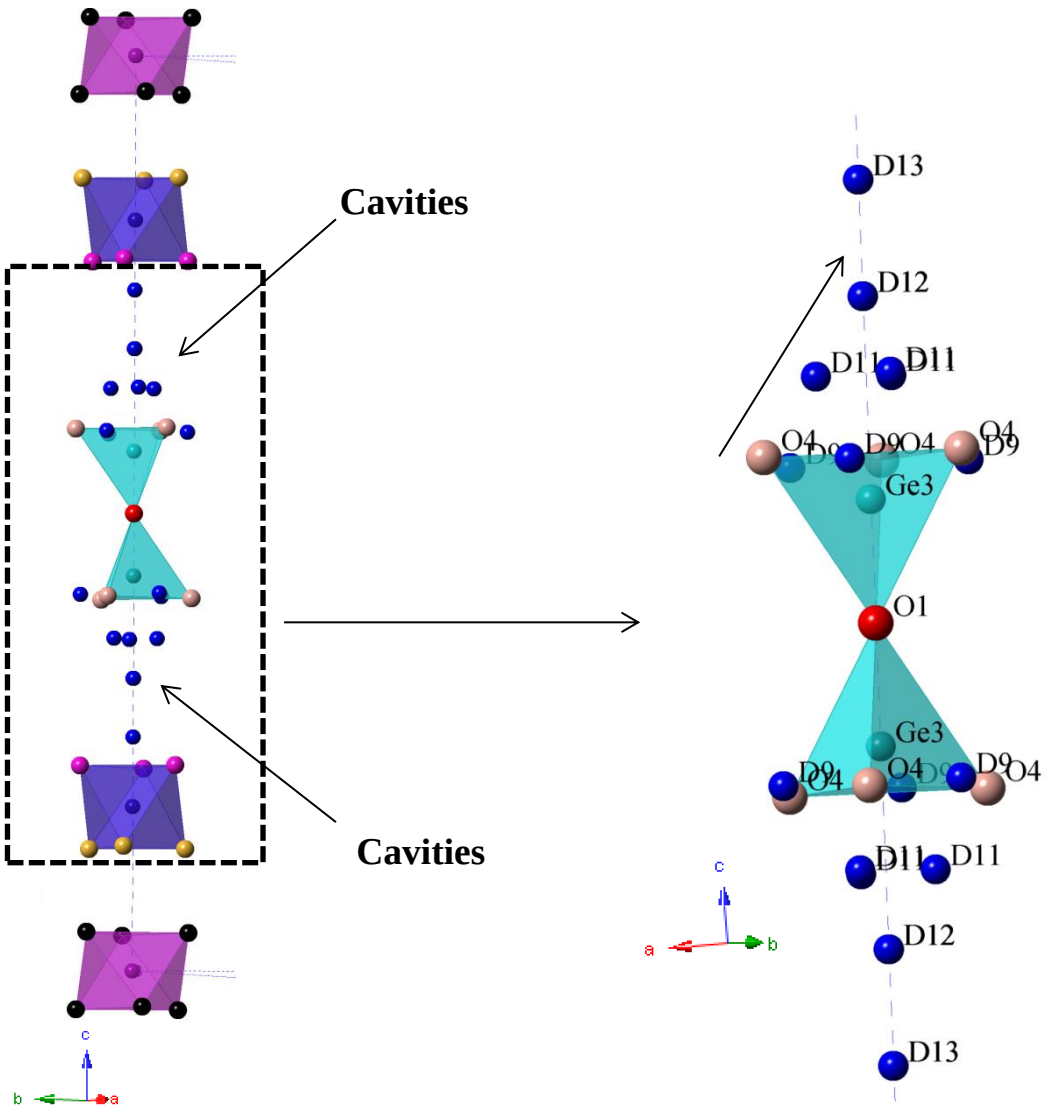

Figure 4-10. Illustration of located positive neutron densities within the cavities. This shows possible sites for mobile interstitial oxide ions as they move into the large cavities that reside within the structure. These densities have been labelled D9-13 depending on location.

More details on the locations of the positive excess densities in relation to neighbouring atoms can be seen in Table 4-6. The D13 density is found within the cavities, however, resides more closely to the GeO_6 local structures as can be seen by the large Ge3-D13 interatomic distances of greater than 3.00 Å.

Density No.	Ge(3)-D Å	O4-D Å
D11	1.838 (7)	1.485 (9)
D12	2.778 (8)	2.687 (9)
D13	> 3.00	> 3.00

Table 4-6. Atomic distances for the positive neutron densities D11-D12 which reside within the cavities to neighbouring atoms within the Ge_2O_7 subunit.

The Fourier peak calculations showed that the displaced oxide ion O4'' does indeed reside within the cavities. The D11 density is located in-between D9 and D12. The bond distance from Ge(3)-D11 is 1.838 Å which is a typical Ge-O bond length. However, the O4-D11 interatomic distance of 1.485 Å shows that D11 is too close to the O4 atom. Therefore, it was concluded that D11 is the prerequisite position for the O4'' as it ultimately resides within the D12 position. Refinement of the interstitial oxygen D12 and D13 yielded an improvement in the fit and can be seen in Table 4-7.

	1073 K					
	χ^2	**wRp (%)**	**X**	**Y**	**Z**	**Fractional occupancy**
Original refinement 1073 K R-factors	7.892	5.39				
D12	7.755	5.34	0.667020	0.333590	0.0134400	0.026(8)
D13			0.66675	0.33313	0.0776600	0.047(8)

Table 4-7. This shows that the structural model is improved with the addition of D12 and D13 densities. This suggested that these site locations may present possible sites for mobile oxide ions for oxygen transport within the material.

The D12 density is located at a distance of 2.687 Å from an O4 atom. This bond distance is a similar distance between the O1-O4 of 2.779 Å. In addition to this, the bond angle between D12-O4-O4 is 59.2 ° which is comparable to the O1-O4-O4 bond angle of 60.66 °. These crystallographic features are representative of the formation of a GeO_4 from O4'' and O4. From this data, a proposed mechanism of the progression of interstitial oxide ions within the cavities can be seen in Figure 4-11.

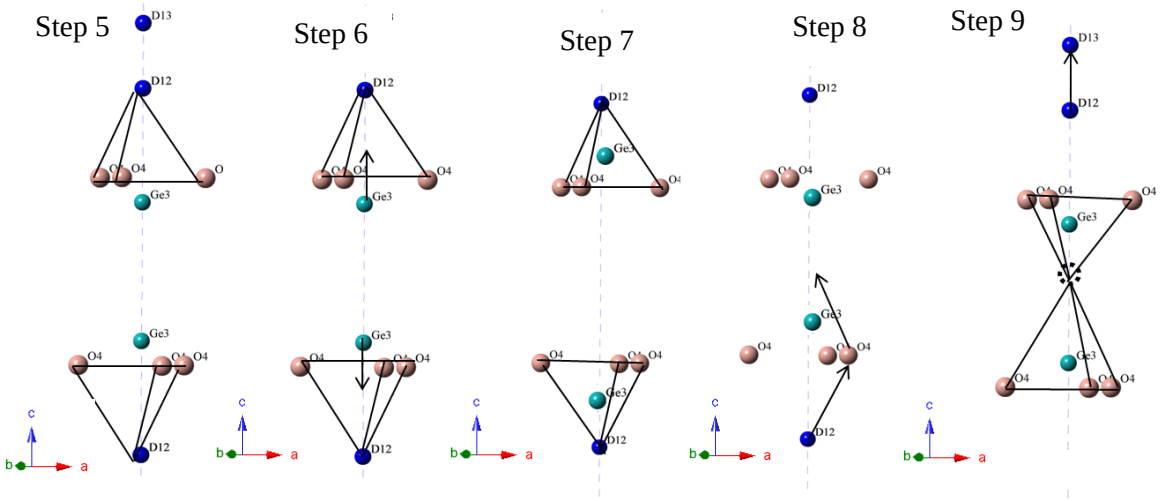

Figure 4-11. Schematic view of the mechanism for the propagation of mobile oxide ions into the large cavities within the structure. Mobile oxide ions are stabilised and mobilised by the flexible Ge cationic lattice afforded by the formation of two inverted tetrahedra.

In step 5, the interstitial O4'' has moved into the D12 position and characteristic GeO_4 tetrahedra is formed. At this stage, the O4'' oxide ion requires stabilisation to maintain charge neutrality within the crystal structure. This is shown in step 6, where O4'' is stabilised by the consequential movement of the Ge3 cation into the tetrahedra unit. In step 7, a rested state is formed where there is the formation of 2 inverted GeO_4 from Ge_2O_7. In step 8, O4 are displaced from its site by interstitial oxide ions via an interstitialcy mechanism. As a result, oxide ions are moved towards the 3b site and the O1 atom is replenished. Finally in step 9, the Ge_2O_7 unit is reformed. Subsequent to this, the O4'' travels into the position that lies on D13 which is further along the *c*-axis.

For this mechanism to occur, O4'' must be stabilised by the movement of Ge3. To determine whether Ge3 does stabilise the O4'', analysis of the mobility of Ge atom was performed. A comparison of the U_{iso} values of the germanium atoms showed that Ge3 has the largest atomic displacement values (Figure 4-12).

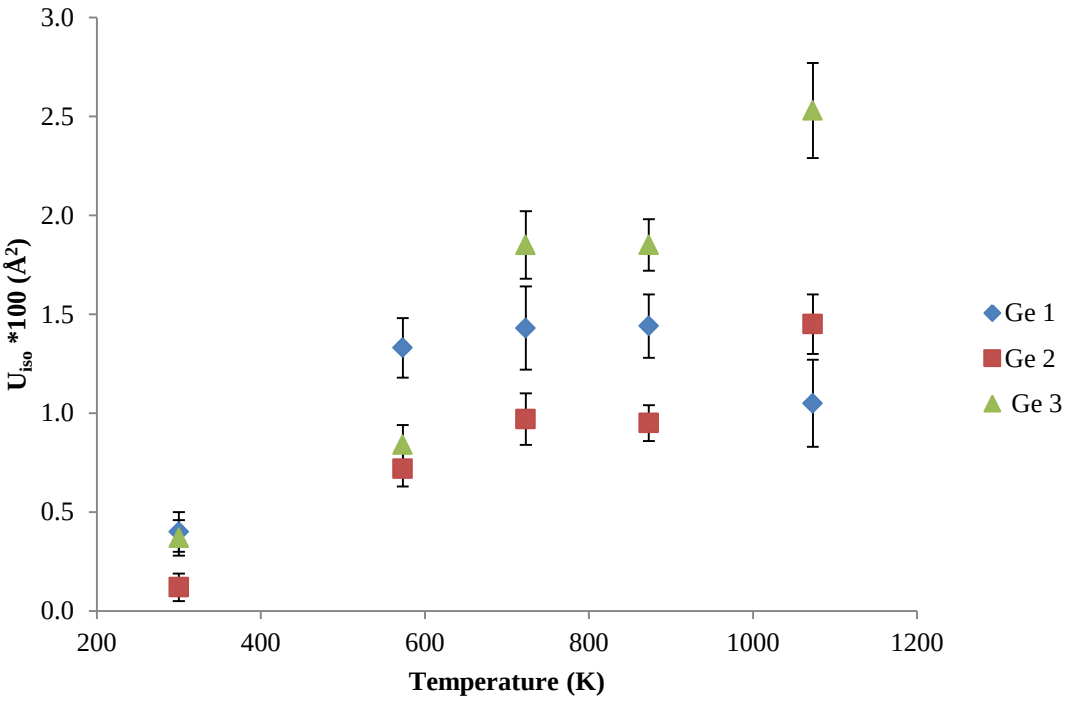

Figure 4-12. A comparison of U_{iso} values for the germanium atoms that are crystallographically defined as Ge1 (Blue diamond), Ge2 (red square) and Ge3 (green triangle) between the temperature range of 300-1073 K. Ge3 shows the highest mobility which is indicative of a large local lattice distortion of the Ge_2O_7 to stabilise mobile oxide ions for oxygen transport.

As shown above, Ge3 has the largest U_{iso} values between 723-1073 K which corroborates with the Fourier peak analysis that suggested the inversion of the Ge_2O_7 is largely a higher temperature process. Conversely, Ge2 U_{iso} trends upwards with temperature which is expected, however, there is a decrease in these values at 1073 K. Again, this is most likely related to the underlying processes of the NTE behaviour of the material as previously seen for the atoms O2, O3 and O5.

As previously mentioned, the Fourier peak at D13 is caused from a reformed Ge_2O_7 subunit. This density is located near the GeO_6 polyhedra, therefore, local densities around these structures were investigated to discern a mechanism for oxygen transport. The densities located around the GeO_6 at 1073 K are shown in Figure 4-13.

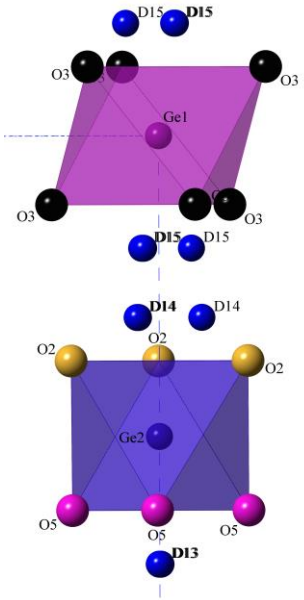

Figure 4-13. Illustration of the positive neutron densities around the GeO_6 units. This shows the possible sites of mobile oxygen atoms around these local structures.

The consequent successful refinement of these densities can be seen in Table 4-8.

	1073 K					
	χ^2	wRp (%)	X	Y	Z	Fractional occupancy
Original refinement 1073 K R-factors	7.892	5.39				
D14	7.881	5.38	0.01380	0.08414	0.10846	0.019(11)

Table 4-8. The structural model statistics for the incorporation of D14 within the refinement process. The results showed an improvement in χ^2 and wRp (%) which suggested a possible site for mobile oxide ions.

A small improvement to the fit can be seen when D14 was refined. The results suggested that there is a possible interstitial site in between the GeO_6. However, the refinement of D15 shows that it led to an unrealistically occupied site. This result may be due to the close relative location of D14 and D15, therefore, difficulties arose when modelling these densities at the same time. The refinement of only D15 led to a low occupancy level of 0.004(8), which is consistent with this conclusion.

The location of the densities D13-D15 in relation to the neighbouring atoms among the GeO_6 polyhedra may be seen in Table 4-9.

Density No.	Ge(1)-D (Å)	Ge(2)-D (Å)	Closest oxygen-D (Å)
D13	> 3.00 Å	1.892(8)	(D13-O5) 1.707(8)
D14	2.76553(12)	1.872(8)	(D14-O2)1.192(8)
D15	1.73396(7)	2.831(8)	(D15-O3) 1.669(8)

Table 4-9. Atomic distances for the positive neutron densities D13-D15 to the neighbouring atoms among the GeO_6 polyhedra subunits.

As can be seen in the table above, interatomic distances may present an insight into the most probable interaction each density has with their neighbouring structures. D13 lies more than 3.00 Å away from Ge1 and is unlikely to interact with Ge1-O_6. Ge(2)-D13 has an interatomic distance of 1.892 (8) Å which may represent a typical Ge2-O5 bond (1.864 (9) Å). Similarly, Ge2-D14 has a characteristic interatomic distance of 1.872 (8) Å which represents a typical Ge(2)-O2 bond of 1.883 (10) Å. D15-Ge1 is shorter than a usual Ge1-O3 bond (1.910 Å), however, falls within a typical Ge-O bond length between 1.693-1.910 Å seen within $Ge_5O(PO_4)_6$ at 1073 K. In addition to this, the interatomic distances analysis shows that the densities reside too close to their closest neighbouring oxygen (1.192 – 1.707 Å). This suggested that when considering the location of the densities and their close proximity to their closest neighbouring oxygen atoms an interstitialcy mechanism is likely to occur through the GeO_6 structures. A mechanism for the movement of mobile oxide ions through the GeO_6 units is shown in Figure 4-14.

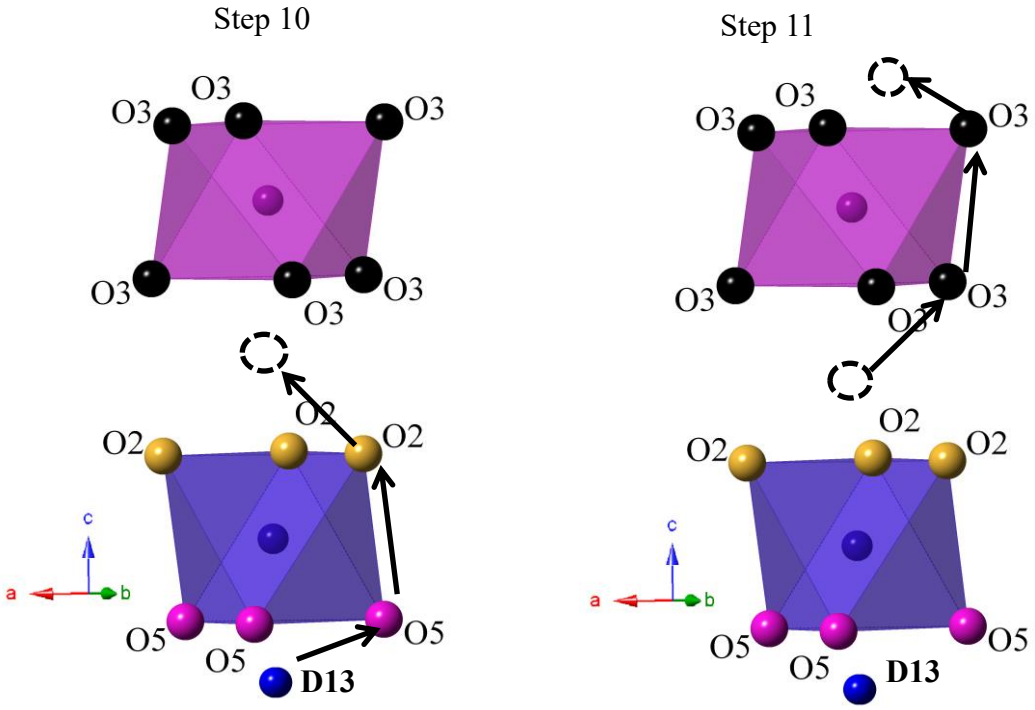

Figure 4-14. Illustration of the proposed oxide ion conduction mechanism considering the site location for the D13 density. It shows the occurrence of an interstitialcy mechanism with the oxide ions which are coordinated on the GeO_6 structures.

In step 10, mobile interstitial oxide ions are propagated through the cavity towards a GeO_6 to where the D13 density lies. The mobile interstitial oxide ion is mobilised and stabilised by an interstitialcy mechanism where O5 is displaced by the mobile oxide ion followed by O2. This resulted in the formation of an interstitial oxide ion which resided closely to the GeO_6 formed from the Ge1 atom.

In step 11, the interstiticialcy mechanism continues as two O3 atom are displaced by the mobile interstitial oxide ion. This resulted in the interstitial oxide ion O3' being displaced into a structural cavity which allows for the continued oxygen transport along a channel in line with the *c*-axis.

4.3.4 Structural refinement with key positive scattering densities

The key neutron positive densities D9, D12, D13 and D14 were added to the Rietveld refinement to determine the overall improvement in structural fit. This yielded an overall improvement in fit from wR_p = 5.39 % to 5.27 %. The refined parameters can be seen in Table 4-10.

Atom	Wyckoff position	X	Y	Z	Site occ.	U_{iso} x 100 ($Å^2$)
Overall						
Ge(1)	3a	0	0	0	1	1.14(22)
Ge(2)	6c	0	0	0.17885(34)	1	1.59(16)
Ge(3)	6c	0	0	0.43223(32)	1	2.75(21)
P(1)	18f	0.2826(10)	0.2667(9)	0.0906(4)	1	1.58(14)
O(1)	3b	0	0	0.5	1	11.07(132)
O(2)	18f	0.1326(13)	0.2157(12)	0.13455(30)	1	2.95(19)
O(3)	18f	0.2260(11)	0.1543(11)	0.04174(34)	1	3.08(24)
O(4)	18f	0.3519(14)	0.4797(12)	0.07353(43)	1	4.79(25)
O(5)	18f	0.4516(11)	0.2550(12)	0.11023(27)	1	2.87(20)
D9	18f	0.157610	0.488000	0.077980	0.101(11)	3.00
D12	18f	0.667020	0.333590	0.013440	0.039(9)	3.00
D13	18f	0.666750	0.333130	0.077660	0.030(7)	3.00
D14	18f	0.013800	0.084140	0.108460	0.057(12)	3.00

Table 4-10. Refined parameters for $Ge_5O(PO_4)_6$ with the densities D9, D12, D13 and D14. It shows that the occupancy of the excess densities D9, D12, D13 and D14 have low site occupancies which may be characteristic of possible sites for mobile oxide ions at temperature.

As can be seen the site occupancy values for the densities range from 0.030-0.101 which is consistent with a lowly occupied site as expected from mobile interstitial oxide ions. Therefore, suggested that these are key sites for the propagation of oxide ions through the structure.

4.4 Conclusion

NPD has outlined a detailed oxide ion conduction pathway and demonstrated the relationship between distorted local structures and the formation of mobilised oxide ions. Oxygen interstitials within $Ge_5O(PO_4)_6$ were mobilised and stabilised by the synergy of three well defined crystallographic features. The first feature is centralised around the Ge_2O_7 subunit where the 'excess' O1 oxygen is hosted and dissociated from the 3b site to form mobilised oxide ions. Consequently, the mobilised oxide ions are stabilised within the large cavities when two inverted tetrahedra are formed from the Ge_2O_7 subunit. The phosphate lattice also played a part in the inversion distortion which effectively acts as a rigid framework to anchor the O4 oxygen and avoid unnecessary distortion to the crystal lattice. Secondly, large cavities within the open framework play an important part. It allowed for the progression of mobile interstitial oxide ions along the *c*-

axis, unimpeded from cationic restrictive energy and provided ample space for the transmission of mobile ions. Finally, the germanium channels provided a flexible cationic network where interstitial oxide ions could be stabilised and permeate anisotropically along the c-axis.

This has been supported from the use of bond distance analysis, bond angles, Fourier difference calculations and $U_{iso.}$ Atomic displacement factors showed that the most mobile atoms were O1 and Ge3 which were required due to the large distortion seen in the Ge_2O_7. Fourier peak analysis showed the location of the mobilised oxide ions and this was used to determine bond distances and angles to give a detailed view into the local structural changes. This material offers an alternative route for the development of oxide ion conductors by introducing novel strategies to improve oxygen transport within this class of material.

Future doping strategies may include the substitution of germanium with various cations such as Ti, Ga and Al which may improve conductivity by promoting the local lattice distortions that occur within the parent composition.

Other materials that show similar structural features can be seen in $Ge_3Si_2O(PO_4)_6$ and $NaGe_2P_3O_{12}$,[17] therefore, may be of interest for future study. $Ge_3Si_2O(PO_4)_6$ presents a structure that has a cationic network which runs along the *c*-axis and contains large cavities[11]. In the case of $NaGe_2P_3O_{12}$ large cavities containing Na^+ has also been seen.

To conclude, $Ge_5O(PO_4)_6$ presents an alternative direction for the development of oxide ion conducting electrolytes. It demonstrated structural features not typically associated with the conduction of oxide ions. In addition to this, these features are capable of providing a less constrained pathway for the transport of oxide ions through the structure.

4.5 References

1. Steele, B. C. H. & Heinzel, A. Materials for fuel-cell technologies. **414,** 345–352 (2001).

2. Goodenough, J. B. Oxide-ion electrolytes. *Annu. Rev. Mater. Res.* **33,** 91–128 (2003).

3. Ramamoorthy, R., Dutta, P. K. & Akbar, S. A. Oxygen sensors : Materials , methods , designs. **8,** 4271–4282 (2003).

4. Fergus, J. W. Electrolytes for solid oxide fuel cells. *J. Power Sources* **162,** 30–40 (2006).

5. Sansom, J. E. H., Richings, D. & Slater, P. R. A powder neutron diffraction study of the oxide-ion-conducting apatite-type phases, $La_{9.33}Si_6O_{26}$ and $La_8Sr_2Si_6O_{26}$. *Solid State Ionics* **139,** 205–210 (2001).

6. Slater, P. R., Sansom, J. E. H. & Tolchard, J. R. Development of apatite-type oxide ion

conductors. *Chem. Rec.* **4,** 373–384 (2004).

7. Islam, M. S., Tolchard, J. R. & Slater, P. R. An apatite for fast oxide ion conduction. *Chem. Commun.* **13,** 1486–1487 (2003).

8. Kuang, X. *et al.* Interstitial oxide ion conductivity in the layered tetrahedral network melilite structure. *Nat Mater* **7,** 498–504 (2008).

9. Park, H. J. *et al.* $Sr_2(Mg_{1-x}Ga_x)Ge_2O_{7+0.5x}$: Melilite-type oxygen ionic conductor associated with fivefold coordinated germanium and gallium. *J. Power Sources* **275,** 884–887 (2015).

10. Mayer, H. & Völlenkle, H. Die Kristallstruktur von $Ge_5O(PO_4)_6$. *Monatshefte für Chemie/Chemical Mon.* **103,** 1560–1571 (1972).

11. Leclaire, A. & Raveau, B. $Ge_3P_6Si_2O_{25}$: A cage structure closely related to the intersecting tunnel structure $KMo_3P_6Si_2O_{25}$. *J. Solid State Chem.* **75,** 397–402 (1988).

12. R. A. Young. *The Rietveld Method*. (Oxford University Press, 1995).

13. Larson, A. C. & Von Dreele, R. B. General Structure Analysis System (GSAS). 86–748 (2004). doi:10.1103/PhysRevLett.101.107006

14. Toby, B. H. General Structure Analysis System - GSAS / EXPGUI, A Graphical user interface for GSAS. *J. Appl. Cryst.*, **34,** 2001 (2001).

15. Tucker, M. G., Keen, D. a, Evans, J. S. O. & Dove, M. T. Local structure in $ZrW_2O_8$from neutron total scattering. *J. Phys. Condens. Matter* **19,** 335215 (2007).

16. Qu, B. Y., He, H. Y. & Pan, B. C. Origin of the Giant Negative Thermal Expansion in. *Adv. Condens. Matter Phys.* **8,** 1–7 (2012).

17. Zhao, D. *et al.* Structure determination, electronic and optical properties of $NaGe_2P_3O_{12}$ and $Cs_2GeP_4O_{13}$. *J. Mol. Struct.* **922,** 127–134 (2009).

5 NPD study on $Si_5O(PO_4)_6$ and $Ge_5O(PO_4)_6$

5.1 Introduction

Silicon oxide phosphate, $Si_5O(PO_4)_6$ was first structurally characterised by Mayer. H *et al*[1] using single crystal X-ray diffraction. The structure is quite unusual due to the silicon atoms adoption of 6-fold and 4-fold coordination state. This is rarely seen in inorganic crystals due to silicon's relatively small size; it does not usually adopt a 6-fold coordination state[2,3]. Further structural studies of the material included the formation of this material via low temperature methods to synthesise powdered $Si_5O(PO_4)_6$. In this work, it was determined that the materials synthesised were structurally the same as that seen for the single crystal $Si_5O(PO_4)_6$. Additional information derived from this study suggested that the material was not part of a solid solution as suggested by Liebau *et al*[4]. The use of $Si_5O(PO_4)_6$ as a functional material has been seen in a wide range of areas such as proton conductors[5], catalysts[6] and oxide ion conductors[7]. However, in regards to its oxide ion conduction properties it is relatively poor. This is in comparison to the isostructural material $Ge_5O(PO_4)_6$ which at 901°C has total conductivity of 1.45 x 10^{-5} Scm^{-1} whereas $Si_5O(PO_4)_6$ is ~2-3 magnitudes lower in conductivity at the same temperature[5,7]. The lower conductivity was attributed to the exchange of germanium with silicon, which negatively impacts ionic conductivity for the following two reasons; Firstly, due to the smaller size of silicon it forms smaller and stronger bonds with oxygen. Therefore, the energy required to break these bonds to mobilise oxide ions is higher than in the germanate analogue. Secondly, it has been suggested that the presence of Si increases the grain resistance.

In this chapter a structural study of $Si_5O(PO_4)_6$ was performed using variable temperature NPD. This was to further the understanding of the structure of $Si_5O(PO_4)_6$ and drive its future development in all its respective applications. This data was used to compare against $Ge_5O(PO_4)_6$ to determine local structural differences. Additionally, a structural relationship with the poor oxide ion conductivity within the silicate was evaluated. Fourier difference calculations were also performed to determine possible interstitial oxide ion sites for the silicate.

5.2 Experimental

The synthesis of $Si_5O(PO_4)_6$ was performed using the ceramic method with fumed SiO_2 (Sigma Aldrich 99.999 %) and $NH_4H_2(PO_4)_6$ (Sigma Aldrich 98+ %). The fumed SiO_2 was heated at 950 °C for 1 hour to drive off water and CO_2 in an alumina crucible. Stoichiometric amounts of hot fumed SiO_2 and $NH_4H_2(PO_4)_6$ were then quickly added together. The two reagents were then ground together and calcined for 3 hours at 180 °C in the same alumina crucible to drive off NH_3 and H_2O. The resultant material was ball-milled for 2 hours in acetone to improve homogeneity of the mixture using 10 mm ZrO_2 balls in a planetary ball-mill. This was then fired for 24 hours at

950 °C and then 24 hours at 975 °C in a platinum crucible with intermittent ball milling performed in the same manner as previously mentioned.

$Si_5O(PO_4)_6$ was synthesised in powdered form and the assessment of its structure was performed using NPD. The NPD data were collected for $Si_5O(PO_4)_6$ at HRPT beamline, PSI, Switzerland at the temperatures 300 K, 573 K, 873 K and 1073 K for three hours per scan with a step size of 0.05 ˚. In addition to this, a 2 hour scan was performed at 723 K with a step size of 0.05 ˚, predominantly for the determination of U_{iso} values and unit cell parameters. The neutron beam was monochromated to a constant wavelength of 1.494 Å. Diffracted neutrons were detected by 3He PSDs over a 2θ range of 0-163 ˚. Rietveld refinement[8] was performed, in which, the following parameters were refined; atomic coordinates, unit cell and peak profile parameters, unless otherwise specified. This was performed using the GSAS[9] software with EXPgui[10]. An 8 mm steel can was used in the collection of this data and was subsequently included in the structural refinement of each pattern. The steel can belongs to the cubic unit cell with the space group *Fm3m*.

5.2.1 Fourier difference calculations

Fourier difference calculations were performed on the material to determine positive scattering excess densities that were not accounted for by the structural model. This information may provide details on missing atoms with increasing temperature. These calculations were performed on NPD data for the material $Si_5O(PO_4)_6$ at the temperatures 300 K, 573 K, 823 K and 1073 K. Fourier difference calculations were performed by selecting the "DELF" function for difference Fourier maps in GSAS. The Fourier difference calculations were performed with a map step value of 0.1 Å along the *a*-,*b*- and *c*-axis with a value of 0 and 1 for the min and max for all cell edges. These values were default parameters suggested by the GSAS manual. Fourier peaks were searched by using the "Forsh" option in GSAS.[9] The min peak value was set to zero so that only positive neutron densities were considered due to the scattering nature of neutrons with oxygen. The located peaks for each temperature were then placed into their respective refinement model to determine whether there was an improvement in structural fit. This was performed by assuming the positive scattering densities were potential interstitial oxygen sites. Therefore, the Uiso value for the positive scattering density was set to an average value of all of the other crystallographically defined oxygen within the structure. To evaluate the potential sites R-factors were referred to observe if there were improvements of the structural fit. In addition to this, site occupancy of the sites were evaluated to determine whether the extracted information was correct. For example, if site occupancy was a negative value the site would be discarded as the information suggests that no significant scattering is occurring. It should also be noted that atomic coordinates were not refined for the positive neutron densities as this was pre-determined by the diffraction data.

5.3 Results and discussion

5.3.1 Rietveld refinement

NPD studies of $Si_5O(PO_4)_6$ were undertaken to gain a further insight into its changing structural parameters with temperature. Initial steps were to obtain a good fit of the 8mm steel can, which was used as a container for the sample. Unfortunately, preferential orientation of the 8 mm steel can did not allow for its successful refinement. The ill fit of the steel pattern arose in the form of the incorrect modelling of peak intensity. Alternatively, the Le bail fit was used to model the steel as *Fm3m*. The use of the Le Bail fit led to a more appropriate fit of the steel peaks, however, there were still minor issues in modelling intensity for the steel peaks at 42 ˚ and 136 ˚ 2θ. The structural fit of the steel improved with increasing temperature. A comparison of the structural fit at 300 K and 1073 K is shown in Figure 5-1. There were small broad peaks associated to SiP_2O_7. These peaks were small and broad therefore, did not influence R-factor greatly.

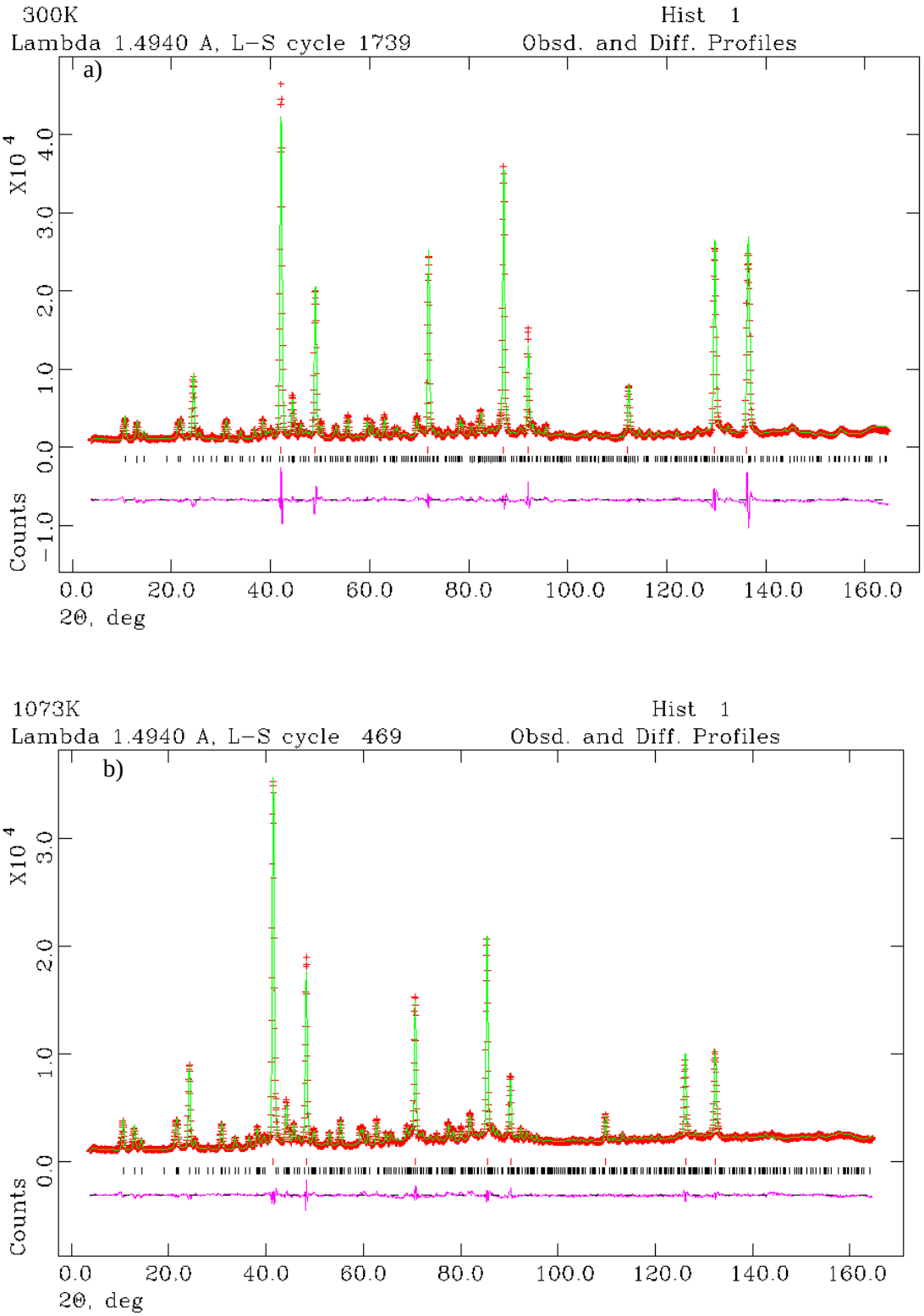

Figure 5-1. Comparison of the difference plots from NPD of $Si_5O(PO_4)_6$ and steel where a) is the 300 K plot and b) is the 1073 K plot. Red tick marks represent steel (Model: *Fm3m*) and black tick marks represent the main phase (Model: *R-3*).

The structural fits were performed by refining peak profiles using the Pseudo-Voight function (profile 2 when using GSAS with EXPGUI), atomic coordinates, atomic displacement factors (Uiso) and unit cell parameters. Site occupancy was constrained to one for all atoms. The phase fraction of steel was also constrained to one as a reference point for the main phase. The refinement showed that the R-factors indicated a satisfactory fit for the main phase with the model *R-3* at all temperatures (Table 5-1)[§§§]

		Fitted		-Background	
Temperature (K)	χ^2	wR_p (%)	R_p (%)	wR_p (%)	R_p (%)
300	14.74	7.58	5.585	7.75	5.84
573	10.32	6.46	5.17	5.87	4.98
723	5.189	5.61	4.43	5.20	4.33
873	6.857	5.28	4.18	4.95	4.12
1073	5.188	4.60	3.57	4.23	3.55

Table 5-1. The R-factors for the structural refinement of $Si_5O(PO_4)_6$ at temperatures range from 300-1073K to show the quality of fit.

In addition to the R-factors the NPD data shows that the atomic coordinates[****] were consistent with single crystal data of $Si_5O(PO_4)_6$ observed in literature[1] at 300K (Table 5-2).

[§§§] Difference plots for $Si_5O(PO_4)_6$ between the temperatures 300-1073 K can be seen in Appendix 1C
[****] Refined structural parameters for $Si_5O(PO_4)_6$ can be seen in Appendix 1D between the temperatures 300-1073 K

Atom	Wyckoff position	X	Y	Z
Single crystal XRD				
Si(1)	3a	0	0	0
Si(2)	6c	0	0	0.1767(1)
Si(3)	6c	0	0	0.4340(1)
P	18f	0.2863(3)	0.2675(6)	0.0924(1)
O(1)	3b	0	0	0.5
O(2)	18f	0.1309(7)	0.2136(8)	0.1372(2)
O(3)	18f	0.2095(8)	0.1459(7)	0.0403(2)
O(4)	18f	0.3549(8)	0.4832(8)	0.0769(2)
O(5)	18f	0.4602(8)	0.2462(8)	0.1116(2)
NPD				
Si(1)	3a	0	0	0
Si(2)	6c	0	0	0.1846(6)
Si(3)	6c	0	0	0.4378(6)
P	18f	0.2844(11)	0.2695(10)	0.0913(4)
O(1)	3b	0	0	0.5
O(2)	18f	0.1342(12)	0.2150(12)	0.13639(30)
O(3)	18f	0.2137(11)	0.1430(12)	0.03903(35)
O(4)	18f	0.3522(12)	0.4841(10)	0.07688(38)
O(5)	18f	0.4617(11)	0.2594(12)	0.11096(31)

Table 5-2. A comparison of atomic coordinates of collected NPD data (300 K) and previously reported single crystal XRD of $Si_5O(PO_4)_6$[1]. The observed NPD data showed that the refined atomic coordinates were consistent with previously reported single crystal data.

The NPD data shows that there are three distinctive crystallographic cationic atoms aligned along the c-axis which is shown in Figure 5-2.

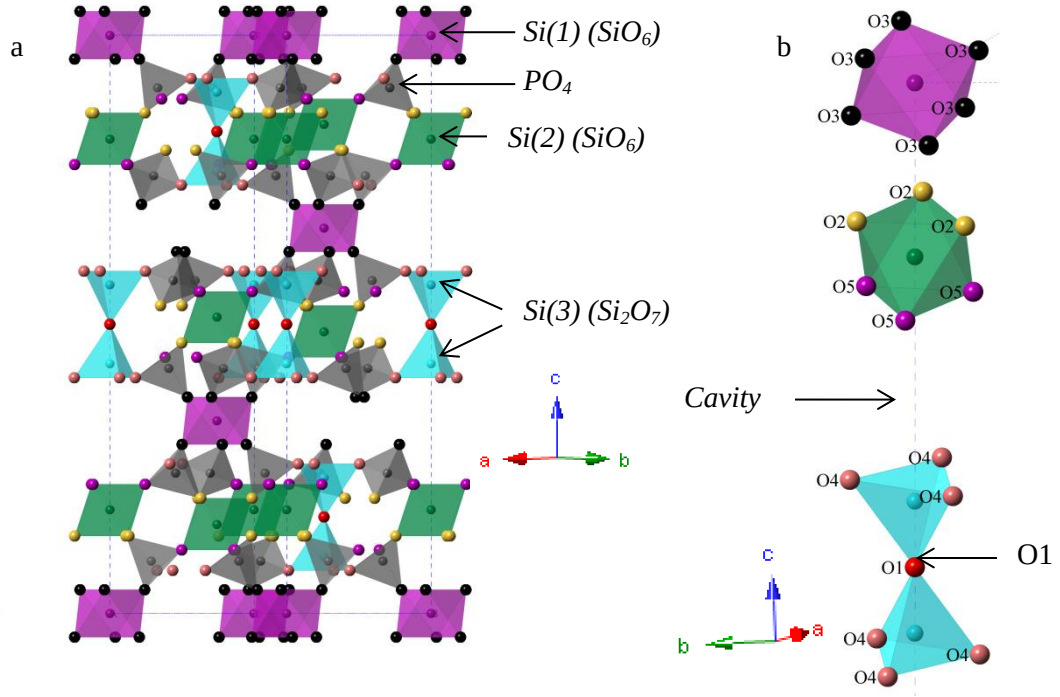

Figure 5-2. Illustration of $Si_5O(PO)_6$ structure where a) highlights the different cationic environments within the structure and how the 3D host lattice is formed with the tetrahedral phosphate structures. b) shows a closer view along the *c*-axis where the three silicon environments are aligned which take either octahedral or tetrahedral coordination. Also, the large cavities are shown in between the Si(2)-O_6 and Si(3)-O_4 local structures

Si(1) and Si(2) adopt the octahedral geometries where Si(1) is coordinated with symmetry related O3 while Si(2) is coordinated with two oxygen environments, O2 and O5. Si(3) is tetrahedrally coordinated by three symmetry related O4 and O1. The location of O1 lies in between two Si(3)-O_4 and is cornered shared between these two structures. As a result, they form a Si_2O_7 subunit. All oxygen are part of the phosphate backbone with the exception of O1. These three cationic environments are interconnected via corner sharing oxygen with a rigid phosphate backbone. Additionally, a structural feature that should be noted is the large cavities that reside in between the Si(2)-O_6 and Si(3)-O_6 units.

5.3.2 Evaluating oxide ion conduction within $Si_5O(PO_4)_6$

5.3.2.1 Negative thermal expansion within the silicate

The NTE behaviour within $Ge_5O(PO_4)_6$ was suggested to aid oxide ion conduction within the material which is described in section 4.3.1. The unit cell parameters of the silicate and germanate was compared to evaluate their similarities and differences with temperature (Figure 5-3).

.

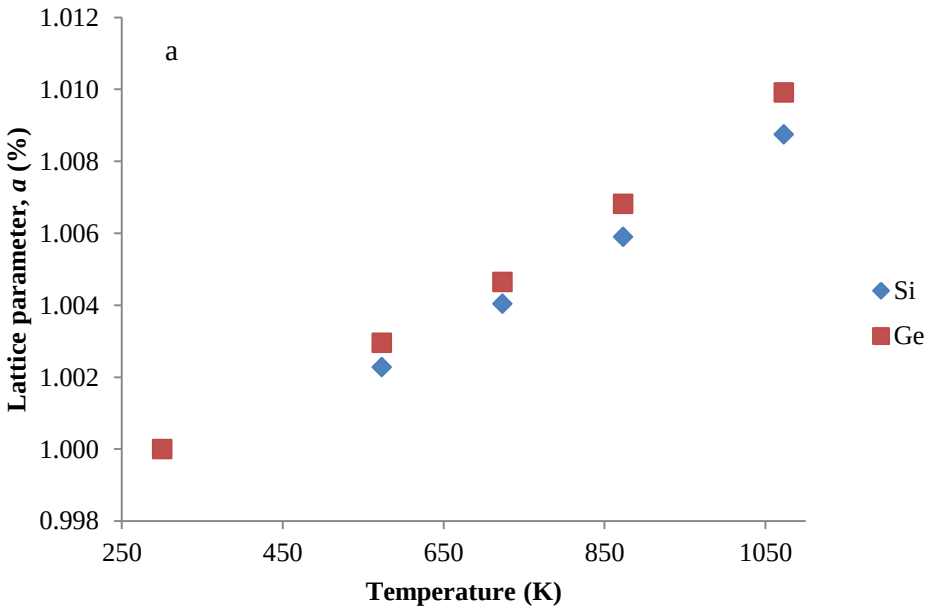
a
1.012
1.010
1.008
1.006
1.004
1.002
1.000
0.998
Lattice parameter, a (%)
250
450
650
850
1050
Temperature (K)
Si
Ge

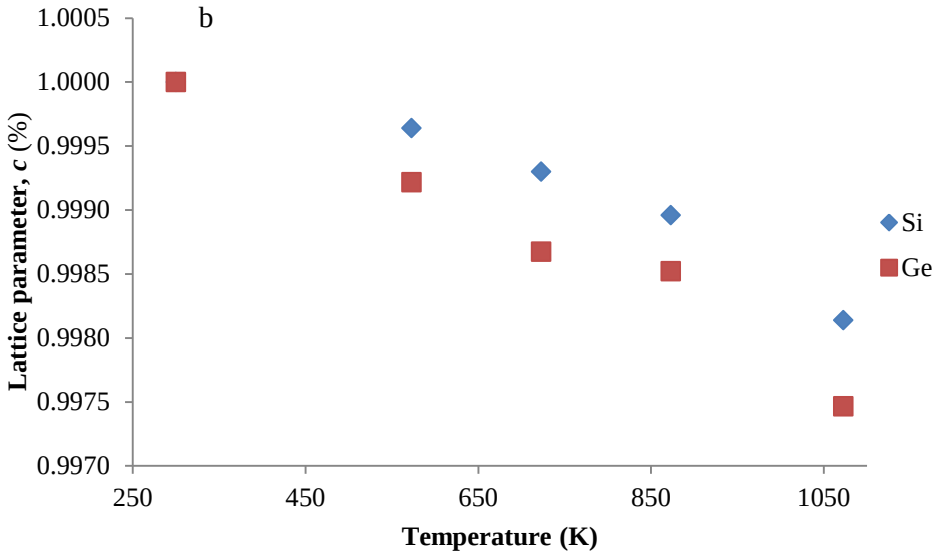
b
1.0005
1.0000
0.9995
0.9990
0.9985
0.9980
0.9975
0.9970
Lattice parameter, c (%)
250
450
650
850
1050
Temperature (K)
Si
Ge

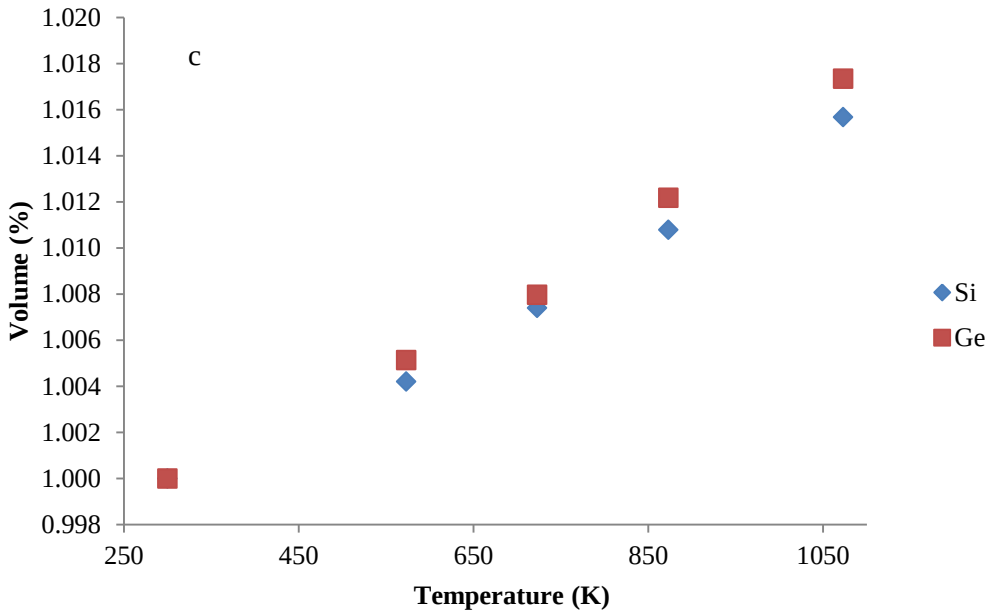

Figure 5-3. Comparison of unit cell parameters (*a*, *c* and *v*) of $Si_5O(PO_4)_6$ (label : Si) and $Ge_5O(PO_4)_6$ (label : Ge) between the temperatures 300-1073 K. a) shows the percentage change in the *a* unit cell parameter, b) shows the percentage change in the *c* unit cell parameter c) shows the percentage change in unit cell volume.

The unit cell parameter ***a*** for $Si_5O(PO_4)_6$ showed that the material expands linearly in the *a*-*b* plane with temperature as expected. The germanate and silicate expand similarly, but the germanate shows a larger increase overall with temperature. The silicate also shows NTE behaviour which arises as a non-linear decrease along the *c*-axis between the specified temperature range. However, the percent change is smaller than that seen within the germanate.

The trend of the germanate showing larger changes in unit cell parameters with temperature is continued when considering the overall unit cell volume (Figure 5-3c). Larger changes in unit cell size have been proposed to be beneficial to the transport of oxide ions for the germanate (in section 4.2.1). Particularly, the NTE behaviour that occurs along the *c*-axis may allow for mobile oxide ions to more readily 'hop' to neighbouring crystallographic sites. The smaller NTE seen within the silicate may inhibit the transport of oxide ions and increase activation energy when considering the proposed oxide ion conduction pathway.

5.3.3 The origin of mobile oxide ions within the silicate

Analysis of the atomic displacement factors within $Ge_5O(PO_4)_6$ suggested that the most mobile oxygen within the structure was the oxygen crystallographically defined as O(1) (Section 4.3.2). This was attributed to the position of the oxygen which is hosted in between the di-tetrahedron subunit which is, more importantly, not part of the rigid phosphate lattice. The U_{iso} of the oxygen

within the silicate analogue was determined to derive the most mobile oxygen within the structure. This is shown in Figure 5-4.

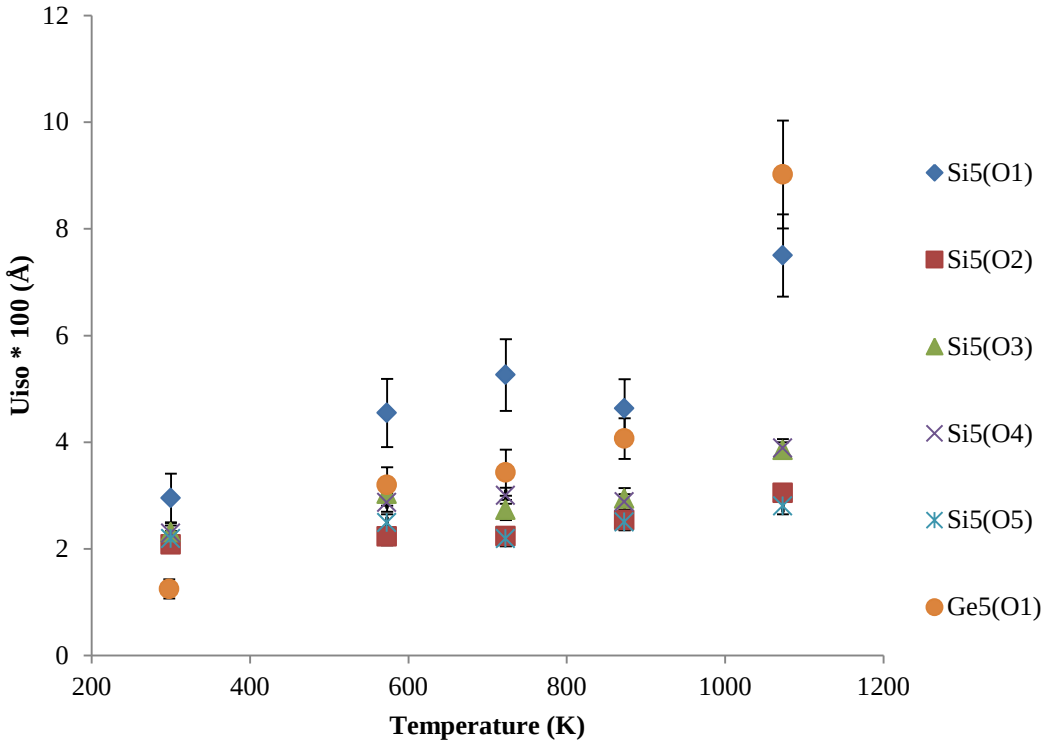

Figure 5-4. U_{iso} values of oxygen within $Si_5O(PO_4)_6$ with a comparison of the O1 within $Ge_5O(PO_4)_6$ (Ge5(O1)) between the temperature range of 300-1073 K. Si5(O) represents the oxygen within the $Si_5O(PO_4)_6$ structure.

The data suggested that there are three key points that can be derived from the oxygen U_{iso} values within $Si_5O(PO_4)_6$. Firstly, O1 represents the most mobile oxygen within the structure at all specified temperatures. Secondly, this increases linearly until ≈ 873 K where there is a significant decrease in the U_{iso} of O1. Finally, at 1073 K there is a larger increase in U_{iso} which may be evidence of mobile O1 ions. This suggested that the structure has an intrinsic ability to form mobile oxide ions, due to the nature of the bonding of O1 within the structure.

On a closer comparison with the O1 oxygen within the germanate (Ge(O1)) shown in the graph above, the data showed that the magnitude U_{iso} of Ge(O1) is larger than that seen with Si(O1). This suggested that, despite the structures inherit ability to form mobile oxide ions around the 3b site, the silicon cation has an effect on its overall mobility. This is attributed to the oxygen on the O1 site being held more tightly within the silicate which may be explained by the difference in the ionic radius between Si^{4+} and Ge^{4+}, as previously mentioned. Hence, its smaller ionic radii forms smaller and stronger bonds with oxygen[3]. To expand on this further it can be suggested that a key factor in the poor oxide ion conductivity within the silicate may be due to the relative inflexibility

of the cationic lattice to mobilise and stabilise mobile oxide ions. Evidence to support this is shown in Figure 5-5. This illustration shows the U_{iso} values for silicon with increasing temperature.

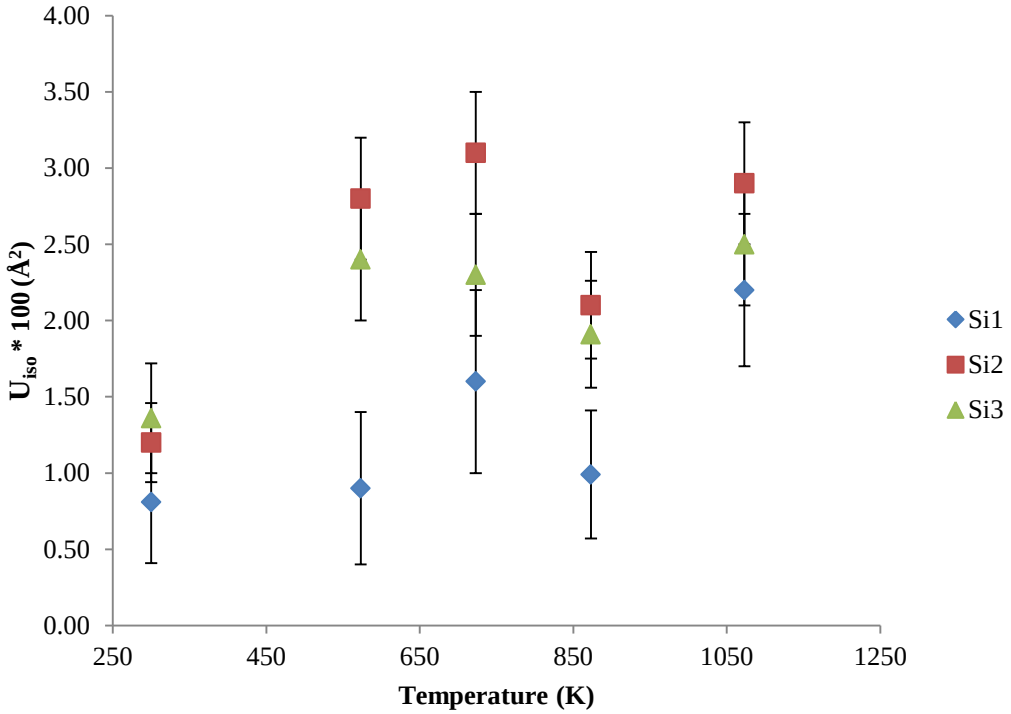

Figure 5-5. U_{iso} of the silicon atoms(1-3) between the temperature range of 300-1073 K.

The Si3 atom does not have the highest U_{iso} value which is seen for Ge(3) in $Ge_5O(PO_4)_6$ (shown in section 4.3.2). This process is vital to the formation of inverted ditetrahedra when the interstitial oxide ion is stabilised within the cavity. This may be indicative of the inability of the silicon cationic lattice to accommodate mobile oxide ions within the structure.

5.3.3.1 Fourier peak calculations – locating possible interstitial oxide ion sites

Fourier difference calculations were also performed on the silicate to find the position of any mobile oxide ions. Figure 5-6 shows the excess densities surrounding the Si_2O_7 subunit. The densities were chosen based on the similarity of position when compared to the germanate.

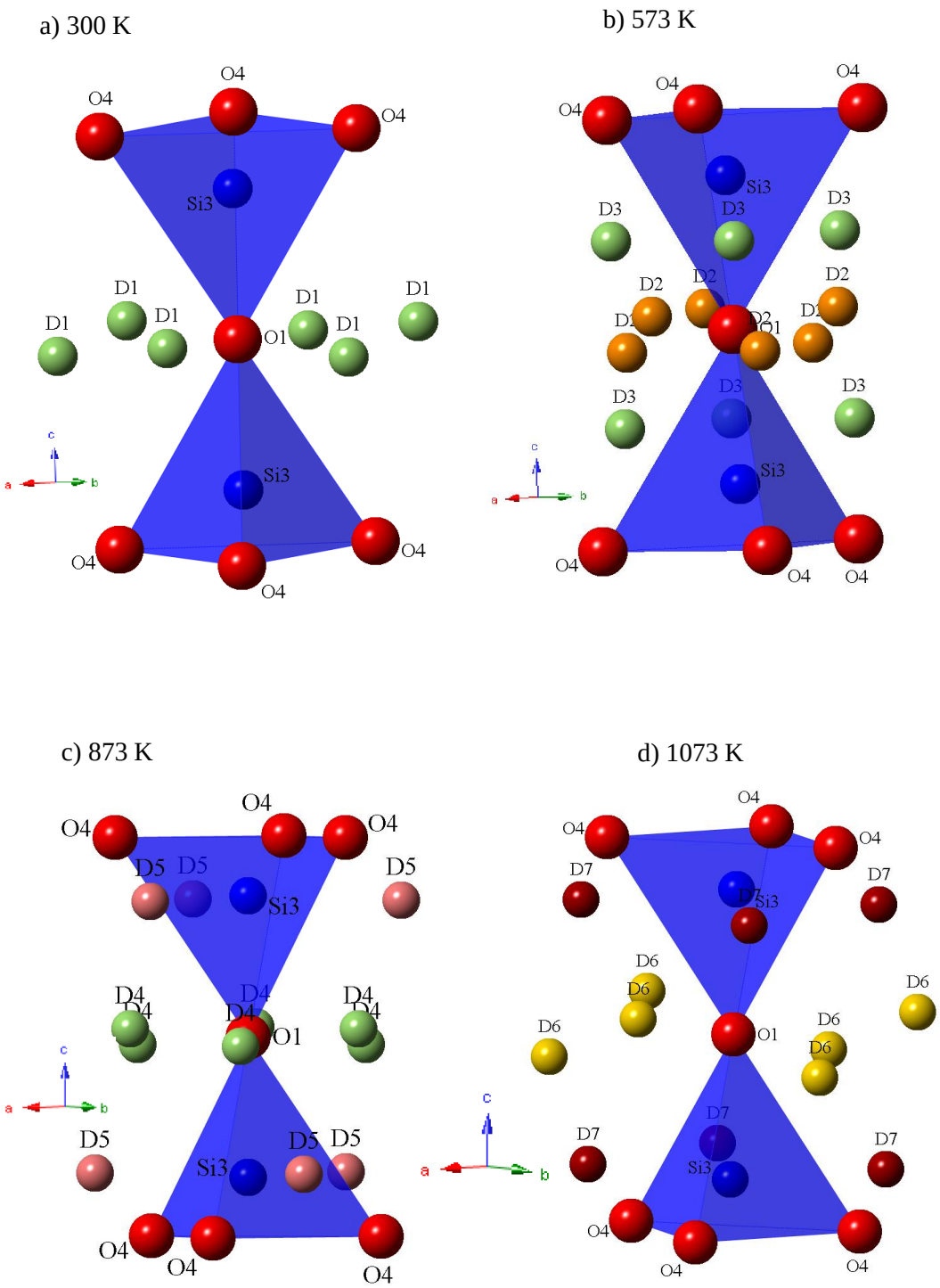

Figure 5-6. schematic view of the location of densities around the 3b site between the temperature range of 300-1073 K. a) shows the densities (D1) at 300 K, b) shows the densities (D2 and D3) at 573 K c) shows the densities (D4 and D5) at 873 K d) shows the densities (D6 and D7) at 1073 K. Oxygen are red spheres and blue spheres are Si(3)

The refinement of these densities can be seen in Table 5-3.

			300 K			
	χ2	**wRp (%)**	**X**	**Y**	**Z**	**Fractional occupancy**
Original refinement (300 K) R-factors	14.19	7.58				
D1	14.22	7.58	0.0709	0.480500	0.16300	0.012(1)
			573 K			
Original refinement (573 K) R-factors	10.32	6.646				
D2	10.33	6.646	0.359700	0.541250	0.158660	-0.002(9)
D3	10.27	6.644	0.161810	0.501910	0.128530	0.041(10)
			873 K			
Original refinement (873 K) R-factors	6.857	5.28				
D4	6.856	5.28	0.389430	0.519200	0.1628100	0.03(8)
D5	6.775	5.525	0.09013	0.509130	0.050460	0.071(11)
			1073 K			
Original refinement 1073 K R-factors	5.180	4.60				
D6	5.174	4.59	0.052090	0.452600	0.1543700	0.045(13)
D7	5.170	4.59	0.165540	0.392420	0.1543700	-0.031(12)

Table 5-3. Comparison of the structural refinement results around the Si_2O_7 at the temperatures, 300 K, 573 K , 823 K and 1073 K.

The structural refinement at 300 K yielded small occupancy of the site (0.0122). However, this did not improve the structural fit (wRp = 7.58%) and increased in χ^2. This is similar to the germanate as the refinement of the density around the 3b site led to an unstable refinement. This is due to the low occupancy of these sites at lower temperatures.

Refinement of the densities at 573 K also did not significantly improve the structural fit. The density labelled D2 showed a small increase in R-factors values indicating a worse fit. Furthermore, refinement of the D3 density only represented a small improvement of the structural fit (from χ^2 = 10.32, wRp = 6.646 % to χ^2 =10.27 , wRp = 6.644 %), and therefore the original model was favoured to reduce the number of variables. Thus, suggesting that between the

temperatures ranges 300-573 K the mobile oxide ions do not have sufficient energy to occupy these sites significantly.

At 873 K, D4 which is located closest to the 3b site also appears to not improve the structural fit. On the other hand, the refinement of D5 led to a reasonable improvement of the structural fit. D5 is located in the periphery of the Si(3) atom which suggested, that a similar mechanism may be occurring to that seen within the germanate where the oxide ion moves towards the O4 atoms.

At the highest temperature 1073 K, the refinement of D6 slightly improved the structural fit with the site occupancy of 0.0456 while D7 did not improve the R-factors and yielded unrealistic site occupancy of -0.0313. These results represent possible evidence that a similar process occurs where the oxide ion O1 moves along the *a*-*b* plane of the 3b site.

5.3.3.2 Positive nuclear densities within the cavities

Analysis of the cavities was also performed to determine whether there was the formation of 2 inverted tetrahedra from the Si_2O_7 subunit. An illustration of specific positive scattering densities of interest can be seen in Figure 5-7.

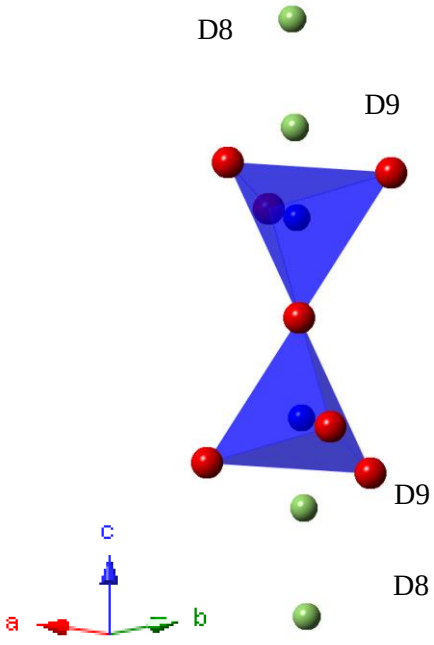

Figure 5-7. Positive scattering density within the cavities, D8 and D9 represented by green spheres.

Table 5-4 shows a comparison of the addition of the positive excess densities to the structural model with the original refinement.

1073 K						
	χ^2	wRp (%)	X	Y	Z	Fractional occupancy
Original refinement 1073 K R-factors	5.188	4.60				
D8	4.980	4.50	0.6673	0.333266	0.03064	0.079(7)
D9			0.332690	0.66890	0.040920	0.018(6)

Table 5-4. A comparison of the structural refinement of the excess densities D8 and D9. The results showed that there is a significant improvement of the R-factors when D8 and D9 were included in the structural model.

Densities D8 and D9 are located in the cavities, and resemble the locations seen within the germanate system. On the structural refinement of D8 and D9 the fit improves significantly (from wRp = 4.60 % to 4.50%). This in turn suggested that these sites may be possible mobile oxide ion sites that form two inverted tetrahedra. The D8 density forms a D8-O4 distance of ~2.977 Å which is larger than a typical O-O distance. In addition to this, the bond angle deviants slightly from the ideal 60° O-O-O bond which has an angle of 64°. The D8-D9 bond distance of 1.723 Å falls within the typical Si-O bond, and therefore suggests D9 is a possible location for a mobile silicon atom that stabilises mobile oxide ions. D9-O4 also shows a typical Si-O bond distances of 1.712 Å. Subsequently, this suggested Si(3) may be able to move to accommodate mobile oxide ions at the highest recorded temperature. Though, the final tetrahedra that are formed are rather strained and distorted according to this analysis**.**

5.3.3.3 Possible interstitial sites around the Si-O_6 octahedra

Analysis of the density around the silicon octahedra is illustrated in Figure 5-8.

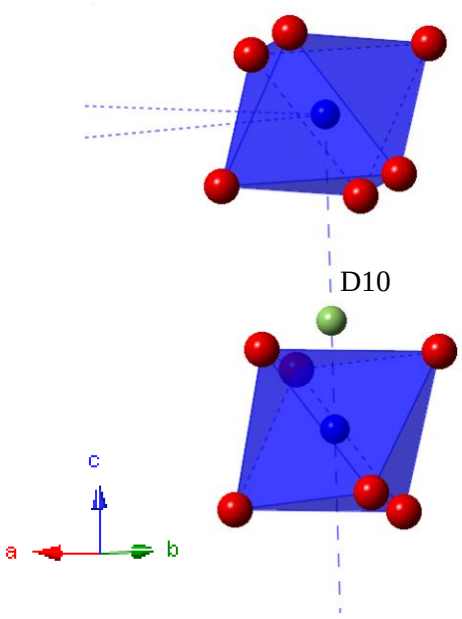

Figure 5-8. Location of D10 density around the Si(2)-O_6 units. (blue spheres are Si(2), red spheres are oxygen and green sphere is the D10 positive scattering density)

The Rietveld refinement of the D10 density at the highest temperature can be seen in Figure 5-8.

1073 K						
	χ^2	wRp (%)	X	Y	Z	Fractional occupancy
Original refinement 1073 K R-factors	5.188	4.60				
D10	4.023	4.05	-0.00005	-0.0038	0.11805	-0.059(19)

Table 5-5. Rietveld refinement results of D10 density suggested that there is a minor improvement in the R-factors but led to an unrealistic value for site occupancy.

The location of D10 resides next to the Ge(2) octahedra and may represent a interstitial site for mobile oxide ions. The structural fit improves with the addition of the D10 density, however, the site occupancy of this crystallographic position appeared to be unrealistic with the value of -0.059. This indicated that D10 as an interstitial site for oxygen may not be frequently occupied which corroborates with conductivity measurements. Therefore, the octahedra structures within the silicate may represent an additional large energy barrier for oxygen transport.

The results suggested that the cationic lattice within the silicate does offer some flexibility within its structure to mobilise and stabilise mobile oxide ions. Particularly, the Si_2O_7 which shows an indication of the mobilisation of O1 oxide ions and the stabilisation of them within the cavities.

5.3.4 Local structural differences between the $Ge_5O(PO_4)_6$ and $Si_5O(PO_4)_6$

As previously mentioned, silicon within the $Si_5O(PO_4)_6$ structure adopts the 6-fold coordination state which is unusual[2]. In this section, the local cationic structures will be compared between the silicate and germanate. This is to evaluate whether there are any differences that occur as a consequence of silicon adopting the octahedral geometry. This was performed by reviewing the bond distances and angles within each cationic environment.

5.3.4.1 M(1)-O6 (M=Si or Ge)

Bond length and angle analysis for the M(1)-O_6 at 300 K can be seen in Table 5-6. The data showed that although M(1) is octahedrally coordinated there are differences between the structure for the silicate and germanate. This is visually represented in Figure 5-9.

300 K

	Bond length (Å)			Bond angle (°)	
Si octahedra					
Si1-O3	1.770(7)	6x	O3-Si1-O3	180.0(0)	3 x
				93.6(4)	6 x
				86.4(4)	6 x
Ge octahedra					
Ge1-O3	1.8547(34)	6x	O3-Ge1-O3	180.0(0)	3 x
				92.68(16)	6 x
				87.32(16)	6 x

Table 5-6. Comparison of the bond length (Å) and bond angles (°) for M(1)-O_6 octahedra (M = Ge or Si on the 3a Wyckoff position at 300 K.

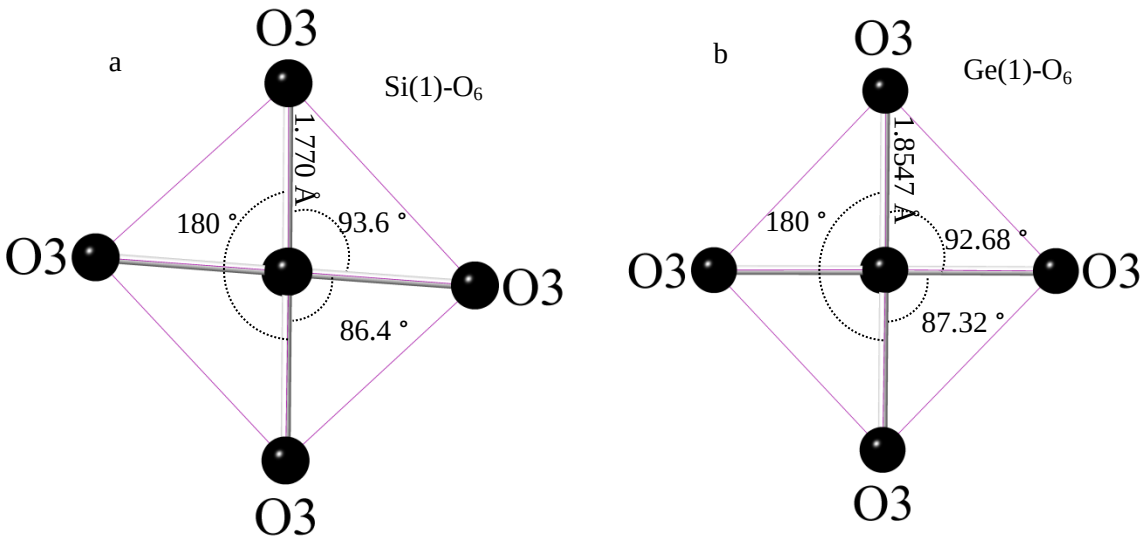

Figure 5-9. Illustration of the M(1)-O_6 (M = Si or Ge) where a) represents Si(1)-O_6 and b) represents Ge(1)-O_6. The difference in bond angles and bond lengths of the differences within the octahedron can be seen for the germanate and silicate octahedron.

The results have shown that there are 6 equal Si(1)-O3 bonds which have the length of 1.770 Å. This suggested that Si(1) is well centred within its polyhedra. However, it appears to have a slightly distorted octahedral geometry which arose in the form of non-ideal cis bond angles of 93.6 ˚or 86.4 ˚. Similarly, for the germanate there are also 6 equal bond lengths of 1.8547 Å with cis bond angles of 92.68° or 87.32°. It should be noted that these values only represent a small deviation from the ideal cis angle of 90°. Nevertheless, Ge(1)-O_6 may represent a less distorted polyhedron when compared to Si(1)-O_6. In both cases, the trans angle is 180° which is expected the octahedral geometry. These bond angles are also observed in published work on single crystal $Ge_5O(PO_4)_6$[11] and $SiO(PO_4)_6$ in single crystal and powdered forms[1,12].

On heating the Ge(1)-O3 bond generally increased with temperature as expected. This is in contrast to the Si(1)-O3, which showed a minimal increase with temperature. This is consistent with the smaller unit cell expansion of the silicate when compared to the germanate (Figure 5-10).

a)

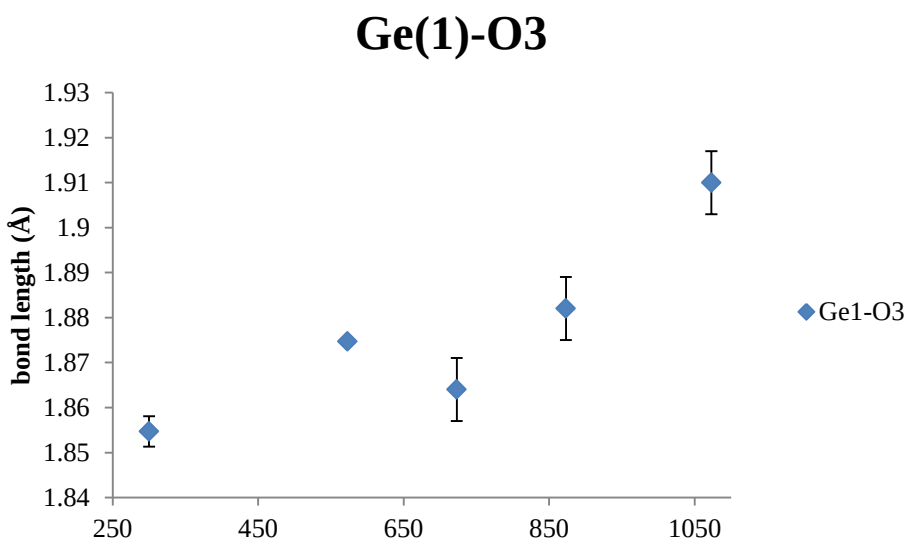

b)

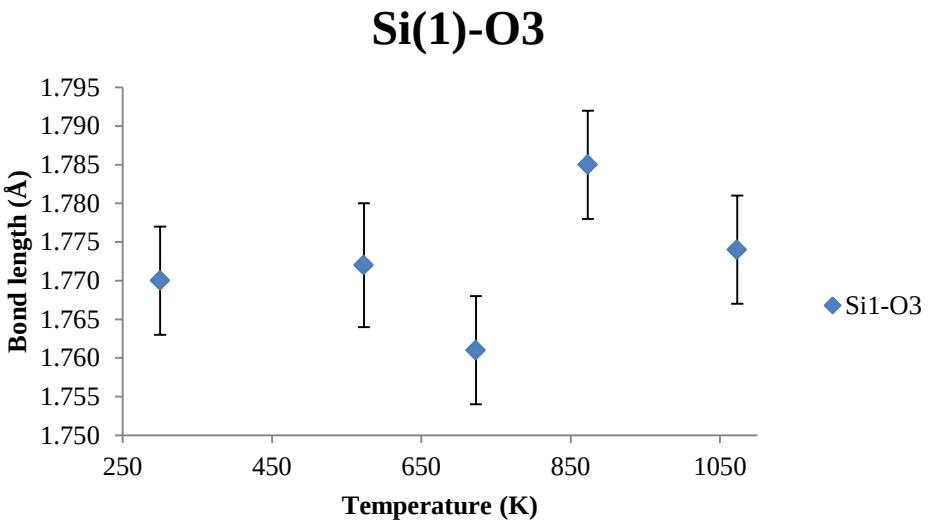

Figure 5-10. Changes of bond length (Å) with temperatures between 300-1073 K within the octahedrally coordinated M(1) (M = Ge or Si) local structure. a) shows Ge(1)-O3 and b) Si(1)-O3.[††††]

5.3.4.2 M(2)-O6 (M=Si or Ge)

In Table 5-7 a comparison of the bond lengths and angles for M(2)-O_6 can be seen for the silicate and germanate. An illustration of M(2)-O_6 octahedra can also be seen in Figure 5-11.

[††††]Bond variation with temperature for M(1)-O_6 (M = Ge(1) or Si(1) may be seen in Appendix 1E

300 K

Si Octahedra	Bond length (Å)			Bond angles (Å)	
Si2-O2	1.847(14)	3 x	O2-Si2-O2	86.1(8)	3 x
Si2-O5	1.708(14)	3 x	O2-Si2-O5	91.7(4)	3 x
Av	1.7775		O2-Si2-O5	89.72(32)	3 x
			O2-Si2-O5	175.4(11)	3 x
			O5-Si2-O5	92.3(9)	3 x
Ge Octahedra					
Ge2-O2	1.895(5)	3 x	O2-Ge2-O2	89.46(22)	3 x
Ge2-O5	1.827(4)	3 x	O2-Ge2-O5	90.90(15)	3 x
Av	1.861		O2-Ge2-O5	90.83(15)	3 x
			O2-Ge2-O5	180.000(2)	3 x
			O5-Ge2-O5	88.81(19)	3 x

Table 5-7. M(2)-O_6 (M = Ge or Si on 6c Wyckoff position) bond length and angles with octahedral geometry. The data shows a comparison of the octahedral bond length (Å) and angles (°) at 300 K for the silicate and germanate.

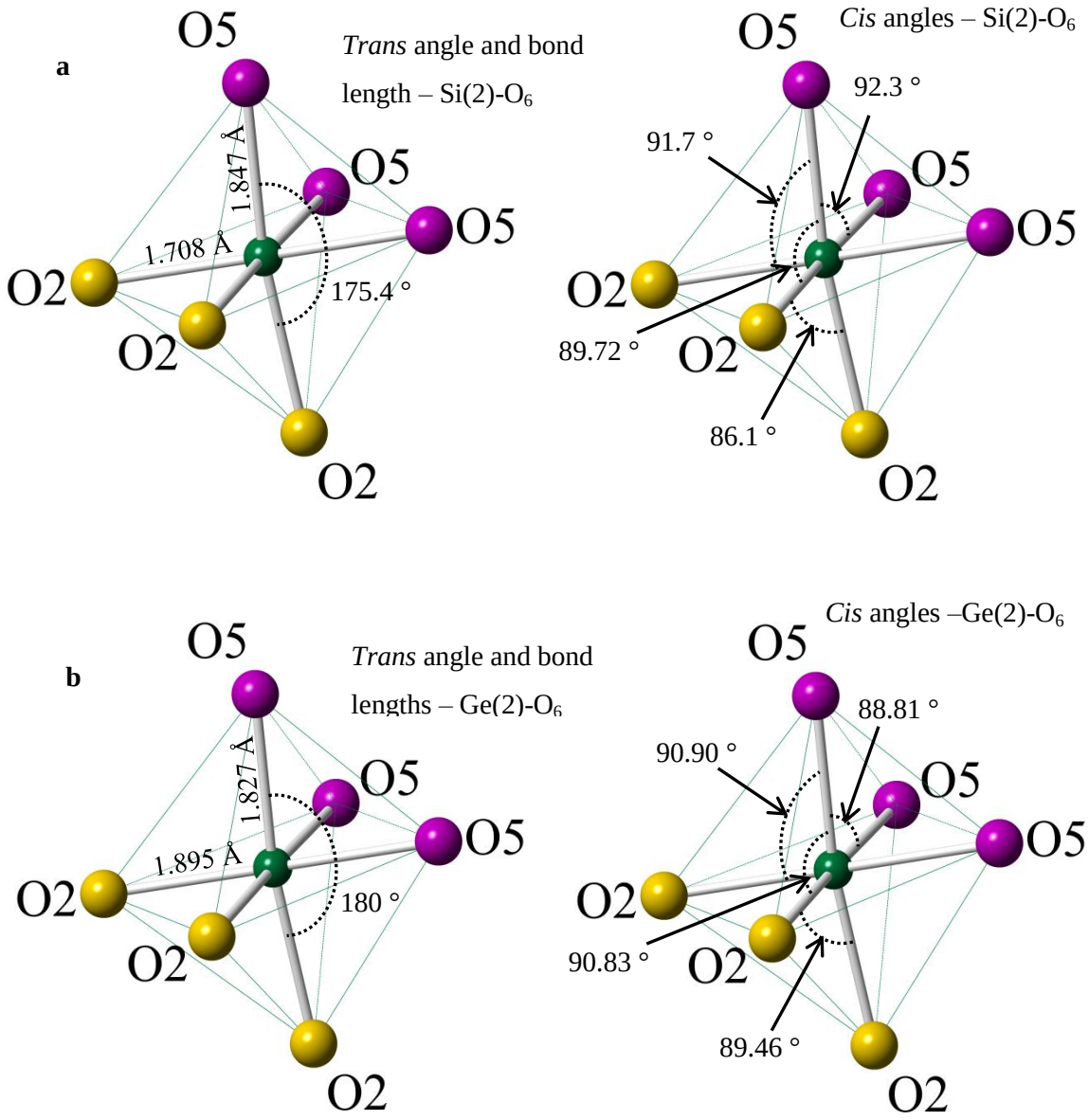

Figure 5-11. Comparative illustrations of the M(2)-O_6 (M = Si or Ge) a) represents octahedrally coordinated Si(1)-O_6 with bond lengths and cis- and trans bond angles. b) represents octahedrally coordinated Ge(1)-O_6 with cis-, trans- bond angles and lengths.

The data have shown that there are two Si(2)-O bond lengths within the octahedron. There are three equivalent bond lengths for Si(2)-O2 and Si(2)-O5 with the values 1.708 and 1.847 Å, respectively. The large difference between the two bond lengths suggested that the Si(2) cation is significantly off centre in its octahedron. The O-Si(2)-O bond angles (Axial-equatorial) deviated significantly from the ideal 90° which are as follows, 86.1 , 91.7, 92.3 and 89.72 °. In addition to this, the trans-bond angle is significantly smaller than 180° with the value of 175.4 °. This has also been observed within the powdered $Si_5O(PO_4)_6$ reported by Poojary *et al*[12]. This work detailed two $Si_5O(PO_4)_6$ samples with the difference being the firing temperature to form the final phase. Crystallographic data of both samples showed that there is a large difference between the two

Si(2)-O bond lengths. This suggested that this Si(2)-O_6 polyhedral unit is highly distorted which has the effect of decreasing the overall unit cell size. These results are in contrast to the reports by Mayer, H *et al*[7] for $Si_5O(PO_4)_6$ where the two bond distances within the octahedra differ minimally (1.791 and 1.744 Å) and bond angles appear to be more consistent with an ideal octahedral geometry. It should be noted, however, that the average bond distance reported is consistent with the collected NPD data.

In the germanate, Ge(2) appears to be off centre in its polyhedron with the distances 1.895 and 1.827 Å. Albeit, a less significant difference is seen between the two bond distances when compared to the silicate. Consequently, the bond angles are more consistent with an ideal octahedron, where the largest deviation from the ideal 90° is 88.81°. Additionally, the trans bond angle is also 180°, which is consistent with ideal octahedral character. The off-centered germanium within its octahedron has also been seen in a related structure $Ge_3Si_2O(PO_4)_6$ reported by Leclaire *et al*[10]. These results have shown that despite the materials being isostructural, there are key differences within the local structures. In the silicate, the Si(2) is displaced from its ideal position to form a largely distorted octahedron. This is attributed to the unusual silicon adoption of the octahedral geometry. Therefore, it may be more likely to form a distorted octahedral geometry. This is made apparent when compared to Ge(2)-O_6, which forms a more characteristic octahedron with ideal octahedral bond lengths and angles.

On heating of the M(2)-O_6 polyhedra it can be seen that the short and long bond lengths converge to a similar value for the germanate. Similarly, this pattern can also be seen for the silicate. This is due to the lower symmetry state of the octahedra seen in both materials moving to a higher symmetry state with temperature. This can be seen in Figure 5-12.

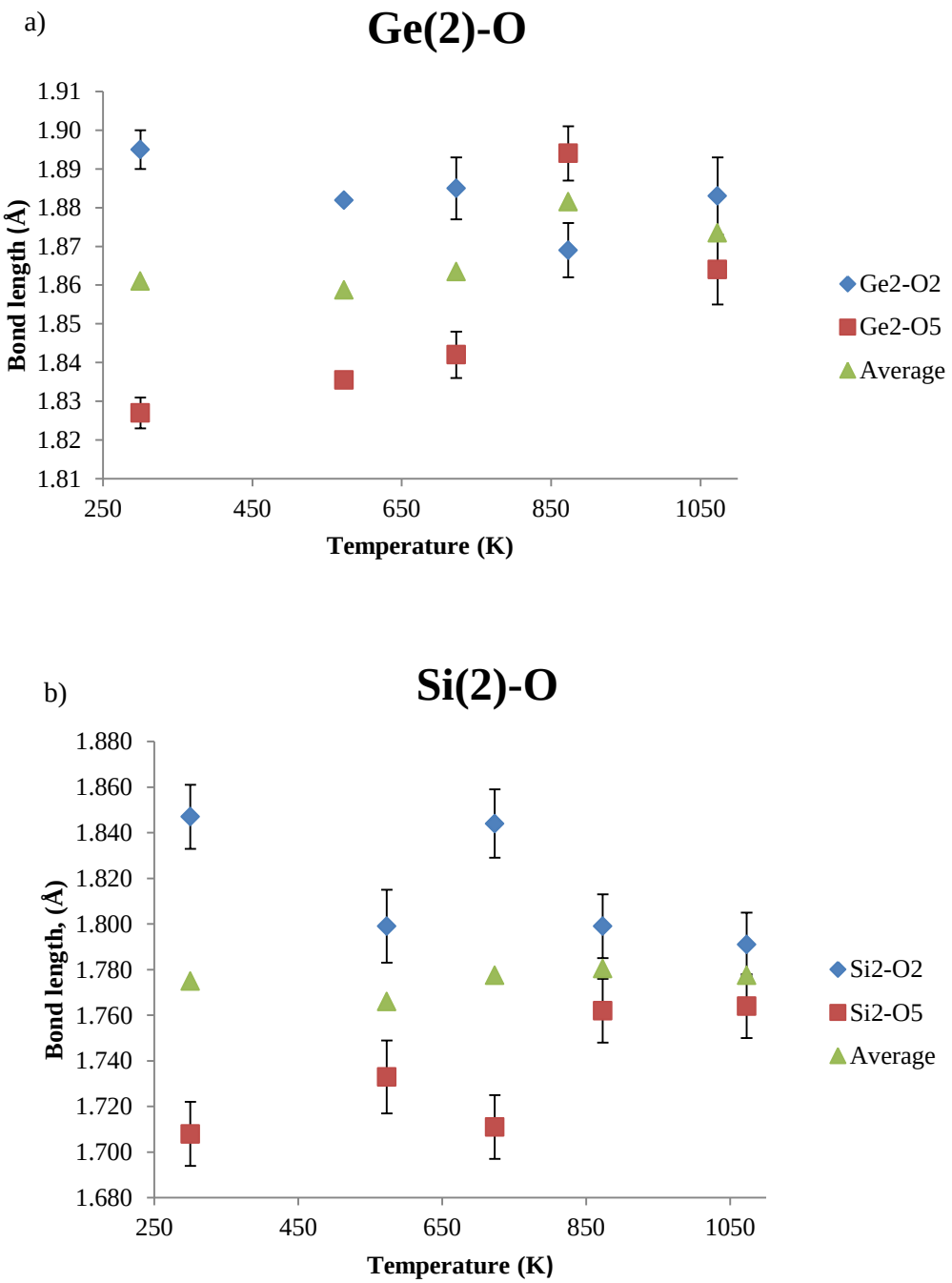

Figure 5-12. Changes of bond length (Å) with temperatures between 300-1073 K within the octahedrally coordinated M(1) (M = Ge or Si) local structure. a) shows Ge(2)-O3 and b) Si(2)-O.[‡‡‡‡]

5.3.4.3 M(3)-O4 (M=Si or Ge)

The crystallographic data of bond distances and angles for M(3)-O_4 can be seen in Table 5-8. This has also been visually represented in Figure 5-13.

[‡‡‡‡] Bond variation for M(2)-O with temperature may be seen in Appendix 1F

300 K

Si tetrahedra	Bond distance (Å)			Bond Angle (Å)	
Si3-O1	1.527(15)	1 x	O4-Si3-O1	113.0(6)	3 x
Si3-O4	1.623(9)	3 x	O4-Si3-O4	105.7(7)	3 x
Av	1.575			109.35	
Ge tetrahedra					
Ge3-O1	1.686(4)	1 x	O4-Ge3-O1	111.63(17)	3 x
Ge3-O4	1.7348(33)	3 x	O4-Ge3-O4	107.23(18)	3 x
Av	1.7104			109.43	

Table 5-8. Comparison of M(3)-O_4 (M = Si or Ge on 3a Wyckoff position) bond length and angles with tetrahedral geometry at 300 K.

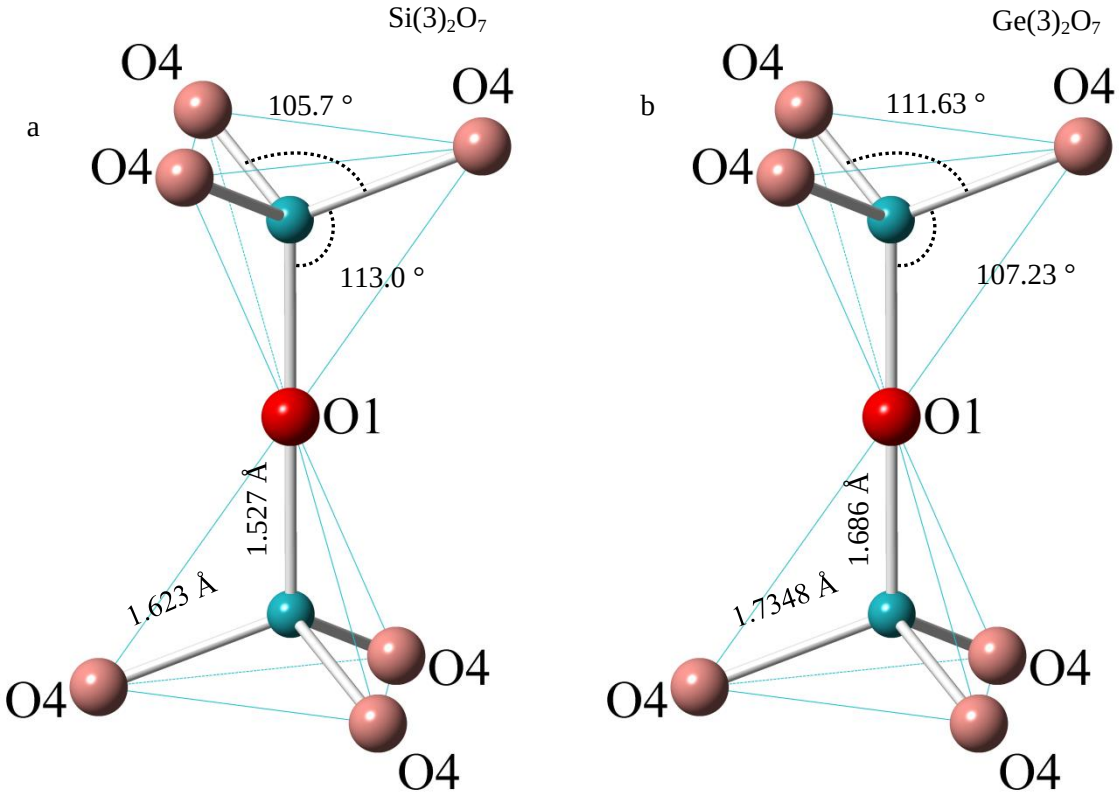

Figure 5-13. Illustration of $M(3)_2O_7$ including bond lengths and angles to describe the tetrahedral character for a) Si(3)-O_4 b) Ge(3)-O_4.

The bond distances reported are 1.527 and 1.623 Å for Si3-O1 and Si3-O4, respectively with an average of 1.575 Å. From literature data, the typical average range for Si(3)-O is between

1.604 - 1.754 Å[1,12,13]. Therefore, the NPD data lies closest to the lower end of this range. The observed NPD bond lengths appear to corroborate with the Ge(3)-O NPD data which have the larger bond lengths of 1.686 and 1.7348 Å for Ge3-O1 and Ge3-O4, respectively with the average of 1.7104 Å. These results showed that the silicate and germanate have slightly distorted M(3)-O4 tetrahedra driven by off-centred cations within the tetrahedral hole. Additionally, the average bond angle for both materials had the values 109.35 ° and 109.43 ° for the silicate and the germanate, respectively. This showed that these local structures present an ideal tetrahedral geometry which typically has a bond angle of 109.45 °. It should also be noted that the Si/Ge-O(1) bond (which is not part of the phosphate lattice) is typically shorter than other Si/Ge-O bond lengths within the structure. This is also been reported within the related structure, $Ge_3Si_2O(PO_4)_6$[14].

On heating of the M(2)-O_6 subunit the two distinct bond lengths at the highest temperature equilibrate to a bond length that is similar to one another suggesting higher crystallographic symmetry for these polyhedra shown in Figure 5-14.

a)

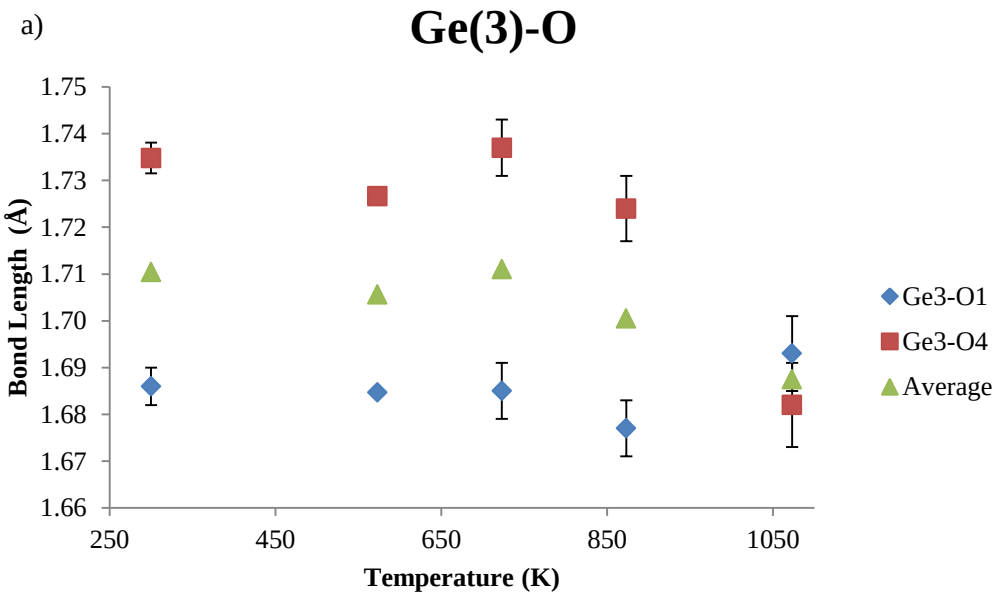

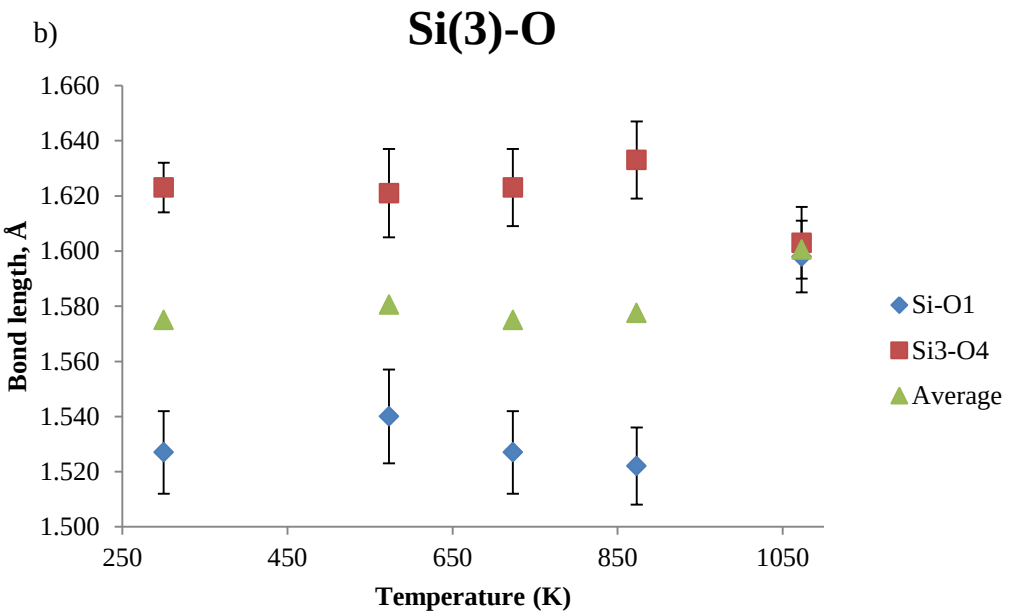

Figure 5-14. Bond lengths with the M_2O_7 subunit a) Ge(3)-O b) Si(3)-O.[§§§§]

5.3.4.4 Phosphate groups (PO_4)

The bond angle and distance analysis of the phosphate lattice for the silicate and germanate can be seen in Table 5-9. The results showed that the phosphate groups within the silicate have an average P-O bond length of 1.51825 Å with an average dihedral bond angle of 109.45°, which is consistent with a tetrahedral geometry. The average values within the germanate are also consistent with a tetrahedron with the average P-O bond length of 1.5305 Å and dihedral angle of 109.465 °. This shows that the phosphate lattice remains largely the same within both structures. This is unsurprising considering the phosphate lattice is isostructural and considered a rigid component in both materials. The NPD data showed similar characteristic P-O bond lengths observed from various sources[1,11.15-19]. In particular, the P-O4 bond that shares its oxygen with a tetrahedron unit is usually the largest bond distance when compared to the other P-O bonds. This has been seen in previously reported $Ge_5O(PO_4)_6$[11] and $Si_5O(PO_4)_6$[1] bond length analysis, also in related structure such as $AMo_3P_6Ge_2O_{25}$,[15–17] MoP_3SiO_{11}[18] and $V_3P_5SiO_{19}$[19].

The bond length analysis shows that the Ge-O bond is much larger than the Si-O bond within all three distinct positions. This can be explained by differences in ionic radii between the two cations. Si^{4+} has a ionic radius of 0.26 Å and 0.4 Å for 4 and 6 fold coordination, respectively. Whereas, Ge^{+4} has an ionic radius of 0.39 Å and 0.53 Å for the 4 and 6 fold coordination, respectively.[20] Consequently, Ge will forms larger M-O bond distances.

[§§§§] Bond variation for M(3)-O with temperature may be seen in Appendix 1G

300 K

	Bond length (Å)			Bond angle (°)
Phosphate group (silicate)				
P-O2	1.510(10)		O2-P1-O3	115.1(6)
P-O3	1.521(11)		O2-P1-O4	105.6(6)
P-O4	1.561(9)		O2-P1-O5	113.8(7)
P-O5	1.481(11)		O3-P1-O4	108.7(7)
			O3-P1-O5	105.5(6)
			O4-P1-O5	108.0(6)
Av	1.51825			109.45
Phosphate group (germanate)				
P-O2	1.536(5)		O2-P1-O3	114.16(26)
P-O3	1.515(5)		O2-P1-O4	105.95(27)
P-O4	1.561(4)		O2-P1-O5	112.35(32)
P-O5	1.510(5)		O3-P1-O4	107.79(31)
			O3-P1-O5	106.11(29)
			O4-P1-O5	110.43(26)
Av	1.5305			109.465

Table 5-9. Bond length (Å) and angle (°) analysis of phosphate groups.

5.4 Conclusion

NPD has shown that there are key structural differences between the germanate and silicate. It shows that Si does indeed enter a 6-fold coordination state. However, this is not without compromise as two distorted Si-octahedra are formed. The largest distortion occurs within Si(2)-O_6 in the form of an off centred cation which consequently forms an non-ideal octahedron which is apparent from its cis and trans bond angles.

Additionally, the NPD data has shown that $Si_5O(PO_4)_6$ has the potential to be a good oxide ion conductor due to its distinctive structural features. These structural features include the location of the O1 oxygen, the formation of large cavities, and the cationic channels running along the c-axis.

The U_{iso} value of O1 within the silicate was indicative of a highly mobile O1 oxide ion, and Fourier difference maps show that mobile oxide ions can be stabilised within the cavities, relatively unhindered. However, the structural refinement of the material has shown that a key difference that affects oxide conductivity is the inflexibility seen in the silicon cationic lattice. This inflexibility is linked to the formation of shorter and stronger Si-O1 bonds which to a certain degree effects O1's mobility. Evidence to support this is seen in the overall lower U_{iso} value of the silicate O1 at the highest recorded temperature when compared to O1 within the germanate. In addition to this, Si(3) does not represent the most mobile cation within the structure. This is in contrast to Ge(3) where it has been proposed in this thesis that Ge(3) mobility is vital for the stabilisation of oxide ions within the cavities.

5.5 References

1. Mayer, H. Die Kristallstruktur von $Si_5O(PO_4)_6$. *Monatshefte für Chemie / Chem. Mon.* **105,** 46–54 (1974).
2. Liebau, F. *Structural Chemistry of Silicates: Structure, Bonding, and Classification*. (Springer Berlin Heidelberg, 2012).
3. Weeding, T. L., De Jong, B., Veeman, W. S. & Aitken, B. G. Silicon coordination changes from 4-fold to 6-fold on devitrification of silicon phosphate glass. *Nature* **318,** 352–353 (1985).
4. Liebau, F., Bissert, G. & Köppen, N. Synthese und kristallographische Eigenschaften einiger Phasen im System SiO_2–P_2O_5. *Zeitschrift für Anorg. und Allg. Chemie* **359,** 113–134 (1968).
5. Saxin, S. A possible low-intermediate temperature proton conductor based on Silicon Oxide Phosphate., PhD thesis, (University of St Andrews, 2014).
6. Styskalik, A. *et al.* Non-aqueous template-assisted synthesis of mesoporous nanocrystalline silicon orthophosphate. *RSC Adv.* **5,** 73670–73676 (2015).
7. Zhang, Y. Exploring Novel Functionalities in Oxide Ion Conductors with Excess Oxygen., PhD thesis, (Unversity of St. Andrews, 2011).
8. R. A. Young. *The Rietveld Method*. (Oxford University Press, 1995).
9. Larson, A. C. & Von Dreele, R. B. General Structure Analysis System (GSAS). 86–748 (2004). doi:10.1103/PhysRevLett.101.107006
10. Toby, B. H. General Structure Analysis System - GSAS / EXPGUI, A Graphical user interface for GSAS. *J. Appl. Cryst.*, **34,** 2001 (2001).
11. Mayer, H. & Völlenkle, H. Die Kristallstruktur von $Ge_5O(PO_4)_6$. *Monatshefte für*

Chemie/Chemical Mon. **103,** 1560–1571 (1972).

12. Poojary, D. M., Borade, R. B. & Clearfield, A. Structural characterization of silicon orthophosphate. *Inorganica Chim. Acta* **208,** 23–29 (1993).

13. Poojary, D. M., Borade, R. B., Campbell III, F. L. & Clearfield, A. Crystal Structure of Silicon Pyrophosphate (Form I) from Powder Diffraction Data. *J. Solid State Chem.* **112,** 106–112 (1994).

14. Leclaire, A. & Raveau, B. $Ge_3P_6Si_2O_{25}$: A cage structure closely related to the intersecting tunnel structure $KMo_3P_6Si_2O_{25}$. *J. Solid State Chem.* **75,** 397–402 (1988).

15. Leclaire, A., Monier, J. C. & Raveau, B. A molybdosilicophosphate with an intersecting-tunnel structure which exhibits ion-exchange properties, $AMo_3P_{5.8}Si_2O_{25}$ (A = Rb, Tl). *Acta Crystallogr. Sect. B* **40,** 180–185 (1984).

16. Leclaire, A., Monier, J. C. & Raveau, B. Structure of $CsMo_3P_{5.8}Si_2O_{25}$. *Acta Crystallogr. Sect. C Cryst. Struct. Commun.* **41,** 1719–1720 (1985).

17. Leclaire, A., Borel, M. M., Grandin, A. & Raveau, B. Silicophosphates with an intersecting tunnel structure: $AM_3P_6Si_2O_{25}$ and $AMo_3P_{5.8}Si_2O_{25}$. *Mater. Chem. Phys.* **12,** 537–543 (1985).

18. Leclaire, A. & Raveau, B. MoP_3SiO_{11}: A silicophosphate of molybdenum(III). *J. Solid State Chem.* **71,** 283–290 (1987).

19. Leclaire, A., Chahboun, H., Groult, D. & Raveau, B. $V_3P_5SiO_{19}$, a vanadosilicophosphate built up from V_2O_9 octahedra clusters. *J. Solid State Chem.* **65,** 168–177 (1986).

20. Shannon, R. D. Revised effective ionic radii and systematic studies of interatomic distances in halides and chalcogenides. *Acta Crystallogr. Sect. A* **32,** 751–767 (1976).

6 $Ge_5O(PO_4)_6$ and related materials

6.1 Introduction

Improving oxide ion conducting properties of electrolytes is driven by the need for improved electrochemical devices. For vacancy oxide ion conductors, this involves introducing oxide ion vacancies into the crystal structure by the doping of aliovalent cations. This allows for oxide ions to 'hop' through the anionic lattice for oxygen transport. This is seen in a variety of electrolytes such as YSZ, CGO and LSGM.[1,2,3,4] The optimisation of the dopant concentration is vital as degradation of conducting performance is seen in excessively doped materials. This occurrence is due to the formation of dopant-vacancy interactions or defect clustering. Consequently, this leads to the trapping of mobile charge carriers. A possible solution to circumvent these issues, is to investigate novel doping strategies for 'excess' oxygen structures such as $Ge_5O(PO_4)_6$ where oxide ions are the mobile charge carrier. Therefore, the material represents an alternative direction for the future development of oxide ion conducting electrolytes. In this chapter, evaluation of a range of isovalent and aliovalent cations as possible dopants for $Ge_5O(PO_4)_6$ were performed. This includes cations such as Si, Sn, Ga, Al, and As. The materials that were produced were assessed using PXRD for phase analysis while AC impedance spectroscopy was performed to determine their conducting properties.

6.2 Experimental

Laboratory based X-ray powdered diffraction (XRPD) was used for the purpose of phase identification and evaluation of unit cell parameters. Two diffractometers were used in this chapter for specified purposes. Firstly, the Panalytical Empyrean X-ray diffractometer with a Cu $K_{\alpha 1}$ source was used over the 2 θ range of 10-90 ° with a step size of 0.017 ° and counting 35.250s per step to obtain high resolution XRD patterns of samples. This was used for phase analysis and unit cell parameter determination. Secondly, a Miniflex rigaku 600 was used for rapid phase identification and determination of unit cell parameters of samples in between firing steps. This diffractometer used Cu $K_{\alpha 1}$ radiation and collection was taken over the 2 θ range of 10-70 ° or 10-90 ° with a step size of 0.02 ° with a counting time of 13 minutes. Unit cell parameters were determined using GSAS[5] with the Expgui[6] or using Stoe WinX pow[7]. For the arsenic based compounds Kapton film was used to keep the sample in place. To determine the level of ionic conductivity, the AC impedance technique has been used. The HP 4194A impedance analyser was used over a range between 8 MHz – 0.1 Hz with a AC amplitude of 10 mV and using 10 points per decade.

Pressed pellets of a range of materials were produced and their conducting properties were measured over a temperature range of 50-900 °C at 50 °C intervals. This was performed with a ramp rate of 3 °C/min with a dwell of 20 minutes at each isotherm before measurements were

taken. Platinum paste was used as an electrode and fired at 900 °C to ensure that the electrode adhered to the sample

6.2.1 Synthesis of germanophosphate series

The germanophosphate series was synthesised using GeO_2 (Alfa Aesar, 99.9999%) and $NH_4H_2PO_4$ (Sigma Aldrich 98+ %). This series of materials was performed to determine whether there are non-stoichiometric compositions that deviated from the parent composition $Ge_5P_6O_{25}$. The synthesis of excess germanium materials, $Ge_{5+x}P_6O_{25+\delta}$ and excess phosphorus materials, $Ge_5P_{6+x}O_{25+\delta}$ were attempted for the germanophosphate series. The x values that were synthesised for the excess germanium series were x = 0.125, 0.25 and 0.5 and the excess phosphorus materials were x = 0.15, 0.24, 0.3 and 0.6. In all these materials, the reagents were added and ground together using a pestle and mortar. They were then calcined at 190 °C to drive off NH_3 and H_2O. The resultant material was reground using the same method as previously mentioned and then fired. The firing temperatures for these materials may be seen in the table below.

Firing step	Ramp rate heating/cooling	Firing temperature	Dwell times (hours)
1	10 °C/min (↑)/5 °C/min (↓)	1000 °C	20
2	10 °C/min (↑)/5 °C/min (↓)	1100 °C	5-6

Table 6-1 synthesis of germanophosphate series materials

If the material was found to have impurities it was fired for an additional 5 hours at 1000 °C. However, this did not improve the composition

6.3 Results and discussion

6.3.1 Germanophosphates

The GeO_2 and P_2O_5 binary system has been previously studied by Mal'shikov *et al*[8] However, a more focused study has been performed in this section to determine whether there is the existence of a solid solution within the stoichiometric phase, $Ge_5O(PO_4)_6$. Similar studies have been performed on the isostructural material, $Si_5O(PO_4)_6$. It has been reported by Liebau *et al*[9] that there is a solid solution with the general formula, $Si_{(1+5x)}P_{4(7-x)}O_{72}$, for this system. On the other hand, Poojary *et al*[10] suggested that $Si_5O(PO_4)_6$, did not exist as a solid solution and was stable over the temperature range between 200-1000 °C. The XRD patterns' for the germanophosphate series can be seen in Figure 6-1.

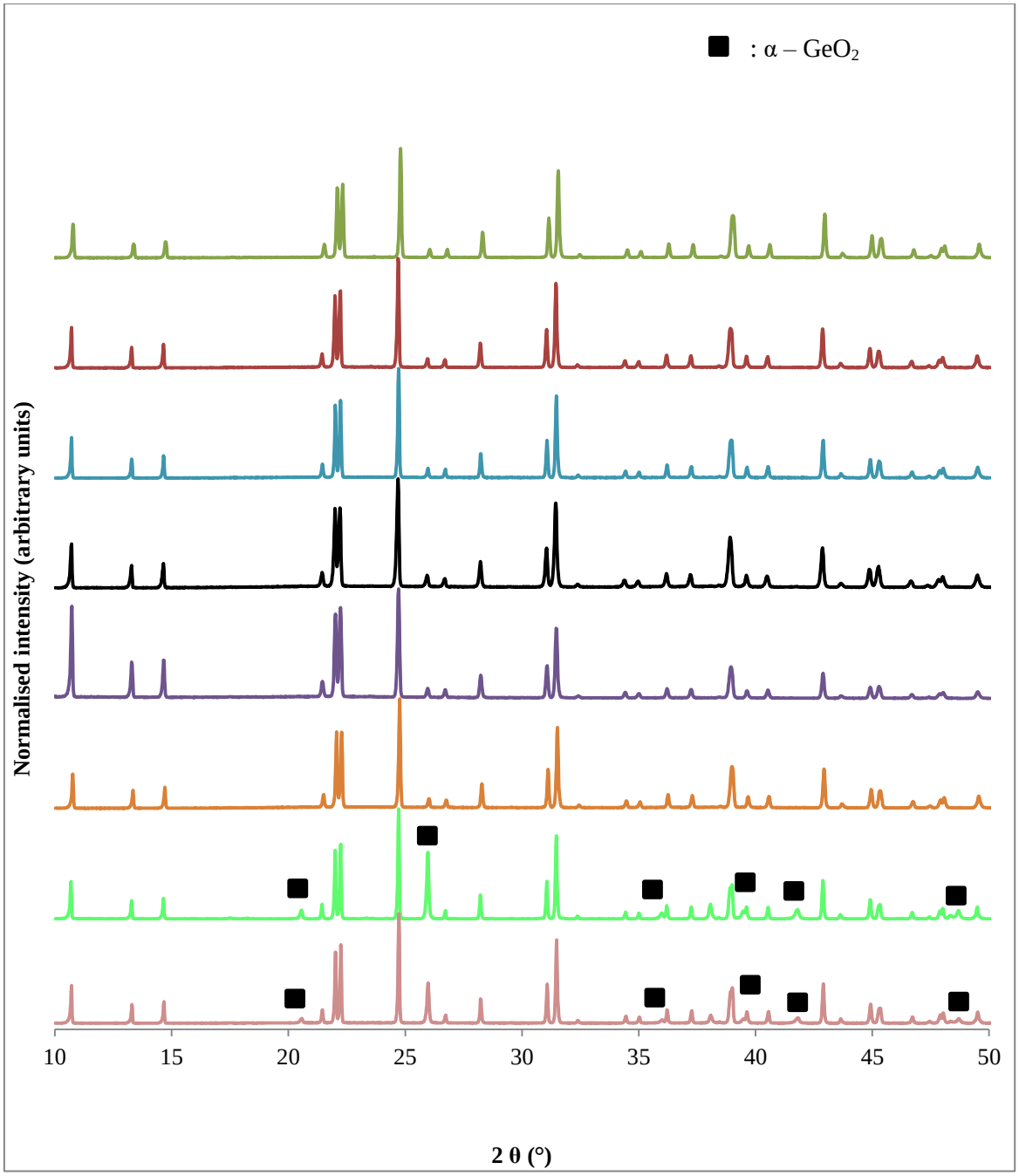

Figure 6-1. The XRD patterns' for the germanophosphate series which shows x = 0.5 (pink XRD pattern), 0.25 (light green XRD pattern), 0.125 (orange XRD pattern) for the germanium excess materials and x = 0.15 (black XRD pattern), 0.24 (blue XRD pattern), 0.3 (red XRD pattern), 0.6 (dark green XRD pattern) for the phosphorus excess compositions. The stoichiometric composition is represented by a purple XRD pattern. Unannotated peaks belong to the *R-3* phase ($Ge_5O(PO_4)_6$ phase).

Figure 6-1 shows the XRD patterns are all very similar and there does not appear to be any systematic change in unit cell sizes based on peak positions. It should also be noted that the germanium excess materials x = 0.25 and 0.5 appears to contain the presence of α-GeO_2. This

suggested that if there is a solid solution the solubility limit is below x = 0.125 for the excess germanium systems. The XRD patterns for all other materials show that they are single phase indexed to the *R-3* space group with the hexagonal unit cell.

The unit cell parameters for the tested compositions for the GeO_2-P_2O_5 binary system can be seen in Figure 6-2.

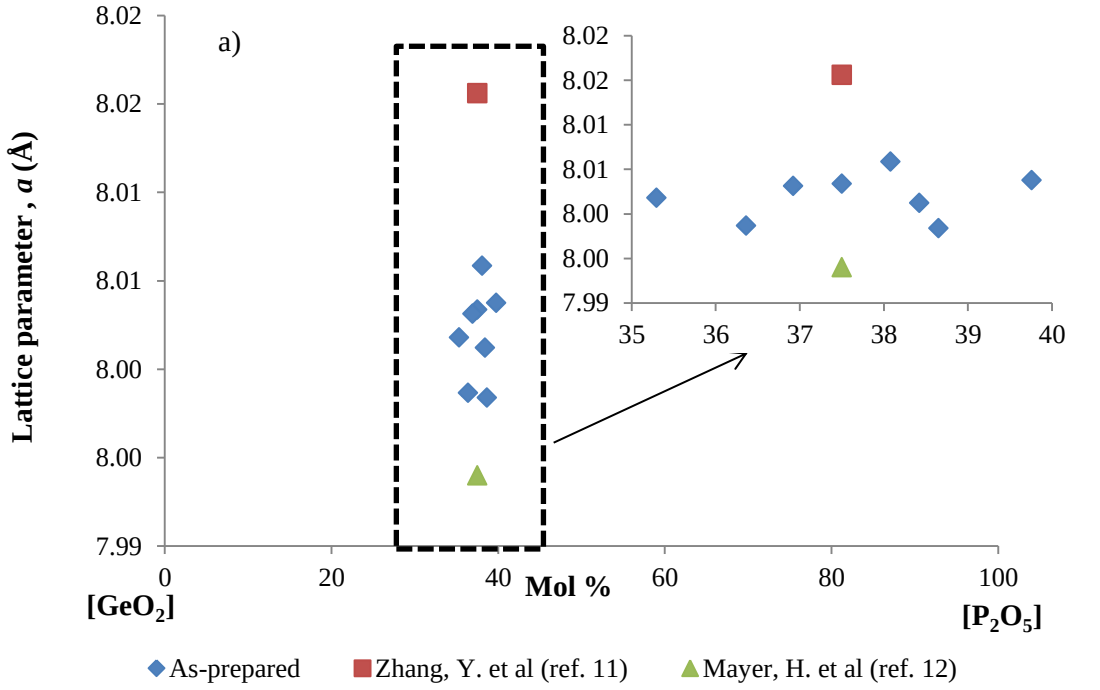

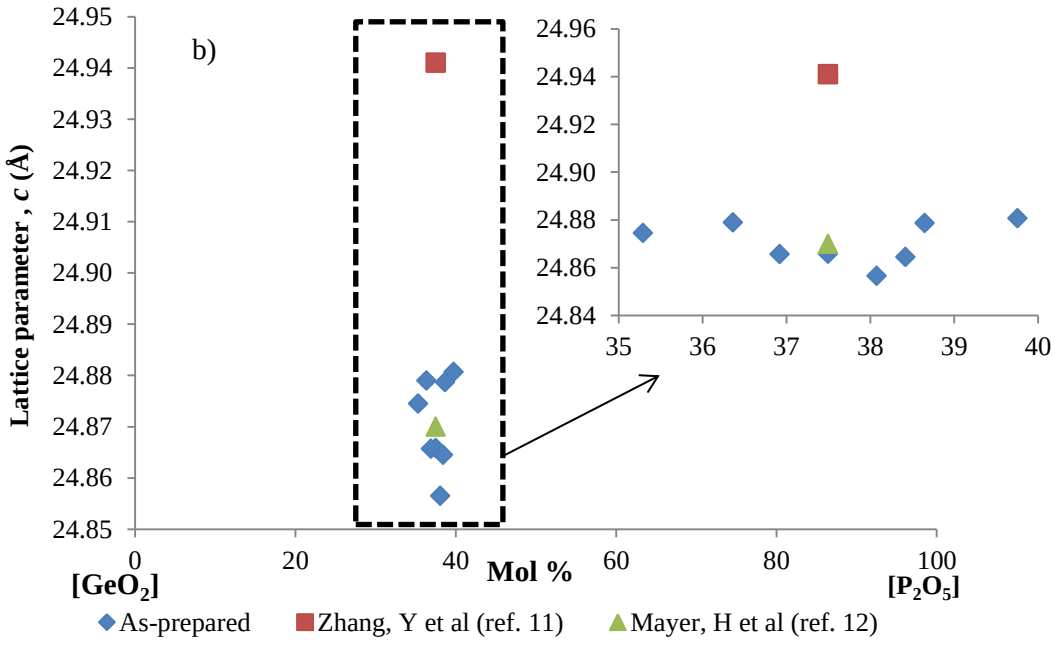

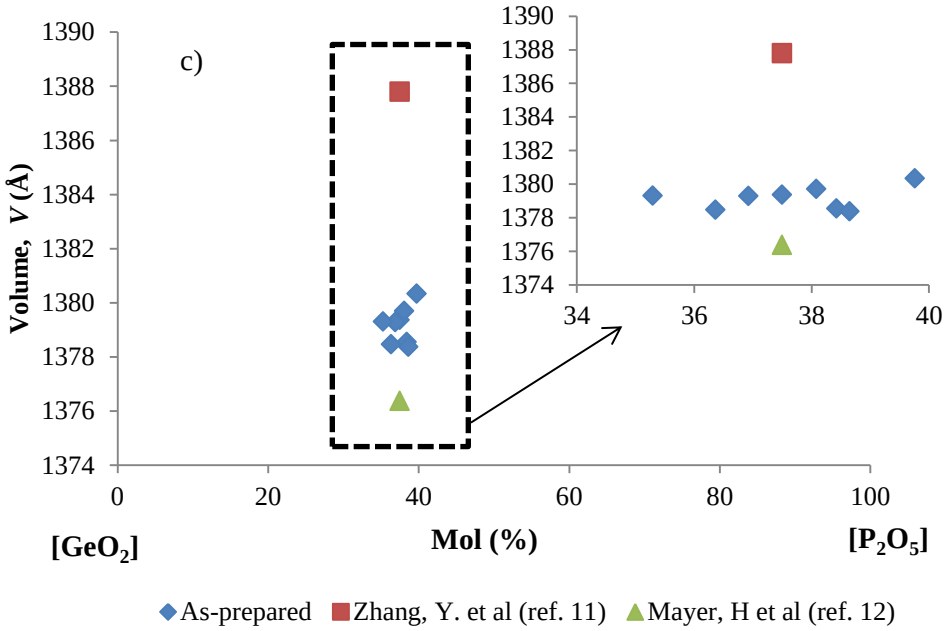

Figure 6-2. Unit cell parameters of excess phosphorus and germanium materials a) shows the unit cell parameter, *a* (Å) (b) unit cell parameter, *c* (Å) and (c) unit cell volume (Å^3).

From the graphs above, the results showed that despite having no consistent changes in unit cell parameters, there appears to be variation in unit cell size. Variation in unit cell has been seen previously within the material. Zhang, Y. *et al*[11] reported that $Ge_5O(PO_4)_6$ had a relatively large unit cell of a = 8.0156 Å and c = 24.941 Å when compared to the prepared $Ge_5O(PO_4)_6$ (a = 8.00337 Å and c = 24.8658 Å shown in Figure 6-2). This is in contrast to a smaller unit cell size reported by Mayer *et al*[12] which was reported as a = 7.994 Å and c = 24.87 Å. The prepared $Ge_5O(PO_4)_6$ resides more closely to Mayer *et al*'s single crystal data with the ***c*** unit cell parameter being very close in size. It was reported that when the isostructural material, $Si_5O(PO_4)_6$ was hydrothermally treated with water there was a marked change in unit cell parameters[13]. This may be attributed to the retention of water with in the large cavities within the structure. It can be suggested the variation in unit cell size for $Ge_5O(PO_4)_6$ may be related to the retention of water within the pores where Mayer *et al*'s sample represents a relatively dry sample.

6.3.2 Germano-silicophosphate series

Leclaire *et al*[14] isolated a single crystal germanosilicophosphate, $Ge_3P_6Si_2O_{25}$, which is structurally related to that of $Ge_5O(PO_4)_6$. The related structure is shown in section 1.5.4.3. The structure consists of mixed cationic polyhedra in the form of ditetrahedral Si_2O_7 and octahedral GeO_6. In this section, germanosilicophosphate series, $Ge_{5-x}Si_xO(PO_4)_6$ were synthesised from x= 0 to 5, and will be discussed with firing temperatures. The reagents that were used are as follows: GeO_2 (Alfa Aesar, 99.9999 %), $NH_4H_2PO_4$ (Sigma Aldrich 98+ %) and fumed SiO_2 (Sigma Aldrich 99.999 %).

The fumed SiO_2 was heated to 950 °C for 1 hour before weighing, to drive of adsorbed H_2O and CO_2. These reagents were than ground together with a mortar and pestle and calcined at 190 °C for 3 hours to drive of H_2O and NH_3. The reaction mixture was than ball milled using the planetary ball mill for 2 hours and then fired for the formation of the final material.

Single phase $Ge_4SiO(PO_4)_6$ was successfully synthesised. The firing scheme for this material can be seen in Table 6-2. XRD data was collected from the Miniflex Rigaku 600 over the 2θ range of 10-70 ° as shown in Figure 6-3. Whereas, the XRD patterns for the final material were collected on the Panalytical Empyrean X-ray diffractometer as shown in Figure 6-4 along with other members of the series.

Firing step	Ramp rate	Temperature (°C)	Dwell times	Phase composition	XRD pattern colour
1	8 °C/ min ↑, 5 °C ↓	1000	12	GeO_2, SiO_2 , β-GeP_2O_7 and SiP_2O_7	Black
2	8 °C/ min ↑, 5 °C/ min ↓	1050	12	GeO_2, SiO_2 , β-GeP_2O_7 and SiP_2O_7	Red
3	8 °C/ min ↑, 5 °C ↓	1050	12	GeO_2, SiO_2 , β-GeP_2O_7 and SiP_2O_7	Green
4	8 °C/ min ↑, 5 °C ↓	1070	12	$Ge_4SiO(PO_4)_6$	Purple

Table 6-2. Firing scheme for the synthesis of the germanosilicophosphate, $Ge_4SiO(PO_4)_6$ including firing temperature and the phase composition after each firing of the material.

The corresponding XRD patterns' can be seen in Figure 6-3.

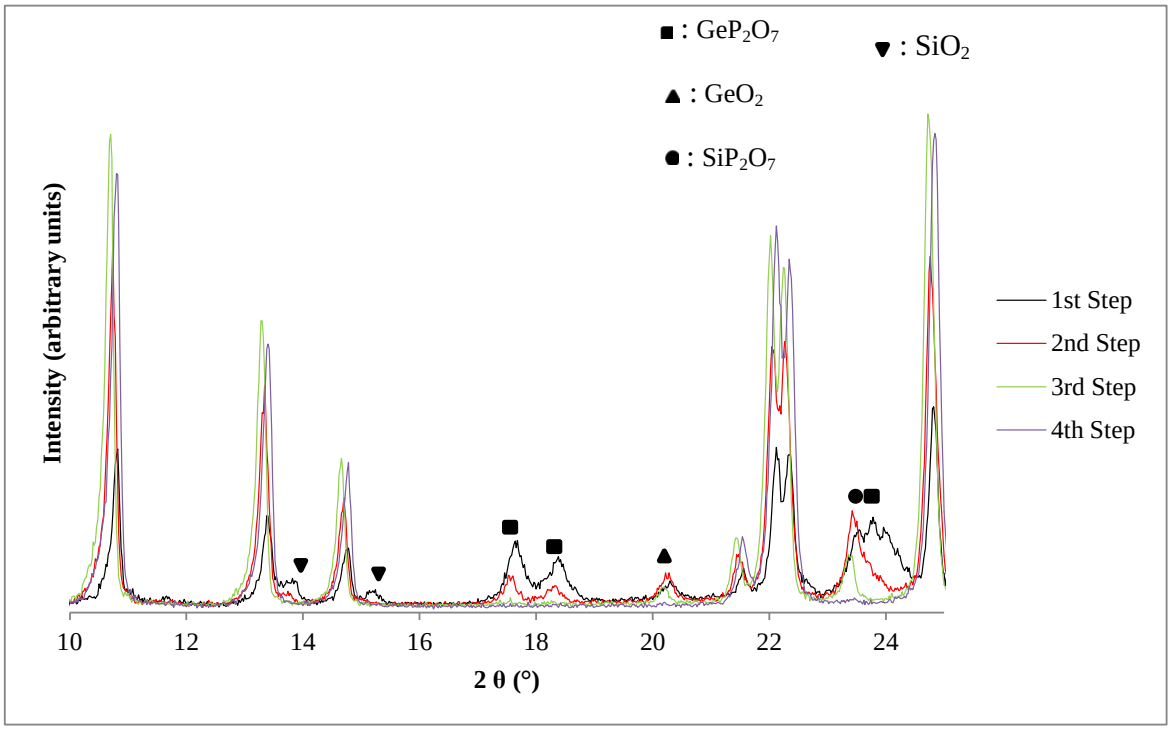

Figure 6-3. XRD patterns' for the synthesis of $Ge_4SiO(PO_4)_6$. The black, red, green and purple XRD patterns represent the 1st , 2nd , 3rd and 4th firings of $Ge_4SiO(PO_4)_6$, respectively. The patterns showed that after each additional firing the phase of interest, $Ge_4SiO(PO_4)_6$, becomes the predominant phase. Unlabelled peaks represent the phase, $Ge_4SiO(PO_4)_6$.

From Figure 6-3, single phase $Ge_4Si(PO_4)_6$ was achieved after a total of 48 hours. It should also be mentioned that firing temperatures of higher than 1000 °C were used but GeO_2 seems to remain within the crystalline state.

Similarly, $Ge_3Si_2O(PO_4)_6$, was synthesised with the same firing conditions with intermittent ball milling for each firing step whereas $Ge_2Si_3O(PO_4)_6$ only required three firing steps to form the single phase material. For the composition x=4, the material went through two firing steps. The first step was 24 hours at 950 °C and then another 24 hours at 975 °C. Ball milling the sample was required between firing steps. Comparisons of the XRD patterns for these materials are shown in Figure 6-4.

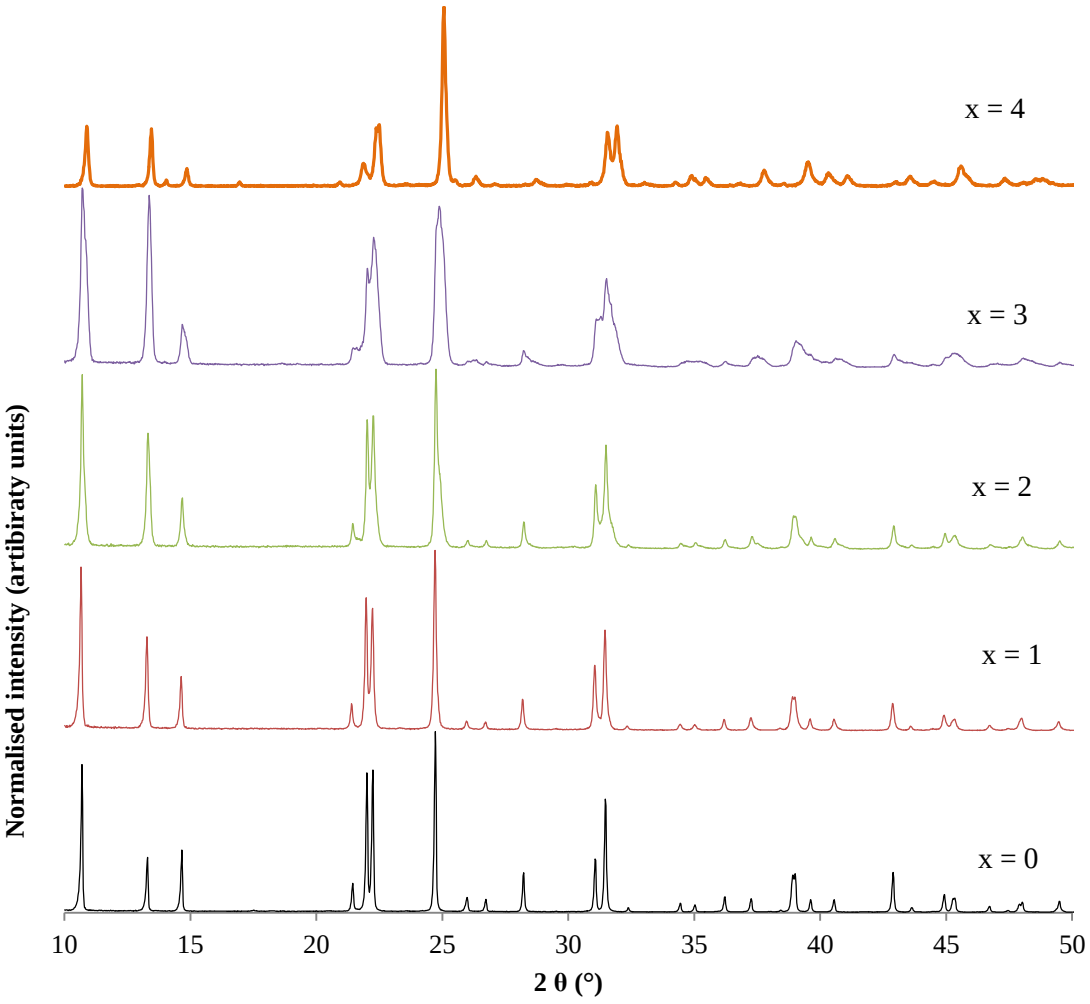

Figure 6-4. A comparison of the XRD patterns' for $Ge_5O(PO_4)_6$ (black), $Ge_4SiO(PO_4)_6$ (red) , $Ge_3Si_2O(PO_4)_6$ (green), $Ge_2Si_3O(PO_4)_6$ purple and $GeSi_4O(PO_4)_6$ (orange). As the molar concentration of [Si] is increased there are changes in the diffractograms such as broader peaks and changes in intensity.

The germanosilicophosphate series shows that there are key changes in the patterns with increasing Si (when $0<x\leq3$) This can be detailed in the following two characteristics; firstly, the first three peaks with the D-spacing 1) 8.29 Å, 2) 6.67 Å and 3) 6.05 Å have the relative intensities in the order of 1>3>2 for the germanium end member. However, on the addition of [Si] to the structure the relative intensities change to 1>2>3. This is similar to that seen for the $Si_5O(PO_4)_6$ reported in literature[10]. This may serve as evidence to suggest that [Si] is entering the structure and/or there are changes in preferential orientation for the silicon doped materials. Further work is required to evaluate the latter with NPD or SXRD to determine changes in texture. Secondly, with increasing [Si] %, there is a stepwise change in the peak shapes. In $Ge_5O(PO_4)_6$, the peaks are sharp but when [Si] % is increased the peaks begin to broaden. This suggested that there may not be a direct

exchange of the cationic species, Ge and Si. For $GeSi_4O(PO_4)_6$, an additional phase is seen in the XRD pattern. These peaks were indexed to *P-31c* crystal system. A closer view of the XRD pattern is shown in Figure 6-5.

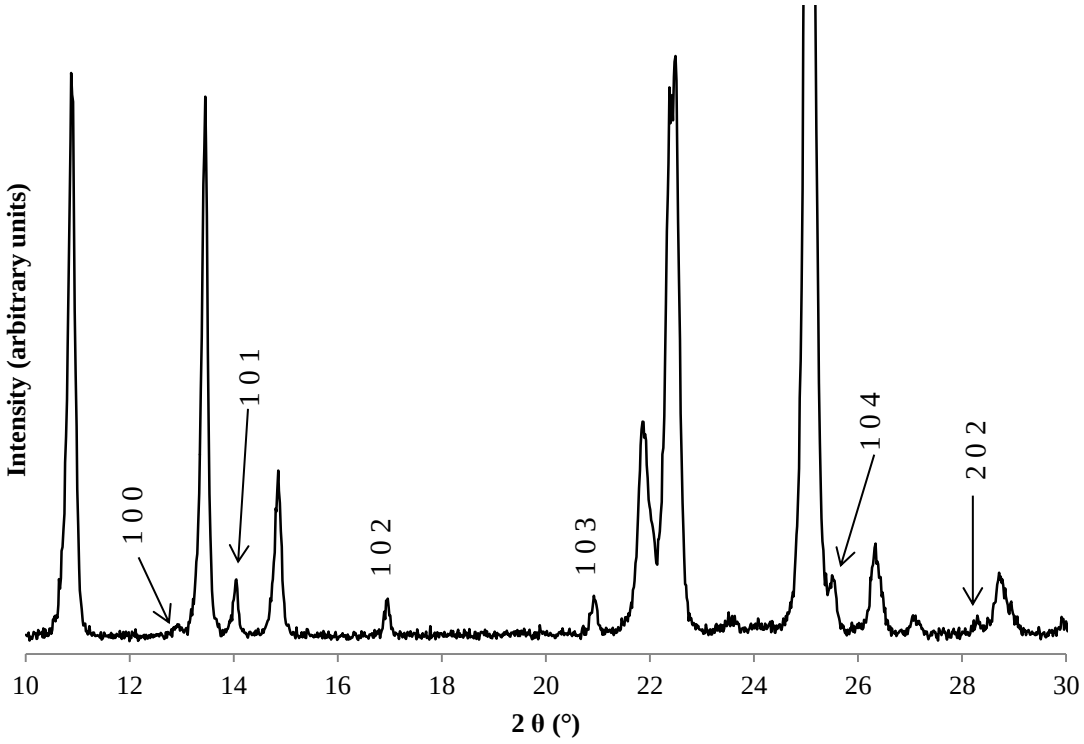

Figure 6-5. XRD pattern of $GeSi_4O(PO_4)_6$ between the 2 θ range between 10-30 °. This shows the peaks indexed to *P-31c*.

The XRD pattern shows the existence of the phase suggested by Leclaire *et al*[14] within the silicogermanophosphate solid solution. The unit cell parameters were determined from these peaks which are ***a*** = 7.904 (4) Å, ***c*** = 16.228 (8) Å and volume = 877.9 (5) $Å^3$. This is smaller than the unit cell parameters of the phase suggested in literature (***a*** = 7.994 (1) Å, ***c*** = 16.513 (2) Å). This showed that there may be a solid solution between $Ge_3Si_2O(PO_4)_6$ and compositions with silicon content higher than x=2. However, there is no clear indication of the phase within the prepared $Ge_3Si_2O(PO_4)_6$ material. Further work is required for this material. Transmission electron microscopy could be used to determine whether the two materials exist as separate phases or the phases coexist where the material contain domains within one another. Additionally, further work is required to establish the solid solution between the materials that have the crystal structure within the *P-31c* crystal system.

The units cell parameters for the silicogermanophosphate series (*R-3* : model : Z=3).were compared with the addition of $Si_5O(PO_4)_6$. This is illustrated in Figure 6-6. It should be noted that the material where x=4 is assumed to contain [Si] 80 % in the following graph.

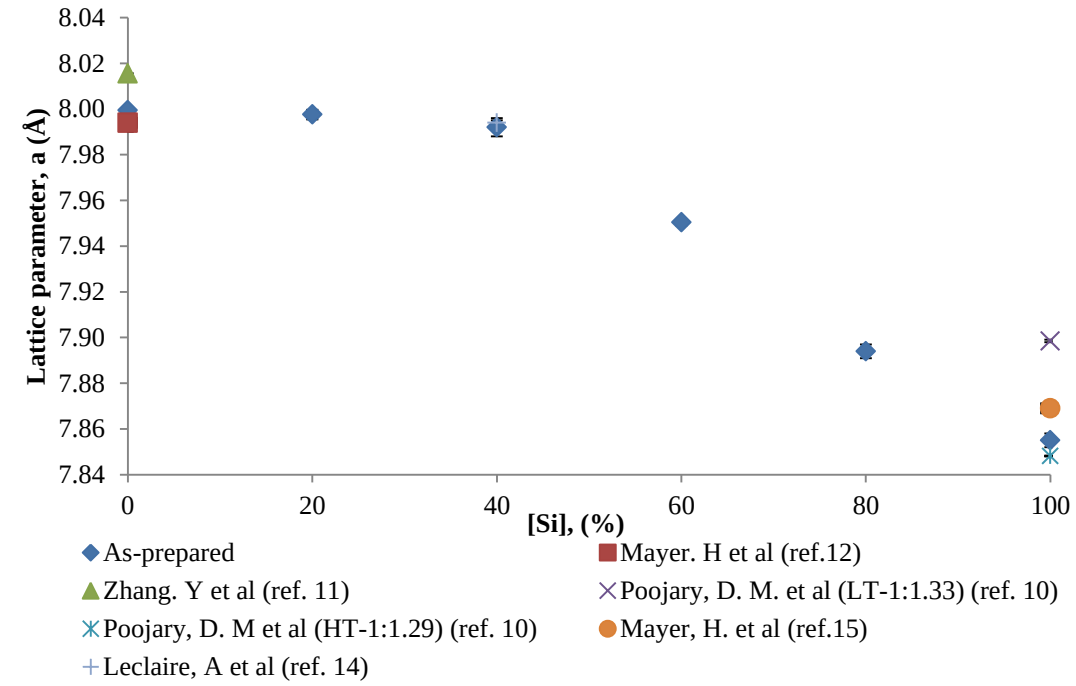
8.04
8.02
8.00
7.98
7.96
7.94
7.92
7.90
7.88
7.86
7.84
Lattice parameter, a (Å)
0
20
40
60
80
100
[Si], (%)
As-prepared
Mayer. H et al (ref.12)
Zhang. Y et al (ref. 11)
Poojary, D. M. et al (LT-1:1.33) (ref. 10)
Poojary, D. M et al (HT-1:1.29) (ref. 10)
Mayer, H. et al (ref.15)
Leclaire, A et al (ref. 14)

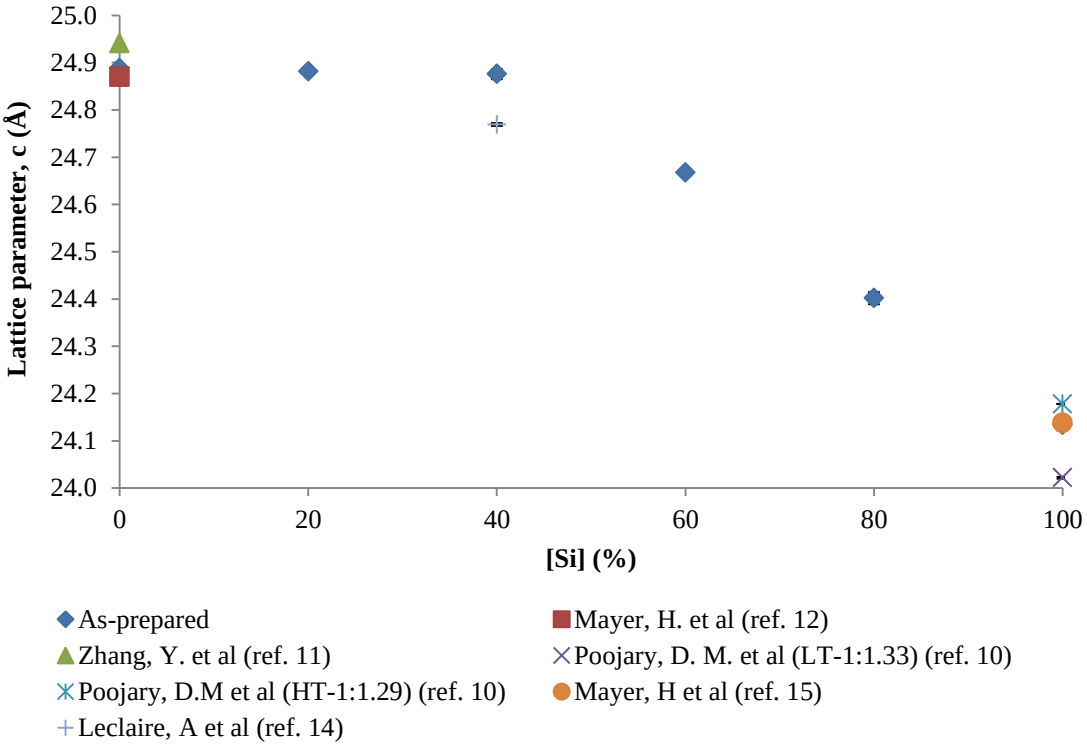
25.0
24.9
24.8
24.7
24.6
24.5
24.4
24.3
24.2
24.1
24.0
Lattice parameter, c (Å)
0
20
40
60
80
100
[Si] (%)
As-prepared
Mayer, H. et al (ref. 12)
Zhang, Y. et al (ref. 11)
Poojary, D. M. et al (LT-1:1.33) (ref. 10)
Poojary, D.M et al (HT-1:1.29) (ref. 10)
Mayer, H et al (ref. 15)
Leclaire, A et al (ref. 14)

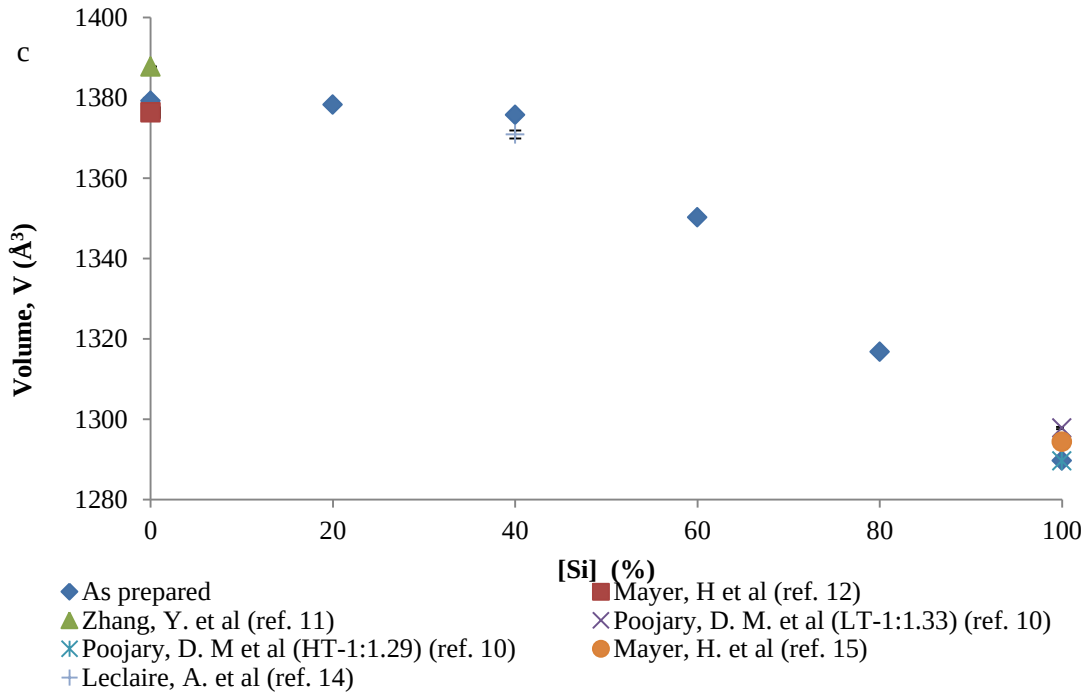

Figure 6-6. A comparison of unit cell parameters of the silicogermanophosphate series, a) shows the unit cell parameter of *a* (Å), b) shows the unit cell parameters for *c* (Å) and c) shows the unit cell volume, *V* (Å^3). This includes are range of other sources from literature.

The graph above shows that there is a large unit cell size difference between the silicate and germanate end members. This is attributed to the size difference between Ge^{4+} and Si^{4+}. As previously mentioned, the unit cell parameters for the prepared material $Ge_5O(PO_4)_6$ is consistent with single crystal data. For the Si end member, the unit cell parameters from a range of sources were compared to the prepared silicate. The literature data showed that there was some variation with the unit cell size, particularly for the samples that were synthesised by Poojary *et al*[10]. These were synthesised with the differing starting molar ratio of 1:1.33 (Si:P) and 1:1.29 (Si:P). The method in which these materials were synthesised entailed heating 85 % H_3PO_4 to 120 °C in a platinum dish then slowly adding silica gel to the acid. Both reaction mixtures were then homogenised by stirring. The reaction temperatures of the mixtures also differed. For the composition Si:P = 1:1.33, it was heated at 200 °C for 5 hours whilst the reaction mixture Si:P = 1:1.29 was heated at 300 °C for 5 hours then fired at a higher temperature of 1000 °C for two hours. The former will be referred to as LT-1:1.33 and the latter will be referred to as HT-1:1.29. LT-1:1.33 showed that there were large differences in the *a* and *c* unit cell parameters when compared to the prepared $Si_5O(PO_4)_6$. Whereas, HT-1:1.29 showed more consistent values with the prepared silicophosphate. As previously mentioned, for $Ge_5O(PO_4)_6$, variation in unit cell parameters within $Si_5O(PO_4)_6$ was attributed to retention of water within the structure. Further discussion from Poojary *et al* supports this. TGA was performed on these materials suggesting that

there is a higher percentage of water loss for the LT-1:1.33 sample over the temperature range 25-200 °C. In addition to this, further weight losses were assigned to dehydroxylation of surface –OH and the volatilisation of chemically bound phosphorus species at higher temperatures. Single crystal $Si_5O(PO_4)_6$ was synthesised by Mayer *et al*[15] and showed similar unit cell parameters to the prepared sample. Leclaire *et al*'s [14] structure was also added to this graph for a comparison to the prepared $Ge_3Si_2O(PO_4)_6$ material, due to its structural similarities to $Ge_5O(PO_4)_6$. Leclaire *et al*'s[14] structure has the unit cell parameters of a = 7.994(1) Å, c = 16.513(2) Å and Z = 2 (space group *P-31c*), which differs in unit cell size and Z number from the structure of $Ge_5O(PO_5)_6$ reported by Mayer *et al* (a = 7.994(4), c = 24.87(1), Z = 3 and space group: *R-3*). According to Leclaire *et al* $Ge_3Si_2O(PO_4)_6$ is a related structure to the $Ge_5O(PO_4)_6$. This is due to both structures forming mixed polyhedral coordination states and cavities within the structure. However, there is a difference in unit cell size related to the difference in the number of formula units per unit cell. For $Ge_5O(PO_5)_6$, there are 3 formula units per unit cell whilst for $Ge_3Si_2O(PO_4)_6$ it has 2 formula units per unit cell. This is reflected in their relative unit cell lengths, where the c-axis for $Ge_3Si_2O(PO_4)_6$ is ~2/3 of the $Ge_5O(PO_4)_6$. Therefore, to extrapolate a lattice parameter c that is directly comparable to the as-prepared $Ge_3Si_2O(PO_4)_6$ it was extended to the same size as the parent composition (Eg. (16.513/2)*3)). The results showed that the unit cell parameters are consistent with the prepared material. It showed that with the addition of silicon at 40 % [Si] dopant levels the change in unit cell size was small. This suggested that the change in unit cell size from the Ge end member to the Si end member was not solely proportionate to the exchange of the smaller cation Si^{+4} with Ge^{4+}. Leclaire *et al*'s $Ge_3Si_2O(PO_4)_6$ structure showed that the predominant change in unit cell size is seen as a decrease along the c-axis. This may be attributed to a change in the size of the cavities that run along the c-axis. However, due to the dominance of a^2 to the unit cell volume, the overall decrease in unit cell volume is small and comparable to the prepared $Ge_3Si_2O(PO_4)_6$.

6.3.2.1 Mechanism for the exchange of Si and Ge within the crystal structure $M_3^{[6]}M_2^{[4]}O(PO_4)_6$ (M = Ge, Si)

As shown in Figure 6-6, there is a small decrease in unit cell parameters at lower concentrations up to 40 % [Si]. At higher concentrations there is a larger decrease in unit cell parameters until 100 % [Si]. This may be related to the preferential exchange of cations. A mechanism for this is shown in Figure 6-7.

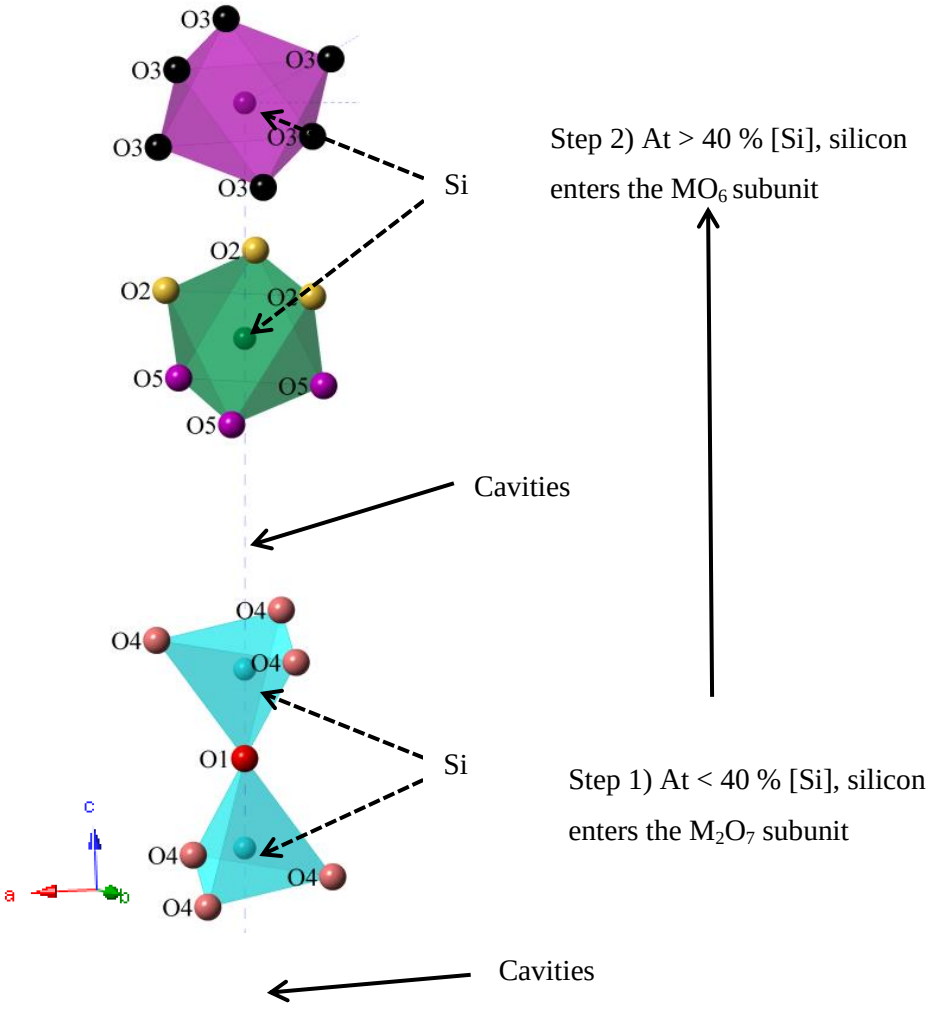

Figure 6-7. Illustration of the two coordination states of $M_3^{[6]}M_2^{[4]}O(PO_4)_6$ Step 1) At <40 % [Si], there is a propensity for silicon to enter the structure via the M_2O_7 structures. In step 2, at higher concentrations of [Si], Silicon begins to enter the structure through the MO_6 octahedral units.

Figure 6-7 shows that there are two processes for the exchange of Ge with Si. Step 1) shows that silicon has the propensity to enter the M_2O_7 subunit at 40 % [Si] or at lower concentrations. In step 2, Si enters the structure via the MO_6 octahedron. This may be related to silicon's propensity to

reside within the 4-fold tetrahedral coordination as silicon does not usually adopt the 6-fold octahedral coordination[16,17]. As the concentration of [Si] increases above 40 %, the M_2O_7 subunits are filled with silicon. As a result, the silicon must adopt the octahedral geometry to enter the MO_6 octahedra. The much larger decrease in unit cell size is attributed to the replacement of GeO_6 octahedra which have ideal octahedral geometry. This is replaced with highly distorted SiO_6 octahedra. This distortion within SiO_6 was observed within neutron powder diffraction of the $Si_5O(PO_4)_6$ end member (see section 5.3.4). As a result, the change in unit cell size is now two-fold. Firstly, a change is caused from the exchange of Ge^{4+} with a smaller Si^{4+}. Secondly, the structure is replaced with highly distorted SiO_6 octahedra. This distortion has the effect of reducing the overall size of the SiO_6 octahedron when compared to SiO_6 with ideal octahedral symmetry.

6.3.3 $Sn_5O(PO_4)_6$ and Tin-doped samples

Tin resides in group 4 of the periodic table. In addition to this, it resides just below silicon and germanium and has the same valency to these cations. Consequently, it was considered a possible dopant for the synthesis of an isostructural material, $Sn_5O(PO_4)_6$, or a series of Stanno-germanophosphates.

6.3.3.1 Experimental – $Sn_5O(PO_4)_6$

For the synthesis of $Sn_5O(PO_4)_6$, stoichiometric amounts of SnO_2 (Sigma Aldrich 99.9+ %) and $NH_4H_2(PO_4)_6$ (Sigma Aldrich 98+ %) were ground together and calcined for 3 hours at 180 °C and then fired for 10 hours at 1000 °C, and ball milled and fired for an additional 1100 °C for 10 hours.

6.3.3.2 Results

After the sample was fired, the material was analysed using PXRD. This can be seen in Figure 6-8.

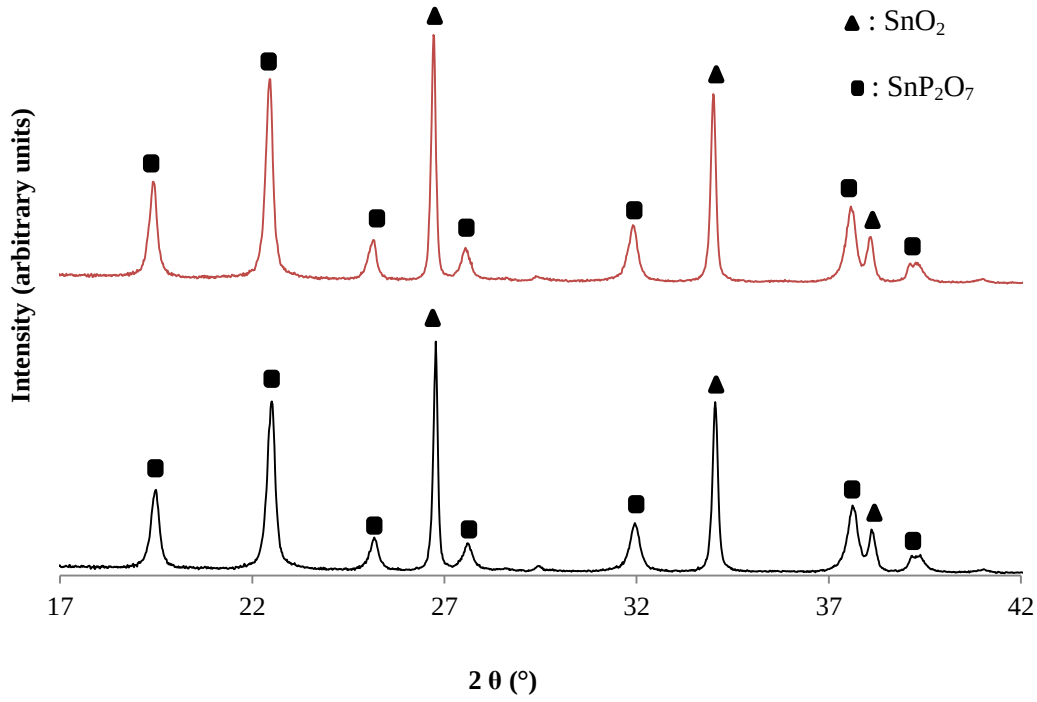

Figure 6-8. A comparison of the XRD patterns' for stoichiometric amounts of SnO_2 and $NH_4H_2PO_4$ for the synthesis of $Sn_5O(PO_4)_6$ after firing. The black XRD pattern shows the final composition after a firing at 1000 °C while the red XRD pattern shows that the SnP_2O_7 was stable up to 1100 °C.

The XRD patterns' showed that the sample consisted of SnP_2O_7 and unreacted SnO_2. This multiphasic composition when fired at 1100 °C suggested that SnP_2O_7 was stable at higher temperatures and longer firing times. As previously mentioned, $Ge_5O(PO_4)_6$ represents a structure with mixed 4-fold and 6-fold cationic states. As a result, Sn^{4+} must be able to adopt both coordination states for $Sn_5O(PO_4)_6$ to form. However, the large ionic radii of Sn^{4+} inhibits its flexibility to accommodate this. When the ionic radii of Sn^{4+} is compared to Si^{4+} and Ge^{4+}, their ionic radii sizes may be ordered as follows; $Si^{4+}<Ge^{4+}<Sn^{4+}$. As the ionic radii sizes increase, there is a change in the propensity for these cations to adopt the 4-fold or 6-fold coordination. For example, silicon is known to adopt the 6-fold coordination state, though; it typically resides in 4-fold structures such as (SiO_4^{4-}). As the ionic radii increases, Ge^{4+} is more readily able to adopt both the 4-and 6-fold coordination states. Finally, Sn^{4+} usually resides within the 6-fold coordination state. The XRD patterns supported this conclusion as the material that was synthesised was SnP_2O_7 which only contains 6-fold Sn^{4+} as can be seen in Figure 6-9.

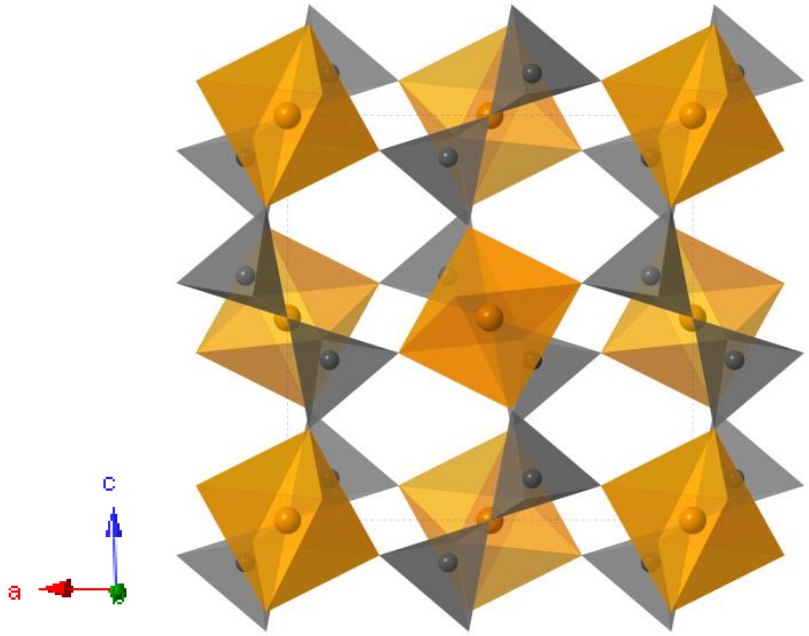

Figure 6-9. Illustration of SnP_2O_7 along the (001) plane showing the 6-fold coordination of Sn. Orange spheres represent tin and grey spheres represent phosphorus. The propensity for tin to remain in a six fold coordination state inhibits the formation of $Sn_5O(PO_4)_6$ which contains mixed 6- and 4-fold cationic environments.

Further studies were pursued in the form of doping tin into the $Ge_5O(PO_4)_6$ structure to determine whether it would occupy the 6-fold coordination state within the material. To evaluate this, the synthesis of a range of tin doped materials were attempted. For these materials, SnO_2 (Sigma Aldrich 99.9+ %) and $NH_4H_2(PO_4)_6$ (Sigma Aldrich 98+%) and GeO_2 (Alfa Aesar, 99.9999%) was used. These were ground together with a pestle and mortar within an acetone medium. The material was calcined at 190 °C for 3 hours to drive off NH_3 and H_2O. This was then ball milled using the planetary method in an acetone medium for two hours before firing. After each firing step, the ball-milling step was repeated. The various compositions are derived from substituting a percent of the GeO_2 with SnO_2 to fill the germanium sites. The firing scheme for these materials can be seen in Table 6-3.

Firing step	Ramp rate	Temperature (°C)	Dwell times
1	8 °C/ min ↑, 5 min °C ↓	1000	12
2	8 °C/ min ↑, 5 °C/ min ↓	1000	12
3	8 °C/ min ↑, 5 °C ↓	1000	12

Table 6-3. Firing scheme for tin doped samples.

The materials that were attempted contained 3%, 5% and 7% [Sn] dopant. A comparison of the XRD patterns for these materials can be seen in Figure 6-10.

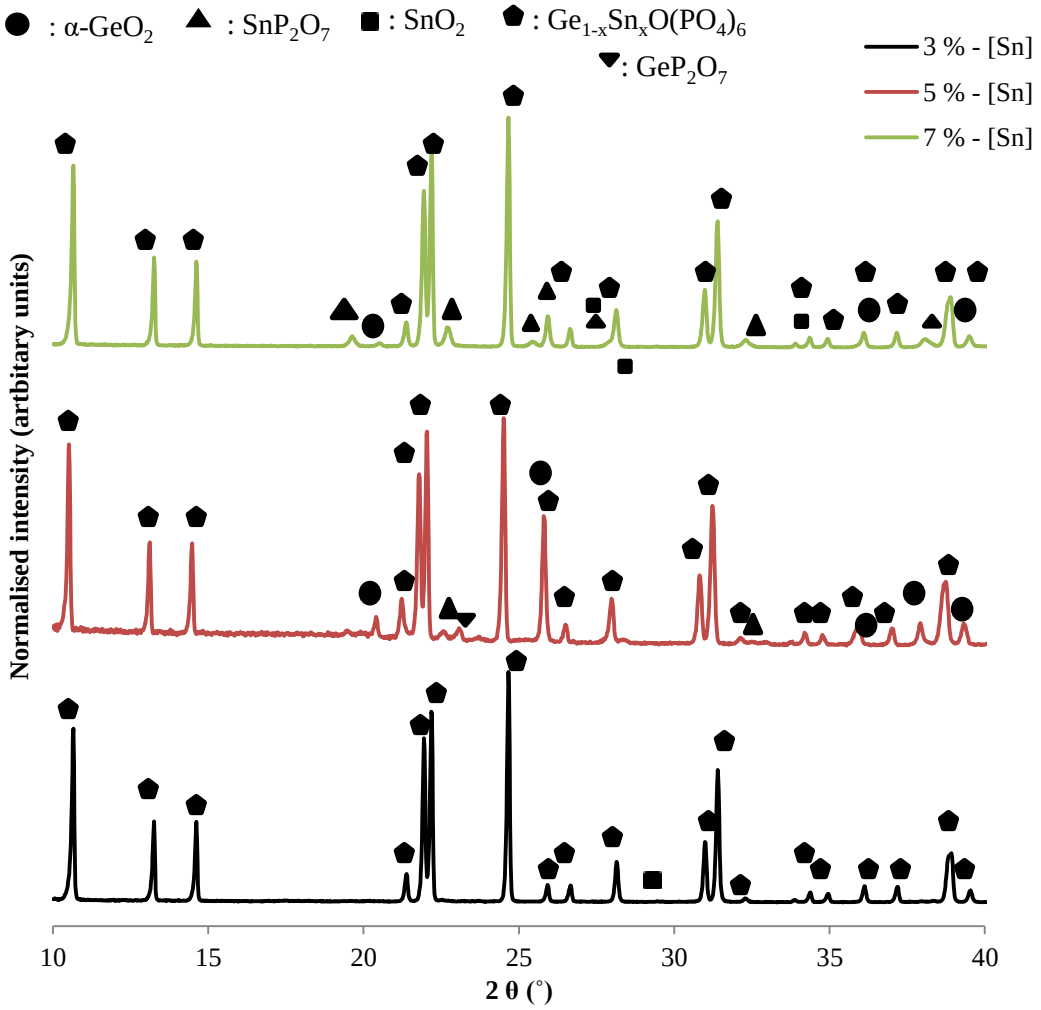

Figure 6-10. Comparisons of 3 % (black XRD pattern), 5% (red XRD pattern) and 7% (green XRD pattern).

The results showed that the 3 % [Sn] doped sample contained minor peaks assigned to unreacted SnO_2. In addition to this, the 5 % and 7 % tin doped materials have impurities in the form of SnP_2O_7, GeO_2 and GeP_2O_7. Figure 6-11 shows the XRD pattern for the 5 % [Sn] -doped composition.

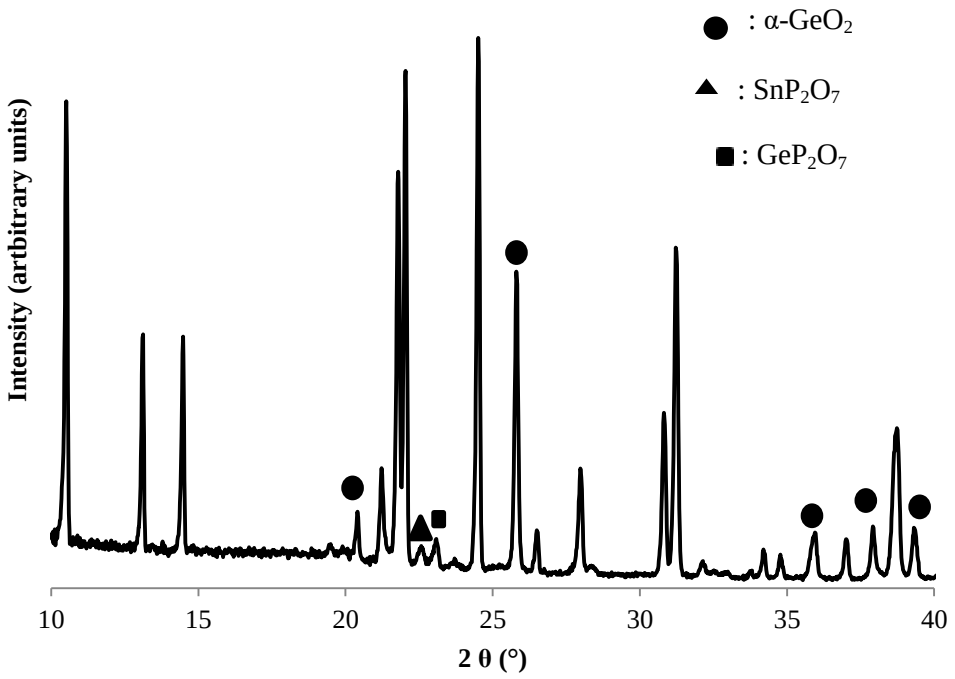

Figure 6-11. The XRD pattern of 5 % [Sn]-doped composition for the assigment of impurities. Unannotated peaks are the main phase. The multiphasic composition includes GeO_2, SnP_2O_7 and GeP_2O_7 impurities.

The impurities within the 5 % and 7 % [Sn]-doped materials suggested that the reaction mixture was not at equilibrium and may need additional firing to gain phase pure materials. Nevertheless, the unit cell parameters for these materials were evaluated as shown in Figure 6-12.

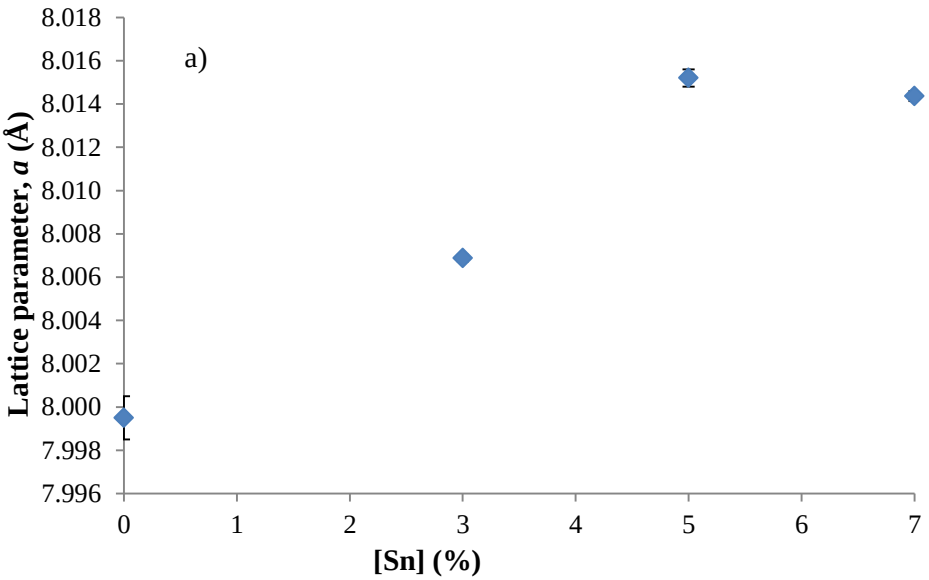
a)
Lattice parameter, a (Å)
8.018
8.016
8.014
8.012
8.010
8.008
8.006
8.004
8.002
8.000
7.998
7.996
0
1
2
3
4
5
6
7
[Sn] (%)

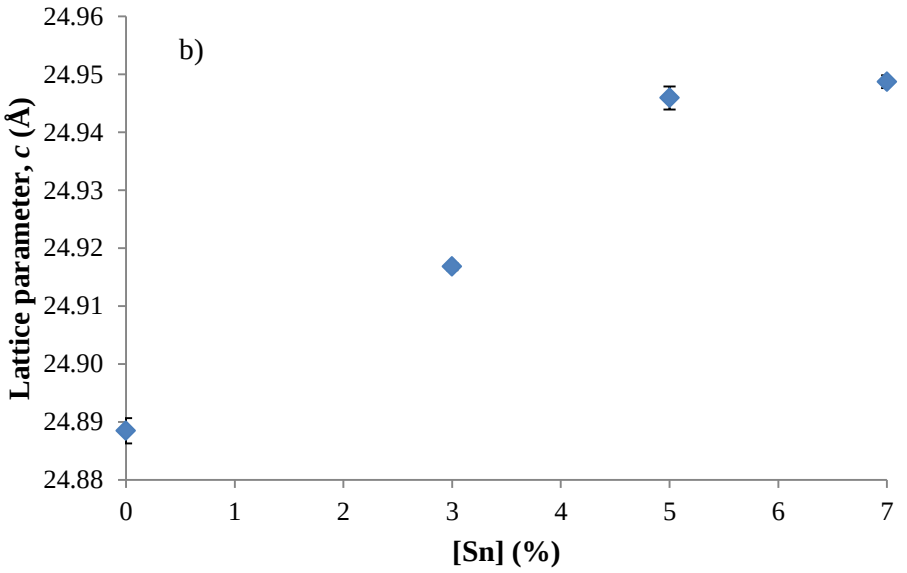
b)
Lattice parameter, c (Å)
24.96
24.95
24.94
24.93
24.92
24.91
24.90
24.89
24.88
0
1
2
3
4
5
6
7
[Sn] (%)

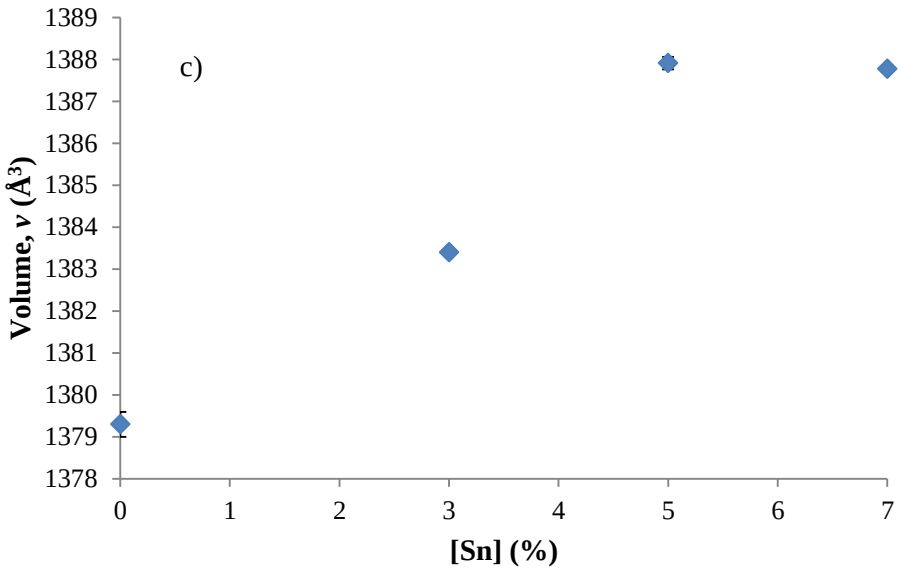

Figure 6-12. A comparison of the unit cell parameters for the stanno-germanophosphates a) shows unit cell parameter, *a* (Å) b) unit cell parameter *c* Å and c) unit cell volume, *V* (Å^3). The graphs show with increasing tin doping there is a general increase in unit cell size.

As can be seen from the unit cell parameters there is an overall increase in unit cell size. This suggested that the Sn^{4+} is successfully doping into the structure. These results showed that the structure is capable of accommodating a mixed Sn and Ge material where Sn occupies the 6-fold coordination state. This is facilitated by the flexibility of Ge to occupy the 4-fold coordination state. This ability to adopt preferred coordination states has also been reported by Leclaire *et al*[18] for the structurally related material silicogermanophosphate, $Ge_3Si_2O(PO_4)_6$. In this material Si preferentially occupies the 4-fold coordination state in a mixed cationic polyhedral material whereas Ge occupies the 6-fold coordination state.

6.3.4 Replacing the phosphorus

6.3.4.1 $Ge_5O(AsO_4)_6$

Arsenic resides below phosphorus within the periodic table. Subsequently, it shares many chemical similarities with phosphorus which include ionic radii, valence electrons and near identical electronegativity and orbital configurations. Most importantly, phosphorus and arsenic both form a 4-fold polyhedron; phosphate (PO_4^{3-}) and arsenate (AsO_4^{-3}). Subsequently, the synthesis of a novel material, $Ge_5O(AsO_4)_6$ was evaluated.

6.3.4.2 Experimental

Stoichiometric amounts of GeO_2 (Sigma Aldrich 99.9999 %) and $NH_4H_2AsO_4$ (Santa Cruz Biotechnology ≥97 %) were ground together. This mixture was then fired at 300 °C for 3 hours and reground using a pestle and mortar. The firing step was performed in a sealed tube furnace with air

passing over the sample to extract any loose Arsenate derivatives. Subsequent to this, the sample was then sealed in platinum foil and placed into an evacuated quartz tube ($4.1x10^{-2}$ mbar) and re-fired at 600 °C for 30 hours. XRD analysis was performed using a Kapton film over the 2θ range 10 ° to 90 °.

6.3.4.3 Results and discussion

The starting regents were white after the initial grinding of the two reactants. After the first calcination step to remove H_2O and NH_3 the mixture turned from a white colour to an orange/brown colour. A comparison of the XRD patterns for the initial calcination step and at 600 °C can be seen in Figure 6-13.

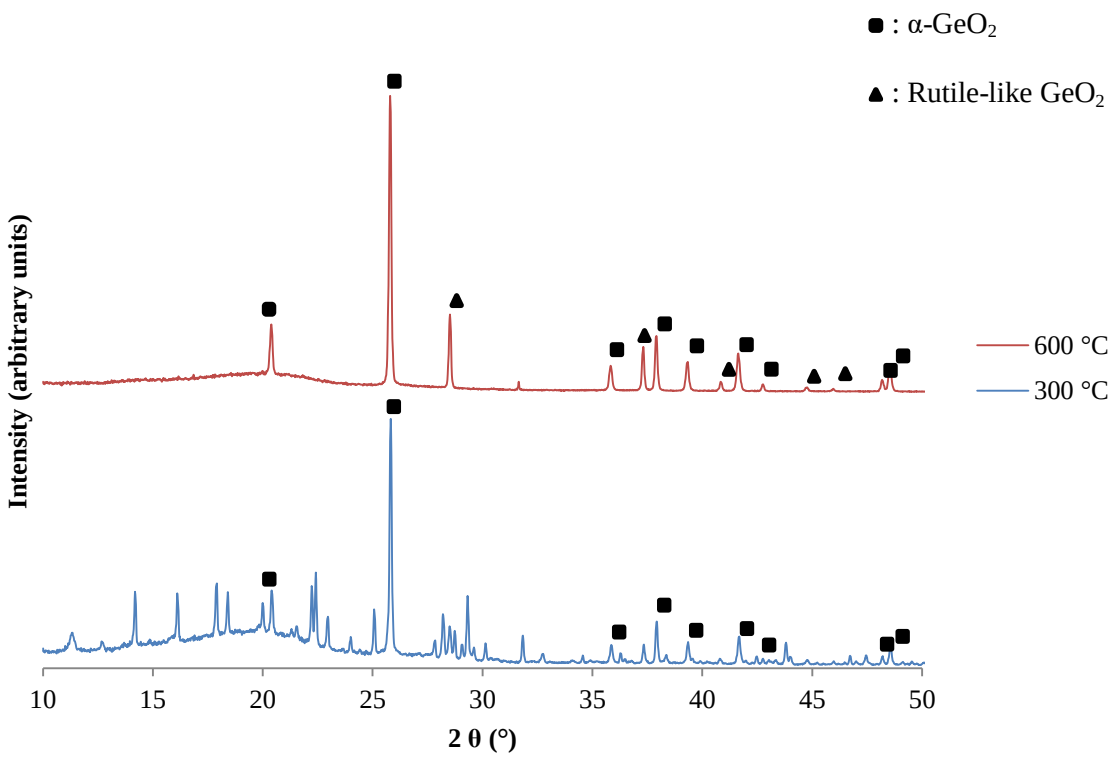

Figure 6-13. Black XRD pattern represents reaction mixture fired for 3 hours at 300 °C. Red XRD pattern represents the reaction mixture fired for 30 hours at 600 °C within sealed evacuated quartz tube.

Both XRD patterns showed an uneven background between the 2θ range of 10-31 ° which is attributed to the sample preparation environment.[*****] The XRD pattern for the initial firing step

[*****] Sample preparation environment involves placing Kapton film over the sample. This causes the uneven background between the 2 θ range of 10-31 °

showed a large number of peaks which corresponded to an arsenate. Unreacted α-GeO_2 has been identified within this material indicated by the most intense peak which suggested a reaction had not taken place. As the temperature increased, the predominant phases that remained in the pattern are α-GeO_2 and rutile-like GeO_2. The latter occurs from the transformation of the metastable high temperature α-GeO_2 to the low temperature rutile-like GeO_2 at 600 °C. The peaks corresponding to the arsenate no longer existed in the pattern which suggested the formation of an amorphous phase or volatilisation of the arsenate species. The latter corroborates with observed themogravimetric data from Helsen *et al*[19] which details the full volatilisation of As_2O_5 at ≈650 °C. Consequently, this appears to be the main inhibitory factor in the formation of $Ge_5O(AsO_4)_6$. Further studies include firing at higher temperatures with larger sample sizes to determine whether there is a gas-solid reaction at these temperatures.

6.3.5 AC impedance

In this section, the electrical properties of $Ge_5O(PO_4)_6$ and related materials were evaluated. This was achieved using manual fit or using an equivalents circuits model (shown in Figure 6-14) for the analysis of each electrochemical process. The identities of the electrochemical processes were defined by their capacitance values. The collection of the data took place between the temperature range of 50-900 °C. Data points were collected at an interval of 50 °C using a ramp rate of 3 °C/min. At each interval there was a dwell of 20 minutes before the measurement was taken. The measurements were taken with AC amplitude of 10 mV with 10 points per decade over the frequency of 8 Mhz – 0.1 Hz in air for all samples.

a)

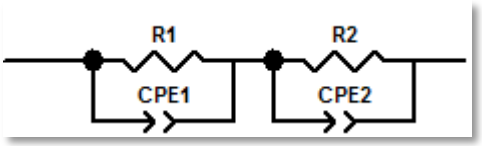

Figure 6-14. Schematic view of equivalent circuits model.

The Nyquist plots for $Ge_5O(PO_4)_6$ at 649 °C and 901 °C can be seen in Figure 6-15.

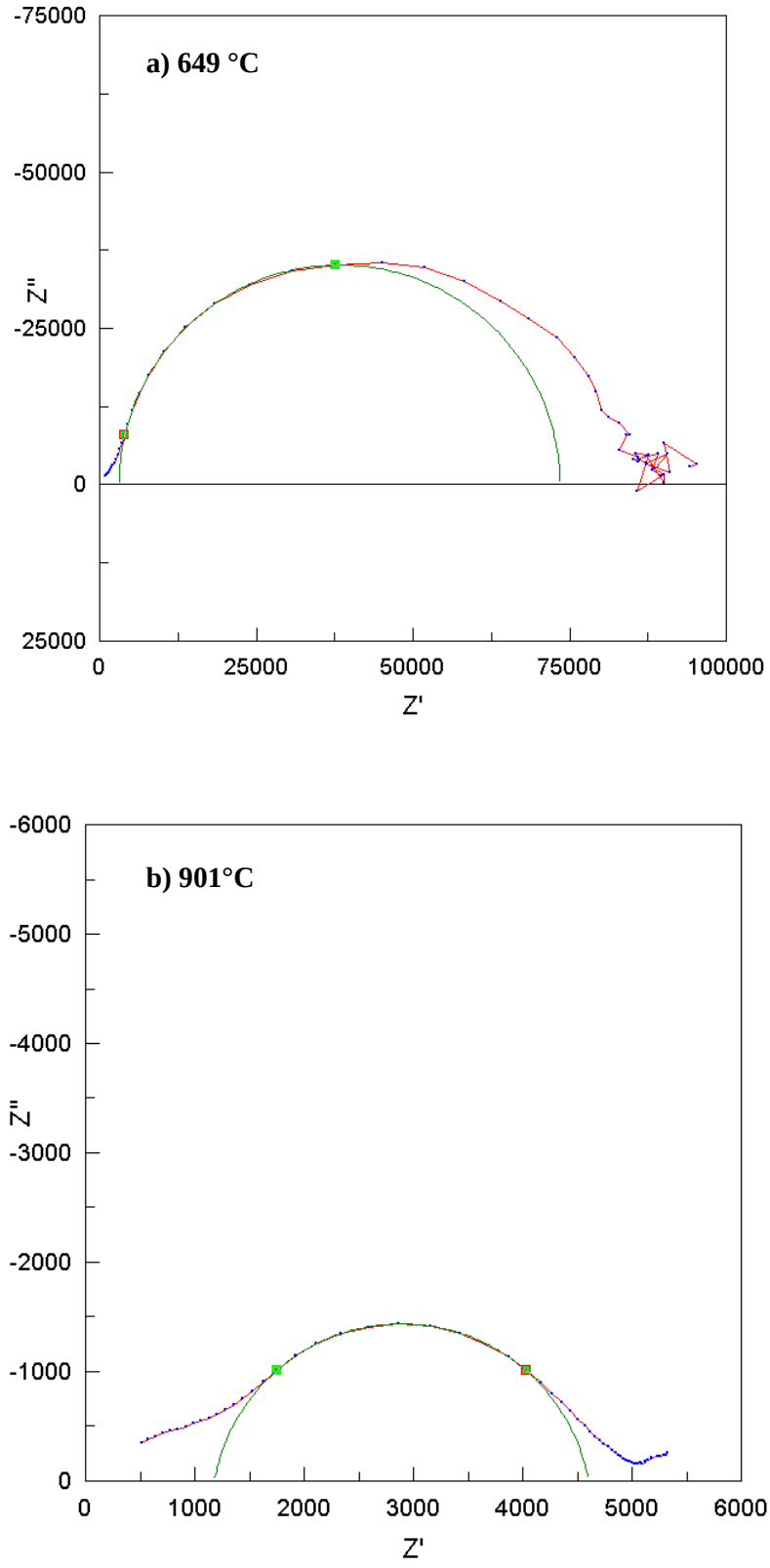

Figure 6-15. Nyquist plot for $Ge_5O(PO_4)_6$ at temperatures a) 650 °C and b) 901 °C.

Due to the relatively low density of the $Ge_5O(PO_4)_6$ pellets (≈82 %) a poorly resolved arc was produced in the complex impedance plot at 649 °C. However, under closer examination of the arc

there appears to be an inflex at higher frequencies. This suggested that there is the occurrence of two electrochemical processes (Figure 6-15). These processes were resolved into the bulk and grain components which were indicated by the characteristic capacitance of ≈ 10^{-12} Fcm^{-1} for the faster bulk conduction process and for the intergrain component ≈ 10^{-10} Fcm^{-1}. It should be noted that there appears to be no indication of an electrode arc at lower frequencies. This is likely to be related to the low density of the sample which causes the intergrain to dominate the spectra at 649 °C. The data above was used to derive an Arrhenius plot for $Ge_5O(PO_4)_6$ as shown in Figure 6-16.

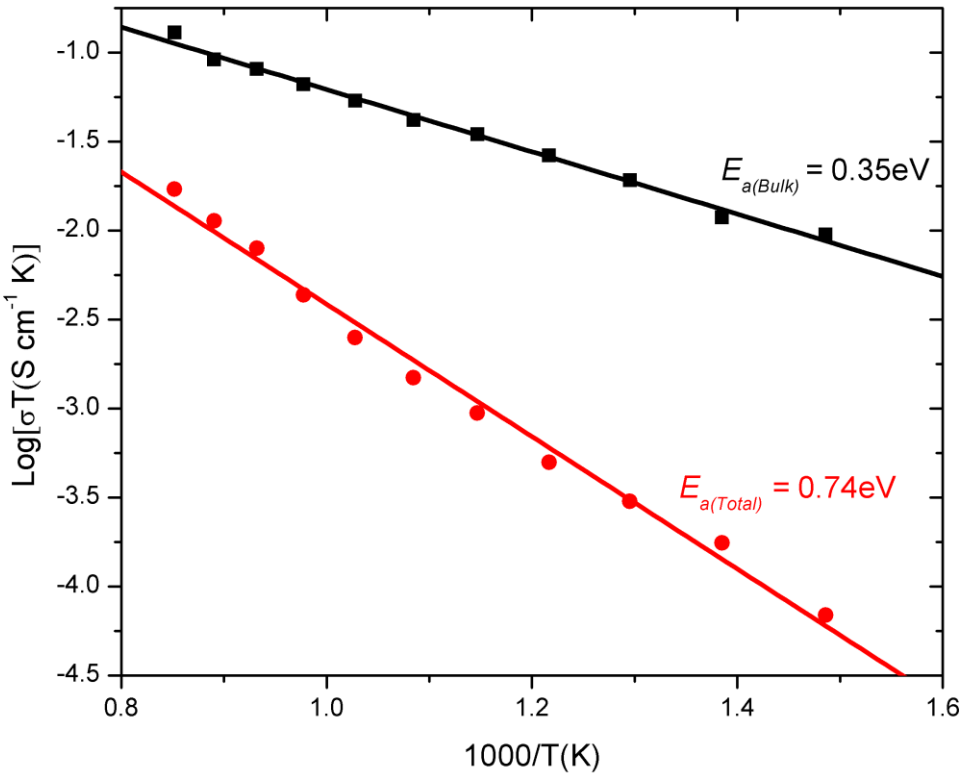

Figure 6-16. Arrhenius plot of the bulk (black) and total (red) conductivities for $Ge_5O(PO_4)_6$ for the temperature range between 350 – 900 °C. Activation is also displayed for each conduction process which is remarkably low when compared to other traditional oxide ion conductors.

In Figure 6-16 an Arrhenius plot of the bulk and total conductivities for this material can be seen. At the highest temperature, the bulk conductivity for $Ge_5O(PO_4)_6$ shows a value of 1.1 x 10^{-4} S cm^{-1} at 901°C while the total conductivity had the value of 1.45 x 10^{-5} S cm^{-1}. The activation energy, E_a, defined by the slope of the Arrhenius plot showed values of 0.35 eV and 0.74 eV for

the bulk and total conduction processes, respectively. This is remarkably low compared to other oxygen conductors such as YSZ, $Ca_{13}Al_{14}O_{33}$ and $La_{9.33}Si_6O_{26}$. This is attributed to the novel oxygen diffusion pathway with less restrictive interactions for oxide mobility. A comparison of conductivity for $Ge_5O(PO_4)_6$ with other well established oxide ion conductors can be seen in Figure 6-17.

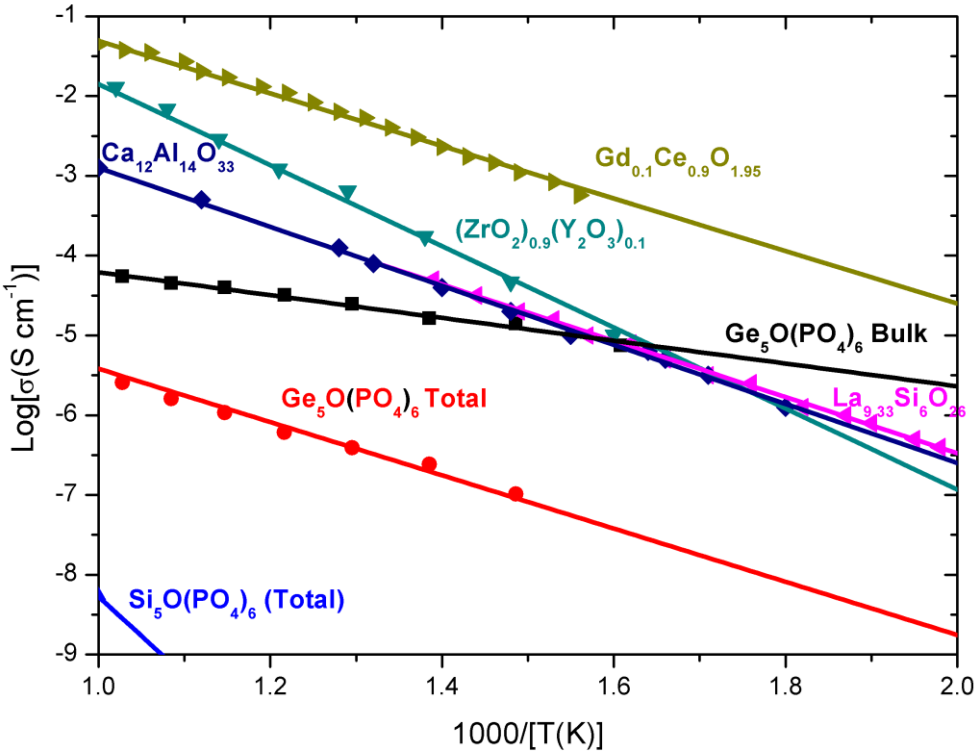

Figure 6-17. A comparison of $Ge_5O(PO_4)_6$ when compared to other well established oxide ion conductors[†††††]. This graph includes the materials $Si_5O(PO_4)_6$[20], $Ca_{12}Al_{14}O_{33}$[21], $(ZrO_2)_{0.9}(Y_2O_3)_{0.1}$[22], $Gd_{0.1}Ce_{0.9}O_{1.95}$[23] and $La_{9.33}Si_6O_{26}$[24].

The plot showed that at the highest temperature the conductivity reported for $Ge_5O(PO_4)_6$ is 1-2 orders of magnitude less than that of $Ca_{12}Al_{14}O_{33}$, $(ZrO_2)_{0.9}(Y_2O_3)_{0.1}$ and $La_{9.33}Si_6O_{25}$ at the highest recorded temperature. At temperatures of ≈350˚C and below, conducting performance is comparable or better than these electrolytes which is attributed to the low activation energy of $Ge_5O(PO_4)_6$. Although, the conducting performance is still lower than $Gd_{0.1}Ce_{0.9}O_{1.95}$, however, the difference is only within 1-1.5 orders of magnitude at the lower temperature ranges. It should also be noted that the isostructural analogue, $Si_5O(PO_4)_6$, represents a significant reduction in conducting performance[11]. This is attributed to the presence of stronger Si-O bonds which require more energy for the mobilisation of oxide ions[11]. In addition to this, the inherent inflexibility of the

[†††††] This graph is modified from Dr. Yaoqing Zhang.

silicon cationic lattice to stabilise mobile oxide ions via local lattice distortions also inhibits oxygen transport within the material. In contrast to this, Ge has been suggested to be flexible in terms of having the ability to more readily adopt various coordination states. Its flexibility has been suggested in the work by Jung *et al*[25] in which mobile oxide ions can be stabilised and mobilised via a germanium 5-fold, trigonal bipyrimidal polyhedron. It appears that a combination of the rigid phosphate lattice and the flexibility of the cationic lattice to accommodate interstitial oxide ions are vital for good conducting performance. This is described in more detail in the previous chapter 5.

6.3.6 Doping of aliovalent and isovalent cation into germanium oxide phosphate

In this section isovalent and aliovalent cations were substituted on the germanium site. The reagents used for these experiments are as follows; GeO_2 (Alfa Aesar, 99.9999 %) and $NH_4H_2PO_4$ (Sigma Aldrich 98+ %), Al_2O_3 (Alfa Aesar, 99.98+ %), Ga_2O_3 (Acros Organics 99.99 + %) and TiO_2. (Alfa Aesar, 99.98 %). These experiments were performed to determine the effect of doping within the structure. Each dopant was added to separate compositions of GeO_2 and $NH_4H_2PO_4$. These mixtures were ground using pestle and mortar and then fired at 180 – 190 °C for 3 hours to drive off NH_3 and H_2O. These materials were fired for 20 hours at 1000 °C with an additional firing at 1100 °C for 4-6 hours. Each firing step required an additional grinding of the material using a pestle and mortar. The substitution of germanium with 2.5 % Al, 2.5 % Ga or 2.5 % Ti was performed. According to PXRD, these materials were single phase materials. The XRD pattern for the Ti-doped material was collected with Kapton film and therefore an uneven background is seen. The XRD patterns for these materials are shown in Figure 6-18.

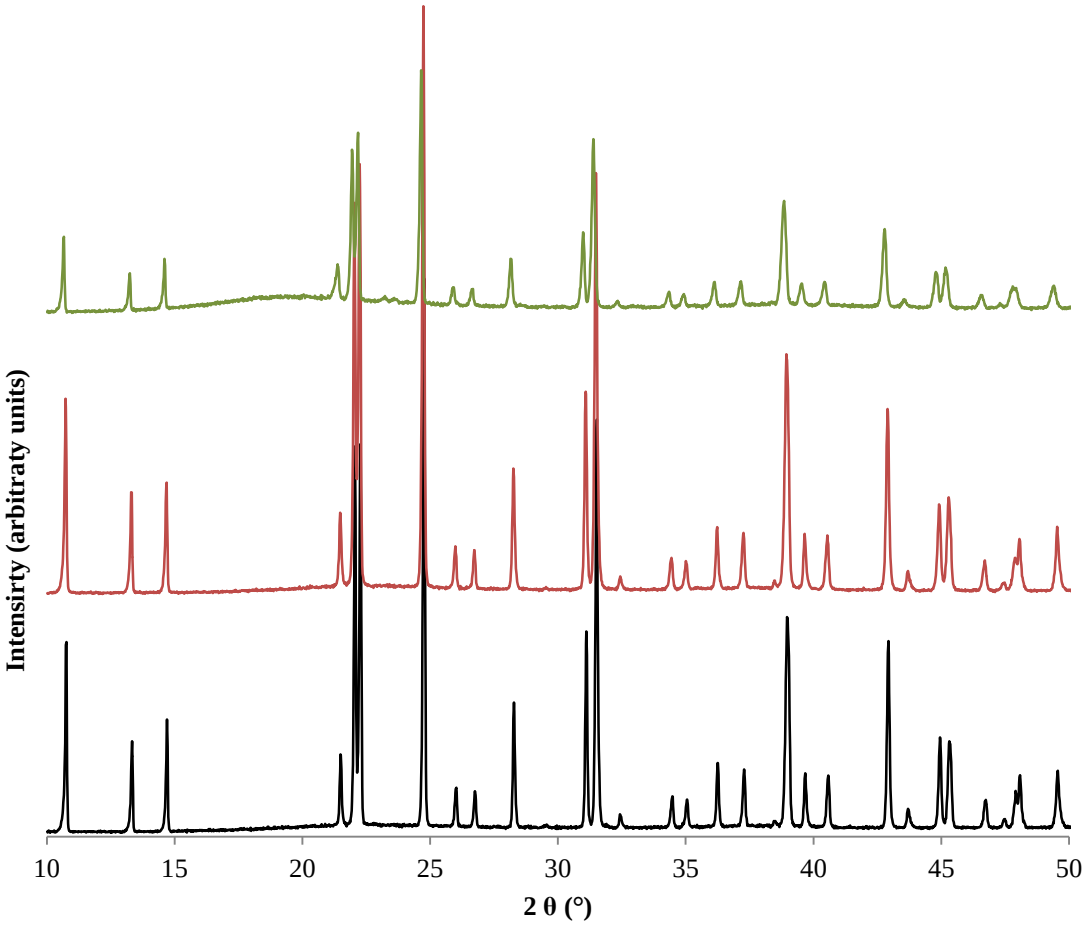

Figure 6-18. XRD patterns' of 2.5 % Ga-doped (black XRD pattern), 2.5 % Al-doped (Red XRD pattern) and 2.5 % Ti (green XRD pattern).

The Nyquist plots for these materials between the temperatures of 650-900 °C are shown in Figure 6-19.

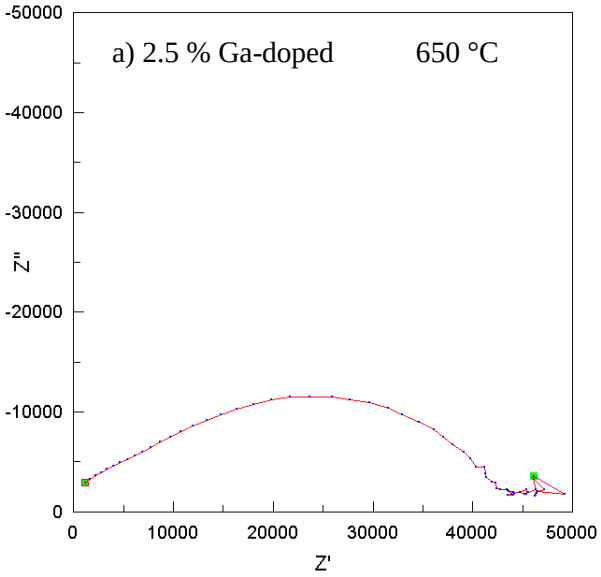
a) 2.5 % Ga-doped
650 °C
-50000
-40000
-30000
-20000
-10000
0
Z''
0
10000
20000
30000
40000
50000
Z'

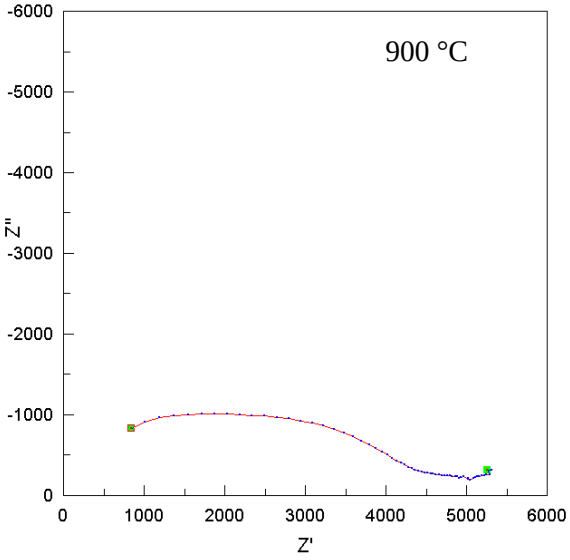
900 °C
-6000
-5000
-4000
-3000
-2000
-1000
0
Z''
0
1000
2000
3000
4000
5000
6000
Z'

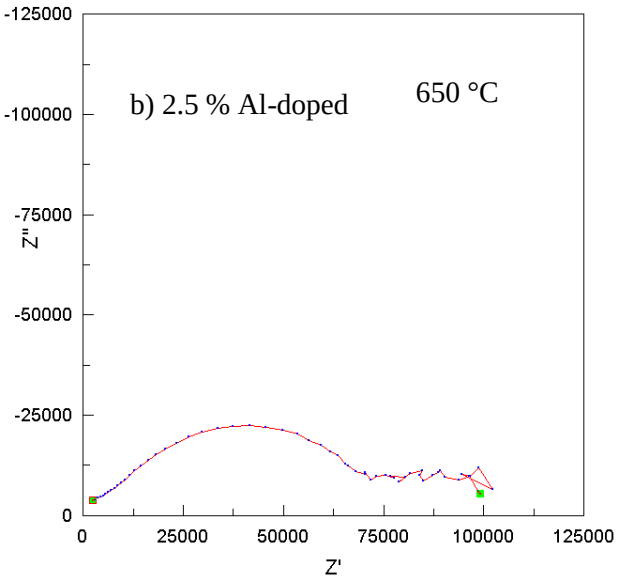
b) 2.5 % Al-doped
650 °C
-125000
-100000
-75000
-50000
-25000
0
Z''
0
25000
50000
75000
100000
125000
Z'

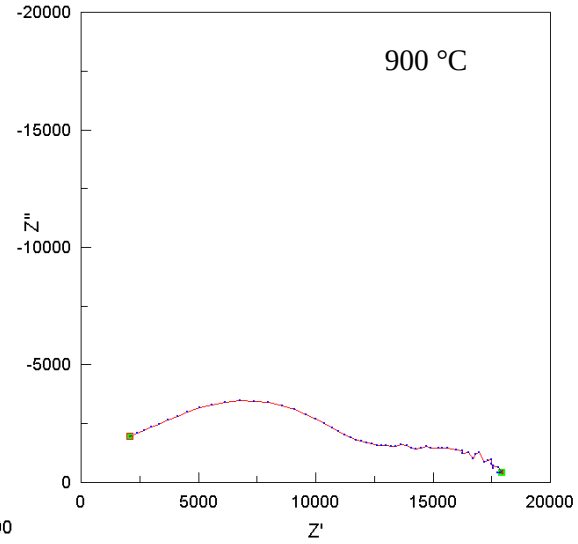
900 °C
-20000
-15000
-10000
-5000
0
Z''
0
5000
10000
15000
20000
Z'

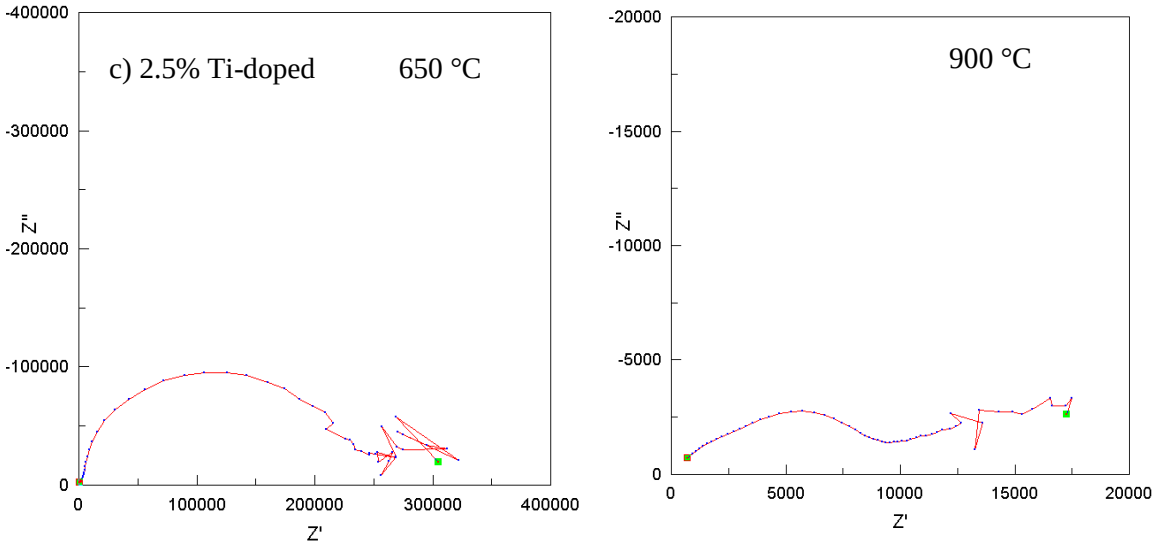

Figure 6-19. The Nyquist plots for the materials a) 2.5 % Ga doped b) 2.5 % Al-doped c) 2.5 % Ti-doped

The Nyquist plots for these materials showed similarities to the parent compound, the electrode response appears to be obscured by the larger intergrain contribution at temperatures of 650 °C. At higher temperature, the low frequency response shows no evidence of a spike. This may suggest that the doping of aliovalent cations may introduce electronic contributions to conductivity. This may be in contrast to the Ti-doped material which may show a spike that is arcing. However, due to the quality of data at low frequencies this is inconclusive.

A comparison of the Arrhenius plots for the doped-$Ge_5O(PO_4)_6$ materials can be seen in Figure 6-20. As can be seen from the 2.5 % Ga-doped material conductivity has improved <0.5 orders of magnitude when compared to the $Ge_5O(PO_4)_6$. The improved conductivity for this sample may be related to the improved sinterability of the material with the addition of Ga. However, the activation energy for the Ga-doped material shows two distinctive differences when compared to the $Ge_5O(PO_4)_6$. These differences include higher activation energy for the bulk conduction process and a change in conduction process at 750 °C. This may be explained by the following: Ga^{3+} introduces oxygen vacancies within the structure. The oxide ion conduction mechanism is proposed to occur via the mobility of an 'excess' oxide ion, however, with the introduction of an oxygen vacancy it could potentially trap mobile oxide ions. To overcome this, additional energy is required to mobilise the oxide ion. The Al-doped material behaves similarly to the Ga-doped material as expected as it is also a +3 cation. The isovalent cation, Ti^{4+}, also represents a minor improvement in oxide ion conductivity, however, there is a small increase in activation energy for the bulk conduction process. The small increase in E_a, may be attributed to a relative inflexibility for Ti^{4+} to mobilise and stabilise oxide ions, however, does not form oxygen vacancies as seen

within the Ga-doped systems. Therefore, in contrast to aliovalent cations there does not appear to be a change with the activation energy at higher temperatures.

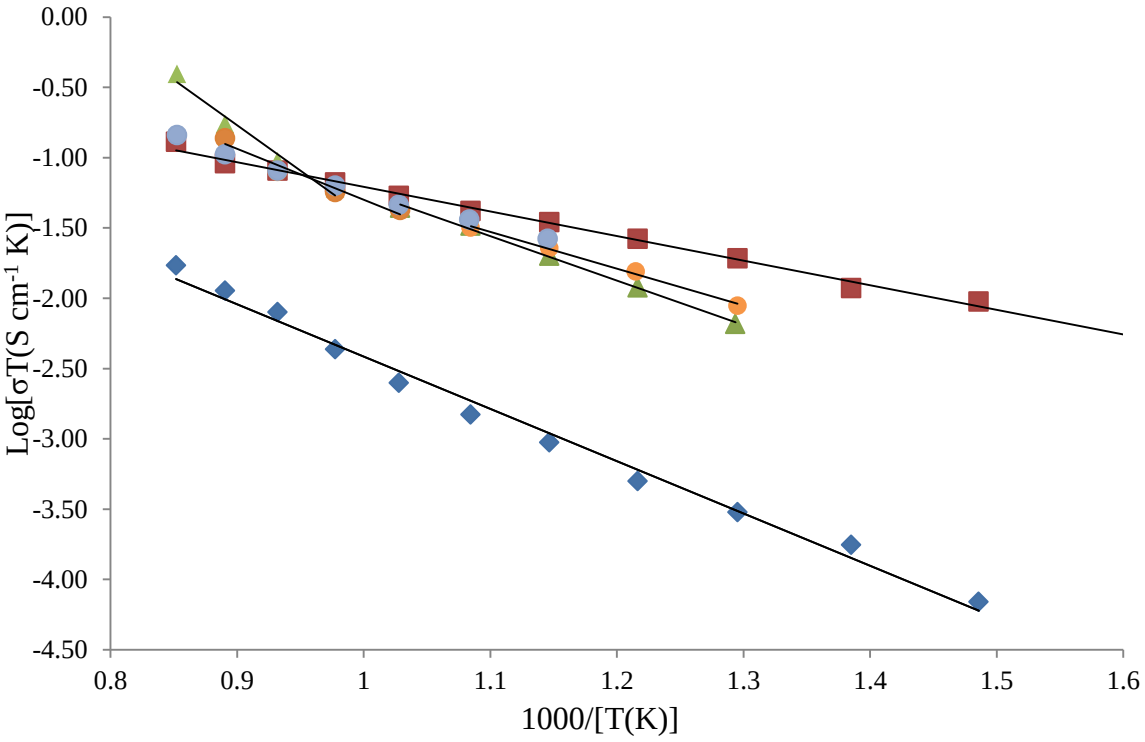

Figure 6-20. A comparison of the materials that were obtained with the doping of aliovalent and isovalent cations. This shows the conduction process for $Ge_5O(PO_4)_6$ total (blue diamond), $Ge_5O(PO_4)_6$ bulk (red square), 2.5 % Ga-doped bulk (green triangle), 2.5 % Al-doped bulk (orange circle) and 2.5 % Ti-doped bulk (blue circle).

Arrhenius plots were also produced for the materials that contained excess phosphorus and germanium with their starting compositions (also shown in section 6.2.1). The XRD patterns for the excess phosphorus materials can be seen in Figure 6-21.

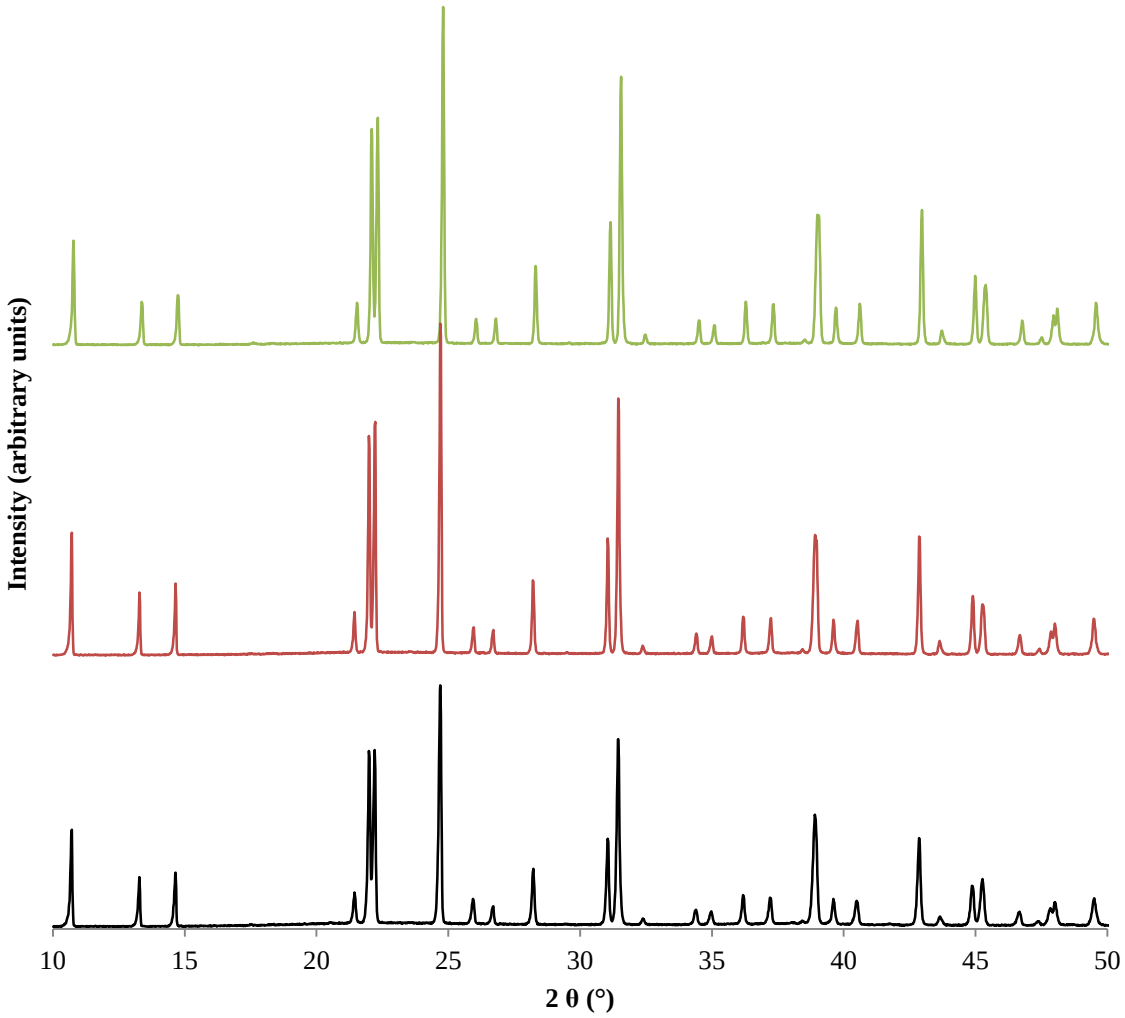

Figure 6-21. The materials synthesised with excess phosphorus content. 2.5 % excess phosphorus/x = 0.15 (Black XRD), 5 % excess phosphorus/x =0.30 (red XRD) and 10 % excess phosphorus/x = 0.6 (green XRD).

The Arrhenius plots for excess phosphorus materials can be seen in Figure 6-22.

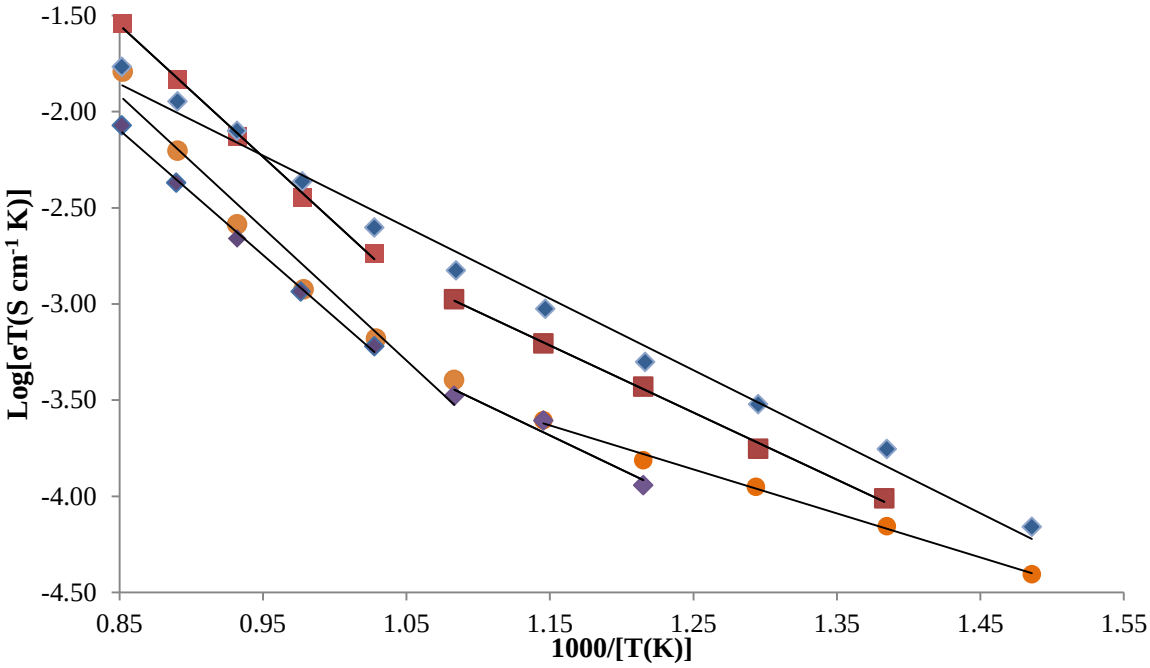

Figure 6-22. Arrhenius plots for excess phosphorus compositions which generally show a large acivation energy and lower conductivity between the temperature range of 500-900 °C for total conductivity. The graph shows the total conduction processes for 2.5 % excess phosphorus (orange circle), 5 % excess phosphorus (purple diamond), 10 % phosphorus excess (red square) and $Ge_5O(PO_4)_6$ (blue diamond).

Due to the poorly resolved arcs, only total conductivity was produced from the excess phosphorus materials. As a result only the total conductivity will be compared to the $Ge_5O(PO_4)_6$ end member. The excess phosphorus materials show a change in the activation energy for the total conduction process. These materials behave similarly at higher temperatures with activation energy being significantly higher between 1.28-1.36 eV. At lower temperatures, the 2.5% excess phosphorus appears to have a lower activation of 0.45 eV when compared to the Ge end member's, 0.74 eV.

For the excess germanium materials, 2.5% germanium excess was single phase. A comparison of total conductivity can be seen in Figure 6-23.

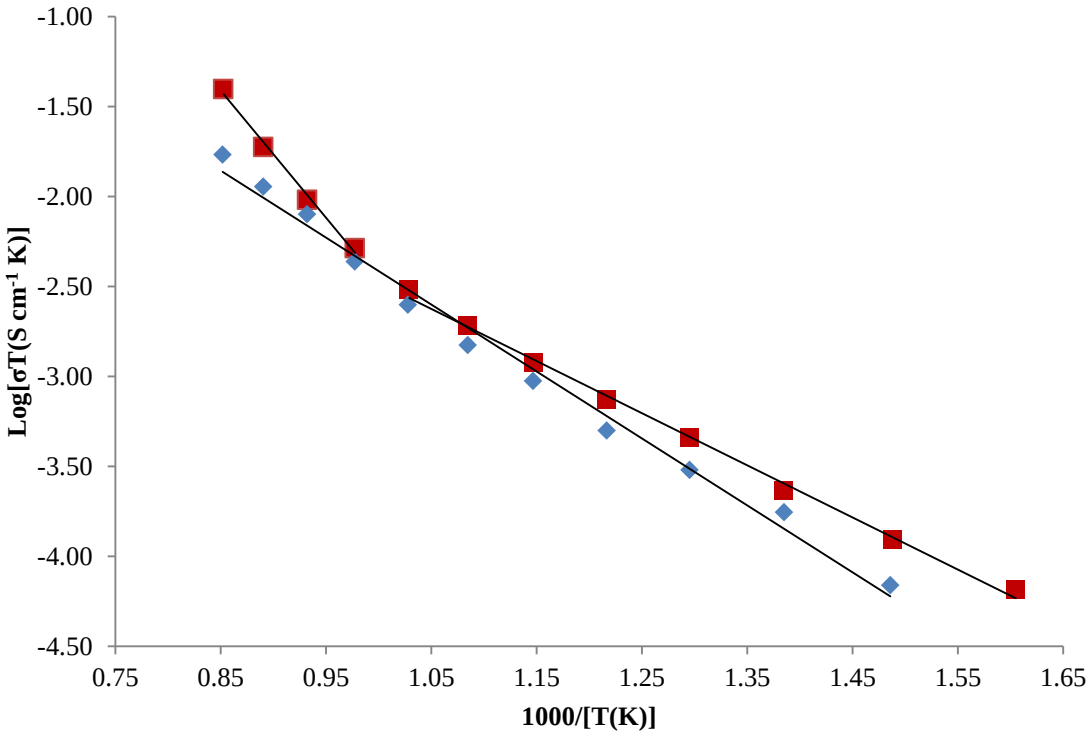

Figure 6-23. Arrhenius plot for total conductivity of excess 2.5 % Ge material/x = 0.125 (red square) compared to the total conductivity of $Ge_5O(PO_4)_6$ (blue diamond).

For this material there appears to be another change in activation energy at 750 °C. The results suggested there is a minor improvement to conductivity for this material when compared to $Ge_5O(PO_4)_6$. There is also a lower activation of 0.57 eV at lower temperatures this quickly rises to a higher value of 1.39 eV at elevated temperatures.

6.4 Conclusion

$Ge_5O(PO_4)_6$ is a novel and promising oxide ion conductor. Its low activation energy is attributed to its distinctive structural features that allow for the propagation of oxide ions through a less restrictive structural lattice.When compared to traditional vacancy oxide ion conductors, activation energy is significantly lower while being comparable to other established interstitial oxide ion conductors.

The distinctive structure allows for various cationic substitutions. Evaluation of possible dopants were performed with the following cations; Si, Sn, Ga, Ti, Al and As. The results suggested that the material does not favour aliovalent cations' as it may introduce oxygen vacancies within the structure which disrupts the mobility of oxide ions. The isovalent cation Ti^{+4}, did not improve conductivity and also increased activation energy which was attributed to a relative inflexibility to accommodate and stabilise mobile oxide ions when compared to the Ge cationic lattice.

The silicogermanophosphate series was synthesised and changes in unit cell parameters suggested that this was successful. The $GeSi_4O(PO_4)_6$ composition contained an impurity related to the structure that was previously reported by Leclaire *et al*[14]. Traditional solid state synthesis of $Ge_5O(AsO_4)_6$ was assessed. The results suggested that the stability of As_2O_5 at intermediate temperatures was an issue in the formation of $Ge_5O(AsO_4)_6$. Higher temperatures may represent a reasonable progression of the synthesis of this material to determine whether there is a gas-solid reaction.

To conclude, AC impedance show that the $Ge_5O(PO_4)_6$ has fast oxide ion conducting properties. More notably, the low activation energy which is attributed to its distinctive structure demonstrates a potential use for intermediate temperature-SOFCs.

Further work includes developing new doped systems and new synthetic routes for these materials for single phase and high density products.

6.5 References

1. Fergus, J. W. Electrolytes for solid oxide fuel cells. *J. Power Sources* **162,** 30–40 (2006).

2. Boivin, J. C. & Mairesse, G. Recent material developments in fast oxide ion conductors. *Chem. Mater.* **10,** 2870–2888 (1998).

3. Inaba, H. & Tagawa, H. Ceria-based solid electrolytes. *Solid State Ionics,* **83,** 1–16 (1996).

4. Malavasi, L., Fisher, C. A. J. & Islam, M. S. Oxide-ion and proton conducting electrolyte materials for clean energy applications: structural and mechanistic features. *Chem. Soc. Rev.* **39,** 4370–4387 (2010).

5. Larson, a C. & Von Dreele, R. B. General Structure Analysis System (GSAS)**,** 86–748 (2004).

6. Toby, B. H. General Structure Analysis System - GSAS / EXPGUI, A Graphical user interface for GSAS. *J. Appl. Cryst.* **34,** 2001 (2001).

7. WinXPOW, S. STOE & Cie GmbH: Darmstadt, Germany, 2004.

8. Mal'shikov, A. E., Egorova, O. V. & Bondar, I.A. Synthesis and Properties of Germanium Phosphate. *Russ. J . Inorg. Chem.* **33,** 722–726 (1988).

9. Liebau, F., Bissert, G. & Köppen, N. Synthese und kristallographische Eigenschaften einiger Phasen im System SiO_2–P_2O_5. *Zeitschrift für Anorg. und Allg. Chemie* **359,** 113–134 (1968).

10. Poojary, D. M., Borade, R. B. & Clearfield, A. Structural characterization of silicon orthophosphate. *Inorganica Chim. Acta* **208,** 23–29 (1993).

11. Zhang, Y. Exploring Novel Functionalities in Oxide Ion Conductors with Excess Oxygen. PhD thesis. (Unversity of St. Andrews, 2011).

12. Mayer, H. & Völlenkle, H. Die Kristallstruktur von $Ge_5O(PO_4)_6$. *Monatshefte für Chemie/Chemical Mon.* **103,** 1560–1571 (1972).

13. Saxin, S. A possible low-intermediate temperature proton conductor based on Silicon Oxide Phosphate. PhD thesis. (Unversity of St. Andrews, 2014).

14. Leclaire, A. & Raveau, B. $Ge_3P_6Si_2O_{25}$: A cage structure closely related to the intersecting tunnel structure $KMo_3P_6Si_2O_{25}$. *J. Solid State Chem.* **75,** 397–402 (1988).

15. Mayer, H. Die Kristallstruktur von $Si_5O(PO_4)_6$. *Monatshefte für Chemie / Chem. Mon.* **105,** 46–54 (1974).

16. Liebau, F. *Structural Chemistry of Silicates: Structure, Bonding, and Classification*. (Springer Berlin Heidelberg, 2012).

17. Dupree, R., Holland, D. & Mortuza, M. G. Six-coordinated silicon in glasses. *Nature*, **328**, 416-417 (1987).

18. Leclaire, A., Monier, J. C. & Raveau, B. A molybdosilicophosphate with an intersecting-tunnel structure which exhibits ion-exchange properties, $AMo_3P_{5.8}Si_2O_{25}$ (A = Rb, Tl). *Acta Crystallogr. Sect. B* **40,** 180–185 (1984).

19. Helsen, L., Van den Bulck, E., Van Bael, M. K., Vanhoyland, G. & Mullens, J. Thermal behaviour of arsenic oxides (As_2O_5 and As_2O_3) and the influence of reducing agents (glucose and activated carbon). *Thermochim. Acta* **414,** 145–153 (2004).

20. Yaoqing Zhang. Exploring Novel Functionalties in Oxide Ion Conductors with Excess Oxygen. PhD thesis. (University of St Andrews, 2011).

21. Lacerda, M., Irvine, J. T. S., Glasser, F. P. & West, A. R. High oxide ion conductivity in $Ca_{12}Al_{14}O_{33}$. *Nature* **332,** 525–526 (1988).

22. Arachi, Y., Sakai, H., Yamamoto, O., Takeda, Y. & Imanishai, N. Electrical conductivity of the ZrO_2-Ln_2O_3 (Ln=lanthanides) system. *Solid State Ionics* **121,** 133–139 (1999).

23. Huang, K., Feng, M. & Goodenough, J. B. Synthesis and electrical properties of dense $Ce_{0.9}Gd_{0.1}O_{1.95}$ ceramics. *J. Am. Ceram. Soc.* **81,** 357–362 (1998).

24. Béchade, E. *et al.* Synthesis of lanthanum silicate oxyapatite materials as a solid oxide fuel cell electrolyte. *J. Eur. Ceram. Soc.* **28,** 2717–2724 (2008).

25. Jung, H. *et al.* $Sr_2(Mg_{1-x}Ga_x)Ge_2O_{7+0.5x}$: Melilite-type oxygen ionic conductor associated with fivefold coordinated germanium and gallium. *J. Power Sources* **275,** 884–887 (2015).

7 Conclusions

The work in this project involves the synthesis and investigation of properties of $Ge_5O(PO_4)_6$ and related materials. This includes the study of the synthesis of the parent composition using the traditional solid state method, thermal properties, structural studies, electrical studies and doping studies.

$Ge_5O(PO_4)_6$ was successfully synthesised using the traditional solid state method with the starting materials GeO_2 and $NH_4H_2PO_4$. Consistency was an issue with the formation of $Ge_5O(PO_4)_6$ but through the use of variable temperature X-ray diffraction it appears that the key to synthesis of the material resided within a very narrow firing temperature. VT-XRD showed when the material was fired past the melting temperature of GeO_2 it forms amorphous GeO_2 which appears to be stable against the formation of $Ge_5O(PO_4)_6$. It was shown that by controlling the ramp rate and starting source of germanium, $Ge_5O(PO_4)_6$ may be synthesised by the traditional ceramic method. The thermal properties of $Ge_5O(PO_4)_6$ were also examined using VT-XRD. These results showed that the material has anisotropic NTE along the *c*-axis with temperature. This has been related to the porous structure of the material which has large cavities aligned along the *c*-axis. As temperature increases there is rotation and counter rotation of polyhedra which then occupy this space and reduce the overall volume of the unit cell.

The ability for the host structure to accept a variety of dopants was evaluated. The results showed that there is a solid solution between the Si and Ge end members. The change in unit cell parameters occurs in a stepwise fashion due to silicon's preference to enter the di-tetrahedral subunit at lower dopant concentrations. A larger decrease in unit cell size was seen with higher Si dopant levels because there is the replacement of ideal GeO_6 octahedra with distorted SiO_6 octahedra. The Stannogermanophoshate series was evaluated and showed that tin enters the structure as there is a clear increase in unit cell size. Electrical properties for $Ge_5O(PO_4)_6$ showed that the material had high oxide ion conducting properties at temperatures below ~350 °C. The Ga, Al and Ti doped structures were synthesised and their electrical properties were tested using AC impedance. The results showed that these materials did not improve conducting properties when compared to $Ge_5O(PO_4)_6$,. However, they gave an insight into how the cationic dopants affected the material.

NPD provided experimental data that detailed an oxide ion conduction mechanism in relation to the materials structural properties. The 'excess' oxide ion which is situated on the 0,0,0.5 site (Wyckoff position : 3b) was determined to be the most mobile oxide ion with the largest isotropic thermal parameters of 1.25-9.02 $Å^2$ over the temperature range 300-1073 K . Its location within the structure (not part of the phosphate lattice) allows for the generation of mobile oxide ions. Isotropic

thermal parameters for the germanium atoms also showed high values. This suggested that the germanium lattice may offer a flexible cationic lattice for the propagation of oxide ions through the structure. Germanium within the Ge_2O_7 subunit showed the highest U_{iso}. This was attributed to local lattice distortions of the Ge_2O_7 subunit to form an inverted GeO_4 tetrahedron to stabilise oxide ions within the cavities. Fourier difference calculations gave an insight into the location of possible interstitial sites and a structural model was produced with the key positive neutron densities which showed an occupancy value between 0.30-0.101.

NPD was also performed on the isostructural material $Si_5O(PO_4)_6$. This data suggested that the structural has an intrinsic ability to produce mobile oxide ions with temperature. Similarly, this was determined via the high U_{iso} value of the oxygen on the 3b site. However, the materials poor oxide ion conductivity may be related to the relatively rigid silicon cationic lattice. This was linked to the shorter and stronger Si-O bonds when compared to the Ge-O bonds.

In addition to this, a comparison of the bond length and angles of the $Si_5O(PO_4)_6$ and $Ge_5O(PO_4)_6$ was performed. These results showed that despite similarities within the average structure of the materials there were significant differences in the local structures. This arises in the form of largely distorted SiO_6 octahedra when compared to the GeO_6 octahedra at room temperature.

8 Suggestions for future work

In this thesis experimental evidence has been provided for an oxide ion conduction mechanism. This was performed to provide a platform for the future development of the material. More studies are required to further establish and provide additional details on the conduction pathway. These details may be derived from atomistic modelling techniques. Further studies for this work include the exchange of Si for Ge to determine an optimised mixed Ge and Si system to increase the flexibility of the silicate structure. This would be performed to provide supporting evidence of the intrinsic flexibility of the Ge lattice to improve conductivity. In addition to this, finding an optimised Si:Ge ratio that maintains good oxide ion conducting properties would be beneficial from a cost point of view of replacing germanium. Additionally, work on the effect the silicon cationic lattice would beneficial. For example if a stepwise increase in silicon content within the structure causes a stepwise decrease in oxide ion conductivity, Furthermore, the effect of the octahedra sites and tetrahedra on oxide ion conductivity may be explored.

This could give further insight into the role of the cationic lattice for the stabilisation and the mobilisation of mobile oxide ions. NPD data of $Si_5O(PO_4)_6$ suggests that the materials with the M_2O_7 subunit may have an intrinsic ability to form mobile oxide ions. This structural motif is seen in other materials such as $Ge_3Si_2O(PO_4)_6$ belonging to the *P-31c* crystal system and $AMo_3P_6Ge_2O_{25}$

(A = K , Rb, Tl, Cs)[1]. Neutron studies on these material can help support the current conclusion that the “excess” oxide ion hosted in this local structure is responsible for high oxide ion conductivity within the $Ge_5O(PO_4)_6$ and further the understanding of how the cationic lattice is important to this property.

APPENDIX 1A DIFFERENCE PLOTS

300 K

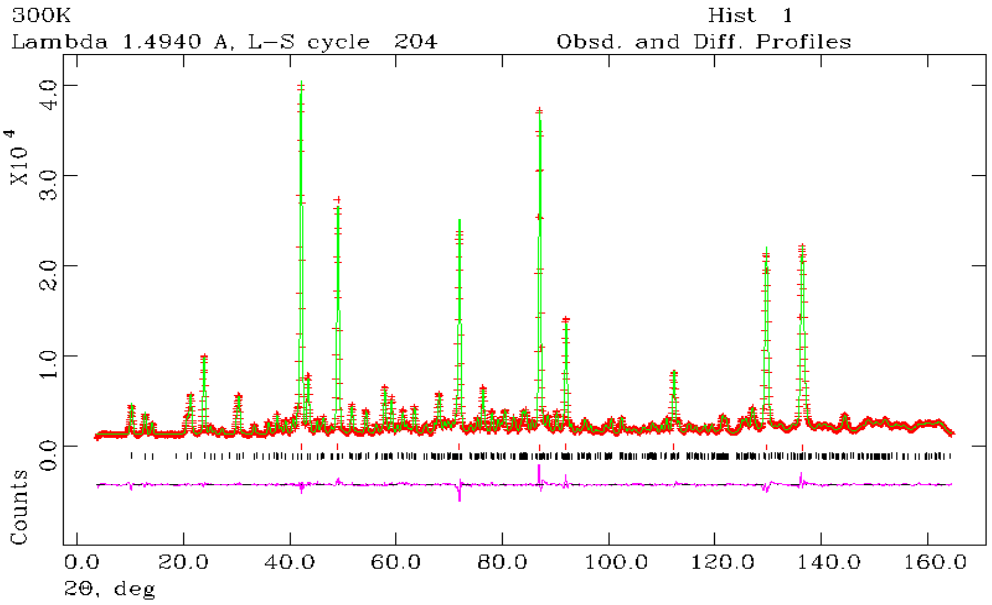

573 K

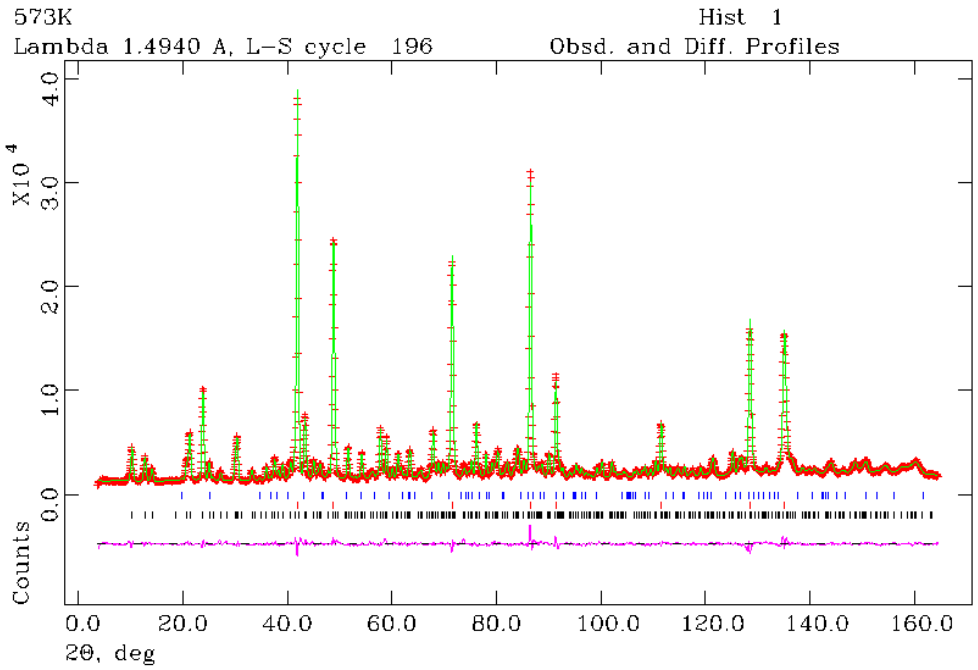

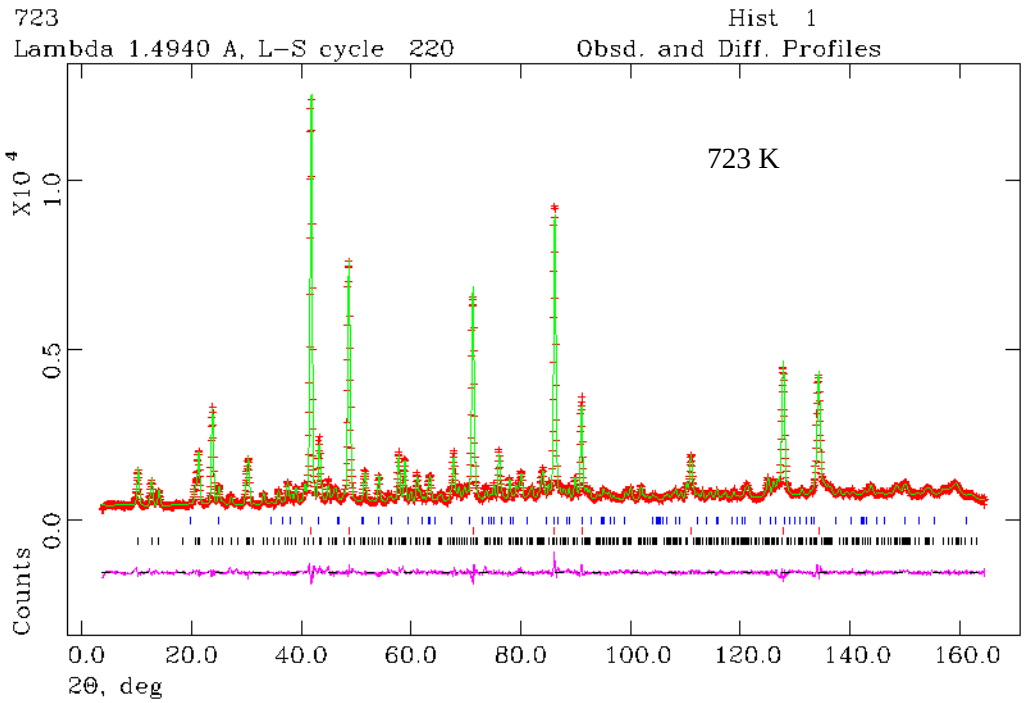
723
Hist 1
Lambda 1.4940 A, L-S cycle 220
Obsd. and Diff. Profiles
723 K
X10 4
1.0
0.5
0.0
Counts
0.0
20.0
40.0
60.0
80.0
100.0
120.0
140.0
160.0
2θ, deg

873 K

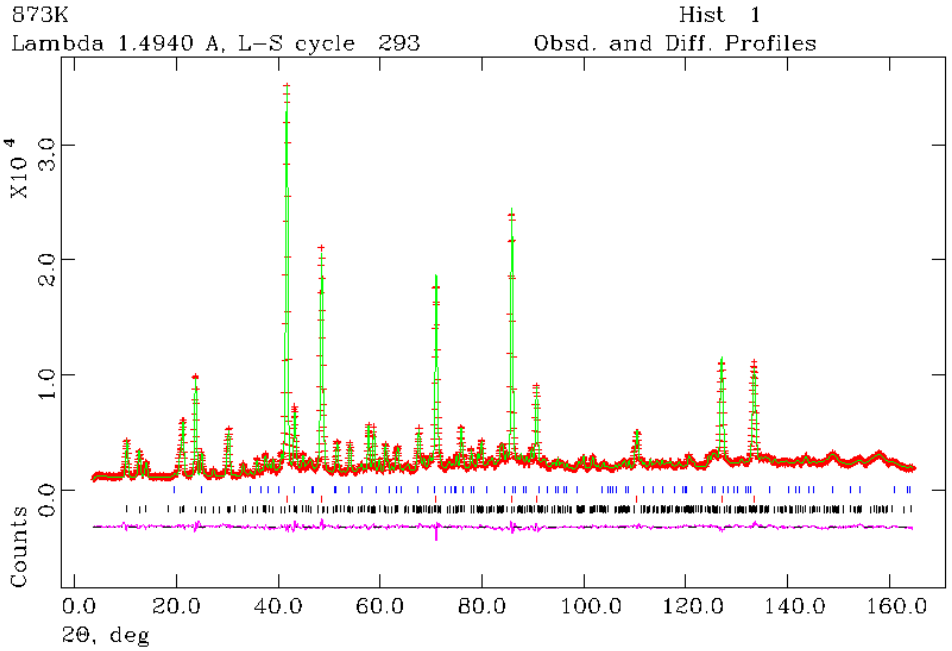
873K
Hist 1
Lambda 1.4940 A, L-S cycle 293
Obsd. and Diff. Profiles
X10 4
3.0
2.0
1.0
0.0
Counts
0.0
20.0
40.0
60.0
80.0
100.0
120.0
140.0
160.0
2θ, deg

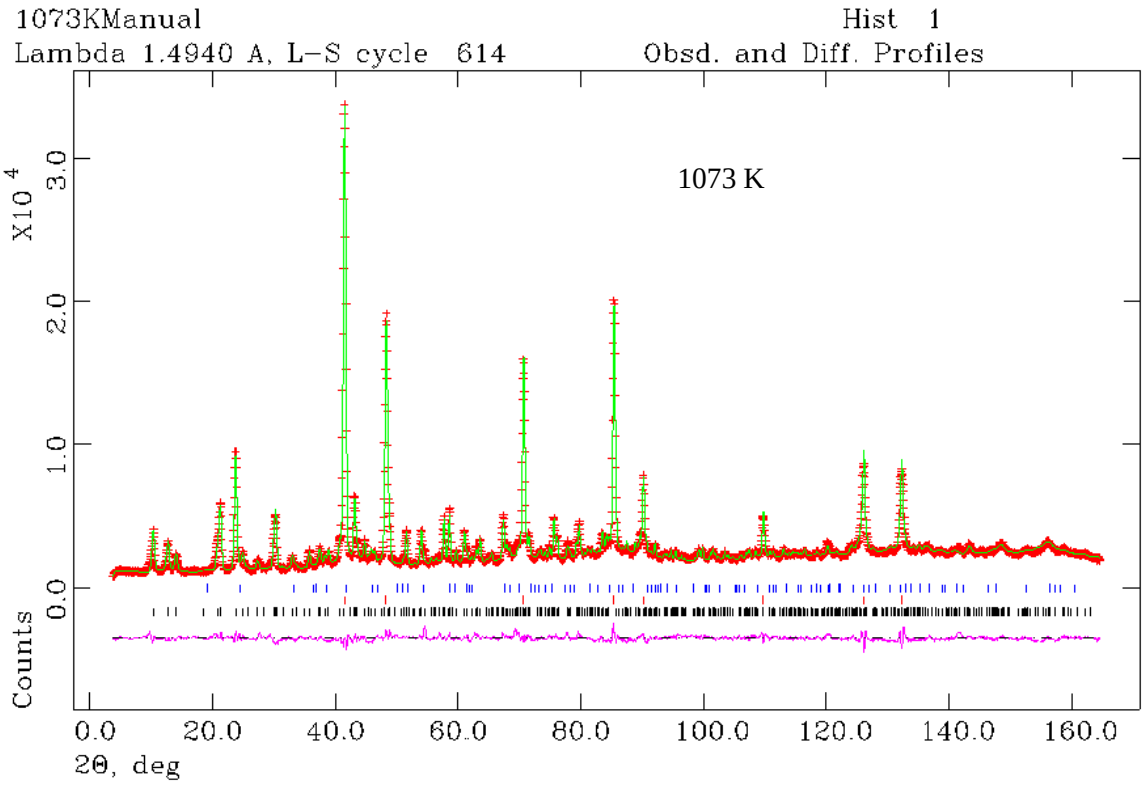

APPENDIX 1B MODEL FOR GERMANIUM ANALOUGE

Average structural models are presented below for $Ge_5O(PO_4)_6$. The refinement was performed by refining atomic coordinates, peak profiles (using Pseudo Voight function), and atomic displacement factors (U_{iso}). Fractional occupancy for each atom was held at 1.

Atom	Wyckoff position	X	Y	Z	U_{iso} x 100 (Å^2)
300 K					
Ge(1)	3a	0	0	0	0.40(10)
Ge(2)	6c	0	0	0.17730(15)	0.12(7)
Ge(3)	6c	0	0	0.43224(15)	0.37(9)
P	18f	0.2901(5)	0.2687(4)	0.09080(16)	0.32(8)
O(1)	3b	0	0	0.5	1.25(18)
O(2)	18f	0.1320(6)	0.2209(6)	0.13293(14)	0.93(7)
O(3)	18f	0.2204(5)	0.1433(5)	0.04097(15)	0.37(8)
O(4)	18f	0.3630(5)	0.4815(4)	0.07321(15)	0.54(7)
O(5)	18f	0.4550(4)	0.2484(5)	0.11278(11)	0.38(7)

Atom	Wyckoff position	X	Y	Z	U_{iso} x 100 (Å^2)
573 K					
Ge(1)	3a	0	0	0	1.32(15)
Ge(2)	6c	0	0	0.17749(19)	0.72(9)
Ge(3)	6c	0	0	0.43227(18)	0.84(10)
P	18f	0.2901(7)	0.2727(7)	0.09020(23)	1.14(11)
O(1)	3b	0	0	0.5	3.20(33)
O(2)	18f	0.1317(8)	0.2201(9)	0.13390(23)	2.26(12)
O(3)	18f	0.2208(8)	0.1460(7)	0.04177(24)	1.44(11)
O(4)	18f	0.3648(7)	0.4832(7)	0.07411(23)	1.74(11)
O(5)	18f	0.4551(6)	0.2525(6)	0.11241(14)	0.82(10)

Atom	Wyckoff position	X	Y	Z	U_{iso} x 100 (Å^2)
723 K					
Ge(1)	3a	0	0	0	1.43(21)
Ge(2)	6c	0	0	0.17846(26)	0.97(13)
Ge(3)	6c	0	0	0.43195(29)	1.85(17)
P	18f	0.2874(9)	0.2693(8)	0.09047(31)	1.30(14)
O(1)	3b	0	0	0.5	3.43(43)
O(2)	18f	0.1273(10)	0.2185(10)	0.13383(25)	2.18(15)
O(3)	18f	0.2179(9)	0.1449(8)	0.04138(28)	1.14(13)
O(4)	18f	0.3606(8)	0.4808(8)	0.07395(29)	1.64(13)
O(5)	18f	0.4536(8)	0.2571(8)	0.11241(18)	1.03(13)

Atom	Wyckoff position	X	Y	Z	U_{iso} x 100 (Å^2)
873 K					
Ge(1)	3a	0	0	0	1.44(16)
Ge(2)	6c	0	0	0.17754(22)	0.95(9)
Ge(3)	6c	0	0	0.43251(23)	1.85(13)
P	18f	0.2825(9)	0.2668(9)	0.09086(31)	2.32(14)
O(1)	3b	0	0	0.5	4.07(38)
O(2)	18f	0.1310(9)	0.2199(9)	0.13508(25)	2.86(14)
O(3)	18f	0.2211(10)	0.1466(10)	0.04180(29)	2.78(15)
O(4)	18f	0.3590(11)	0.4814(9)	0.07393(32)	3.50(15)
O(5)	18f	0.4506(9)	0.2510(10)	0.11035(21)	2.63(14)

Atom	Wyckoff position	X	Y	Z	U_{iso} x 100 ($Å^2$)
1073 K					
Ge(1)	3a	0	0	0	1.05(22)
Ge(2)	6c	0	0	0.17945(34)	1.45(15)
Ge(3)	6c	0	0	0.43181(32)	2.53(21)
P	18f	0.2835(10)	0.2686(9)	0.0908(4)	1.69(14)
O(1)	3b	0	0	0.5	9.02(101)
O(2)	18f	0.1310(13)	0.2146(11)	0.13433(31)	3.10(20)
O(3)	18f	0.2260(10)	0.1536(11)	0.04111(33)	2.96(23)
O(4)	18f	0.3547(14)	0.4836(11)	0.07436(40)	4.55(24)
O(5)	18f	0.4536(11)	0.2556(12)	0.10979(27)	2.86(20)

APPENDIX 1C DIFFERENCE PLOTS FOR SILICON ANALOUGE

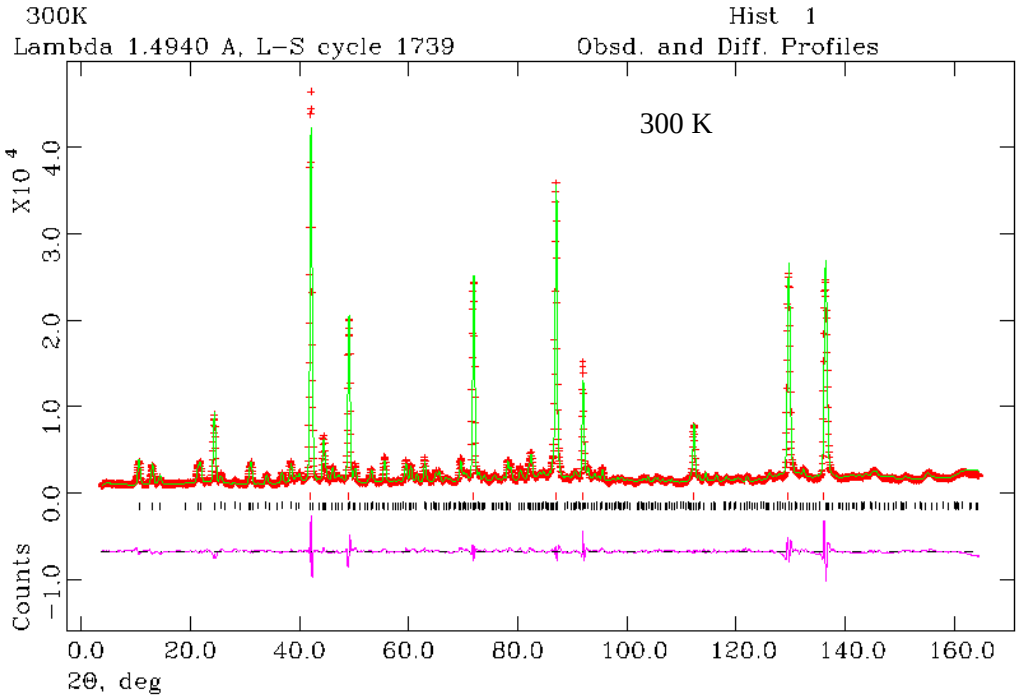

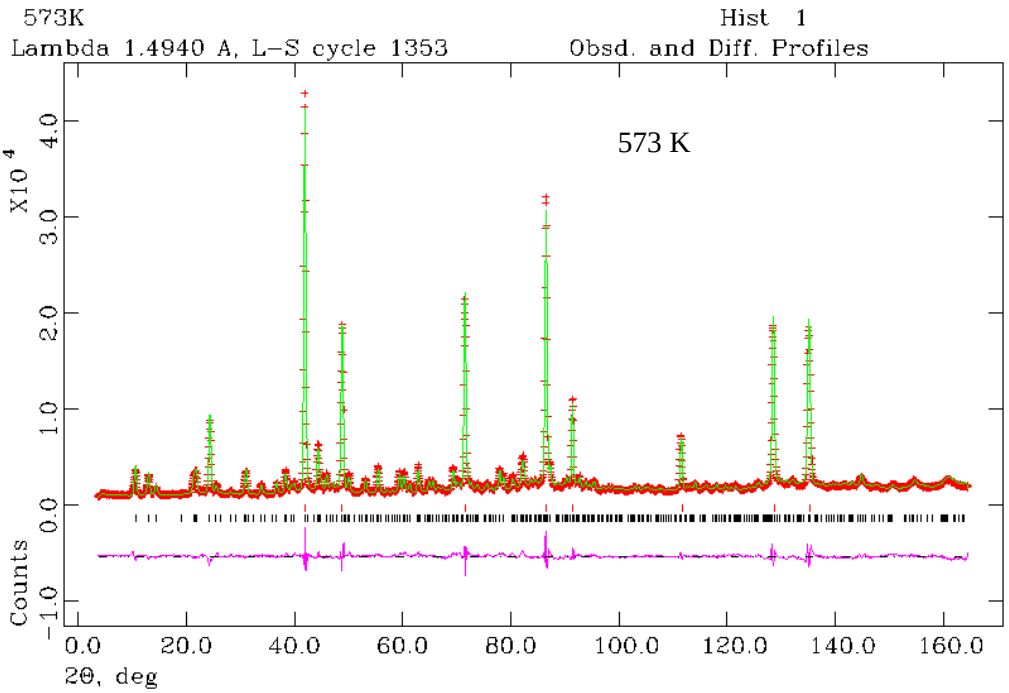
573K
Hist 1
Lambda 1.4940 A, L-S cycle 1353
Obsd. and Diff. Profiles
573 K
X10 4
4.0
3.0
2.0
1.0
0.0
-1.0
Counts
0.0
20.0
40.0
60.0
80.0
100.0
120.0
140.0
160.0
2θ, deg

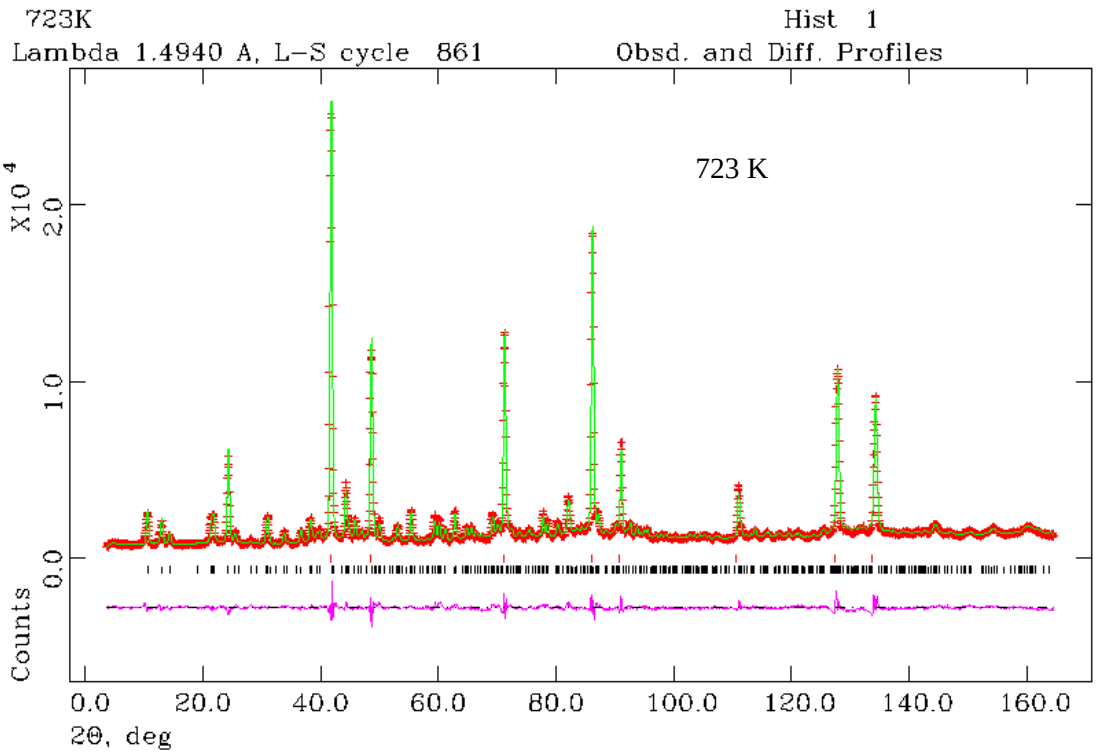
723K
Hist 1
Lambda 1.4940 A, L-S cycle 861
Obsd. and Diff. Profiles
723 K
X10 4
2.0
1.0
0.0
Counts
0.0
20.0
40.0
60.0
80.0
100.0
120.0
140.0
160.0
2θ, deg

873 K

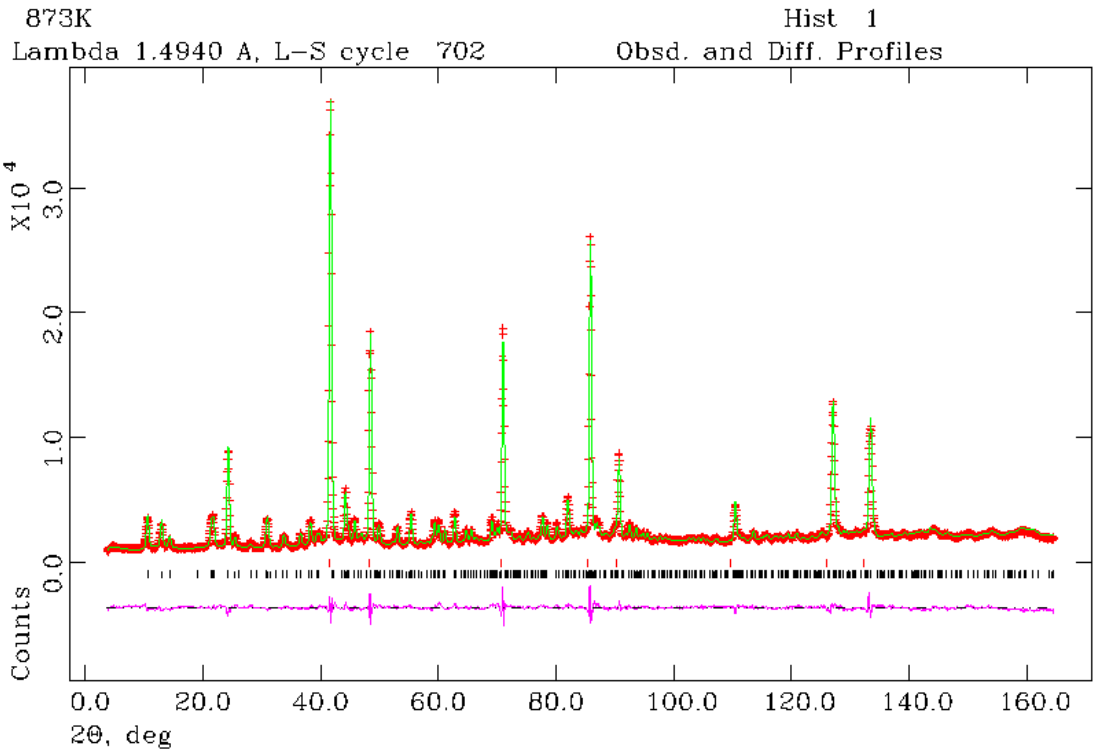
873K
Hist 1
Lambda 1.4940 A, L-S cycle 702
Obsd. and Diff. Profiles
X10 4
3.0
2.0
1.0
0.0
Counts
0.0
20.0
40.0
60.0
80.0
100.0
120.0
140.0
160.0
2θ, deg

1073 K

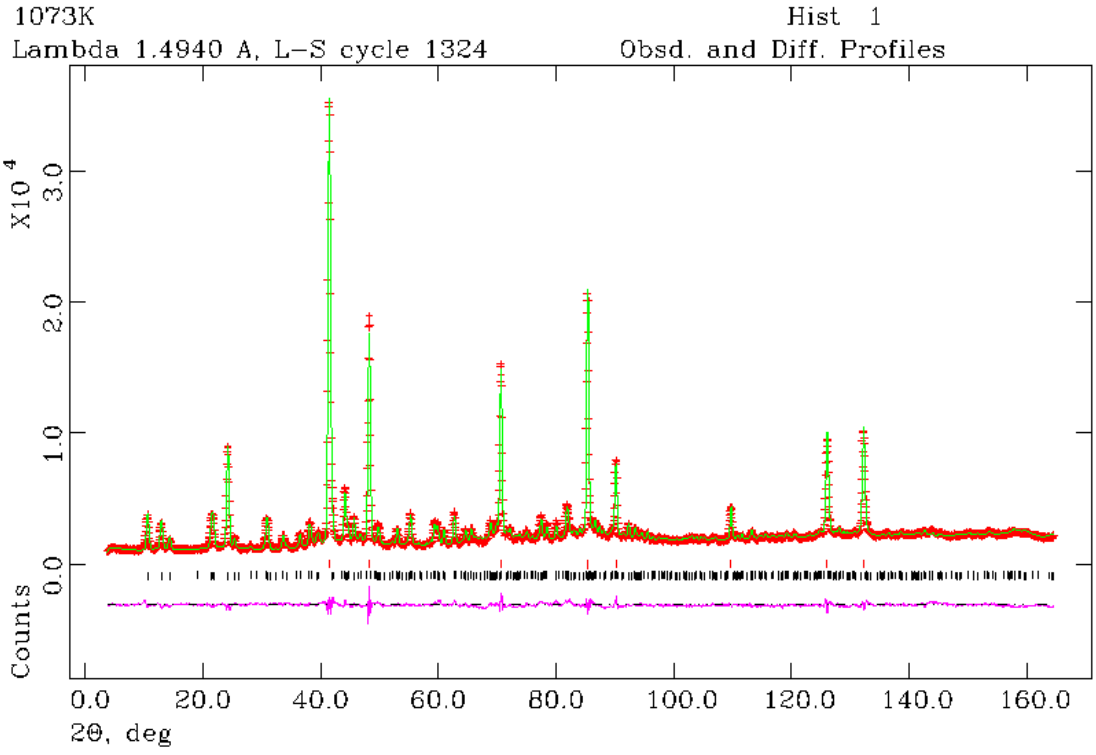
1073K
Hist 1
Lambda 1.4940 A, L-S cycle 1324
Obsd. and Diff. Profiles
X10 4
3.0
2.0
1.0
0.0
Counts
0.0
20.0
40.0
60.0
80.0
100.0
120.0
140.0
160.0
2θ, deg

APPENDIX 1D MODEL FOR SILICON ANALOUGE

The refinement was performed by refining atomic coordinates, peak profiles (using Pseudo Voight function), and atomic displacement factors (U_{iso}). Fractional occupancy for each atom was held at 1. The modelling of the steel holder was performed using the Le bail fit.

Atom	Wyckoff position	X	Y	Z	U_{iso} x 100 (Å^2)
300 K					
Si(1)	3a	0	0	0	0.81(40)
Si(2)	6c	0	0	0.1846(8)	1.20(26)
Si(3)	6c	0	0	0.4378(6)	1.36(36)
P	18f	0.2844(11)	0.2695(10)	0.0913(4)	1.36(14)
O(1)	3b	0	0	0.5	2.95(46)
O(2)	18f	0.1342(12)	0.2150(12)	0.13639(30)	2.08(15)
O(3)	18f	0.2137(11)	0.1430(12)	0.03903(35)	2.31(19)
O(4)	18f	0.3522(12)	0.4841(10)	0.07688(38)	2.29(15)
O(5)	18f	0.4617(11)	0.2594(12)	0.11096(31)	2.19(15)

Atom	Wyckoff position	X	Y	Z	U_{iso} x 100 (Å^2)
573 K					
Si(1)	3a	0	0	0	0.9(5)
Si(2)	6c	0	0	0.1812(9)	2.8(4)
Si(3)	6c	0	0	0.4362(7)	2.4(4)
P	18f	0.2844(11)	0.2697(10)	0.0914(4)	1.65(15)
O(1)	3b	0	0	0.5	4.55(64)
O(2)	18f	0.1328(12)	0.2120(11)	0.13755(30)	2.23(16)
O(3)	18f	0.2156(12)	0.1436(12)	0.03938(36)	3.03(22)
O(4)	18f	0.3525(13)	0.4873(10)	0.07664(39)	2.87(17)
O(5)	18f	0.4645(11)	0.2649(12)	0.10991(31)	2.49(16)

Atom	Wyckoff position	X	Y	Z	U_{iso} x 100 (Å^2)
723 K					
Si(1)	3a	0	0	0	1.6(6)
Si(2)	6c	0	0	0.1834(10)	3.1(4)
Si(3)	6c	0	0	0.4365(7)	2.3(4)
P	18f	0.2854(10)	0.2713(8)	0.0909(4)	1.62(13)
O(1)	3b	0	0	0.5	5.26(67)
O(2)	18f	0.1352(10)	0.2125(10)	0.13745(29)	2.24(16)
O(3)	18f	0.2116(11)	0.1459(11)	0.03988(34)	2.73(19)
O(4)	18f	0.3490(12)	0.4865(10)	0.07636(38)	3.00(15)
O(5)	18f	0.4623(10)	0.2622(11)	0.11002(29)	2.19(14)

Atom	Wyckoff position	X	Y	Z	U_{iso} x 100 (Å^2)
873 K					
Si(1)	3a	0	0	0	0.99(42)
Si(2)	6c	0	0	0.1805(8)	2.10(35)
Si(3)	6c	0	0	0.4363(6)	1.91(35)
P	18f	0.2838(9)	0.2721(8)	0.0910(4)	1.65(13)
O(1)	3b	0	0	0.5	4.63(55)
O(2)	18f	0.1360(11)	0.2119(10)	0.13749(28)	2.54(17)
O(3)	18f	0.2154(10)	0.1470(11)	0.03978(32)	2.94(20)
O(4)	18f	0.3475(12)	0.4848(9)	0.07622(35)	2.88(15)
O(5)	18f	0.4651(10)	0.2650(10)	0.10832(27)	2.50(15)

Atom	Wyckoff position	X	Y	Z	U_{iso} x 100 ($Å^2$)
1073 K					
Si(1)	3a	0	0	0	2.2(5)
Si(2)	6c	0	0	0.1814(8)	2.9(4)
Si(3)	6c	0	0	0.4336(6)	2.5(4)
P	18f	0.2789(10)	0.2681(9)	0.0904(4)	2.70(14)
O(1)	3b	0	0	0.5	7.50(77)
O(2)	18f	0.1405(9)	0.2131(9)	0.13891(29)	3.05(15)
O(3)	18f	0.2109(10)	0.1450(11)	0.04042(34)	3.85(15)
O(4)	18f	0.3495(10)	0.4863(8)	0.07663(35)	3.89(17)
O(5)	18f	0.4625(9)	0.2642(10)	0.10961(26)	2.80(15)

APPENDIX 1E BOND VARIATION O-M(1)-O, M=GE OR SI

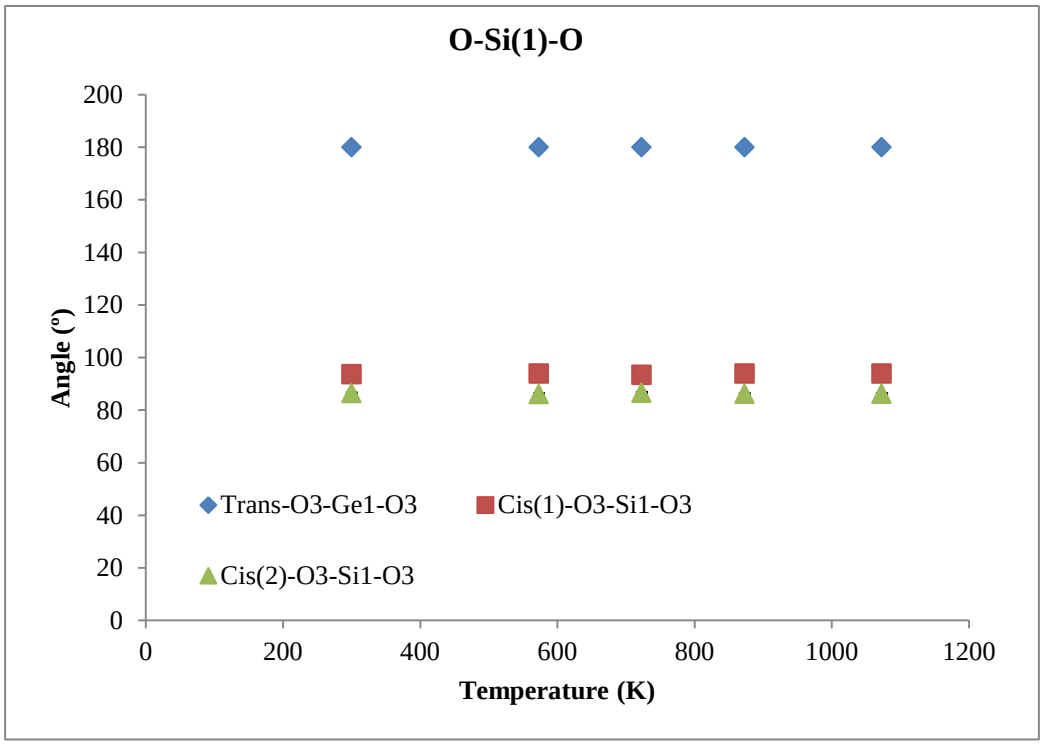

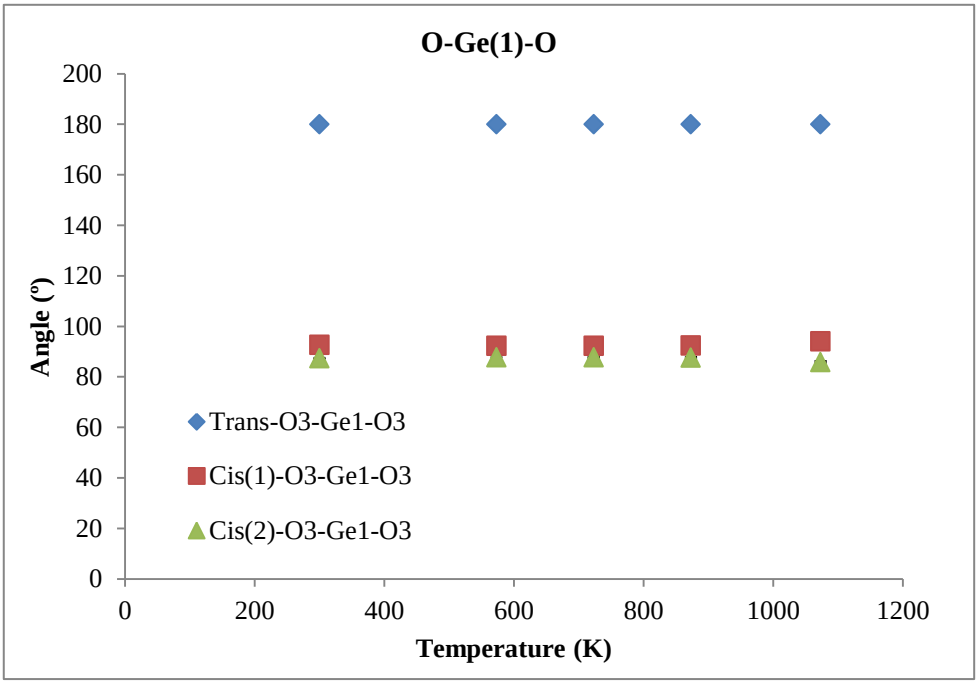

APPENDIX 1F BOND VARIATION – M(2)-O_6, M = GE(2) OR SI(2)

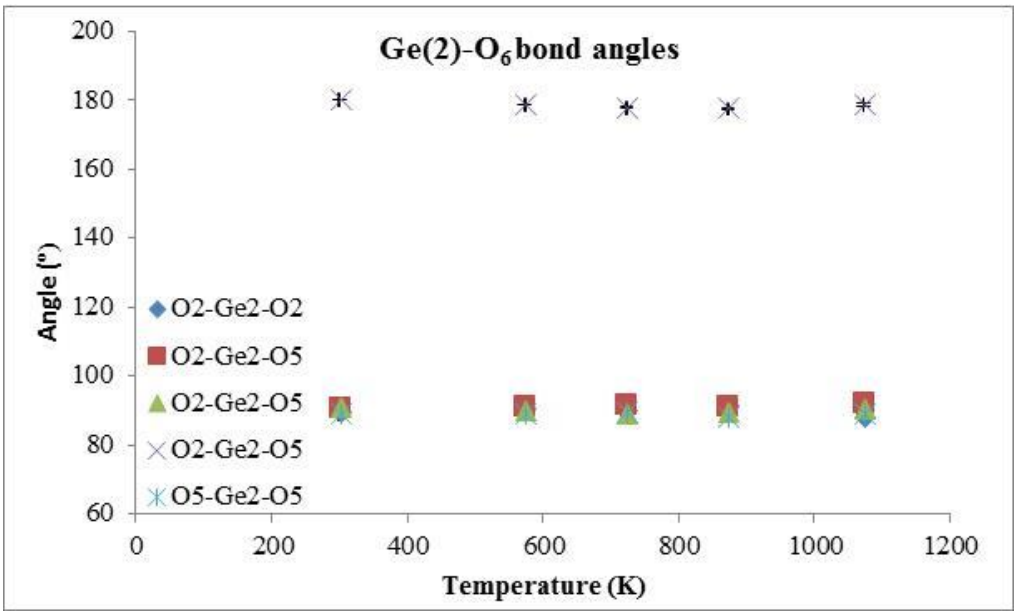

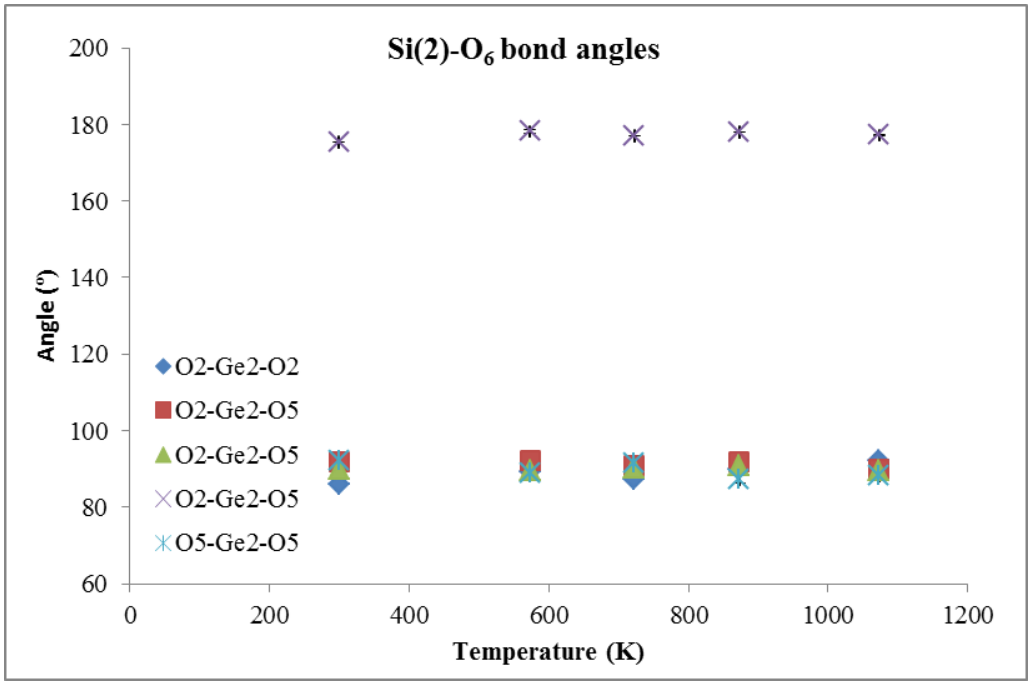

APPENDIX 1G BOND VARIATION M(3)-O_4, M(3) = GE(3) OR SI(3)

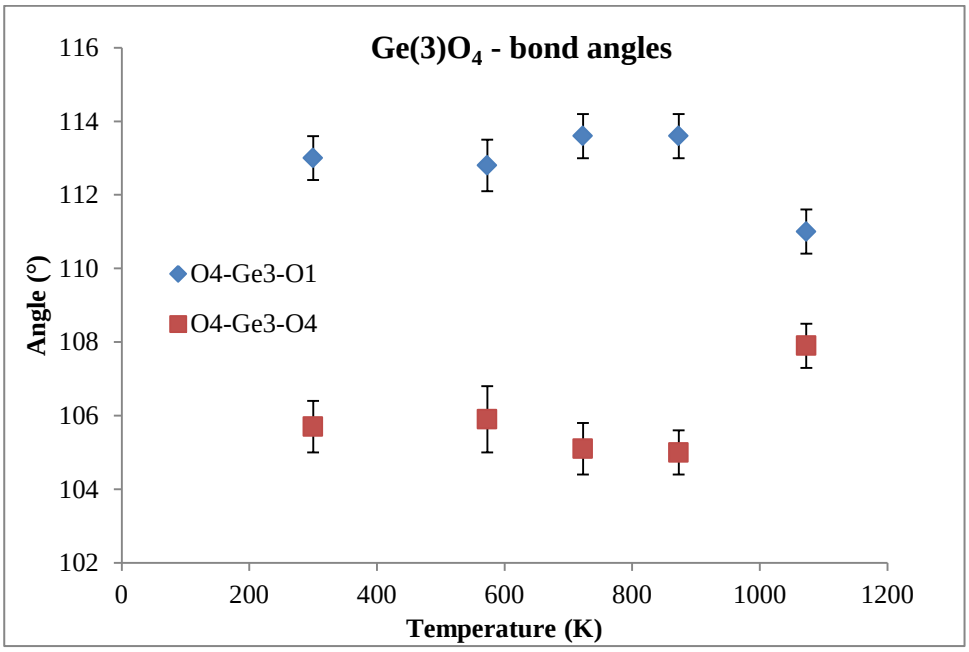

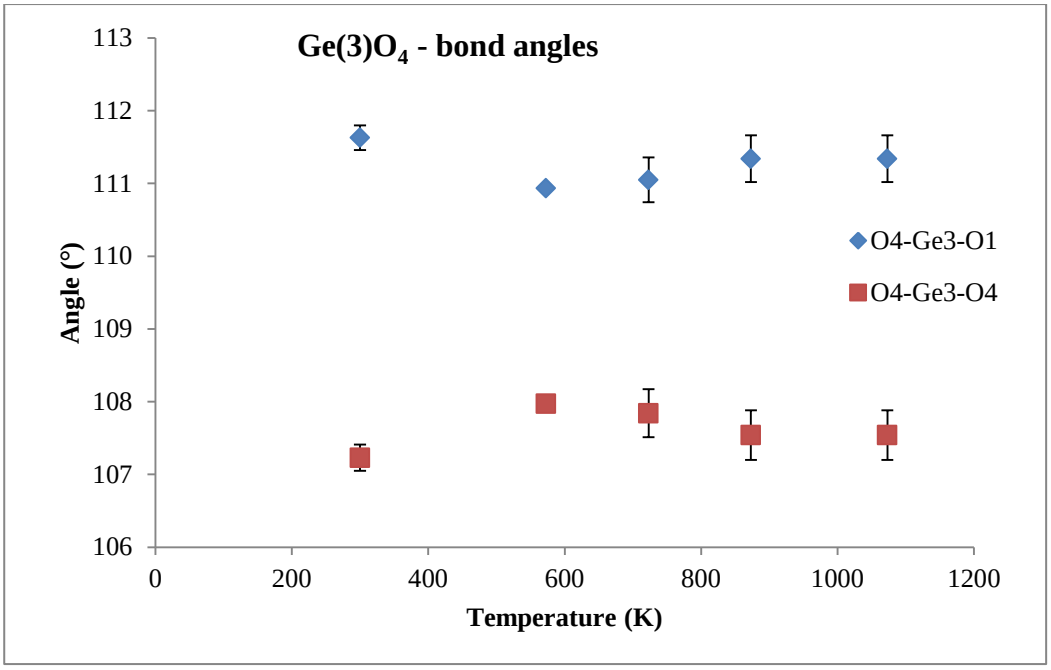

APPENDIX 1H PHOSPHATE BOND ANGLES

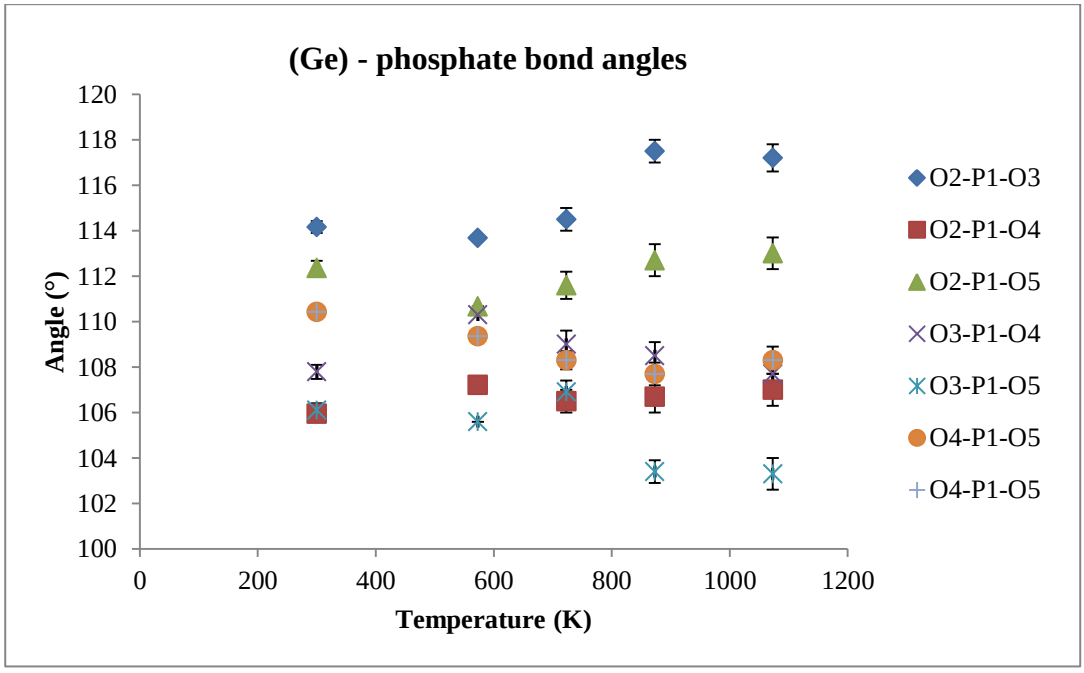

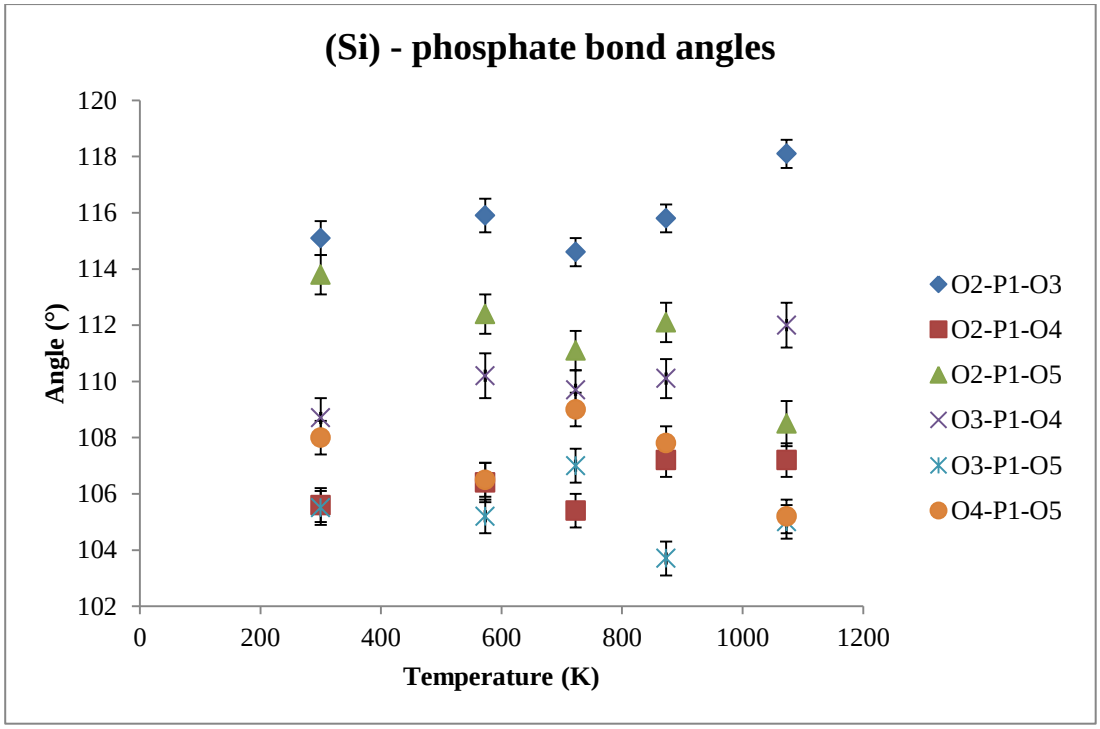
(Si) - phosphate bond angles
Angle (°)
120
118
116
114
112
110
108
106
104
102
0
200
400
600
800
1000
1200
Temperature (K)
O2-P1-O3
O2-P1-O4
O2-P1-O5
O3-P1-O4
O3-P1-O5
O4-P1-O5